Regulation of Natural Killer cell cytotoxicity by shedding of the Fc receptor CD16

A thesis submitted to the University of Manchester for the degree of Doctor of Philosophy in the Faculty of Biology, Medicine and Health

2017

Katja Srpan

School of Biological Sciences

The University of Manchester

Contents

List of Figures 6
List of tables 9
Abbreviations 10
Abstract 14
Declaration 15
Copyright statement 16
Publications 17
Acknowledgements 18
Chapter 1: Introduction 20
1.1. Natural Killer cells 20
1.1.1. NK cell development and education 22
1.1.2. NK cells in diseased conditions 23
1.1.3. Memory NK cells 26
1.2. NK cell effector functions 28
1.2.1. Cytotoxicity 28
1.2.2. Cytokine and chemokine production 30
1.2.3. Hierarchy of NK cell responses 31
1.3. Immunological synapse 31
1.3.1. Assembly of the immune synapse 32
1.3.2. Cytolytic immune synapse 33
1.3.3. Inhibitory immune synapse 35
1.4. NK cell activating receptors 35
1.4.1. CD16 (FcγRIII) 38
1.5. NK cell inhibitory receptors 45
1.6. Aims 48
Chapter 2: Materials and Methods 49
2.1. Cell culture 49
2.1.1. Human primary NK cells 49
2.1.2. Cell lines 49
2.1.3. Culturing of cell lines 50
2.2. Molecular Biology 50
2.2.1. Plasmid construction 50
2.2.2. Retroviral transduction of NK92 cell line 52
2.3. Antibodies and recombinant proteins 53
2.3.1. Antibodies 53

2.3.2. Directly labelled antibodies 54
2.3.3. Fluorescent labelling of anti-CD16 antibody (clone SP175) 55
2.3.4. Recombinant proteins 56
2.4. Functional assays 56
2.4.1. Preparation of coated slides for NK cell stimulation 56
2.4.2. Perforin capture assay 57
2.4.3. Flow Cytometry 58
2.4.4. IFN-γ detection by enzyme-linked immunosorbent assay (ELISA) 61
2.4.5. Soluble CD16 detection by enzyme-linked immunosorbent assay (ELISA) 61
2.5. Confocal microscopy 62
2.5.1. Cell migration assay 62
2.5.2. Internal reflection microscopy (IRM) 62
2.5.3. Live imaging in microwells 63
2.5.4. Imaging F-actin rings 63
2.5.5. Confocal microscopy 64
2.6. TIRF and GSD microscopy 64
2.6.1. Preparation of the sample 64
2.6.2. TIRF and GSD imaging 65
2.6.3. GSD data processing 65
2.6.4. Cluster analysis of GSD images 67
2.6.5. Statistical analysis 69
Chapter 3: Effect of shedding CD16 on NK cell serial killing 70
3.1. Introduction 70
3.2. Aims and objectives 72
3.3. Results 73
3.3.1. Glass surfaces coated with activating ligands trigger NK cell degranulation 73
3.3.2. Timing of degranulation is different on rituximab than on MICA 78
3.3.3. Higher ligand concentration does not increase perforin secretion 80
3.3.4. Rituximab and MICA trigger similar proportion of NK cells to degranulate 82
3.3.5. The sequence of receptor ligation determines the amount of secreted perforin 86
3.3.6. NK cell stimulation affects receptor expression levels 89
3.3.7. CD16 is shed from cell surface upon NK cell activation 95
3.3.8. Pre-activation of NK cells on slides reduces their cytotoxicity towards target cells 96

3.3.9. The order of target cell engagement determines the efficiency of serial killing 99
3.3.10. CD16 loss is long-lived 107
3.3.11. IL-10 improves CD16 recovery 109
3.4. Discussion 113
3.4.1. Summary of results 113
3.4.2. Significance of the results 114
Chapter 4: Effects of CD16 shedding on ADCC synapse 119
4.1. Introduction 119
4.2. Aims and objectives 121
4.3. Results 122
4.3.1. NK cells do not form actin rings on rituximab-coated surface 122
4.3.2. Cells spread differently on rituximab-coated surface than on MICA-coated surface 125
4.3.3. NK cells are more motile on rituximab-coated surface than on MICA-coated surface 127
4.3.4. Inhibition of CD16 shedding does not affect NK cell cytotoxicity, but it does increase the production of IFN-γ on rituximab coated slides 134
4.3.5. Donors that do not shed CD16 136
4.3.6. ADAM17-induced cleavage promotes NK cells detachment from opsonized targets 139
4.3.7. Analysis of $CD16^{+}$ NK92 cell line 148
4.3.8. Detachment of NK92/CD16-S197P from opsonized targets is impaired 151
4.3.9. NK92/CD16-S197P form more F-actin rings on rituximab-coated surface 154
4.4. Discussion and further directions 156
4.4.1. Summary of results 156
4.4.2. Significance of results 157
Chapter 5: Nano-scale organisation of CD16 at the NK cell surface 160
5.1. Introduction 160
5.2. Aims and objectives 162
5.3. Results 163
5.3.1. Optimisation of CD16 staining for super-resolution microscopy 163
5.3.2. GSD data processing 167
5.3.3. Quantification of the surface protein distribution by spatial point pattern analysis 173
5.3.4. Nanoscale organization of CD16 on rituximab-coated slide 177
5.3.5. Super-resolution imaging of intracellular CD16 181

5.3.6. CD16 nanoscale distribution upon the inhibition of CD16 shedding 184
5.4. Discussion and further directions 188
5.4.1. Summary of results 188
5.4.2. Relation to earlier studies 188
5.4.3. Future directions 192
Chapter 6: Final conclusions 194
Bibliography 196

Word Count

60,422 words in total

48,851 words excluding bibliography

List of Figures

Figure 1.1:	NK cell recognition of target cells …….	21
Figure 1.2:	Schematic representation of the formation and function of the NK cell lytic synapse …….....	34
Figure 1.3:	NK cell mediated ADCC ……..…	38
Figure 1.4:	CD16 shedding ……..…	40
Figure 1.5:	CD16 cleavage by ADAM17 ……...…	42
Figure 2.1:	Site directed mutagenesis …….….....	51
Figure 2.2:	Sequential stimulation on coated slides ……..…	57
Figure 2.3:	Principle of the assay of killing of Daudi with NK cells pre-stimulated on slides …….…..	60
Figure 2.4:	Schematic representation of sequential stimulation with target cells ……..……..	60
Figure 2.5:	GSD image reconstruction workflow ……..……..	66
Figure 3.1:	Rituximab and MICA coated surfaces trigger IFN-γ production from NK cells ……..……..…..	73
Figure 3.2:	Perforin capture assay ……..…..….	75
Figure 3.3:	Controls for perforin capture assay ……..……..…	77
Figure 3.4:	Time course of perforin secretion on rituximab …..……..…	78
Figure 3.5:	Time course of perforin secretion on MICA ……..……..….	79
Figure 3.6:	Rituximab concentration affects the extent of perforin secretion ……..…..….	80
Figure 3.7:	MICA concentration affects the extent of perforin secretion	81
Figure 3.8:	Proportion of perforin secreting cells …….	83
Figure 3.9:	Surface levels of CD107a upon NK cell stimulation ……	85
Figure 3.10:	Perforin secretion per cell upon sequential stimulation ….....	87
Figure 3.11:	Perforin secretion per cell upon sequential stimulation ….....	88
Figure 3.12:	Surface expression of NK cell markers …….	89
Figure 3.13:	Surface expression of NK cell markers upon non-activating procedure ……	91
Figure 3.14:	CD16 expression upon sequential stimulation …….….	93
Figure 3.15:	NKG2D expression upon sequential stimulation ……..	94
Figure 3.16:	Soluble CD16 upon NK cell stimulation …….	95

Figure 3.17: Rituximab and MICA on Daudi cells ……..…….. 96
Figure 3.18: Gating strategy for Daudi population in co-culture with NK cells ……..…. 97
Figure 3.19: Target cell death upon incubation with pre-stimulated NK cells …….. 98
Figure 3.20: Gating strategy for Daudi-violet population ……... 99
Figure 3.21: CD16 and NKG2D on NK cells upon incubation Daudi cells .. 100
Figure 3.22: Target cell death upon incubation with pre-stimulated NK cells ……..… 102
Figure 3.23: Time-lapse imaging of NK cells Daudi-rituximab and Daudi-MICA interactions in microchips ……..… 104
Figure 3.24: Efficiency of NK cell cytotoxicity in serial killing …… 106
Figure 3.25: CD16 expression over 24h after stimulation ……. 108
Figure 3.26: CD16 recovery post rituximab-stimulation upon IL-10 or IL-18 treatment ……..…. 110
Figure 3.27: CD16 recovery post MICA-stimulation upon IL-10 or IL-18 treatment ……..…….. 111
Figure 3.28: CD16 levels upon IL-10 or IL-18 treatment …… 112
Figure 4.1: F-actin accumulation ..……..… 123
Figure 4.2: Time course of F-actin accumulation on rituximab …….. 124
Figure 4.3: Live imaging of the immunological synapse formation on rituximab and MICA ……..… 126
Figure 4.4: Molecular structure of TAPI-0 ……..…… 127
Figure 4.5: TAPI-0 titration ..…….... 128
Figure 4.6: TAPI-0 does not affect NKG2D or cell viability ……..…. 129
Figure 4.7: NK cell motility on coated surfaces …… 131
Figure 4.8: Effect of rituximab concentration on NK cell motility …… 132
Figure 4.9: Effect of MICA concentration on NK cell motility ……. 133
Figure 4.10: TAPI-0 affects IFN-γ secretion on rituximab, but has no effect on NK cell degranulation ……..…. 135
Figure 4.11: Cells that do not cleave CD16 upon NK cell activation …….. 136
Figure 4.12: Motility of NK cells from donor that did not shed CD16 …….. 138
Figure 4.13: Time-lapse imaging in small microwells with NK cells and opsonized Daudi targets ……... 140

Figure 4.14: Killing of opsonized Daudi-rituximab cells in small microwells ……... 141
Figure 4.15: The detachment from opsonised Daudi cells is impaired upon the inhibition of CD16 shedding, imaged in small microwells …… 142
Figure 4.16: Time-lapse imaging in large microwells with NK cells and Daudi-rituximab ……. 143
Figure 4.17: Inhibition of CD16 shedding does not affect target cell lysis .. 144
Figure 4.18: NK cell detachment from Daudi-rituximab was impaired when CD16 shedding was inhibited, as imaged in large microwells ……... 146
Figure 4.19: NK cell death upon the conjugate formation ……. 147
Figure 4.20: NK92 cell line ……..… 148
Figure 4.21: NK92 transduced with CD16-WT and CD16-S197P ……... 149
Figure 4.22: Degranulation of NK92/CD16-WT and NK92/CD16-S197P …… 150
Figure 4.23: Time-lapse imaging of NK92/CD16+ cells with Daudi-rituximab in large microwells …… 152
Figure 4.24: Interactions between NK92/CD16+ cells and opsonized Daudi cells in large microwells ……. 153
Figure 4.25: Peripheral F-actin rings on rituximab coated surface ……. 154
Figure 5.1: CD16 staining with two different clones of anti-CD16 AF647 mAbs …… 164
Figure 5.2: Specificity of anti-CD16 (clone 3G8) AF647 mAb staining …. 165
Figure 5.3: Expression of CD16 on primary NK cells ……... 166
Figure 5.4: GSD data post-processing flowchart ……. 168
Figure 5.5: Parameters used for CD16 GSD data filtering ……. 169
Figure 5.6: Drift correction by image cross-correlation …… 170
Figure 5.7: Elimination of re-appearing events by merging …… 171
Figure 5.8: Resolution improvement from TIRF to GSD microscopy …… 172
Figure 5.9: Post-detection GSD data analysis workflow ……. 174
Figure 5.10: Selection of a binary threshold for CD16 cluster analysis ….. 176
Figure 5.11: Analysis of CD16 clustering on resting and activating surfaces ……... 178
Figure 5.12: Representative maps of randomised CD16 data ……. 179
Figure 5.13: Quantitative analysis of CD16 clustering ..…….. 180

Figure 5.14: Confocal images of CD16, stained with SP175 clone ……. 182
Figure 5.15: Comparison of CD16 clusters stained with 3G8 and SP175 anti-CD16 clones …….. 183
Figure 5.16: Clustering of the intracellular and extracellular portion of the surface CD16 …… 184
Figure 5.17: Clustering of CD16 on resting and rituximab-activated NK cells …….. 185
Figure 5.18: Analysis of CD16 clusters upon the receptor ligation …….. 187

List of tables

Table 1.1: Activating receptors and their ligands……. 37
Table 1.2: Inhibitory receptors and their ligands…….. 46
Table 2.1: Primers used for site directed mutagenesis…… 51
Table 2.2: Monoclonal antibodies used for functional experiments…… 53
Table 2.3: Monoclonal antibodies used for IFN-γ and soluble CD16 detection by ELISA……... 53
Table 2.4: Directly labelled monoclonal antibodies used for flow cytometry and microscopy ……. 54
Table 2.5: Recombinant proteins used for NK cell stimulation……. 56

Abbreviations

ADAM	A disintegrin and metalloproteinase
ADCC	Antibody-dependent cellular cytotoxicity
ADCP	Antibody-dependent cellular phagocytosis
AF	Alexa Fluor
APC	Antigen presenting cell
ATP	Adenosine triphosphate
AU	Arbitrary unit
BAFF	B-cell activating factor
BCR	B cell receptor
BiKe	Bispecific killer engagers
BSA	Bovine serum albumin
CCL	C-C chemokine ligand
CDC	Complement-dependent cytotoxicity
CHS	Contact hypersensitivity
CTK	Cytokine
CTL	Cytotoxic T lymphocyte
CXCL	C-X-C chemokine ligand
dAb	Domain antibody
DAP	DNAX activation protein
DC	Dendritic cell
DCM	Dead cell marker
DISC	Death-inducing signalling complexes
DMEM	Dulbecco's Modified Eagle Medium
DMSO	Dimethyl sulfoxide
DNA	Deoxyribonucleic acid
E:T	Effector to target ratio
EBV	Epstein-Barr virus
EC	Extracellular
EGFR	Epidermal growth factor receptor
ELISA	Enzyme-Linked ImmunoSorbent Assay
EMCCD	Electron-multiplying charge-coupled device
Fab	The antigen-binding fragment
F-actin	Filamentous actin
FasL	Fas ligand

FBS	Foetal bovine serum
Fc	Fragment crystallisable region
FcR	Fc receptor
FcγR	Fc gamma receptor
GM-CSF	Granulocyte-macrophage colony-stimulating factor
gMFI	Geometric mean fluorescence intensity
GSD	Ground-state depletion
HCMV	Human cytomegalovirus
HIV	Human immunodeficiency virus
HLA	Human leukocyte antigen
HPA	Hypothalamic–pituitary–adrenal
HPV	Human papillomavirus
HSV	Herpes simplex virus
IC	Intracellular
ICAM	Intercellular cell adhesion molecule
IFI	Integrated fluorescence intensity
IFN	Interferon
Ig	Immunoglobulin
IL	Interleukin
IQR	Interquartile range
IRM	Interference reflection microscopy
IS	Immune synapse
ITAM	Immune tyrosine-based activating motif
ITIM	Immune tyrosine-based inhibitory motif
KIR	Killer-cell immunoglobulin-like receptor
KLRG1	Killer-cell lectin like receptor G1
LAMP	Lysosomal-associated membrane protein
LAT	Linker for activation of T cells
LB	Luria-Bertani
Lck	Lymphocyte-specific protein tyrosine kinase
LFA	Lymphocyte function-associated antigen
mAb	Monoclonal antibody
MCAO	Middle cerebral artery occlusion
MCMV	Mouse cytomegalovirus
MEM	Minimum Essential Medium
MFI	Mean fluorescence intensity

MHC	Major histocompatibility complex
MICA/B	MHC class I polypeptide-related sequence A/B
MMP	Matrix metalloproteinase
MTOC	Microtubule organizing centre
MULT	Murine UL16 binding protein-like transcript
NA	Numerical aperture
NCR	Natural cytotoxicity receptors (of the family NKp30/NKp46/NKp44)
NIR	Near infra-red
NK	Natural killer
NKT	Natural killer T
NKG2D/A	NK group 2 member D/A
NOD	Non-obese diabetic
PLL	Poly-L-lysine
PBMC	Peripheral blood mononuclear cells
PBS	Phosphate-buffered saline
PCR	Polymerase chain reaction
PEG	Polyethylene glycol
PFA	Paraformaldehyde
PSF	Point spread function
RAG	Recombination-activating gene
RPMI	Roswell Park Memorial Institute 1640 media
RT	Room temperature
Rtx	Rituximab
scFv	Single-chain variable fragment
SD	Standard deviation
SEM	Standard error of the mean
SHP	SH2 domain-containing tyrosine phosphatase
SLE	systemic lupus erythematosus
SMAC	supramolecular activation cluster
Syk	spleen tyrosine kinase
TACE	Tumour necrosis factor-alpha-converting enzyme
TCR	T cell receptor
TIRF	Total internal reflection fluorescence
TNF	Tumour necrosis factor
TRAIL	Tumour necrosis factor-related apoptosis-inducing ligand
TriKe	Trispecific killer engagers

ULBP	UL-16 binding proteins
US	Unstimulated
VZV	Varicella Zoster virus
WNV	West Nile Virus
WT	Wild-type
ZAP-70	ζ-associated protein kinase of 70 kDa

Abstract

Natural Killer (NK) cells are cytotoxic lymphocytes that can recognize and kill virally infected or tumour transformed cells by the secretion of cytolytic granules containing perforin. An individual NK cell can kill several target cells sequentially. Each target cell can trigger NK cell activation via different activating ligands and here we report that the order in which ligands are encountered affects the NK cell response. When NK cells are repeatedly activated via their Fc receptor CD16, with the therapeutic antibody rituximab, perforin secretion decreases with each stimulation. However, perforin secretion is restored to its initial level upon subsequent activation by MICA, which ligates NKG2D. Repeated stimulation of NK cells via MICA also decreases the degranulation capacity of NK cells but, strikingly, this effect cannot be rescued by a subsequent stimulation with rituximab. The strength of perforin secretion is also translated to killing of Daudi target cells, expressing different ligands. When Daudi, opsonised with rituximab is the first target NK cell encounters, the sequential killing of another opsonised rituximab or Daudi, expressing MICA will not be affected. But, when Daudi-MICA is met first, the consecutive killing of Daudi-MICA as well as Daudi-rituximab will be impaired. We found that the mechanism underlying these differential outcomes involves shedding of CD16, which occurs upon NK cell activation through both, CD16 and NKG2D. Shedding of CD16 renders the cells insensitive to further activation via that receptor but they remain competent for further activation through NKG2D. Interestingly, however, we also identified the beneficial role of CD16 shedding for NK cell serial killing. NK cells are more motile on rituximab-coated surfaces than on MICA-coated surfaces and their migration speed decreases upon inhibition of CD16 shedding. Moreover, the inhibition of CD16 shedding also prevents the NK cell detachment from rituximab opsonised Daudi cells. Thus, the shedding of the receptor can serve to augment NK cell motility to move between target cells. Efficient NK cell detachment also correlated with their increased survival. Finally, we report that CD16 is constitutively organised in small, dense nanoclusters and that the ligation with rituximab does not affect their spatial distribution. Despite the shedding of the receptor, leading to less protein molecules at the surface, the area of these clusters remains the same. Together these data suggest that CD16 shedding hinders NK cell cytotoxicity against opsonised targets, but promotes their movements between different targets. Thus, receptor shedding is important for efficient NK cell serial killing. Manipulation of CD16 shedding, perhaps by boosting its recovery, might therefore represent an important target for NK cell-based therapies including treatments with therapeutic antibodies.

Declaration

No portion of the work referred to in the thesis has been submitted in support of an application for another degree or qualification of this or any other university or other institute of learning.

The data presented in this thesis are my own work, with the following exceptions described below.

- IRM imaging in Chapter 4 was performed in our laboratory at the University of Manchester by Mezida Saeed.
- In Chapter 5, David J. Williamson wrote the custom MATLAB scripts used for the super-resolution data analysis.

Copyright statement

i. The author of this thesis (including any appendices and/or schedules to this thesis) owns certain copyright or related rights in it (the “Copyright”) and s/he has given The University of Manchester certain rights to use such Copyright, including for administrative purposes.

ii. Copies of this thesis, either in full or in extracts and whether in hard or electronic copy, may be made only in accordance with the Copyright, Designs and Patents Act 1988 (as amended) and regulations issued under it or, where appropriate, in accordance with licensing agreements which the University has from time to time. This page must form part of any such copies made.

iii. The ownership of certain Copyright, patents, designs, trade marks and other intellectual property (the “Intellectual Property”) and any reproductions of copyright works in the thesis, for example graphs and tables (“Reproductions”), which may be described in this thesis, may not be owned by the author and may be owned by third parties. Such Intellectual Property and Reproductions cannot and must not be made available for use without the prior written permission of the owner(s) of the relevant Intellectual Property and/or Reproductions.

iv. Further information on the conditions under which disclosure, publication and commercialisation of this thesis, the Copyright and any Intellectual Property University IP Policy
(see http://documents.manchester.ac.uk/display.aspx?DocID=24420), in any relevant Thesis restriction declarations deposited in the University Library, The University Library’s regulations
(see http://www.library.manchester.ac.uk/about/regulations/) and in The University’s policy on Presentation of Theses.

Publications

Srpan, K., Saeed, M., Cartwright, A.N.R., Guldevall, K., Frisk, T., Dos Santos Cruz De Matos, G., Önfelt, B., Davis, D.M. Unzipping the Natural Killer cell immune synapse by shedding CD16. *Submitted*.

Acknowledgements

Doing PhD was one of the most rewarding and yet, most difficult experiences in my life. There is a long list of people, without whom I would not be here and I am very grateful to you.

First of all, I would like to thank my supervisor, Professor Daniel M. Davis for giving me the opportunity to pursue a PhD degree. Dan, thank you for granting me the freedom to explore and yet, to make sure I did not lose the direction. I am grateful for all your guidance, support and inspiration. By always expecting the best from me you have helped me to become a better scientist.

Thanks also to my advisor, Dr. Mark Travis for valuable feedback on my work. Furthermore, my appreciation goes to those within the Manchester Collaborative Centre for Inflammation Research (MCCIR) and Faculty of Life Sciences who offered their advice on this project, as part of their internal assessments and other meetings. Also, I would like to thank Fiona for her administrative support, whenever I needed it.

In addition, I would also want to thank my industrial collaborator Gabriela Dos Santos Cruz De Matos for giving me the opportunity to experience work in big pharma. Thank you for your kind welcome in Stevenage and for your contributions to my work.

Moreover, I would like to show appreciation to my collaborators in Sweden, Bjorn Önfelt and his group. Bjorn, Karolin, Quentin and Per, thank you for your warm reception in cold Stockholm. And more importantly, thank you for teaching me the techniques, for engaging in helpful discussions and giving me valuable chips, which have all been crucial for the work presented in this thesis.

Further, I would like to thank my lab members - Mezida, Katie, Ania, Eric, Kevin, Danny, Ashley, Pippa, Dave and Dave, Adam, Charlotte, Kat, Sam, Alex, Filipa, and Stefan - who made the lab a truly enjoyable place to work in! I am also grateful for all your contributions to my work and for the valuable discussions we had during the endless incubation times and elsewhere. My special thanks go to Mezida. Mezida, I could not wish for a better person to take this journey with. It was a great pleasure sharing the work space with you. Not only that you constantly took time to evaluate my work with me, challenged my ideas and inspired new ones, you are also a wonderful friend. You are a person that I can always count on, someone that was

supporting me in my hardest moments and got excited with me in happy times. I am truly grateful for everything you have done for me and for you being you!

I would also like show my appreciation to my friends in Manchester that kept my spirits up. To name a few, Rajia thank you for always having something sweet in your office, Karen thank you for listening to all my existential crisis-problems with a big smile on your face and Pablo, thank you for sharing the La Tasca passion with me. Thanks to everyone from Michael Smith Crew for all the pints and the fun that came with them. Also, thanks to the dance school La Suerte for providing a perfect distraction from my work and to all with whom I shared the dance-floor. Thanks to Michal, Diego, Araceli, Iza, Tiago and Jessica for teaching me the moves, and to Michal, Mike and Ivelin who believed in me and gave me the opportunity to teach it. I loved every part of it!

I am extremely grateful to my family; mum and dad, you have always encouraged me to follow my dreams. You have never stopped believing in me and have always given me a lot of support in all my endeavours. You have inspired my curiosity for the world and nature from my young days on and have thought me not to give up when times get rough. Thank you for making me a person I am today and for all the love you are giving me! Teja, Nik, Zan, and Boro – you make me wish coming home more often and help me see what truly matters in life. Thanks to my grandparents, who have always showed me how proud they have been of every little step I have made. Thank you for your love and support. I would also like to mention my grandfather, who knew that will not live until the day I finish my PhD. Ata, thank you for your loving me and patiently teaching me from my early steps on. I am also grateful to my uncles, aunt and their families and Miha's family for their support and happy moments we share every time I come home.

Finally, I would like to thank my wonderful boyfriend Miha. Thank you for always being there for me, even when far apart. Thank you for not giving up on me every time I turned up late, because I was stuck in the lab. And thank you for keep loving me, no matter what.

Chapter 1: Introduction

1.1. Natural Killer cells

Natural Killer cells (NK cells) are cytotoxic lymphocytes, considered as an arm of the innate immune system. They comprise 5 - 15 % of all peripheral blood lymphocytes (Lanier et al., 1986, Walzer et al., 2007). NK cells were first discovered in the 1970s in mice as cells exerting significant cytotoxicity towards tumour cells without antigen specific receptors and were initially thought to be an experimental artefact in T cell cytotoxicity assay (Oldham and Herberman, 1973, Herberman et al., 1975a, Kiessling et al., 1975). Soon after they were also identified in humans (Pross and Jondal, 1975) and were later characterized as non-adherent, non-phagocytic, large granular lymphocytes (LGL) (Trinchieri, 1989).

Today, human NK cells are identified by the absence of the T-cell receptor complex CD3, the presence of neural cell adhesion molecule CD56, and the expression of a member of natural cytotoxicity receptor (NCR) family NKp46. $CD3^{-}CD56^{+}NKp46^{+}$ can be further divided into two major subsets according to the surface density of CD56. Around 90 % of all NK cells from peripheral blood and spleen have low expression of CD56 ($CD56^{dim}$) and are fully mature. They also express low affinity IgG Fc receptor CD16 (FcγRIIIa) and perforin and are effective in cell killing while being less effective in the production of cytokines and chemokines. The other 10% of NK cells have a higher expression of CD56 ($CD56^{bright}$) and little or no CD16 at their surface, and are most abundant in lymph nodes and tonsils. They are immature and poorly cytotoxic, but they can secrete high amounts of cytokines and chemokines upon activation (De Maria et al., 2011, Orange, 2013, Vivier et al., 2008, Cooper et al., 2001b).

NK cells can discriminate between healthy and diseased cells by a multitude of germ-line encoded inhibitory and activating receptors expressed on their surface. The balance between the inhibitory and activating signals received from a target cell defines the outcome of individual cell-cell interaction (Figure 1.1) (Tomasello et al., 2000, Vivier et al., 2004, Long et al., 2013). Ligation of inhibitory receptors on healthy cells by “self-molecules”, instruct the NK cell to leave the target unharmed. And contrary, when activating receptors bind to stress-induced ligands, or when the “self-molecule” is missing, NK cell cytolytic machinery is triggered. A diseased cell will be killed by the release of cytolytic granules into the interface between the cells.

Additionally, NK cells can also respond to a milieu of cytokines that contribute to shaping the adaptive immune responses (Vivier et al., 2008).

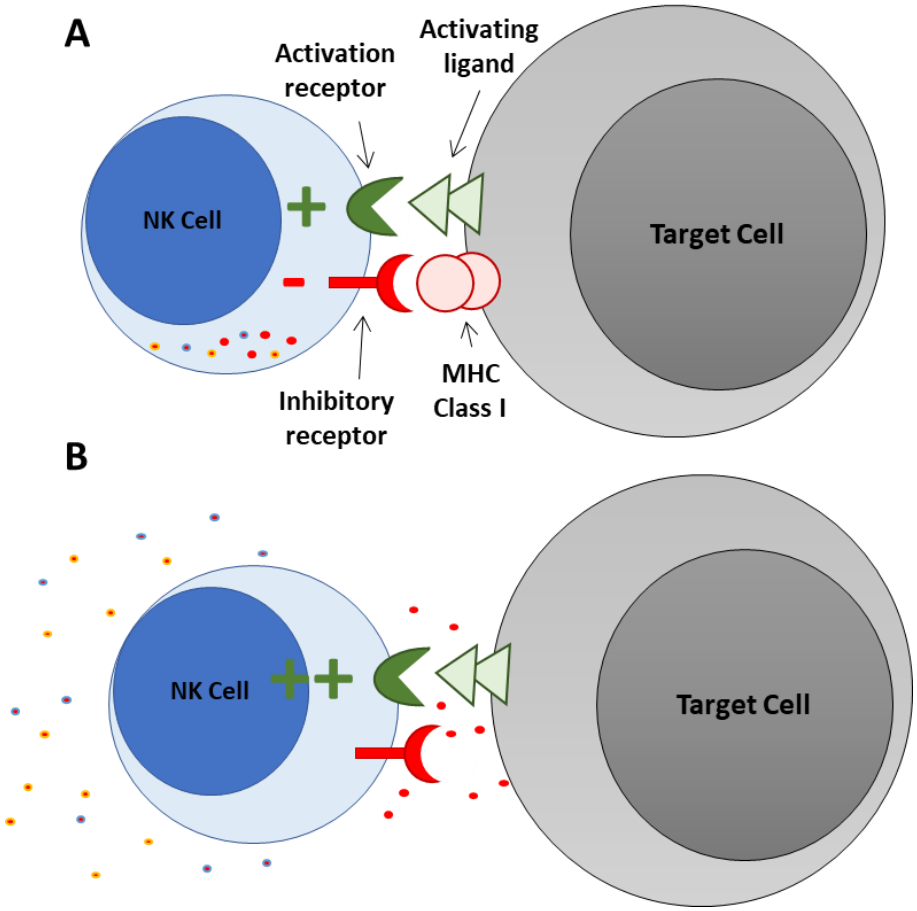

Figure 1.1*:* NK cell recognition of target cells. Schematic illustration of how NK cell receptors are used to detect diseased target cells. **(A)** NK cells are selectively tuned to constitutive levels of activating and inhibitory ligands on normal cells, to maintain tolerance towards healthy cells. Healthy cells will typically present only inhibitory ligands. When activating and inhibitory ligands are present, the outcome of the interaction depends on the balance between both signals. **(B)** Presence of only ligands for the activating receptors in the absence of self-MHC leads to target cell lysis and/or cytokine release.

1.1.1. NK cell development and education

Together with B and T cells, NK cells constitute the third major lineage of lymphocytes originating from the common lymphoid progenitors. They develop primarily in bone marrow and unlike T cells, do not require the thymus for their development (Herberman et al., 1975b, Kiessling et al., 1975, Su et al., 1993). In humans, a $CD34^{+}$ population of haematopoietic precursor cells was reported to develop into $CD56^{high}$ NK cells in lymph nodes (Freud et al., 2005). NK cells are believed to be relatively short-lived with a turnover in blood of around 2 weeks (Zhang et al., 2007b).

There are likely more than two billion NK cells circulating in an adult at a time (Blum and Pabst, 2007). They can also be found in peritoneal cavity, spleen, liver, lung, lymph nodes, thymus, and in uterus during gestation.

Their development and maturation is regulated by several transcription factors. Ets-1, Id2, Ikaros and PU.1 have been associated with their generation, Gata-3 and IRF-2 have been shown to contribute to maturation of immature NK cells and CEBP-γ, MEF and MITF are involved in functional differentiation of matured NK cells (Barton et al., 1998, Boggs et al., 1998).

Several cytokines have been shown to impact NK cells homeostasis and function. IL-15 is thought to be essential for NK-cell differentiation, proliferation, survival, and activation (Ma et al., 2006, Di Santo, 2006, Farag and Caligiuri, 2006, Mrozek et al., 1996, Waldmann et al., 2001). IL-2 acts as growth factor for NK cell progenitors and mature NK cells and contributes to their cytolytic functional maturation by inducing the production of NK cell effector molecules and enhancing NK cell lytic activity (Freud et al., 2005). IL-21 has been reported to favour the expansion of the cytotoxic $CD56^{dim}CD16^{+}$ NK cell subset and to augment its cytotoxicity (Parrish-Novak et al., 2000, Brady et al., 2004).

NK cells' tightly controlled effector function is acquired through the process termed licensing, or education. This involves the recognition of major histocompatibility (MHC) class I ligands by inhibitory NK cell receptors, as well as the interactions with other molecules expressed on stromal and haematopoietic cells (Schönberg et al., 2011, Höglund and Brodin, 2010, Kumar and McNerney, 2005). This founds a repertoire of educated NK cells with permanent expression of a distinct combination of available inhibitory receptors (Johansson et al., 1998). Once mature, NK cells exit the bone marrow and are trafficked to lymphoid and non-lymphoid tissues via chemokines, in order to perform their effector functions as innate sentinels (Vivier et al., 2008).

The educated NK cells are fully functional, displaying dynamic migration behaviour and capable of making multiple cytolytic contacts with diseased cells (Forslund et al., 2015). On the other hand, uneducated cells are less dynamic, unable to recognize endogenous MHC-I and upon the ligation of activating receptors they have been shown to be hypo-responsive (Cooley et al., 2007, Anfossi et al., 2006, Forslund et al., 2015). Such a hypo-responsive state is characteristic of all NK cells in MHC-I-deficient mice and humans (Furukawa et al., 1999, Liao et al., 1991).

However, cytokine stimulation can induce normal effector function and expression of inhibitory receptors in uneducated cells (Campbell and Hasegawa, 2013). Uneducated NK cells can secrete the same levels of IFN-γ as educated NK cells during *Listeria monocytogenes* infection (Fernandez et al., 2005) and uneducated murine NK cells respond more strongly against mouse cytomegalovirus (MCMV) infection (Orr et al., 2010). Thus, the hypo-responsiveness of uneducated NK cells can be debated.

1.1.2. NK cells in diseased conditions

NK cells have diverse physiological functions, of which one of the most important ones is the immuno-surveillance of our body. In the circulation, NK cells are mainly in the resting state, but different chemo-attractants can induce their migration into tissues where they screen for abnormal cells (Glas et al., 2000, Fogler et al., 1996, Robertson, 2002).

The significance of NK cell immune surveillance is most apparent in patients with genetic NK cell deficiencies (NKD), where the abnormalities in NK cells result in severe infections, while their complete absence results in fatal viral infections during childhood (Buckley et al., 1997, Orange, 2013). From 19 reported cases of an absence of NK cells and their functions, 42% died prematurely and 53% suffered severe consequences of herpesvirus infections. Varicella zoster virus (VZV) was the most common, but cytomegalovirus (CMV), Epstein-Barr virus (EBV) and herpes simplex virus (HSV) were all represented. 21% of patients also experienced malignancies, including EBV-driven smooth muscle tremor, human papilloma virus (HPV)-related cancers and leukaemia (Orange, 2013).

Other evidence includes reports of reduced expression of activation associated molecules, as well as compromised cytolytic function and cytokine production of NK cells observed in acute and chronic viral hepatitis (Lunemann et al., 2013). Multiple studies demonstrate the role of NK cells in fighting human immunodeficiency virus

(HIV), cytomegalovirus, influenza virus, flaviviruses (Japanese encephalitis virus, yellow fever virus, dengue virus, tick-borne encephalitis virus and West Nile virus (WNV)), and other viral infections (Leung and Leung, 1981, Guo et al., 2009, Alter et al., 2007, Martin et al., 2002, Stein-Streilein et al., 1983, Gazit et al., 2006).

In addition to fighting viral infections, the role of NK cells in tumour rejection has been extensively studied. Many *in vitro* and *in vivo* studies have shown that NK cells kill cancerous cells and thus inhibit tumour growth and metastasis. Most *in vivo* studies use implanted syngeneic tumour cells in mouse models with genetically deficient NK cell functions or depleted NK cells by the administration of antibodies (Smyth et al., 2001, Smyth et al., 2002, Wu and Lanier, 2003). Eliminating NK cell function often led to more aggressive tumour growth and metastasis. However, genetic defects or administered antibodies did not exclusively target NK cells and thus the direct involvement of NK cells could not be clearly dissected. To overcome this, Schreiber et al. developed an alternative approach using mice, genetically deficient for key effector NK cell molecules or their respective receptors (perforin, IFN-γ, IFN-γR or STAT1, an important signal transduced of type I and type II IFN receptors) (Kaplan et al., 1998, Shankaran et al., 2001). Combining these deficiencies with deficiencies specifically abrogating T cells (e.g. recombinase activating genes – RAG) allowed them to assess the contribution of NK cells in tumour surveillance. Upon treatment with the chemical carcinogen methylcholanthrene (MCA), mice deficient for both STAT1 and RAG2 spontaneously developed adenocarcinoma at higher rates as compared with mice deficient only for RAG2 (Shankaran et al., 2001, Dunn et al., 2004, Swann and Smyth, 2007). Thus, NK cells contribute to tumour rejection independently from T cells.

In human studies, the 11-year follow-up epidemiological survey of a Japanese population demonstrated a link between low NK cell cytotoxic activity in peripheral blood, as measured by isotope-release assay, and increased cancer risk in adults (Imai et al., 2000). Furthermore, NK cell infiltration of tumours represents a positive prognostic marker in different carcinomas (Coca et al., 1997, Ishigami et al., 2000, Villegas et al., 2002). However, in human tumours there are often only a few infiltrating NK cells, possibly due to inefficient homing into malignant tissues and thus their contribution in solid tumour eradication is questionable (Albertsson et al., 2003, Esendagli et al., 2008). More convincing are evidence for the role of NK cells in the control of human leucocyte malignancies. In clinical studies, myeloid leukaemia patients lacking HLA class I ligands for donor-inhibitory killer cell Ig-like receptors (KIR) showed a remarkable increase in survival and protection from relapse when

receiving alloreactive NK cells in the course of allogeneic haematopoietic stem cell transplantation (Hsu et al., 2005, Ruggeri et al., 2007).

NK cells have also been associated with the elimination of certain bacterial infections. This is mainly due their ability to secrete IFN-γ (Harty and Bevant, 1995, Hamon et al., 2006, Pamer, 2004). Specifically, adoptive transfer of NK cells into $Rag^{-/-}$ $Il2rg^{-/-}$ mice (deficient for T B, NK and NKT cells) that underwent middle cerebral artery occlusion (MCAO) - induced ischemic stroke reduced their mortality upon the infection with *Listeria monocytogenes* (LM). That outcome coincided with increased levels of IFN-γ. Moreover, restoring peripheral NK cell function and their IFN-γ release by pharmacological blockade of adrenergic and hypothalamic–pituitary–adrenal (HPA) axis prevented post-ischemic death caused by pneumonia (Liu et al., 2017).

Soluble cytokines, produced by NK cells can also stimulate many other immune functions. IFN-γ can activate macrophage killing of obligate intracellular pathogens (Filipe-Santos et al., 2006) and up-regulate the expression of IgG Fc receptor FcγRI in monocytes to increase opsonisation-dependent phagocytosis (Schroder et al., 2004). Moreover, NK cell secretion of GM-CSF promotes fungicidal activity of neutrophils against *Candida albicans* (Bär et al., 2014).

However, as potent killers, NK cells could also contribute to the onset, the maintenance or the progression of autoimmune diseases. Rheumatoid arthritis (RA) patients have accumulation of NK cell in their synovial fluid. $CD56^{bright}$ NK cells found in the synovial fluid secrete more IFN-γ than peripheral blood NK cells from the same patients (Dalbeth and Callan, 2002, Pazmany, 2005).

Several studies have proposed that reduced NK cell activity in non-obese diabetic (NOD) mice, a mouse model for Type 1 diabetes, substantially inhibits diabetes development (Poirot et al., 2004, Alba et al., 2008). The activating receptor NKp46 has been shown to be essential for the development of type 1 diabetes in mice and humans (Gur et al., 2010). NK cells appeared in the pancreas when insulitis progressed to type 1 diabetes, and NKp46 engagement by beta cells led to degranulation of NK cells. NKp46-deficient mice had less development of type 1 diabetes induced by injection of a low dose of streptozotocin. Injection of soluble NKp46 proteins into non-obese diabetic mice during the early phase of insulitis and the pre-diabetic stage prevented the development of type 1 diabetes.

Moreover, a study in obese mice demonstrated that NK cells represent key regulators in insulin resistance in response to obesity-induced adipocyte stress. Adipocytes from mice on high-fat diet had elevated levels of NCR1 ligands which led to increased NK

cell IFN-γ production upon NCR1 ligation. This triggered the differentiation of pro-inflammatory macrophages that promoted insulin resistance (Wensveen et al., 2015).

In some autoimmune diseases, NK cells have been associated with a protective or disease controlling role. In systemic lupus erythematosus (SLE) patients show a moderate reduction of NK cell numbers (Erkeller-Yuksel et al., 1997, Erkeller-Yüksel et al., 1993) with reduced NK cell cytotoxic activity (Hervier et al., 2011, Park et al., 2009). These defects are associated with clinical conditions such as nephritis (inflammation of the kidneys) and thrombocytopenia (Erkeller-Yüksel et al., 1993, Erkeller-Yuksel et al., 1997, Hervier et al., 2011, Park et al., 2009).

1.1.3. Memory NK cells

Immune memory is defined as an ability of an immune cell to respond more robustly to a secondary infection from the same pathogen. Memory cells are phenotypically and epigenetically distinct from their naïve counterparts and have a long life-span.

NK cells are traditionally considered as innate immune cells with a life-span of 10 - 20 days (Zhang et al., 2013). They are believed to be incapable of undergoing somatic rearrangements of their receptors and thus not able to form memory. However, recent evidence that indicates that they possess an adaptive memory-like function that mediates responses lasting for months (Min-Oo et al., 2013). In T and B cells, RAG recombinase enzyme mediates the generation of a multitude of T cell and B cell antigen receptors by rearranging variable-joining gene segments. NK cells do not express RAG recombinase and mechanisms of how they develop and maintain selective memory is still largely unclear (Paust and von Andrian, 2011). In mouse model of cytomegalovirus (MCMV) infection, a specific subset of NK cells contracts after the virus control and generates long-lived memory cells that are more efficient in immune protection during a secondary infection with same pathogen (Lopez-Vergès et al., 2011). IL-12 signalling is critical for such antigen-driven expansion (Min-Oo et al., 2013). NK cells lacking IL-12 receptor do not proliferate in response to virus and do not generate memory NK cells.

In humans, the expression of CD57 on NK cells is strongly correlated with a mature phenotype of the $CD56^{dim}CD16^{+}$ population. Thus, upregulated CD57 might be a marker for clonally expanded NK cells following infection. Moreover, a unique population of $CD57^{+}NKG2C^{hi}$ NK cells has been demonstrated to be present in CMV^{+} healthy adults, years after the primary viral infection (Lopez-Vergès et al., 2011). $CD57^{+}NKG2C^{hi}$ frequency within the total $CD56^{dim}CD16^{+}$ population increased as the

viral load decreased during the antiviral therapy. The expression of some inhibitory receptors, like NKG2A and KIR3DL1 was strongly down-regulated in CMV^+ donors.

Furthermore, $CD56^{dim}CD3^-$FcγR-deficient NK cell population has been reported to be present in peripheral blood of about one third of healthy individuals (Zhang et al., 2013). These γ^-NK cells express CD3ζ, high levels of CD57 and low levels of NKD2A independently from NKG2C expression. In many donors γ^-NK cells predominantly express a particular killer cell Ig-like receptor (KIR). The ability of IFN-γ and TNF-α production of these γ^-NK cells from HCMV and HSV-1 seropositive patients, respectively, with conventional NK cells. During reactivation, the cytokine production of γ^-NK cells was significantly increased, suggesting that they might be important in an adaptive role of NK cells. γ^-NK cells also displayed a significant upregulation of the anti-apoptotic protein Bcl-1 compared to conventional NK cells. Bcl-1 is normally elevated in memory $CD8^+$ T cells. Moreover, γ^-NK cells expand in an antibody-dependent fashion in response to HCMV or influenza infection (Lee et al., 2015). γ^-NK cells might be important in controlling viral reactivation from latency and could also help in the control of other chronic or recurrent viral infections.

Based on the experimental data, mainly from contact hyper-sensibility (CHS) studies, the following memory NK cell pathway has been proposed: a naïve NK cell surveys the blood until the recognition of activating ligands. Upon ligation, it differentiates into a memory cell that finds long-term shelter in the liver. To maintain immune surveillance some cells are probably released into the blood, from the hepatic memory pool, at a low but constant level. When the recall antigens emerge at some distant point in body, antigen-specific NK cells would gather at the site of infection, most probably after having been released from the liver (Paust and von Andrian, 2011).

1.2. NK cell effector functions

NK cell responses towards a target are tightly regulated by the balance between activating and inhibitory signals. Upon the dominance of activating signals, NK cells can execute cytolytic action via perforin/granzyme or death receptor (e.g. Fas or TRAIL)-related pathways and/or respond with the secretion of cytokines and chemokines (Orange, 2008, Tripp et al., 1993). However, human NK cells are highly heterogeneous and some cells respond preferentially with high cytokine secretion while others are primarily cytolytic (Fauriat et al., 2008). When the inhibitory signals prevail, NK cells do not respond and detach from the target cell with no consequences (Orange, 2008, Abeyweera et al., 2011).

1.2.1. Cytotoxicity

Granule mediated killing

Ligation of NK cell activating receptors can trigger a series of events leading to the release of specialized secretory lysosomes, termed “lytic granules” into the synaptic cleft (Mace et al., 2014). These toxic granules are complex organelles containing a mixture of proteins (perforin, granzymes, granulysin) (Ritter et al., 2013). Their release induces target cell “suicide” by triggering mechanisms of programmed cell death (apoptosis).

Perforin is known as a membrane disrupting protein. Its release via exocytosis causes pore formation on the target cell membrane. The specific mechanism of cell death was first thought to be induced by the damaged membrane and the osmotic instability leading to excessive ion uptake through the disrupted membrane. But, since the discovery of pro-apoptotic properties of granzymes, a family of structurally related serine proteases, it has been widely accepted that granule-mediated apoptosis is performed jointly, by the collaboration of perforin and granzyme proteins.

According to the perforin-granzyme synergy concept, granzymes enter target cell cytoplasm through pores induced by perforin. There they activate an apoptotic pathway leading to target cell death. Apoptosis can be triggered by the caspase-dependent pathway by granzyme B (Trapani et al., 1998) or caspase-independent pathway by granzyme A (Martinvalet et al., 2005). In that way, lytic granules can ensure rapid and efficient target cell death even when caspases are inactivated due to inhibitory viral proteins or due to mutation.

In non-lytic concentrations, perforin has been suggested to permeabilise the target cell membrane so that granzymes can be endocytosed in the form of large vesicles in the target cell cytosol (Kurschus et al., 2008). Studies demonstrating that the deletion of perforin from mice lymphocytes completely abolished granule-dependent target cell lysis while the disruption of granzymes led to more subtle phenotypes suggest the vital role of perforin (Bolitho et al., 2007, Voskoboinik and Trapani, 2006, Müllbacher et al., 1999, Pardo et al., 2002, Simon et al., 1997). Moreover, congenital perforin deficiency has been linked with the fatal human hyper-inflammatory disease FHK (Stepp et al., 1999).

Granulysin is another protein secreted by the lytic granules. It is a small toxin that kills intracellular bacteria, like *Listeria monocytogenes* or *Mycobacterium tuberculosis* by rupturing their membranes. Like granzymes, they enter target cell through perforin-formed pores and they kill pathogenic bacteria that might otherwise escape from the endolysosomal compartment of dying target (Anderson et al., 2003, Stenger et al., 1998, Walch et al., 2014).

Apoptotic cell death causes less inflammatory response than necrotic cell death. In order to prevent immune hyperactivation, it is important that target cells are killed by apoptosis. Phagocytes can specifically identify changes on the membrane of apoptotic cells and remove them rapidly without causing inflammation (Huynh et al., 2002). The apoptotic pathway is ensured by both, perforin and granzymes; Ca^{2+} flux coming through perforin-induced pores triggers a membrane repair response that can save the target from necrosis while granzymes induce apoptosis (Trump and Berezesky, 1992, Keefe et al., 2005).

Receptor mediated killing

Target cell lysis can be also caused by the engagement of death receptors (e.g. Fas or DR4) expressed by targets with their physiological ligands such as FasL or tumor necrosis factor-related apoptosis-inducing ligand (TRAIL) (Wiley et al., 1995, Zamai et al., 1998). In this pathway, the apoptotic cell death results from receptor-ligand signaling and is independent from lytic granule release.

FAS (also known as APO-1 or CD95) is a surface membrane receptor belonging to the tumor necrosis factor receptor (TNF-R) family. Upon the recognition of its cognate ligand FAS-L, it triggers caspase-mediated apoptosis (Strasser et al., 2009). Other members of this family include the death receptor DR4 (R1) and DR5 (R2) inducing

apoptosis upon the ligation of their soluble ligand, the TNF-related apoptosis-inducing ligand (TRAIL).

The ligation of Fas results in rapid formation of death-inducing signalling complexes (DISCs) containing apoptotic enzyme caspase 8. In DISC, caspase 8 becomes fully active by changing its conformation. Autoproteolysis allows the enzyme to cleave, leave the DISC and continue its biochemical path by activating other caspases in different cell compartments and finally leading to death.

1.2.2. Cytokine and chemokine production

NK cells also contribute to regulation of the immune system by secretion of inflammatory and immunoregulatory cytokines and chemokines. Among the most prominent cytokines are interferon gamma (IFN-γ) and tumour necrosis factor α (TNF-α) but NK cells have been shown to produce several other soluble factors, including IL-5, IL-10, IL-13 GM-CSF, MIP-1α (CCL3), MIP-1β (CCL4), IL-8 (CXCL8) and RANTES (CCL5) (Fauriat et al., 2010). The nature of cytokine response depends on type and duration of stimulation. When incubated with the K562 cell line, chemokine (MIP-1α MIP-1β, RANTES) secretion was detected within one hour, while TNF-α and IFN-γ secretion occurred later. Maximum secretion of all was reached by 6 hours of activation.

Using *Drosophila* S2 cells opsonised with antibodies against NK cell activating receptors it has been demonstrated that ICAM1 alone can trigger low levels of secretion of MIP-1α, but colligation of multiple receptors is required for secretion of IFN-γ or TNF-α. IFN-γ has been shown to be dependent on LFA-1 engagement, while this was not the case for TNF-α (Fauriat et al., 2010). Failure to kill targets due to the perforin and granzymes knockout led to significantly amplified secretion of IFN-γ and TNF-α as well as MIP-1α, MIP-1β and RANTES. In perforin-deficient infants this probably contributes to the fatal cytokine storm, resulting from the over-activation of macrophages (Jenkins et al., 2015). The ability to secrete IFN-γ has been shown to be dependent on NK cell differentiation and maturation status to the epigenetic remodelling to the IFNG promoter. The $CD56^{dim}CD62L^{-}CD57^{+}sKIR^{+}$ (sKIR refers to the expression of self MHC-specific educating KIR) subset produced more IFN-γ than $NK56^{bright}$ or $NK56^{dim}CD62L^{+}CD57^{-}sKIR^{-}$ subsets upon stimulation with activating ligands, but less IFN-γ upon stimulation with soluble cytokines, IL-12 + IL-18 (Luetke-Eversloh et al., 2014).

Secretion of pro-inflammatory cytokines can also play a significant role in tumour eradication. In a mouse model, NK cells contributed to elimination of methylcholanthrene-induced tumour metastases and sarcoma by IFN-γ secretion (Street et al., 2001). Moreover, IFN-γ and TNF-α can together with the ligation of CD40 stimulate dendritic cells (DCs) that release IL-12 in return. Such NK cell – DC crosstalk helps to initiate and maintain an efficient T cell mediated anti-tumour response (Adam et al., 2005).

1.2.3. Hierarchy of NK cell responses

The $CD56^{dim}$ NK cell subset has been demonstrated to be efficient in both, cytotoxic responses and cytokine production (Fauriat et al., 2010). The type of the response has been reported to be dependent on the combination of activating receptor engaged. When the S2 *Drosophila* cell line expressed one ligand for NK cell activating receptors, NK cells responded with chemokine secretion. For the degranulation responses, at least two activating ligands needed to be presented on the surface. The activation threshold was the highest for the production of IFN-γ and TNF-α, which required the co-expression of two activating ligands and intracellular cell adhesion molecule ICAM1 (Fauriat et al., 2010). The secretion of TNF-α and IFN-γ can have a broad impact on the immune system and thus it maybe requires more stringent regulation.

1.3. Immunological synapse

The immunological synapse (IS) is a finely tuned, specialized interface formed by the immune cells. The IS has been initially described in the 90's as the junction between the helper T cell and antigen presenting cell (APC) (Monks et al., 1998). Its role in the cytolytic function of cytotoxic T lymphocytes (CTL) and NK cells was recognized soon after (Davis et al., 1999, Grakoui et al., 1999, Stinchcombe et al., 2001). The name immune synapse was coined based on the similarities with the synapses between the neurons in the brain. Like the neuronal synapse, the IS provides a dynamic platform for intercellular communication and for the polarized secretion of effector molecules (Dustin, 2012, Norcross, 1984). In the IS close contact between cells ensures that cytolysis is induced only to a single diseased cell without any toxic effect on bystander cells (Cartwright et al., 2014, Hsu et al., 2016).

Numerous molecules have been shown to play a part in IS formation, including activating and inhibitory receptors, signalling molecules, cytoskeletal elements and cellular organelles. Upon the engagement with the target, the activity of NK cells is tightly regulated by the balance of signals transduced from activating and inhibitory receptors (Lanier, 2008, Long, 2008, Culley et al., 2009). The outcome of the interaction is defined by the repertoire of NK cell receptors and the quantity and quality of their ligands. When activating signals prevail, the interaction results in the formation of a cytolytic synapse, causing target cell lysis, whereas if inhibitory signals dominate, the target cell is spared (Orange, 2008, Eissmann and Davis, 2010).

In recent years, it has been shown that effector function is not based only on a linear cascade of receptor-ligand reactions. Immune cell responses are also regulated by the dynamic changes in the receptor organisation occurring upon the contact between NK cell and its target. Fluorescence imaging of T, B and NK cells revealed that immunological recognition involves segregation and reorganisation of many surface receptors and their signalling molecules into micro- and submicroscale domains (Monks et al., 1998, Davis et al., 1999, Grakoui et al., 1999, Vyas et al., 2001, Vyas et al., 2002). At the NK cell synapse, activating receptors such as NKG2D (Abeyweera et al., 2011) and CD16 (Liu et al., 2012), as well as the inhibitory receptor KIR2DL1 (Oddos et al., 2008) accumulate into microclusters. Microscale distribution of KIR2DL1 at the IS varies with the density of its ligand on the target cell surface (Almeida and Davis, 2006) while the size and dynamics of CD16 clusters depends on the density of adhesion molecule ICAM1 (Steblyanko et al., 2015).

Several studies have reported the importance of structural organisation at the NK cell synapse. Perhaps the most direct link was demonstrated by Köhler *et al*, showing that alteration of ligand length leads to proteins exclusion from the synapse which disrupts NK cell activation or inhibition (Köhler et al., 2010). Taken together, these data highlight the critical role of synaptic organization for the coordination of transient receptor-ligand interaction modulating activating or inhibitory signals.

1.3.1. Assembly of the immune synapse

The assembly of the IS starts with a close cell-cell contact that might be similar to tethering. Then, receptor-ligand interactions of higher affinity facilitate firm adhesion (Orange, 2008). Some of the most crucial molecules involved at first stage are from integrin families, such as lymphocyte function-associated antigen-1 (LFA-1). At the contact interface integrins accumulate in a unique supramolecular organisation

termed central supramolecular activation cluster (c-SMAC) (Davis and Dustin, 2004). LFA-1 ligation alone is sufficient to trigger the reorganisation of F-actin. In synergy with activating receptors, LFA-1 also signals to arrest cell migration in order to form a stable symmetrical synapse. On the other hand, the co-ligation with inhibitory receptors results in asymmetry and resumption of migration (Culley et al., 2009, Vyas et al., 2001). Moreover, the convergence of lytic granules upon microtubule organizing centre (MTOC) can be triggered by the engagement of LFA-1. Convergence of lytic granules occurs also when NK cell is conjugated to the non-susceptible target as well as when the inhibitory synapse is formed (Mentlik et al., 2010). This suggests that granules convergence precedes the commitment of cell to cytotoxicity.

1.3.2. Cytolytic immune synapse

When signals from activating receptors override signals from inhibitory receptors, a cytolytic synapse may assemble (Figure 1.2). For the successful execution of cytotoxic function, several steps have to occur. First, a stable NK cell-target cell interface with a cleft into which cytolytic granules are secreted has to be formed. Next, lytic granules need to be recruited to the synapse. The convergence of lytic granules can occur before the cytolytic synapse is formed (Mentlik et al., 2010, Hsu et al., 2016, Ritter et al., 2015). But, MTOC reorientation towards the synapse occurs only upon activating signalling. A study using non-lytic tumour infiltrating lymphocytes showed that the inability of the MTOC to polarize prevents the secretion of the lytic granules and therefore abrogates the subsequent lysis of the target cell (Radoja et al., 2001). Finally, granule membranes have to be fused with the plasma membrane for the release of the lytic granule contents (Orange, 2008).

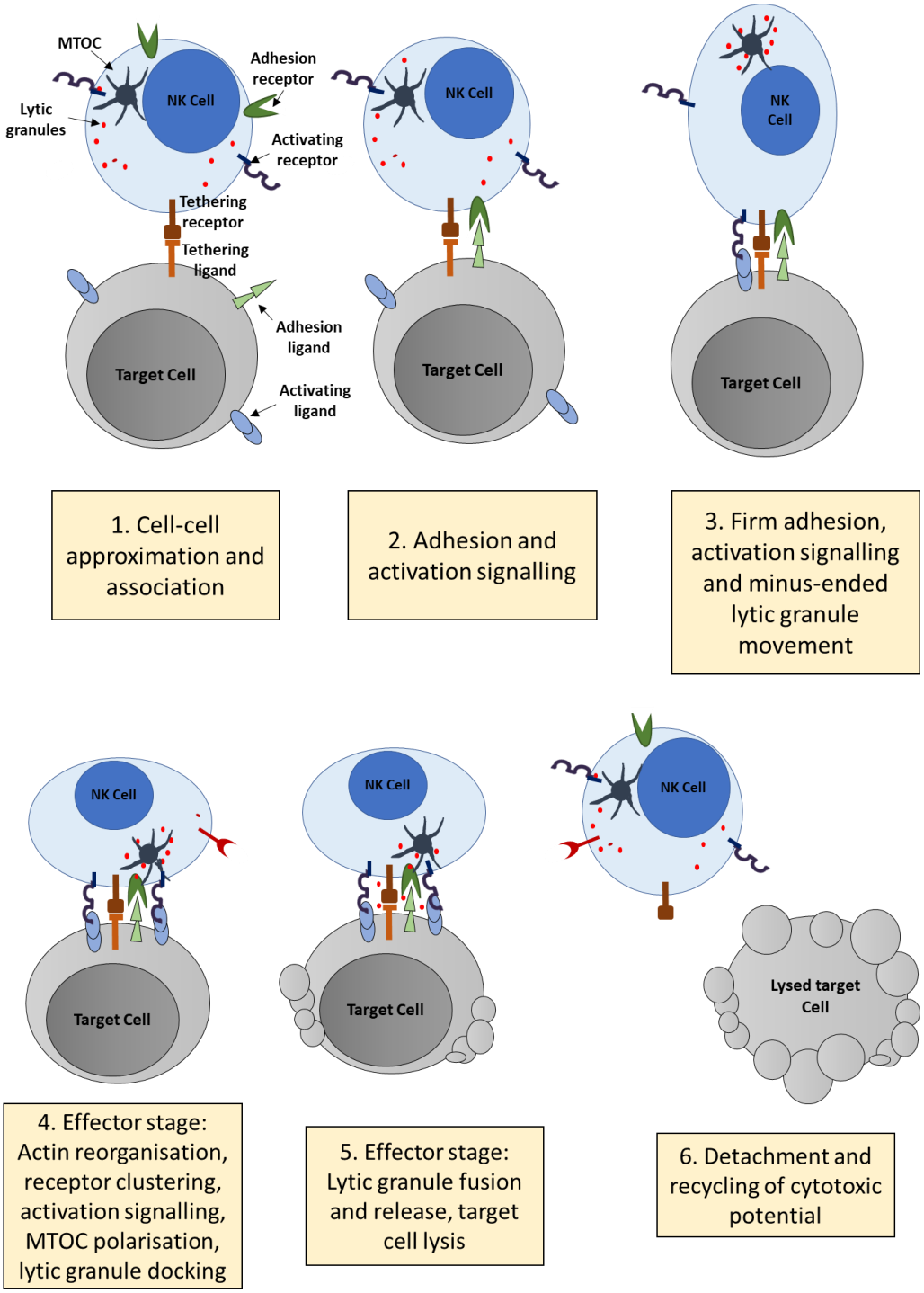

Figure 1.2: Schematic representation of the formation and function of the NK cell lytic synapse. An execution of NK cell cytotoxic function can be described the steps described in this figure. First, NK cell needs to come in close contact with the potential target. Then, the adhesion and initial signalling have to occur. This triggers the movement of the lytic granules towards the microtubule-organising centre (MTOC). If the target presents activating ligands, synapse enters the effector stage, where F-actin and activating receptors reorganise their distribution at the cell-cell interface. Lytic granules polarise alongside MTOC to the synapse area and dock. Finally, granules are fused with the membrane and released. This results in the target cell lysis. Upon the termination of the process, NK cell detaches and recycles its cytotoxic machinery (Orange 2008).

1.3.3. Inhibitory immune synapse

NK cell forms an inhibitory synapse when the inhibitory signals on a target cell surface dominate. It is structurally distinct from the cytolytic synapse. Culley et al. showed that inhibitory synapse is smaller and less stable (Culley et al., 2009). Inhibitory synapse formation occurs quickly to allow rapid inhibition of any activating signals that would otherwise prepare the NK cell for a cytolytic attack (F-actin reorganisation, granule polarisation, etc.). Upon binding, inhibitory receptors organise into micro- and nano- clusters in an ATP-independent manner (Davis et al., 1999, Oszmiana et al., 2016). In an inhibitory synapse, receptor-ligand interactions are rapidly broken and removed which results in disassembly of immune synapse and unzipping from the target (Eissmann and Davis, 2010).

1.4. NK cell activating receptors

One of the best characterized NK cell activating receptors is NKG2D, a protein that is only distantly related to the NKG2 family. NKG2D forms a homodimer and signals via phosphorylation of the adaptor DNAX-associated protein 10 (DAP10) (Pegram et al., 2010, Billadeau et al., 2003, Zompi et al., 2003). NKG2D recognizes various ligands, including the stress-induced MHC class I chain related protein A or B (MICA/B) and UL16-binding protein (ULBP) 1-6 both of which are found on tumour or virally infected cells (González et al., 2008, Champsaur and Lanier, 2010). Importantly, in healthy tissues or benign tumours the expression of NKG2D ligands is limited, whereas the infection or transformation triggers their upregulation (López-Soto et al., 2013a, López-Soto et al., 2013b). However, on the surface of gastro-intestinal epithelium of healthy people relevant amounts MICA/B and ULBP1 can be found (López-Soto et al., 2013b, López-Soto et al., 2013a, López-Soto et al., 2009).

Another group of activating receptors is known as the natural cytotoxicity receptors (NCRs). NCRs belong to the IgG superfamily. In humans, NKp46, NKp30 and NKp80 are expressed on activated and resting NK cells while NKp44 is upregulated on some NK cells upon stimulation with IL-2 (Pegram et al., 2010). A broad range of ligands for NCRs have been reported, including viral hemagglutinins (NKp44 and NKp46) (Arnon et al., 2001, Mandelboim et al., 2001), nuclear factor HLA-B-associated transcript 3 (NKp30) (Pogge von Strandmann et al., 2007), heparin sulphate proteoglycans (NKp46 and NKp30) (Bloushtain et al., 2004, Welte et al., 2006), activation-induced C-type lectin (NKp80) (Bloushtain et al., 2004, Welte et al., 2006)

and recently discovered, complement factor P (NKp46) (Narni-Mancinelli et al., 2017). Experiments in which anti-NCR antibodies abrogate NK cell-mediated lysis of different tumour cell types suggest the existence of some non-reported NCR ligands (Pende et al., 1999, Mandelboim et al., 2001, Pegram et al., 2010). The deletion of a single NCR reduces the NK cell ability to kill malignant cells *in vivo*, thus NCRs may play an important role for NK cell mediated tumour cell killing (Pessino et al., 1998, Sivori et al., 1999).

In addition to natural cytotoxicity, NK cells are potent mediators of antibody dependent cellular cytotoxicity (ADCC). The ligation of the low affinity activating receptor CD16 (FcγRIIIa) by an Fc portion of an IgG antibody opsonising a target can lead to cytotoxic response and/or cytokine secretion. Such CD16-dependent triggering of an effector function has been shown to be an important mode of action of many Ab-based therapies (Orange, 2013, Nimmerjahn and Ravetch, 2008). While most activating receptors require a combination of activating signals for strong NK cell response, the ligation of CD16 alone has been shown to be sufficient for both, cytotoxic effect the release of cytokines (Bryceson et al., 2006).

More activating receptors and their ligands are summarised in the Table 1.1.

Table 1.1: Activating receptors and their ligands

Activating receptors	Known ligands	Reference
CD16 (FcγRIIIA)	IgG	(Lanier et al., 1986, Vivier et al., 1991, Vivier et al., 1993)
NKG2D	MICA, MICB, ULBPs	(Bauer et al., 1999, Steinle et al., 2001)
Natural cytotoxicity receptors: NKp30, NKp44, NKp46	B7-H6, HLA-B-associated transcript 3, CMV pp65, viral haemagglutinins, haemagglutinin-neuraminidase, complement factor P	(Arnon et al., 2001, Arnon et al., 2005, Brandt et al., 2009, Mandelboim et al., 2001, Pogge von Strandmann et al., 2007, Narni-Mancinelli et al., 2017)
KIR family: KIR2DS1, KIR2DS2, KIR2DS4, KIR2DS5, KIR3DS1, (KIR2DL4)	Various allotypes of classical HLA class I molecules and the non-classical HLA-G	(Chewning et al., 2007, Graef et al., 2009, Stewart et al., 2005)
DNAM-1	PVR, Nectin-2	(Bottino et al., 2003)
2B4 (CD244)	CD48	(Brown et al., 1998)
CD28	CD80, CD86	(Chen and Shi, 2006)
LFA-1 (CD11a/CD18)	ICAM1 (CD54)	(Barber et al., 2004)

1.4.1. CD16 (FcγRIII)

CD16 receptor, also known as Low affinity immunoglobulin gamma Fc region receptor III (FcγRIII) is a member of a human leukocyte Fcγ receptor family. In immune cells, it can be found in two types, CD16a and CD16b. In humans, it is encoded by the FCGR3A or FCGR3B gene (Qiu et al., 1990). CD16a is a trans-membrane protein, highly expressed on $CD56^{dim}$ NK cells, monocytes, macrophages and dendritic cells. Most $CD56^{bright}$ NK cells in the peripheral blood express little to no CD16a (Smith and Clatworthy, 2010). CD16b receptor with a highly homologous extracellular domain and glycosylphosphatidylinositol (GPI) anchor is expressed on neutrophils. Throughout this thesis we use the term CD16 to refer to CD16a on NK cells.

The CD16 extracellular part binds the Fc portion of immunoglobulin G (IgG) antibodies at the lower hinge region with low affinity (Sondermann et al., 2000). Its ligation induces a series of signals resulting in cytokine secretion and cytotoxic activity via antibody-dependent cell cytotoxicity (ADCC) (Figure 1.3). Unlike most other NK cell activating receptors that must be engaged in combinations to trigger efficient target cell killing, the ligation of CD16 alone is sufficient for successful target cell lysis (Bryceson et al., 2006). Moreover, its ligation can overcome inhibitory signalling (Chan et al., 2012). However, for the directed secretion of cytolytic granules into the synaptic cleft the colligation with ICAM1 is required. In the absence of ICAM1 non-directed granule secretion results in collateral killing of bystander cells (Hsu et al., 2016).

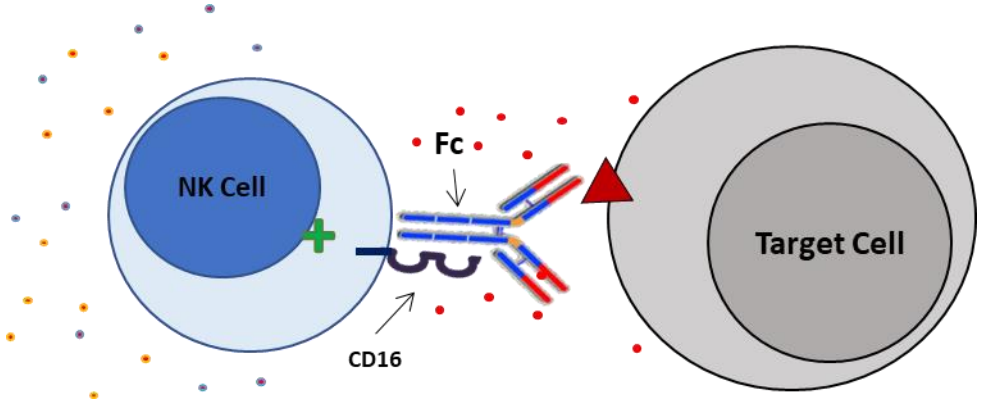

Figure 1.3: NK cell mediated ADCC. Fab fragment of an IgG antibody binds to its ligand at the surface of a target cell (e.g. CD20 at the surface of malignant B cells. Fc portion recognised by an effector cell (CD16 on NK cells) can trigger cytotoxic response.

CD16 structure and ligand binding

CD16 is a type I transmembrane protein consisting of two extracellular Ig domains, a short cytoplasmic tail, and a single transmembrane domain (Hibbs et al., 1994). Its relative molecular mass is estimated to be 50-80 kDa (Takai, 2002). Crystallographic studies, together with molecular modelling have provided an insight into CD16-ligand interactions. A three-dimensional structural model demonstrated that human IgG1 binds to soluble extracellular CD16 via its second, membrane-proximal IgG domain asymmetrically in 1:1 stoichiometry (Sondermann et al., 2000). High avidity for specific binding to antibodies required for efficient signalling ensures that cells are activated when IgGs have bound to a multimeric or multivalent cognate antigen only (Banks et al., 2002). However, the monomeric binding by IgG is unable to induce NK cell activation (Alber et al., 1992). CD16 has the strongest binding affinity to human IgG1 and IgG3 (2×10^7 M^{-1}) and weaker to IgG2 and IgG4 subclasses (Chan et al., 2012). Affinity of antibodies can be increased 5- to 100-fold by substituting certain amino acids (Shields et al., 2001, Lazar et al., 2006) in the Fc portion and by modifying Fc-linked glycosylation (Umana et al., 1999, Davies et al., 2001, Shinkawa et al., 2003).

CD16 signalling

Like most others FcγRs, CD16 cannot transduce an activating signalling pathway autonomously. For functional activation, the receptor's α-chain must associate with an ITAM-containing signal transduction adaptor molecule. CD16 can associate with CD3-ζ (CD247) or FcεR1γ homodimers or CD3-ζ- FcεR1γ heterodimers (Figure 1.4) (Lanier et al., 1991, O'Shea et al., 1991). Both adaptors have very short extracellular domains and cytoplasmic tails that contain ITAMs. The assembly of the receptor with the signalling adaptors requires aspartate residues in the transmembrane domain of CD16 (Lanier et al., 1989, Lanier et al., 1991) and depends on a network of polar and aromatic residues along the length of the transmembrane domain (Blázquez-Moreno et al., 2017).

Ligation of CD16 causes a series of events, starting with the phosphorylation of the ITAM tyrosines by Src family kinases (including Lck, Fyn, Src, Yes, Lyn and Fgr). Following the recruitment of SYK family kinases – spleen tyrosine kinase (Syk) and zeta-chain associated protein kinase (ZAP70) results in reorganisation of the actin cytoskeleton, production of cytokines and chemokines and in cytotoxic activity via Ca^{2+}-depending mechanism (Liu et al., 2009, Lanier, 2008). The recruitment of SHIP

to the phosphorylated CD3-ζ subunits negatively regulates CD16 activity (Galandrini et al., 2002).

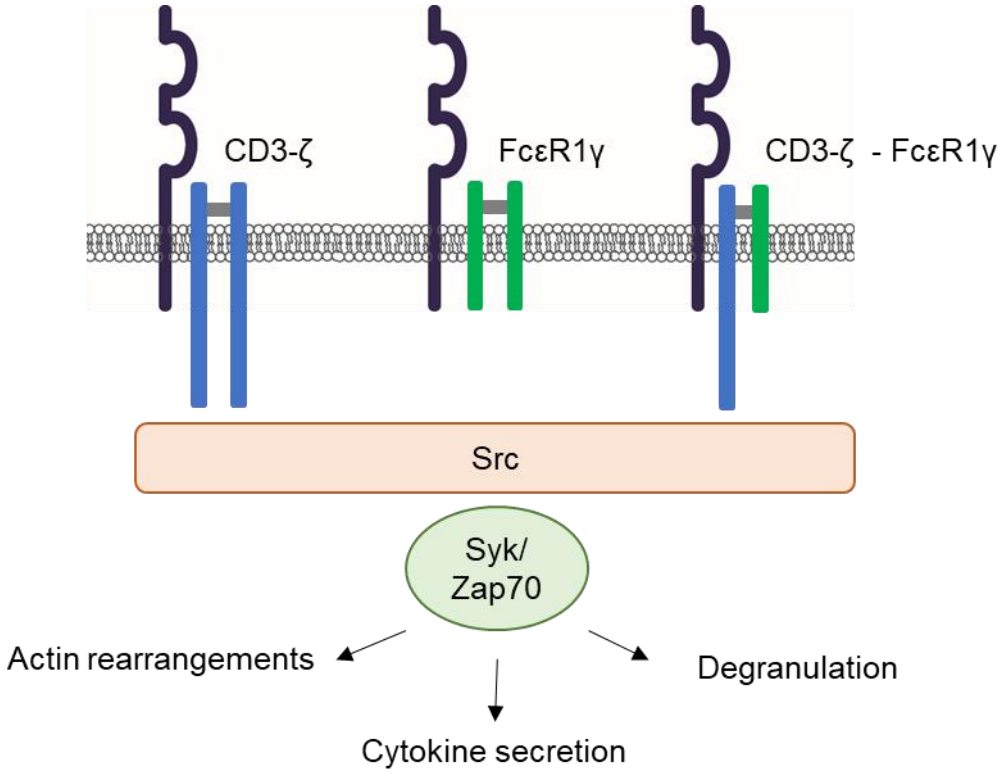

Figure 1.4: CD16 signalling: CD16 signals through ITAM motifs of its adaptor molecules; CD3-ζ (CD247) or FcεR1γ homodimers or CD3-ζ- FcεR1γ heterodimers. CD16 ligation leads ITAM's phosphorylation by Src family kinases. The recruitment of spleen tyrosine kinase (Syk) and zeta-chain associated protein kinase (ZAP70) leads to the reorganisation of the actin cytoskeleton, production of cytokines and degranulation.

CD16 Polymorphism

FCGR3A, the CD16 encoding gene, bears a functional single nucleotide polymorphism (SNP) at nucleotide 526 with a substitution of thymidine (T) with guanine (G). This results in an amino acid substitution at position 158 in the membrane-proximal Ig-like domain of phenylalanine (F) with valine (V) (Ravetch and Perussia, 1989). The allotype governs the affinity of the receptor IgG as well as the strength of effector functions induced by CD16 ligation (Koene et al., 1998, Wu et al., 1997). CD16–V/V-158 genotype binds human IgG1 with higher affinity than CD16–F/V-158 or CD16–F/F-158 (Wu et al., 1997). However, the polymorphism does not affect CD16 expression levels (Dall'Ozzo et al., 2004, Congy-Jolivet et al., 2008).

In the population, the frequency of a CD16 allotype is influenced by race and ethnicity (Osborne et al., 1994). For example, a study comparing Dutch Caucasian and Japanese subjects revealed that only 4 % of Japanese blood donors carry CD16–V/V-158 while 17 % of Dutch Caucasians carry this allotype (van der Pol and van de Winkel, 1998, Leppers-Van de Straat et al., 2000).

CD16 polymorphism has been reported to be associated with certain autoimmune diseases. CD16-F/F-158 phenotype is a suggested susceptibility factor for systemic lupus erythematosus (SLE) (Koene et al., 1998, Wu et al., 1997, Salmon et al., 1999) or rheumatoid arthritis (Nieto et al., 2000). Moreover, it has also been related to the clinical responses to therapies with monoclonal antibodies. In studies using samples of patients during treatments with rituximab (anti-CD20 mAb), transtuzumab (anti-HER-2 mAb) or cetuximab (anti-EGFR mAb), CD16-V/V-158 allotype has been correlated with better response to therapy (Cartron et al., 2002, Musolino et al., 2008, Zhang et al., 2007a). Specifically, patients who responded to trastuzumab with complete or partial remission have been found to have a higher capacity to induce *in vitro* ADCC in response to trastuzumab than patients whose tumours failed to respond to therapy (Musolino et al., 2008). Similarly, patients with non-Hodgkin's lymphoma carrying CD16–V-158 encoding allele have better prognosis when treated with rituximab (Cartron et al., 2002, Weng and Levy, 2003).

CD16 immuno-deficiency

A homozygous substitution of leucine with a histidine (L66H) at the 66th amino acid of CD16 causes a rare mutation in the distal immunoglobulin domain of the extracellular portion of CD16. This domain is not required for IgG binding, but it has been recently demonstrated to link CD16 to the NK cell costimulatory molecule CD2. Hence, L66H mutation impairs CD16 from being used as a costimulatory receptor when CD2 is bound. This reduces spontaneous cytotoxicity, but does not impair ADCC function. Patients with this mutation can suffer severe herpesvirus infections (Jawahar et al., 1996, de Vries et al., 1996). The mutation can be detected by the combination of two clones of anti-CD16 mAbs, 3G8 and B73.1. These two clones recognise two different epitopes on CD16; 3G8 binds to the proximal immunoglobulin domain and B73.1 recognises distal immunoglobulin domain, which is changed in patients with L66H mutation (Grier et al., 2012).

CD16 shedding

CD16 undergoes rapid proteolytic cleavage upon NK cell activation by various stimuli (Romee et al., 2013, Lajoie et al., 2014). Such shedding is an irreversible removal of many membrane proteins. Most studies identified a disintegrin and metalloprotease 17 (ADAM17, also known as a tumour necrosis factor-α-converting enzyme, TACE) as proteinase responsible for CD16 cleavage (Romee et al., 2013, Lajoie et al., 2014, Jing et al., 2015). However, matrix metalloproteinase MMP25 (also known as MT6) has also been reported as a CD16-cleaving enzyme (Peruzzi et al., 2013).

Receptor cleavage occurs proximal to the cell membrane and leads to the release of an intact and functional receptor (Figure 1.5)(Jing et al., 2015). The specific nucleotide sequence of ADAM17-cleavage site has been identified by two independent studies. In the first one, MALDI-TOF analysis revealed that CD16 is cleaved between alanine195/valine196 (Lajoie et al., 2014). In the second study, three separate cleavage sites in close proximity; alanine195/valine196, valine196/serine197, and threonine198/isoleucine199 were also identified by mass spectrometry (Jing et al., 2015). A substitution of the serine at position 197 in the middle of the cleavage region for a proline (S197P) effectively blocked CD16 cleavage.

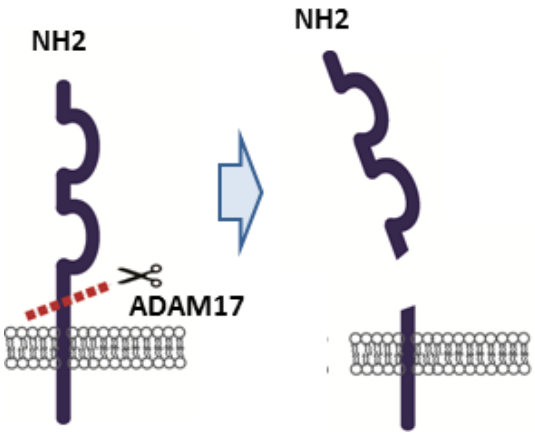

Figure 1.5: CD16 cleavage by ADAM17. ADAM17 cleaves CD16 in a membrane-proximal region. Its cleavage leads to the irreversible release of the extracellular portion from NK cell surface.

The shedding of CD16 is strongly correlated with the strength of NK cell stimulation and degranulation (Lajoie et al., 2014). The greatest loss of CD16 occurs upon NK cell stimulation with a combination either activating ligands or cytokines (Lajoie et al., 2014, Romee et al., 2013). The fact that it only occurs in activated cells indicates that cleavage occurs in cis. The inhibition of shedding results in increased cytokine secretion while target cell lysis is not affected (Romee et al., 2013). Therefore, the density of CD16 receptor might be more important for the production of cytokines than for ADCC responses.

CD16 (CD16b) is also cleaved from the surface of neutrophils by ADAM17. This can occur upon neutrophil activation or apoptosis (Wang et al., 2013). Neutrophil shedding of CD16 is the main source for soluble CD16 detected in the plasma of healthy individuals (Huizinga et al., 1990, Teillaud et al., 1994). CD16 ligation induces strong NK cell activation on its own and thus, it is possible that shedding of the receptor occurs to control the NK cell mediated responses and prevent the hyperactivation of the immune system. However, no studies have reported any functional benefits of this process yet.

Therapeutic antibodies and ADCC

The ability of immune cells, in particularly NK cells, to recognize and kill antibody-coated target cells is known as antibody-dependent cellular cytotoxicity (ADCC). ADCC occurs upon the ligation of activating Fcγ receptors, such as CD16, by the Fc portion of an IgG antibody. It is driven by IgG antibodies produced by B cells, but it can be also triggered by therapeutic antibodies and can thus be exploited for therapeutic purposes. The successful execution of ADCC requires three components: (i) antigen expression on the surface of target cells, (ii) the presence of antigen specific antibodies of the appropriate isotype and (iii) expression of Fc receptor that recognises the Fc portion of the antibody on effector cells.

The interactions between FcγR and Fc portions of certain mAbs have been reported to be important for the anti-tumour effect in murine models and in clinical trials. For example, the antitumor activities of trastuzumab (anti-HER-2 mAb) or rituximab (anti-CD20 mAb) were lower in FcγR-deficient mice than in wild-type mice (Clynes et al., 2000). However, it is not known whether or not ADCC itself is sufficient for tumour rejection (Hubert et al., 2011). But, since the outcomes of anti-cancer therapy are notably improved in the presence of ADCC, many pharmaceutical companies focused

their development of cancer treatments to new antibody-like structures with ability to enhance ADCC (Ravetch, 2010, Cheson and Leonard, 2008, Scott et al., 2012).

Today, therapeutic antibodies represent an important, indispensable part in treatments of cancers, autoimmune and inflammatory diseases. Most of the antibodies used at the moment are of human origin and are typically derived from large phage display libraries or transgenic mice engineered with human immunoglobulin genes (Chan and Carter, 2010). They can act through various mechanisms. For example, some interact with ligands and block them from binding to their receptors (infliximab (anti-TNF-α mAb) or belimumab (anti-BAFF mAb)), others affect tumour growth by modulating or blocking receptor signalling (transtuzumab (ani-Her2 mAb) or cetuximab (anti-EGFR mAb)) while some induce effector mechanisms such as ADCC (rituximab (anti-CD20 mAb) or alemtuzumab (anti-CD52 mAb)), antibody dependent cellular phagocytosis (ADCP) or complement dependent cytotoxicity (CDC) that result in eradication of antigen-bearing cells (Hubert et al., 2011). Despite the promising potential, mechanisms triggering effector function have been less studied (Levy et al., 2011).

To overcome certain clinical disadvantages of large antibody molecules, several small protein-based drugs and modified antibody formats are currently being investigated, such as Fab fragments (one light chain and half a heavy chain), single-chain variable fragments (scFv; two variable domains, one from a light and one from a heavy chain) or domain antibody (dAb, called also nanobody or VH; single monomeric variable antibody domain) and their various combinations. These minimized molecules display better penetration into solid tumours, reduced immunogenicity and faster blood clearance (Huston et al., 1996, Jones and Marasco, 1998, Colcher et al., 1998). However, they lack the Fc portion and therefore they cannot trigger ADCC. To overcome this, small molecules crosslinking two antigen-recognising parts (Fabs) - one directed to a diseased cell and another aiming to engage Fc receptor on an effector cell - have been investigated. One type of such molecules are “bi – or tri-specific killer cell engagers” or shorter BiKE / TriKE. They engage CD16 on NK cells by the additional Fab portion, directed against it, rather than by their Fc. Gleason et al. showed that NK cells activated with this-type of molecule secrete lytic granules and produce cytokines and chemokines (Gleason et al., 2012).

1.5. NK cell inhibitory receptors

The family of killer cell immunoglobulin-like receptors (KIRs) has evolved from the immunoglobulin (Ig) superfamily. It contains molecules that recognize MHC class I on target cells. The MHC class I is known as “self” as the KIR-MHC interaction provides the tolerance to healthy cells in body. KIRs are type 1 transmembrane glycoproteins consisting of two or three Ig-like domains with either a short or long cytoplasmic tail (Colonna and Samaridis, 1995). The expression on each NK cell seems to be random and is regulated by the methylation of KIR gene loci (Chan et al., 2003). The genetic loci are highly polymorphic among different individuals. Interestingly, some alleles can encode even an activating counterpart to the inhibitory receptor (Thielens et al., 2012). Three KIR genes (KIR2DL4, KIR3DL2, KIR3DL3) are common to every haplotype but the overall composition of KIR haplotype varies significantly between people (Caligiuri, 2008).

NK cells self-tolerance can be sustained even in the absence of MHC class I by other inhibitory receptors. Receptors CD94-NKG2A/C/E from C-type lectin family of CD94-NKG2 heterodimers bind to HLA-E, which is a non-classical MHC molecule (Braud et al., 1998b). Cytokines present in the cell local environment can modulate the expression levels of these receptors (Mingari et al., 1998, Bertone et al., 1999, Derre et al., 2002).

Additionally, other inhibitory non-MHC class I binding receptors have been reported. For example, a lectin-like receptor KLRG1 recognizes members of the classical cadherin family (Ito et al., 2006), and NKR-P1 recognizes lectin-like LLT1 molecule (Rosen et al., 2005). A list of inhibitory receptors and their ligands is summarised in the Table 1.2.

Table 1.2: Inhibitory receptors and their ligands

Inhibitory receptors	Known ligands	Reference
KIR family: KIR2DL1, 2DL2/3, 2DL4, 2DL5, 3DL1, 3DL2, 3DL3	Various allotypes of classical HLA class I molecules (HLA-A, HLA-B and HLA-C)	(Biassoni et al., 1995, Ciccone et al., 1992, Döhring et al., 1996, Faure and Long, 2002, Gumperz et al., 1997, Pende et al., 1996, Stern et al., 2008)
NKG2A/CD94	HLA-E	(Braud et al., 1998a)
LIR-1 (also known as LILRB1 and ILT2)	Various classical (HLA-A and HLA-B) and non-classical HLA class I (HLA-G) molecules, HCMV-derived UL-18	(Colonna et al., 1997, Cosman et al., 1997)
2B4	CD48	(Brown et al., 1998, Eissmann et al., 2005)
KLRG1	Cadherins	(Ito et al., 2006)
SIGLEC-7, SIGLEC-9	Sialic acids	(Avril et al., 2004, Nicoll et al., 2003)
NKR-P1A	LLT1	(Lanier et al., 1994, Rosen et al., 2005)

Inhibitory receptors' signalling

All inhibitory receptors signal through intracellular immunoreceptor tyrosine-based inhibitory motifs (ITIMs) that are located in the cytoplasmic part of these receptors. Ligation of inhibitory receptors results in the phosphorylation of tyrosine residues on the ITIMs which further recruit Src homology domain 2-containing protein tyrosine phosphatase 1 or 2 (SHP1 or 2) (Binstadt et al., 1996, Burshtyn et al., 1996, Tomasello et al., 2000). B-arrestin has been demonstrated to be involved in inhibition of NK cell activation through SHP1 and 2 recruitments (Yu, Su et al. 2008). Inhibitory signals result in inactivation of key components in the signalling for NK cell activation, including Vav1 (Stebbins et al., 2003). Recent findings suggest that engagement of ITIMs induce phosphorylation of a tyrosine adaptor Crk molecule that blocks essential

Crk-dependent signalling of NK cell activation (Liu et al., 2012). However, the interference of inhibitory signals with activating signals is not well described.

1.6. Aims

CD16 is an important activating receptor expressed on almost all circulating NK cells. Its ligation to the Fc portion of IgG antibodies triggers antibody-dependent cellular cytotoxicity (ADCC). Because of this it plays a pivotal role in mediating the tumour rejection in mAb-based therapies. However, NK cell activation leads to irreversible cleavage of CD16 extracellular portion. Prolonged exposure to activating signals, like in cancer patients or patients with chronic diseases, leads to severe CD16 downregulation. This has been linked with lower NK cell cytotoxicity.

Here I set out to address the functional outcomes of CD16 shedding. Specifically, I aimed to investigate how CD16 cleavage affects NK cell effector function. Moreover, I wanted to evaluate the impact CD16 shedding has on the immune synapse formation and the stability of the conjugate. Finally, little is known about the organisational changes, resulting from NK cell-mAb-coated-target cell interaction. To address these, I used a combination of microscopy techniques, including live imaging of cells interacting with activating ligands, and flow-cytometry based approaches. To image the nanoscale organisation of CD16 at the NK cell synapse super-resolution microscopy technique, GSD was used.

The overarching aim of the thesis was to establish how the shedding of CD16 affects NK cell serial killing.

The specific questions I tried to answer in this work were:

i. How does stimulation through CD16 or NKG2D, another NK cell activating receptor, affect the sequential NK cell responses? (Chapter 3)
ii. How does CD16 shedding affect formation of a conjugate with an opsonised target cell? (Chapter 4)
iii. What is the relationship between the nanoscale organisation of CD16 and efficient ADCC? (Chapter 5)

Chapter 2:

Materials and Methods

2.1. Cell culture

2.1.1. Human primary NK cells

Primary human NK cells were obtained from the peripheral blood of healthy volunteer donors purchased from the National Blood Service. Briefly, peripheral blood monocyte cells (PBMC) were purified by density gradient centrifugation using Ficoll-Paque (GE Healthcare, Life Sciences). NK cells were subsequently isolated from PBMCs by negative magnetic selection, using the human NK cell isolation kit (Miltenyi Biotec). Isolated cells were cultured at 37°C and 5 % CO_2 in DMEM medium containing 10 % human AB serum, 30 % Ham's F-12, 2 mM sodium pyruvate, 50 units/ml penicillin, 50 µg/ml streptomycin, 1 mM non-essential amino acids (all Sigma), 2 mM L-glutamine and 20 µM β-mercaptoethanol (both Gibco). Primary NK cells were additionally stimulated with 200 U/ml IL-2 (Roche). NK cells were rested for 6 days prior to experiments.

2.1.2. Cell lines

Several different human immortalised cell lines were used to study effects of CD16 shedding on NK cell effector function. Specifically, NK92 cell lines were used to create $CD16^+$ NK cell lines. NK92/CD16-WT and NK92/CD16-S197P were obtained by retroviral transduction with a retroviral vector pIB2, in which the coding sequences of CD16-WT or CD16-S197P were inserted (details in section 2.2).

NK92 is an immortalized cell line, established in 1992 from an NK cell lymphoma patient (Gong et al., 1994). It was purchased from the American Type Culture Collection (ATCC).

The Phoenix Ampho cell line was obtained from the Nolan laboratory at Stanford University, where it was originally developed. This cell line is a variant of the 293T cell line that has been stably transfected to express Moloney Murine Leukaemia Virus packaging proteins and can serve to produce amphotropic retroviruses.

Daudi cell line was used as an NK cell susceptible target. Daudi is a well characterized B lymphoblast cell line derived from a Burkitt's lymphoma patient in 1967 (Klein, 1975). Daudi-MICA had been created by the retroviral transduction of the Daudi cell line and had been used as target cells in the experiments previously published (Pageon et al., 2013).

2.1.3. Culturing of cell lines

All cells were cultured at 37°C and 5% CO_2. NK92 cell line was cultured at in alpha Minimum Modified Eagle Medium supplemented with 0.2 mM myoinositol, 0.02 mM folic acid, 2 mM L-Glutamine, Non-Essential Amino Acids 1x, 100 U/ml Penicillin, 100 µg/ml Streptomycin (all Sigma), 12.5 % fetal bovine serum (FBS), 12.5% Horse Serum and 0.1 mM, beta-mercaptoethanol (all Gibco).

Daudi and Phoenix Ampho cell lines were cultured in Roswell Park Memorial Institute (RPMI) 1640 culture medium (Sigma) supplemented with 10% FBS, 2 mM L-glutamine, and 1 % penicillin and streptomycin (all Gibco).

NK92 cell line was cultured in the presence of IL-2 (100 U/ml; Roche). NK92 cell lines created by retroviral transduction were maintained in the presence of 20 µg/ml of the selecting antibiotic blasticidin (InvivoGen).

All cell lines were routinely tested for mycoplasma infection using a PCR-based kit (PromoCell), which utilizes specific primers designed from DNA sequences coding for highly conserved ribosomal RNAs (16S-rRNA). All cells were tested negative.

2.2. Molecular Biology

2.2.1. Plasmid construction

Construction of retroviral pIB2-CD16

The retroviral vector pIB2 was a gift from M. Purbhoo, Imperial College London. The CD16 coding sequence has been designed for the previous work by our group (Rudnicka et al., 2013).

Site directed mutagenesis

A single nucleotide mutation in CD16-WT sequence was introduced using Q5 Site-directed Mutagenesis Kit (New England Biolabs), according to the manufacturer's instructions. This kit ensures exponential amplification by using non-overlapping primers. The reverse primer is designed so that the 5' ends of the two primers anneal back-to back, as illustrated by Figure 2.1. The desired sequence was incorporated into the middle of the forward primer sequence. Primers were designed and annealing temperatures were calculated using the New England Biolabs online primer design software, NEBaseChanger™. Primers sequences are listed in Table 2.1.

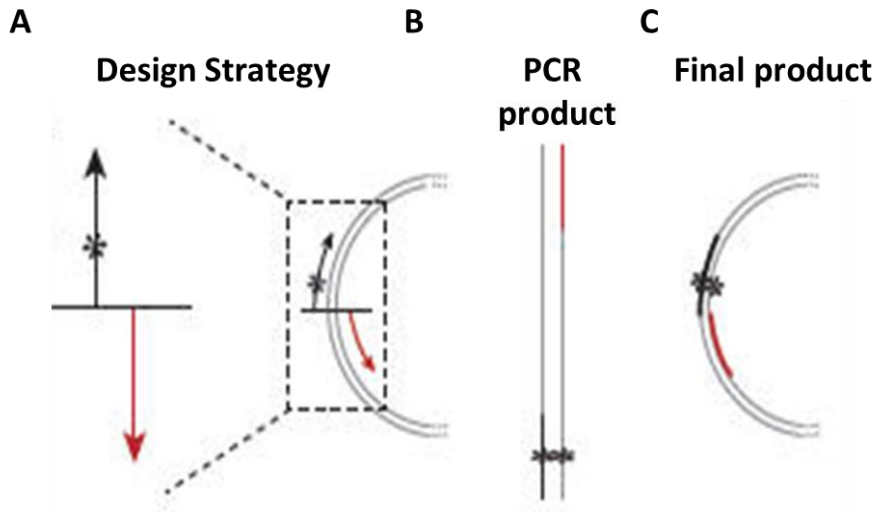

Figure 2.1: Site directed mutagenesis: The desired nucleotide changes were introduced in the middle of the forward primer (black, mutation marked with asterisk). The reverse primer (red) was designed so that the 5' ends of the two primers anneal back-to back **(A)**. The linear product with inserted mutation obtained from the PCR reaction **(B)** underwent ligation in the following step **(C)** (Adapted from: https://www.neb.com/products/e0554-q5-site-directed-mutagenesis-kit).

Table 2.1: Primers used for site directed mutagenesis

Mutation	Primer sequence	Annealing temperature
CD16-S197P	Forward primer: 5'TTTGGCAGTGcCAACCATCTC3' Reverse primer: 5'CCTTGAGTGATGGTGATG3'	60°C

The presence of point mutation was confirmed by DNA sequencing performed by GATC Biotech. All sequence alignments were performed using the BioEdit sequence alignment editor (version 7.2.5; Tom Hall, Ibis Biosciences). Plasmid containing mutated DNA sequence was purified from 200 ml of liquid cultures of NEB 5-alpha Competent E. coli (supplied as part of the Q5 Kit) transfected with the appropriate plasmids according to manufacturer's instructions. The cultures were grown in Luria-Bertani (LB) medium for 16 hours, at 37°C, under constant shaking and in the presence of 100 µg/ml of ampicillin (Sigma). Plasmids were purified using the PureYield Plasmid Maxiprep Kit (Promega) according to manufacturer's instructions.

2.2.2. Retroviral transduction of NK92 cell line

NK92 cells were transduced to express CD16 and its mutated form by retroviral transduction using the packaging cell line Phoenix Ampho. First, 10 µg of plasmid DNA and 10 µl of PLUS^{TM} reagent (Invitrogen) were mixed in Opti-MEM® reduced serum media (Invitrogen). After 10-minute incubation at room temperature the cationic lipid Lipofectamine® LTX reagent (Invitrogen) was added and the mixture was incubated for another 30 minutes at room temperature. Next, the solution was added to approximately 80% confluent 75 cm^3 tissue culture flask of Phoenix Ampho cells. After 3-day incubation at 37°C and 5 % CO_2 viral supernatant was removed from cells and 5 µl of 10 mg/ml Polybrene (Merck Millipore) was added. The solution was then filtered through 0.4 µm filter to remove cell debris and used for spinfection of NK92 cells. For this, 2 x 10^6 cells were resuspended 5 ml of filtered viral solution and placed in a well of a 6-well tissue culture plate. Cells were then centrifuged at 400 x g for 2 hours at 32°C and incubated for 3 hours at 37°C. Finally, the viral media was removed with and cells were cultured in normal media supplemented with IL-2. Two days after the infection 10 µg/ml of blasticidin was added to the culture medium for selection of transduced cells.

2.3. Antibodies and recombinant proteins

2.3.1. Antibodies

Antibodies, used to coat surfaces for functional assays and imaging are listed in the table below.

Table 2.2: Monoclonal antibodies used for functional experiments.

Antigen	Clone	Isotype	Supplier
CD16	3G8	Mouse IgG1, κ	BioLegend
NKG2D	1D11	Mouse IgG1, κ	BioLegend
Perforin	CE2.10	Mouse IgG2b, κ	Abcam
Isotype control	MOPC-21	Mouse IgG1, κ	BioLegend

Antibodies used for IFN-γ and soluble CD16 release detection by sandwich ELISA are detailed in the Table 2.3.

Table 2.3: Monoclonal antibodies used for IFN-γ and soluble CD16 detection by ELISA.

Antigen	Clone	Type	Conjugate	Concentration	Supplier
IFN-γ	NIB42	Capture	-	1 µg/ml	BD Biosciences
IFN-γ	4S.B3	Detection	Biotin	1 µg/ml	BD Biosciences
CD16	3G8	Capture	-	1 µg/ml	BioLegend
CD16	DJ130c	Detection	Biotin	1µg/ml	Bio Rad

2.3.2. Directly labelled antibodies

The directly labelled monoclonal antibodies used for staining for flow cytometry and imaging are shown in the following table.

Table 2.4: Directly labelled monoclonal antibodies used for flow cytometry and microscopy.

Antigen	Clone	Isotype	Conjugate	Supplier
CD16	3G8	Mouse IgG1, κ	AF488	BioLegend
CD16	3G8	Mouse IgG1, κ	AF647	BioLegend
CD16	3G8	Mouse IgG1, κ	PE	BioLegend
CD16, C-terminal	SP175	Rabbit IgG	AF647*	Abcam
NKG2D	1D11	Mouse IgG1, κ	PE	BioLegend
CD56	HCD56	Mouse IgG1, κ	BV421	BioLegend
CD19	HIB19	Mouse IgG1, κ	AF647	BioLegend
CD69	FN50	Mouse IgG1, κ	AF488	BioLegend
CD107a	H4A3	Mouse IgG1, κ	AF647	Santa Cruz
Anti-MICA	159227	Mouse IgG2b	APC	R&D Systems
Anti-human IgG (Fc specific)	polyclonal	Goat IgG	FITC	Sigma
Perforin	dG9	Mouse IgG2b, κ	AF488	BioLegend
Isotype control	MOPC-21	Mouse IgG1, κ	AF488	BioLegend
Isotype control	MOPC-21	Mouse IgG1, κ	AF647	BioLegend
Isotype control	MOPC-21	Mouse IgG1, κ	PE	BioLegend
Isotype control	MOPC-21	Mouse IgG1, κ	BV421	BioLegend
Isotype control	MOPC-173	Mouse IgG2b, κ	AF488	BioLegend
Isotype control	-	Rabbit IgG	AF647*	Sigma

*The antibodies were fluorescently labelled in our laboratory (See Antibodies labelling)

2.3.3. Fluorescent labelling of anti-CD16 antibody (clone SP175)

Anti-CD16 antibody (clone SP175, Abcam) was labelled with Alexa Fluor 647 dye, by conjugating the N-hydroxysuccinimide (NHS) ester portion of fluorescent dye to primary amines in the antibody. Briefly, 50 µl of antibody at concentration 1 mg/ml was added to 6 µl of 1M $NaHCO_3$ and 5 µl AF647 at 2 µg/µl in anhydrous DMSO (Molecular Probes, Life Technologies). The antibody-dye conjugation reaction was run for 45 minutes at room temperature. Once conjugated, the antibody solution was topped up with 200µl PBS and loaded into a Sephadex column (GE healthcare, Life Sciences) pre-washed with 5 ml of PBS. Once the antibody solution entered the column, 550 µl PBS was added and allowed to flow through. Last drop of the flow through fraction contained the labelled antibody and was thus collected in a clean Eppendorf tube. Next, 300 µl PBS was added and the remaining eluent was collected.

The final antibody concentration and labelling efficiency (the average ratio of dye to antibody) was determined from absorbance readings at 280 nm and 650 nm (NanoDrop 200 spectrophotometer, ThermoFisher Scientific), using the following equation:

$$Moles\ of\ dye\ per\ mole\ of\ protein = \frac{(\mathrm{A}_{max}\ \mathrm{x}\ \varepsilon_{protein})}{\varepsilon_{max}(\mathrm{A}_{280} - \mathrm{A}_{max}\ \mathrm{x}\ \mathrm{C}_{280})}$$

(Equation 2.1)

where A_{max} is the absorption of the dye at its maximum absorption wavelength (e.g. 650nm for Alexa Fluor 647), $\varepsilon_{protein}$ is the molar extinction coefficient of mouse IgG antibody at 280nm, ε_{max} is the molar extinction coefficient of the dye at its maximum wavelength, A_{280} is the absorbance at 280 nm, and C_{280} is a correction factor used to account for the absorbance of the fluorophore at 280 nm.

2.3.4. Recombinant proteins

To induce NK cell activation, surfaces were coated with recombinant proteins, listed in Table 2.5.

Table 2.5: Recombinant proteins used for NK cell stimulation.

Protein	Concentration	Supplier
MICA-Fc	2.5 µg/ml	R&D Systems
ICAM1-Fc	2.5 µg/ml	R&D Systems

In addition to these proteins, surfaces were also coated with the humanised anti-CD20 monoclonal antibody rituximab (GSK), which is known to stimulate NK cells through CD16 ligation. Unless indicated otherwise, rituximab was used at 10 µg/ml.

2.4. Functional assays

2.4.1. Preparation of coated slides for NK cell stimulation

Preparation of 8-chamber glass coverslips was adapted from published protocols (Culley 2009). Briefly, slides (#1.5 Lab-Tek II, Nunc) were coated with 200 µl poly-L-lysine (PLL, Sigma), diluted in sterile water at concentration 0.01%. Lab-Teks were incubated at RT for 10 min, the solution was removed and Lab-Teks were dried in a heating chamber at 60°C. NK cell ligands were diluted in PBS in the following combinations:

a) 2.5 µg/ml rhMICA-Fc + 2.5 µg/ml rhICAM1 (both R&D Systems)
b) 10ug/ml rituximab (GSK) + 2.5 µg/ml rhICAM1 (R&D Systems)
c) 2.5 µg/ml rhICAM1 alone (R&D Systems)

For each solution, 200 µl was added to the wells and coverslips were incubated overnight at 4°C. On the following morning, solutions were removed and wells were washed three times with 200 µl of PBS.

2.4.2. Perforin capture assay

To capture perforin, secreted from NK cells upon their activation, chambered coverslips were coated with 5 µg/ml anti-perforin mAb (clone CE2.10, AbCam) alongside NK cell ligands. $5x10^5$ primary NK cells were incubated at $1x10^6$ cells/ml on coated slides for 1h (unless indicated otherwise) at 37°C, 5% CO_2. Supernatants were removed and cells interacting with the surface were gently detached using 500 µl non-enzymatic cell dissociation solution (Sigma) by further incubation at 37°C for 15 min and gentle pipetting. Slides were then washed three times with 200 µl PBS and blocked with 1% BSA/PBS for 15 min. Captured perforin was stained with anti-perforin AF488 mAb (clone dG9, BioLegend) overnight at 4°C. The following day slides were washed and imaged by inverted confocal microscope (Leica TCS SP8) with a 100X/1.4 NA oil immersion objective. Images were analysed using ImageJ software (National Institutes of Health).

Sequential stimulation on coated slides

$5x10^5$ primary NK cells were incubated in 500 µl on slides, coated with NK cell ligands and anti-perforin mAb (clone CE2.10, AbCam) at 37°C. After 1h supernatants were removed and cells were gently detached using 500 µl non-enzymatic cell dissociation solution (Sigma) by 15 min incubation at 37°C and gentle pipetting. Collected cells were then washed in 500 µl clone media and resuspended in fresh clone media. A large portion of cells was then used for a sequential stimulation step on fresh activating surfaces and the rest was used for the assessment of their surface receptors expression. Captured perforin was stained as described above.

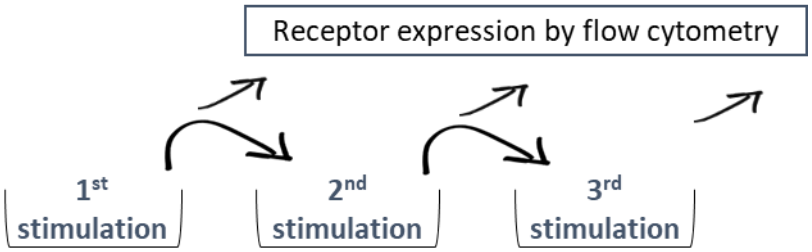

Figure 2.2: Sequential stimulation on coated slides. NK cells were stimulated on coated surfaces repeatedly. A portion from each stimulation was taken to assess receptor expression.

2.4.3. Flow Cytometry

Receptor expression assay

Surface receptor expression levels were determined by flow cytometry. Approximately $1x10^5$ unstimulated cells or cells collected from coated slides were washed in washing buffer, which consisted of PBS supplemented with 1% FBS. Fc receptors were blocked with 15 min incubation in washing buffer containing 2% human AB serum (Sigma) at 4°C. Cells were then stained for 30 min in 100 µl washing buffer containing the relevant antibodies or isotype controls. The specific antibodies used for staining are listed in Table 2.4. Following staining, cells were washed in 3 ml of washing buffer and fixed in 2% para-formaldehyde in PBS. Surface receptor staining was assessed by flow cytometry using the FACS Canto II cell analysers (Becton Dickinson, BD) and analysed with FlowJo software (FlowJo).

NK cell receptor expression upon the co-incubation with target cells

To assess the levels of NK cell receptors upon the co-incubation with target cells, target cells were labelled with Cell Trace Violet cell proliferation dye (Thermo Fisher) to distinguish from NK cells. For this, cells were washed three times in 5 ml of cold RPMI and then Cell Trace Violet dye was added in warm RPMI at 5 µM. Cells were incubated for 15 min at 37°C and then washed with full media three times to remove the excess dye. Finally, cells were resuspended in clone media at $1x10^6$ cells/ml. Daudi cells were opsonised with rituximab by adding 10 µg/ml of antibody to cells and incubating for 1h at 37°C. $1x10^5$ NK cells were then mixed with $1x10^5$ targets in 96-well plate in 200 µl of clone media. After 1.5h incubation at 37°C cells were stained for receptor expression by flow cytometry as described above.

Degranulation assay

Primary NK cells were incubated on coated surfaces, as indicated, in the presence of GolgiPlugTM (1/1000 dilution, BD Biosciences), monesin (1/1000 dilution, Biolegend) and anti-LAMP-1 AF647 mAb (clone H4A3, Santa Cruz Biotechnology) or isotype control AF647 mAb (mouse IgG1 isotype control, clone MOPC-21, Biolegend), for 4 hours at 37ºC. After incubation, cells were washed and stained with Zombie NIR™ viability dye (Biolegend), anti-CD56-BV421 mAb (clone HCD56, Biolegend) and anti-LAMP-1 AF647 mAb or isotype-matched control mAbs. Finally, cells were washed in

1% FBS/PBS, fixed in 2% PFA/PBS, assessed by BD FACS Canto II flow cytometer (BD Biosciences) and analysed (FlowJo_V10 software).

Killing assay

NK cell killing of Daudi target cells was assessed by the activity of Caspase 3/7. First, Daudi cells were labelled with cell proliferation dye (Cell Trace Violet cell proliferation dye, Thermo Fisher), to distinguish them from NK cells. For this, cells were washed three times in 5 ml of cold RPMI and stained with 5 µM Cell Trace Violet dye in warm RPMI for 15 min at 37°C. Cells were then washed with full media three times to remove the excess dye and resuspended at $1x10^6$ cells/ml in clone media with 2 µM Cell Event™ Caspase-3/7 Green Detection Reagent (Thermo Fisher). To opsonize Daudi cells, 10 µg/ml rituximab was added to $1x10^6$ stained cells/ml and incubated for 1h at 37°C. NK cells were washed and resuspended at $1x10^6$/ml in clone media with 2 µM Cell Event™ dye. For killing assay, NK cells and targets were incubated at E:T = 1:1 in 200 µl in the U-bottom 96-well plate (Thermo Fisher) for 1.5h. Then, cells were washed with 3 ml washing buffer, blocked with 2% human AB serum for 10 min at 4°C and stained with anti-CD16 AF647 mAb (details in Table 2.4) for 30 min at 4°C. Finally, cells were washed with 3 ml washing buffer and fixed with 2% PFA/PBS. Killing rate and CD16 expression on NK cells was assessed by BD FACS Canto II flow cytometer (BD Biosciences) and analysed (FlowJo_V10 software).

- ***Sequential pre-stimulation on slides***

$5x10^5$ primary NK cells were incubated in 500 µl of clone media on slides coated with NK cell ligands (ICAM1, ICAM1 + MICA, ICAM1 + rituximab) at 37°C. After 1h supernatants were removed and cells were gently detached using 500 µl non-enzymatic cell dissociation solution (Sigma) by 15 min incubation at 37°C and gentle pipetting. Collected cells were then washed in 500 µl clone media, resuspended in fresh clone media and incubated on coated slides for another hour at 37°C. After the second pre-stimulation, NK cells were again gently detached, washed and resuspended in fresh clone media at concentration $1x10^6$ cells/ml. Pre-stimulated NK cells were then mixed with Daudi targets (Daudi, Daudi-MICA or Daudi-rituximab) at E:T=1:1 for 1.5 h at 37°C in 200 µl of clone media in the presence of Cell Event™ Caspase-3/7 Green Detection Reagent (Thermo Fisher) (Figure 2.3). Finally, cells were washed with 3 ml washing buffer and stained for surface receptors, CD16 and

CD19 (to distinguish between NK cells and targets), as described above. Target cell death was assessed by BD FACS Canto II flow cytometer (BD Biosciences) and analysed (FlowJo_V10 software).

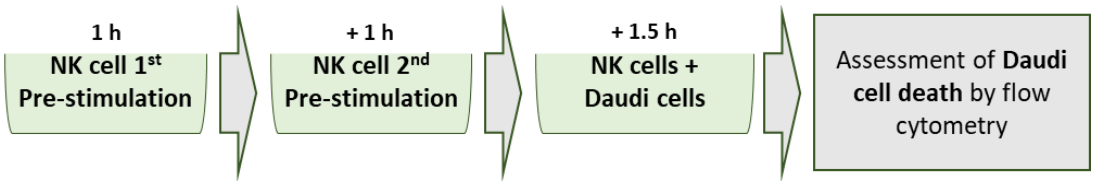

Figure 2.3: Principle of the assay of killing of Daudi with NK cells pre-stimulated on slides. 5x10^5 primary NK cells were stimulated on coated surfaces twice sequentially for 1h. Then, Daudi cells (Daudi, Daudi-MICA or Daudi-rituximab) were added at E:T=1:1. Cell death was assessed by Caspase 3/7 staining by flow cytometry. To distinguish between NK cells and Daudi cells, cells were labelled with anti-CD16 AF647 and anti-CD19 PE mAbs.

- ***Sequential stimulation with target cells***

To assess sequential killing of target cells, 10^5 Daudi, Daudi-MICA or Daudi-rituximab were incubated for 1.5 h with NK cells at E:T = 1:1 ratio in 200 µl clone media. Following this, 10^5 Daudi-MICA or Daudi-rituximab labelled with cell proliferation dye (Violet Cell Trace Proliferation Kit, Thermo Fisher) were added for another 1.5 h (Figure 2.4). Samples were incubated in the presence of Caspase 3/7 Green stain (Life Technologies) at 37°C. Cells were then washed with 3 ml washing buffer, fixed in 2% PFA/PBS, assessed by BD FACS Canto II flow cytometer (BD Biosciences) and analysed (FlowJo_V10 software).

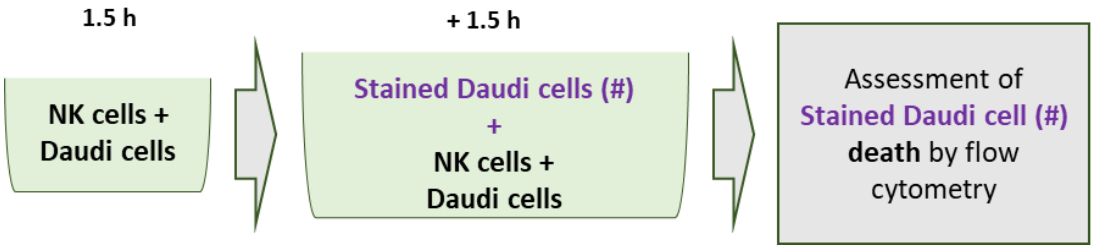

Figure 2.4: Schematic representation of sequential stimulation with target cells. 105 NK cells were incubated with Daudi, Daudi-MICA or Daudi-rituximab at E:T = 1:1 for 1.5h. Then 105 Daudi-MICA or Daudi-rituximab, labelled with violet cell tracer dye (Stained Daudi Cells #) were added. The mixture was incubated for additional 1.5h. Cell death of stained Daudi cells was assessed using Caspase 3/7 dye by flow cytometry.

2.4.4. IFN-γ detection by enzyme-linked immunosorbent assay (ELISA)

Primary NK cells were incubated on polystyrene flat bottom 96-well plate (Nunc) coated with rhMICA-Fc or rituximab, both with ICAM1, or ICAM1 alone, at 37ºC for 18 hours. Cell supernatants were collected and centrifuged at 350 x g for 10 min at 4°C to remove cell debris. IFN-γ secretion was quantified from the supernatants by sandwich ELISA. For this ELISA plates were coated with anti-IFN-γ mAb (clone NIB42, BD Biosciences, 1 µg/ml) in binding buffer (carbonate bicarbonate; Sigma) and blocked with 1% bovine serum albumin (BSA)/0.05% Tween-20/PBS. Supernatants were added to the plate and incubated for 1 hour at RT. Plates were washed and incubated with biotinylated IFN-γ mAb (clone 4S.B3, 1 µg/ml, BD Biosciences) and then streptavidin HRP (1/1000, BD Biosciences). The plates were developed with TMB ELISA substrate (Sigma) and the reaction was stopped with 1N H_2SO_4. Absorbance was measured at 450 nm using a 570 nm reference line to compensate for optical interference.

2.4.5. Soluble CD16 detection by enzyme-linked immunosorbent assay (ELISA)

Primary NK cells were incubated on polystyrene flat bottom 96-well plate (Nunc) coated with rituximab, or anti-CD16 mAb (clone 3G8), both with ICAM1, or ICAM1 alone, at 37ºC for 18 hours. Cell supernatants were collected and centrifuged at 350 x g for 10 min at 4°C to remove cell debris. Soluble CD16 was quantified by sandwich ELISA. For this ELISA plates were coated with anti-CD16 mAb (clone 3G8, BioLegend, 1 µg/ml) in binding buffer (carbonate bicarbonate; Sigma) and blocked with 1% bovine serum albumin (BSA)/0.05% Tween-20/PBS. Supernatants were added to the plate and incubated for 2 hours at RT. Plates were washed and incubated with biotinylated anti-CD16 mAb (clone DJ130c, 1 µg/ml, BioRad) and then streptavidin HRP (1/1000, BD Biosciences). The plates were developed with TMB ELISA substrate (Sigma) and the reaction was stopped with 1N H_2SO_4. Absorbance was measured at 450 nm using a 570 nm reference line to compensate for optical interference.

2.5. Confocal microscopy

2.5.1. Cell migration assay

Primary NK cells were stained with 1 µM Calcein Red-Orange (Thermo Fisher). For this, cells were first washed three times with 10 ml RPMI media. Then, cells were incubated in RPMI with dye for 15 min at 37°C, washed with 2 ml clone media three times and seeded at $5x10^5$ cells/ml into coated chambered glass coverslips. Where indicated, 1 µM TAPI-0 (Santa Cruz) was added prior to acquisition. Time-lapse imaging was performed on a TCS SP8 CW scanning laser confocal microscope with a 20X/0.75NA air objective lens (Leica) at 37°C and 5% CO_2 immediately after cells landed on slides at rate of 1 frame per 30 secs for 45 min. Acquired fluorescent, bright-field and IRM images were merged and individual cells were manually tracked using MatLab based software, Cell Tracker (Piccinini et al., 2015).

2.5.2. Internal reflection microscopy (IRM)

To define the interaction between NK cells and coated glass coverslips, interference reflection microscopy (IRM) was used. IRM has been previously used to determine the lifetime of dynamic contacts made by cells interacting with coated glass coverslips or glass supported lipid-bilayers (Bunnell et al., 2002, Ashdown et al., 2017). It is a label-free technique, where the intensity of the signal is a measure of proximity of the object to the glass surface. The technique is based on the observation that when cell membrane is close to the glass, the reflected light from the glass is shifted half a wavelength due to a change in refraction index. The interference causes that the light waves reflected from the glass and from the membrane cancel each other out, resulting in a dark pixel in the final image. When the membrane is not attached to the glass, the reflection from the membrane has a smaller phase shift compared to the reflected light from the glass resulting in a brighter pixel. When there is no specimen, only the light from the glass is detected and appears as a bright pixel in the final image (Verschueren, 1985).

To visualise NK cell contacts with coated surfaces, live IRM imaging was performed on a TCS SP8 CW scanning laser confocal microscope with a 100X/1.4NA oil-immersion objective lens (Leica) at 37°C and 5% CO_2. 560 nm excitation at a low laser power and signal detection on a photo multiplier tube detector set to 555 nm-570 nm detection wavelengths on reflection mode were used. IRM images were recorded at rate of 1 frame per second. For analysis stacks were reduced 1:5 using

the Stacks plugin in Image J (National Institutes of Health). Stacks were smoothed and thresholded using Otsu method. Spreading area and circularity was analysed using Analyse Particles plugin.

2.5.3. Live imaging in microwells

Sterile microwells were coated with 10 µg/ml fibronectin (Sigma), and blocked with full media. To facilitate the access of the liquid inside microwells, chips were first degassed, using vacuum chamber. Primary NK cells or NK92/CD16^{+} were stained with 1 µM Calcein Red-Orange (Invitrogen) or 5 µM Cell Trace Violet Proliferation Kit (Thermo Fisher) and Daudi cells were labelled with 0.3 µM Calcein Green (Invitrogen) or 1 µM Calcein Red-Orange (Invitrogen) and Daudi-MICA labelled with 0.3 µM Calcein Green (Invitrogen). To stain, cells were first washed three times with 10 ml RPMI and then incubated with the dye solution in RPMI for 15 at 37°C. Then, cells were resuspended at 1x10^{6} cells/ml in clone media when using primary NK cells and NK92 media when using NK92 cells.

Labelled NK cells were then added to Daudi-rituximab at E:T = 1:3 or to Daudi-rituximab and Daudi-MICA at E:T:T = 1:1.5:1.5 as indicated, in clone media supplemented with 1 µl ToPro-3 (Thermo Fisher) to discriminate dead cells. Cell solution was immediately placed onto microchip with wells of dimensions 450 x 450 x 300 µm^{3} (large wells) or 50 x 50 x 300 µm^{3} (small wells) and imaged using TCS SP8 CW scanning laser inverted confocal microscope with a 20X/0.75NA objective (SP8, Leica). Time-lapse imaging was performed at 37°C and 5% CO_2 for 8h, and an image was acquired every 3 min. Where indicated 1 µM TAPI-0 (Santa Cruz) was added to cells prior the acquisition. Wells with or without TAPI-0, and wells with NK92/CD16-WT or NK92/CD16-S197P were imaged in parallel by using two separate basins, each covering multiple wells of the microchip. Fluorescent and bright-field images were merged and cell-cell interactions were analysed manually using ImageJ (National Institutes of Health).

2.5.4. Imaging F-actin rings

For actin ring analysis, cells were allowed to settle on the coated slides for 5 min (unless indicated otherwise) at 37ºC, fixed in 4% PFA/PBS (Sigma) at RT for 20 min and permeabilised with 0.1% Triton X-100/PBS (Sigma) at RT for 10 min. Actin was

stained with AF488-labeled phalloidin (Invitrogen, 1/200 dilution in PBS) and imaged by confocal microscopy (Leica TCS SP8) with a 100X/1.4 N.A. oil immersion objective. Images were exported to ImageJ (National Institutes of Health) and the percentage of cells forming peripheral actin rings was scored.

2.5.5. Confocal microscopy

Live and fixed cells and captured perforin were imaged using the Leica LAS AF software and with a TCS SP8 STED CW inverted confocal microscope (Leica Microsystems). Bright-field, IRM and fluorescence images were obtained using a HC PL APO 100X/1.40 oil-immersion objective, 63X/1.20NA oil-immersion objective and 20X/0.75NA air-objective. Images were taken in 512 pixels x 512 pixels or 1024 x 1024 formats. Images of fixed samples were acquired at room temperature while live imaging was performed at 37°C, 5% CO_2.

2.6. TIRF and GSD microscopy

2.6.1. Preparation of the sample

To visualize CD16 on NK cell surface, cells were let to spread on coated coverslips for 5 min and fixed with 4 % paraformaldehyde/PBS for 20 min at RT. Then, fixed cells were washed three times with PBS and blocked with 3% BSA/PBS for 1 hour at RT. Extracellular CD16 was stained with 10 µg/ml of anti-CD16 AF647 mAb (clone 3G8 or B73.1, both BioLegend) and intracellular CD16 was stained with 10 µg/ml anti-CD16 mAb conjugated to AF647 (clone SP175, AbCam), both diluted in 3% BSA/PBS for 1h at RT. Cells were then extensively washed with 0.2 % BSA/PBS, to remove all non-bound dye molecules. To stain for intracellular CD16 and/or F-actin, cells were permeabilised with 0.1 % Triton X-100/PBS (Sigma) at RT for 10 min. Actin was stained with AF488-labeled phalloidin (Invitrogen, 1/200 dilution in PBS). Before GSD imaging, 200 µl of fresh imaging buffer [50 mM Tris-HCI (pH 8.0), 10 mM NaCl, 10% glucose and 1%(v/v) β-mercaptoethanol and 1% (v/v) GLOX solution (56 mg/ml glucose oxidase, 17 mg/ml of catalase, all from Sigma-Aldrich) mixed extemporaneously] was added to each well.

2.6.2. TIRF and GSD imaging

TIRF and GSD imaging was performed on a wide-field Leica SR GSD microscope using an 160X/1.43NA oil immersion objective. The fluorescence was collected on an electron-multiplying charge-coupled device (EMCCD) camera (Andor iXon DU897EC50-#BV) with a CCD sensitivity of 12.4 electrons per analogue to digital (A/D) count, single pixel noise of 52.95 electrons and pixel size of 100 nm. During the acquisition, samples were illuminated with 488 and 642 nm lines of the laser. For 488 and 642 nm lines, 60 % and 25 % of the maximum laser power were used, respectively. Cells were illuminated in TIRF mode which limits the imaging to molecules that are within ≈200 nm of the glass surface. TIRF auto-alignment was run each time at the start of the session and later every 2 hours. The electron-multiplying (EM) gain was set to 120. Up to 3 x 10^4 frames were acquired with a camera integration time of 15 ms (less if no photo-switching events could be detected in at least 2 x 10^3 consecutive frames). The mean fluorescence intensity of receptor staining in imaged cells was measured in TIRF microscopy images, using the ImageJ processing software (National Institutes of Health).

2.6.3. GSD data processing

Localisations of detected molecules were defined by ImageJ plug-in, ThunderSTORM from fluorescence intensity images captured by GSD camera (Ovesný et al., 2014). The use of ThunderSTORM for the processing of GSD data was chosen because of its excellent performance in comparison to a broad range of similar software dedicated to analysis of single-molecule localisation data (Sage et al., 2015).

Data extraction is illustrated in Figure 2.3. First, a wavelet transform using a convolution kernel based on normalised B-spline basis function of the third order with a scaling factor of 2 was applied (Izeddin et al., 2012). The approximate position of the molecules was calculated by the local intensity maxima method. For this, the intensity of each pixel of the image was compared to a specified threshold and at the same time evaluated whether it is greater than or equal to all values within a 4- or 8-connected neighbourhood. The threshold was 3 times the standard deviation of the intensity values from the first wavelet level F1 and was defined empirically. Connectivity was set to 8-neighbourhood, as suggested by Izeddin et al. (Izeddin et al., 2012).

Sub-pixel localisations of detected molecules were extracted by a PSF Integrated Gaussian method. The Gaussian function has been described to provide a good

approximation of the real PSF of a microscope and its integrated form considers the discrete nature of pixels present in digital cameras (Thompson et al., 2002, Stallinga and Rieger, 2010, Smith et al., 2010). A fitting radius of 5 pixels has been applied. Molecular (x-y) coordinates were finally obtained using least-squares fitting method with initial sigma parameter (standard deviation of the Gaussian distribution) set to 1.6 pixels. Poorly localised molecules were filtered out with based on their low intensity (<500 photons), sigma value (<15 nm or >250 nm) and uncertainty (>50 nm).

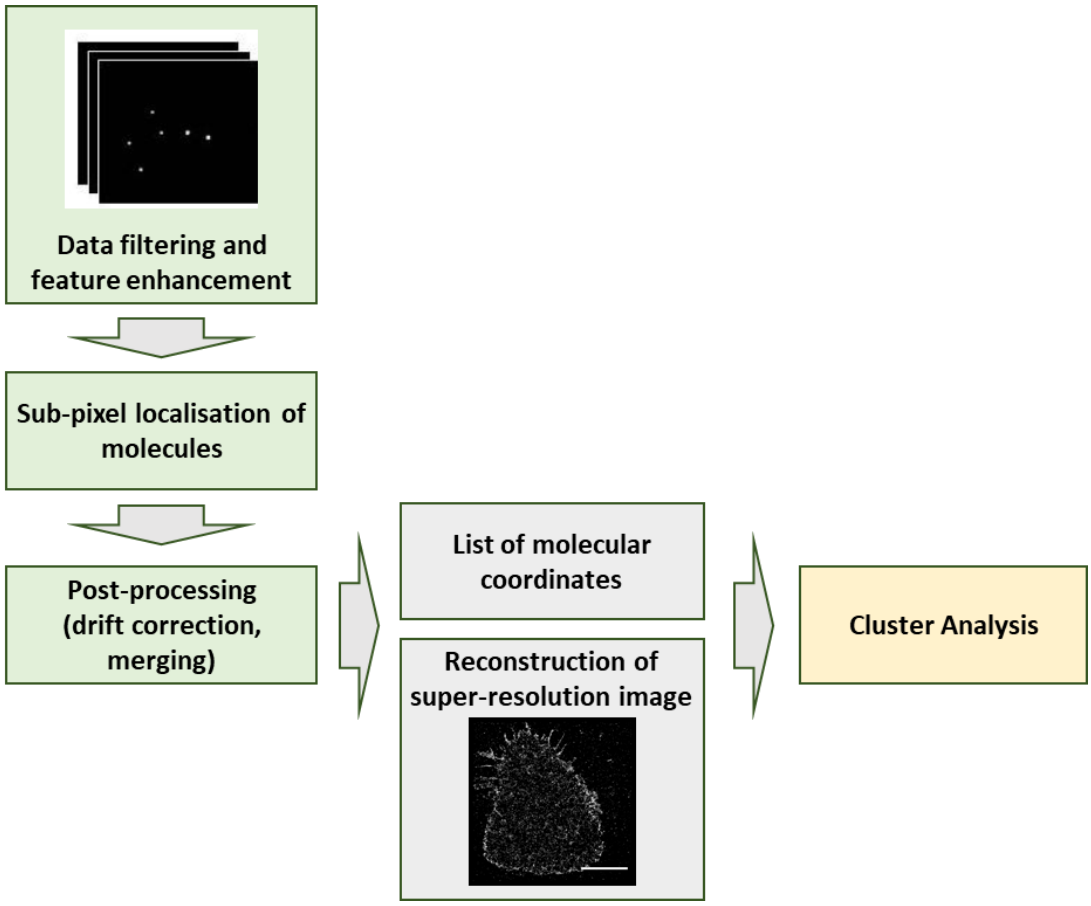

Figure 2.5: GSD image reconstruction workflow.

Like in other single-molecule localisation microscopy techniques, in GSD imaging dye molecules undergo multiple rounds of photo-activation leading to multiple localisations of the same molecule. To account for this, the events whose localisations appeared within a short distance and a defined number of consecutive frames (off-gap) were merged into one localisation. The position of the merged molecule was

calculated as the mean value of the original data. The merging radius and off-gap value were empirically defined (Chapter 5).

Long acquisition times required for GSD imaging of each sample result in lateral drift. To account for this, cross-correlation method was used to determine the shift between the first image and each of the subsequent images. The presumption of this method is that similar structures will appear in all reconstructed images. The shift in the position caused by the drift in cross-correlated images corresponds to the relative position between the global intensity maximum peaks. The original coordinates are corrected for drift using estimated values (Mlodzianoski et al., 2011).

The list of filtered and corrected (x-y) coordinates of detected molecules was used to reconstruct a 2D super-resolution image using Gaussian rendering. This method draws a normalised symmetric 2D Gaussian function integrated over the pixel area for every localised molecule within a standard deviation equal to the computed uncertainty.

2.6.4. Cluster analysis of GSD images

Quantitative assessment of the distribution of molecule distribution was carried out by two different methods; Ripley's K function and local point pattern analysis based on Getis and Franklin's method. For both, several non-overlapping 3x3 μm^2 regions were selected from central areas of the cell first. Then, the cluster analysis was performed for the selected regions.

Ripley's K function was calculated in SpPack, an add-in for Microsoft Excel (Perry, 2004):

For i ≠ j

$$K(r) = A\sum_{i=1}^{n}\sum_{j=1}^{n}\left(\frac{\delta_{i,j}}{n^2}\right) \text{ where } \delta_{i,j} = 1, \text{ if } \delta_{i,j} < r, \text{otherwise } 0$$

(Equation 2.2)

where A is the area of the analysed region (here 3 x 3 μm^2), n is the number of points, r is the spatial scale (radius) for the K-function calculation and $\delta_{i,j}$ is the distance between points i and j.

This counts the number of molecules localized within concentric rings centred on each event, normalized to the average molecular density of the entire region.

The function was then linearized to generate the L-function according to:

$$L(r) = \sqrt{K(r)/\pi}$$

(Equation 2.3)

so that L(r) scales linearly with radius.

For completely spatially random distributions of molecules, L(r) = r. Here L(r) – r was plotted against r so that a random distribution has L(r) - r = 0 for all r. Therefore, for length scales at which the distribution is more clustered than a random distribution, L(r) - r was positive, whereas L(r) - r was negative if the points are less clustered than for random events. Points at the edge of the distribution region were weighted to negate edge-related effects. Confidence intervals were generated by simulating 100 spatially random distributions with the same average molecular density as the data regions.

Quantitative pseudo-colour heat maps and binary maps of clusters were created using a custom MatLab script written by Dr David J. Williamson from the University of Manchester (Oszmiana et al., 2016). To create quantitative pseudo-colour cluster maps, values of L(r) for each point (ignoring the j-sum in Equation 4, according to univariate Getis and Franklin's local point pattern analysis method) at a value of r = 30 nm (L(30)) were calculated. The radius of 30 nm was chosen empirically by analysing the same representative dataset with identical parameters and only increasing the radius. Two-dimensional pseudo-colour heat-maps were created by interpolating a surface plot of L(30) on a grid of resolution 5 nm.

To compare the clustering patterns, binary maps were generated by overlaying a disc element of 25 nm radius around all point localizations with L(30) above a threshold value, L(30) ≥ 70. An appropriate threshold value was chosen based on randomised datasets of the same area and molecule densities as representative regions selected from acquired images. L(30) values were calculated for molecules within the randomised regions and distribution of L(30) values was compared between regions from experimental data and their corresponding randomised regions. This led to setting the threshold value to L(30) ≥ 70, above which molecules were identified as localized within a cluster and included in the binary maps. From the binary map, cluster size and circular shape (defined as 4π*area/perimeter^2, which equals to 1 for a perfect circle) and number of clusters were extracted using ImageJ and analysed.

2.6.5. Statistical analysis

Sample sizes chosen were appropriate to provide enough power for statistical tests used in this study. For each data set, a D'Agostino & Pearson omnibus test was first used to evaluate the distribution of obtained values. When all data sets had a normal Gaussian distribution, statistical analysis was evaluated using parametric statistical tests. Specifically, the statistical significance of differences between two groups of data was examined using a two-tailed t-test with Welch's correction, in order to account for variation in standard deviations. The statistical significance between three or more conditions was assessed by one-way ANOVA.

If at least one of the conditions did not have a normal distribution, non-parametric tests were used to assess statistical significance. A Mann-Whitney test was used to compare two groups of data and multiple comparisons were evaluated using a Kruskal-Wallis test or matched-values Friedman test with Dunn's post-testing. Differences were defined as non-significant (NS) where $p \geq 0.05$ and statistically significant where $p < 0.05$ (indicated by a single asterisk *), $p < 0.01$ (**), $p < 0.001$ (***) and $p < 0.0001$ (****). All statistical analyses were performed using GraphPrism 7.0 (GraphPad Software, version 7).

Chapter 3:

Effect of shedding CD16 on NK cell serial killing

3.1. Introduction

Cytolytic activity of NK cells is initiated when the activating signals coming from the diseased cell prevail over the inhibitory ones. It is mediated by the release of cytolytic granules containing lytic granzymes and pore-forming perforin into the target cell through the cytolytic synapse (Jenkins and Griffiths, 2010, Cartwright et al., 2014, Orange, 2008). The lytic granules are delivered to the synapse within minutes of initial NK cell activation by moving along microtubules in a dynein-mediated minus-end direction (Stinchcombe et al., 2006, Mentlik et al., 2010, Ritter et al., 2015, Carisey et al., under review). For cytotoxic T lymphocytes (CTLs), it has been shown that such granule polarization occurs in two distinct stages; first granules converge towards the centrosome and then they all polarize together and reach the synapse at the same time (Ritter et al., 2015). Granules then pass the actin meshwork and fuse with the NK cell membrane and release their contents (Brown et al., 2011, Lagrue et al., 2013, Lagrue et al., 2015). Many granules however, release only a portion of their content into the synapse, while the rest is re-internalised (Liu et al., 2011).

Lytic granule polarization can be triggered by the ligation of the integrin LFA-1 as well as by other activation receptors (James et al., 2013). But, the polarization alone is not always leading to degranulation, nor is prerequisite for a successful secretion of the granules. Using *Drosophila* insect cells, expressing ligands of human NK cell receptors, Bryceson et al. showed that the ligation of ICAM1 was sufficient to induce polarization of granules, but not degranulation. On the contrary, engagement of CD16 by rabbit IgG induced degranulation without specific polarization (Bryceson et al., 2005). Colligation of both, CD16 and LFA-1 is required for the directed secretion into the synaptic cleft, resulting in greater efficiency of specific target cell lysis and reduced bystander killing (Hsu et al., 2016).

Upon delivery of the lytic hit, NK cells can dissociate and start the search for new potential targets (Martz, 1976, Vanherberghen et al., 2013). In vivo imaging of CTL cells has shown that one CTL can kill 2-16 virus-infected cells per day (Halle et al., 2016). Similarly, in vitro assays showed that individual NK cells can kill up to 7 targets in 12 hours (Vanherberghen et al., 2013). Importantly, the ability of NK cells to kill sequentially varies significantly even within an individual donor. It is possible that this is dictated by the education status of NK cells (Yu et al., 2007, Cooley et al., 2007, Fauriat et al., 2008). Forslund et al. demonstrated that cells expressing NKG2A are more potent killers and have greater potential to kill sequentially than NK cells lacking inhibitory receptors on their surface (Forslund et al., 2015). It is not known whether or not other cell surface markers can indicate the ability of NK cells to engage in serial killing. However, there are a few other potential causes affecting their responses. Killing action alone, coinciding with the depletion of lytic granule content can lead to loss of NK cell function. Moreover, tumour infiltrating NK cells or NK cells isolated from blood of patients with chronic diseases, such as HIV, commonly display very low levels of activating receptors (Groh et al., 2002, Costello et al., 2002, Coudert et al., 2005, Coudert et al., 2008, Wiemann et al., 2005, Konjević et al., 2007, Dugast et al., 2011, Liu et al., 2009). This has been associated with decreased NK cell cytotoxicity and increased disease severity.

Repertoire of ligands expressed by target cells also plays an important role in determining NK cell responses. Study in mice demonstrated that cancer cells shedding soluble MULT-1, an NKG2D ligand, boost NK cell-induced cancer rejection through NKp46 and NKRP1C (Deng et al., 2015). Bhat et al. established that the opsonisation of target cells with a therapeutic antibody rituximab triggering NK cells through CD16 enhances NK cell anti-tumour activity (Bhat and Watzl, 2007). However, the sequential killing of targets expressing different ligands has not yet been addressed.

NK cells are key players in anti-viral and anti-tumour defence. Because of their limited numbers, their ability to kill multiple targets is crucial to their function. Therefore, studying mechanisms enhancing serial killing capacity, understanding effects that diverse tumour phenotypes have on NK cell cytotoxicity and its manipulation for therapeutic purposes can have important clinical implications.

3.2. Aims and objectives

Tumour cells display a heterogeneous array of NK cell ligands and how efficiently NK cells kill multiple targets in such complex environments has never been studied. The overarching aim of this chapter was to study effects of repeated NK cell stimulation on their cytotoxic responses and other phenotypic changes.

The secretion of perforin is a hallmark of NK cell cytotoxicity, occurring upon NK cell activation. As an advancement to commonly used indirect measurements of population-based perforin secretion, such as flow cytometry-based detection of CD107a degranulation marker, or target cell lysis, we developed a microscopy-based assay allowing quantification of secreted perforin from individual NK cell. Using this we wanted to establish how the sequential engagement of NK cell receptors, CD16 and NKG2D affects their degranulation on a single cell level. Moreover, we aimed to address whether the order in which these two receptors are engaged on different target cells, encountered sequentially, effects the strength of NK cell degranulation. Next, we tested the lysis of target cells encountered sequentially. Population-level responses were assessed using flow cytometry, while single cell data were obtained using specially designed microchips, allowing imaging of individual NK cell - target cell interactions (Guldevall et al., 2010, Guldevall et al., 2016).

The specific aims of the study were as follows:

i. To validate the method for studying the secretion of perforin from individual NK cells;
ii. To investigate the ability of different ligands to trigger perforin secretion;
iii. To assess the secretion of perforin upon sequential stimulation with different ligands;
iv. To evaluate phenotypic changes upon NK cell activation;
v. To study NK cell serial killing of targets expressing different ligands;
vi. To address whether phenotypic changes that affect serial killing can be reversed.

3.3. Results

NK cell cytotoxic responses are regulated by activating and inhibitory signals integrated at the immune synapse established between an NK cell and target cell. When activation signals prevail, rapid secretion of granules containing perforin and granzymes can be triggered and/or pro-inflammatory cytokines, such as interferon gamma (IFN-γ) can be secreted.

3.3.1. Glass surfaces coated with activating ligands trigger NK cell degranulation

Slides, coated with activating ligands have been shown to be an efficient simplified model for studying the events occurring at the NK cell immune synapse (Culley et al., 2009, Larghi et al., 2013, Williamson et al., 2011). To determine the amount of activating ligands required for a full NK cell response, we first measured the IFN-γ secretion upon the stimulation with increasing concentrations of activating ligands, a therapeutic antibody rituximab, ligating CD16 through its Fc portion (0.1, 1.0, 10.0, 20.0 µg/ml), or recombinant human MICA, ligating NKG2D (0.25, 2.5, 5.0 µg/ml), both in the presence of 2.5 µg/ml ICAM1. 2.5 µg/ml ICAM1 alone (-) was used as a control. NK cells were incubated on coated surfaces for 18 hours, and then the concentration of secreted cytokine was measured from the collected supernatant.

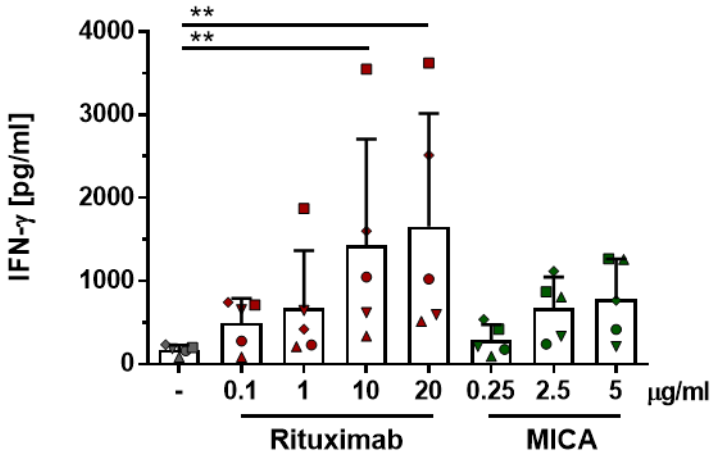

Figure 3.1: Rituximab and MICA coated surfaces trigger IFN-γ production from NK cells. Primary human NK cells were incubated in 96-well plate coated with increasing concentrations, as indicated, of activating ligands (rituximab or recombinant human MICA) for 18h. All surfaces were coated with 2.5 µg/ml ICAM1. IFN-γ production was measured from the supernatants by ELISA (n = 5, mean ± SD). **p<0.01 calculated by Friedman test.

Both ligands triggered higher secretion of IFN-γ than ICAM1 alone (Figure 3.1). For rituximab, the maximum responses peaked at 10 µg/ml, while for MICA responses peaked at 2.5 µg/ml. Four out of five donors responded with greater IFN-γ secretion upon stimulation with rituximab than MICA. However, the secreted amount varied between individual donors, especially on rituximab.

Next, we wanted to assess whether the conditions inducing maximum IFN-γ secretion can also trigger perforin secretion. For this, a perforin capture assay was developed (Chapter 2: Materials and methods: Perforin capture assay). To capture secreted perforin, slides were first coated with poly-L-lysine (PLL) to increase the adherence of proteins to the surface, and then with anti-perforin mAb in addition to the activating ligands (10 µg/ml rituximab or 2.5 µg/ml MICA, both with 2.5 µg/ml ICAM1) or 2.5 µg/ml ICAM1 alone. NK cells were then incubated on these surfaces for 1h. After incubation, cells were gently removed, and captured perforin was stained with an anti-perforin mAb labelled with AF488 fluorophore and imaged by confocal microscopy.

This method enabled us visualise patches of perforin secreted from individual cells. Interestingly, cells on rituximab secreted perforin in elongated shapes, while the perforin pattern on MICA formed dense circular clusters, as represented in Figure 3.2A. Analysis of such perforin patches allowed quantification of the relative secretion of perforin from individual cells on different activating conditions. While there was only a little perforin secreted on ICAM1 control surfaces, both, rituximab and MICA induced strong degranulation. Cells stimulated by rituximab secreted on average 2.8 times more perforin per cell than cells on ICAM1, while cells on MICA secreted 7.6 times more perforin. However, there was a notable variability of secreted perforin per cell within one donor (Figure 3.2B) and in between donors (Figure 3.2C).

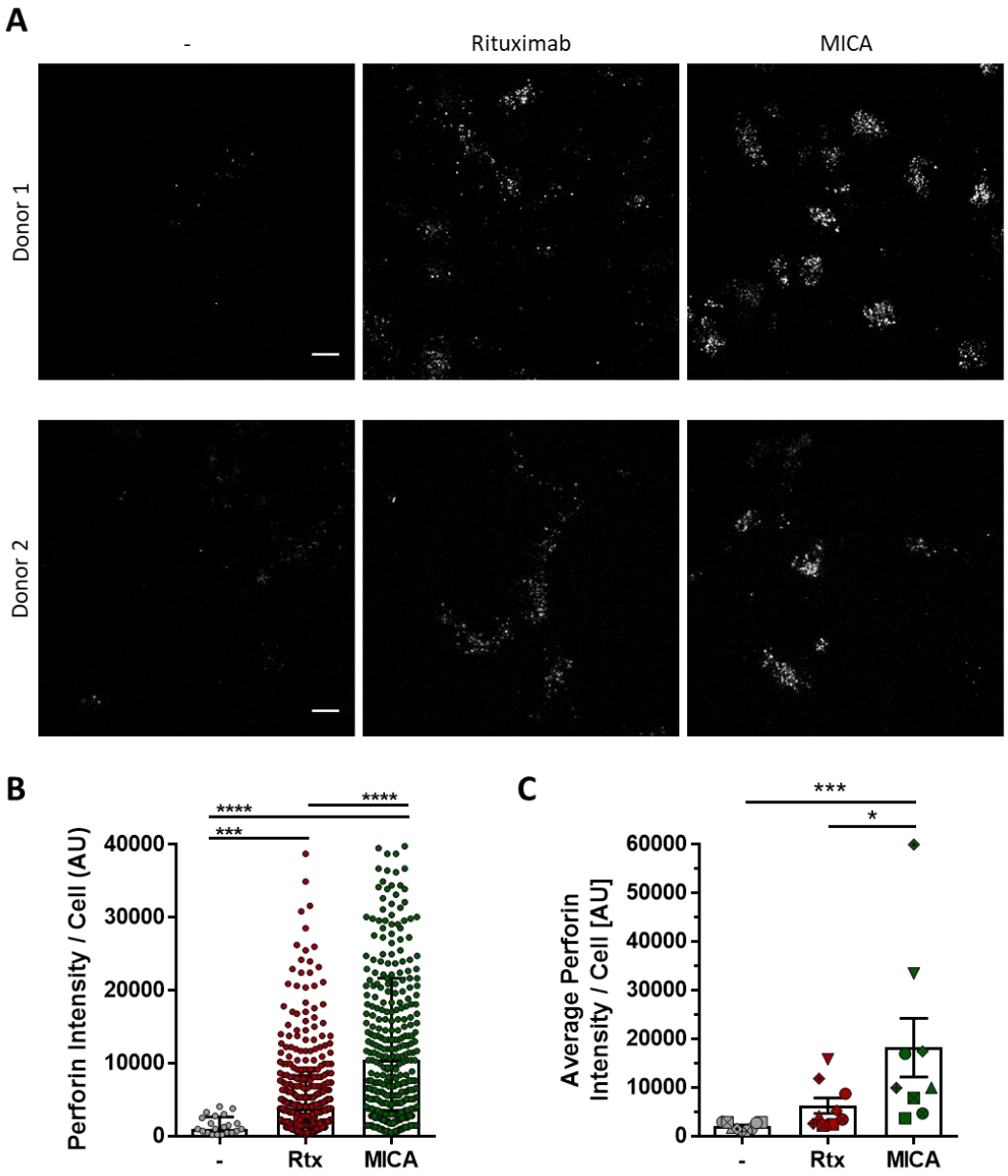

Figure 3.2: Perforin capture assay. (A) Representative confocal images of captured perforin upon 1h stimulation in chambered coverslips coated with rituximab (Rtx) or MICA, both with ICAM1, or ICAM1 alone (-). After cells were removed, captured perforin was stained with anti-perforin AF488 mAb. The scale bar is 10 µm. **(B)** Integrated fluorescence intensity (IFI) values of captured perforin per cell from a representative donor. Each dot represents a mean value per cell (median ± IQR). **(C)** Mean IFI values from nine different donors (n = 9, mean ± SEM). *p<0.05, **p<0.01, ***p<0.001, ****p<0.0001 calculated by Kruskal-Wallis test for B and Friedman test for C.

Both recombinant proteins used, ICAM1 and MICA, contain an Fc portion that could potentially activate NK cells through CD16. To ensure that Fc on its own does not induce degranulation, surfaces were coated with recombinant Noggin-Fc, a protein that does not interact with NK cells.

NKG2D ligation alone was shown to be unable to trigger NK cell responses and additional signals are required. Conversely, engagement of CD16 alone is sufficient for the lysis of targets (Bryceson et al., 2005, Bryceson et al., 2006). A recent study demonstrated that the addition of ICAM1 to CD16-induced activation leads to directed secretion of cytolytic granules into the synaptic cleft, while the absence of ICAM1 leads to collateral killing of bystander cells (Hsu et al., 2016). To assess the role of ICAM1 for perforin secretion, slides were coated with either rituximab or MICA, with or without ICAM1.

As represented in Figure 3.3, all negative controls induced very little degranulation from only a few individual cells, while activating surfaces proved to be potent stimulators. The ligation of the Fc control, Noggin-Fc, showed that the Fc portion of the chimera proteins was insufficient to induce perforin secretion. This confirmed that degranulation induced by MICA is specific to its NKG2D binding.

In our experiment, the addition of ICAM1 to the activating surfaces did not have a significant impact on the extent of degranulation. ICAM1 is an adhesion molecule and is required to ensure tight contact with target cell membrane (Gross et al., 2010). Here, cells were stimulated on coated glass, which is much stiffer than cell membrane and can facilitate stronger cell adherence (Bao and Suresh, 2003). Thus, although ICAM1 plays a key role in NK cell interactions with targets, it is not required for degranulation responses on coated surfaces.

In summary, perforin capture assay is a reliable method for studying NK cell degranulation. It allows the relative comparison of perforin secretion from individual cells by visualisation and quantification of captured perforin molecules on different conditions.

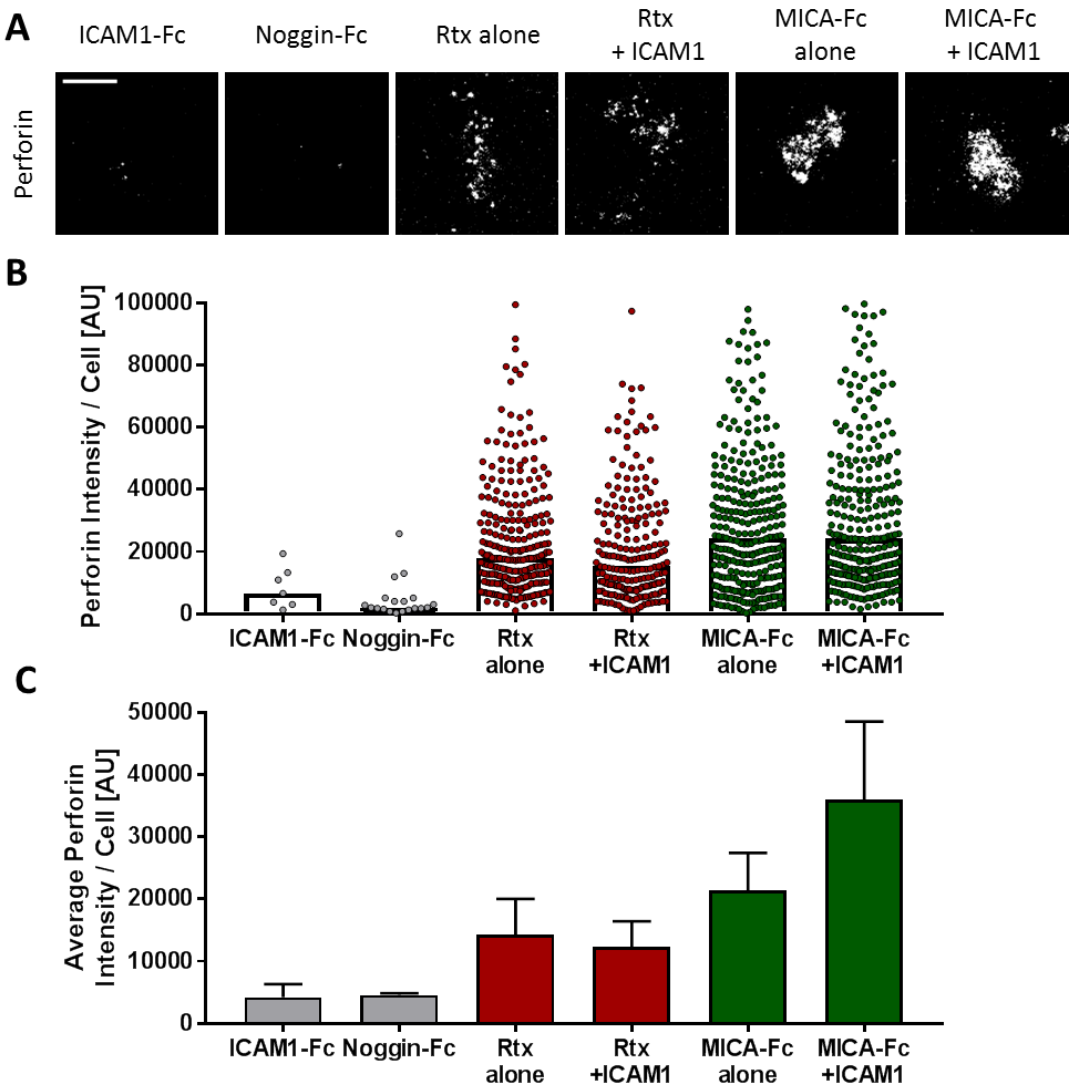

Figure 3.3: Controls for perforin capture assay. (A) Representative confocal images of captured perforin secreted from one cell upon 1h stimulation in chambered coverslips coated with activating ligands or corresponding negative controls. After cells were removed, captured perforin was stained with anti-perforin AF488 mAb. The scale bar is 10 µm. **(B)** Integrated fluorescence intensity (IFI) values of captured perforin per cell from a representative donor. Each dot represents a mean value per cell (median ± IQR). **(C)** Median IFI values from three different donors (n = 3, mean ± SEM). Rtx: rituximab. *p<0.05, **p<0.01, ***p<0.001, ****p<0.0001 calculated by Kruskal-Wallis test for B and Friedman test for C.

3.3.2. Timing of degranulation is different for rituximab than for MICA

To address how long it takes for cells to secrete perforin on rituximab or MICA, NK cells were stimulated for 5 – 120 min on activating surfaces (rituximab or MICA, both with ICAM1).

Analysis of the fluorescent captured perforin revealed that secretion of perforin on rituximab increased over time. The curve of the secretion reached a plateau at around 45 min. At 5 minutes, only very few cells secreted perforin. The number of perforin secreting cells increased over time and it reached a plateau at 30 min. (Figure 3.4).

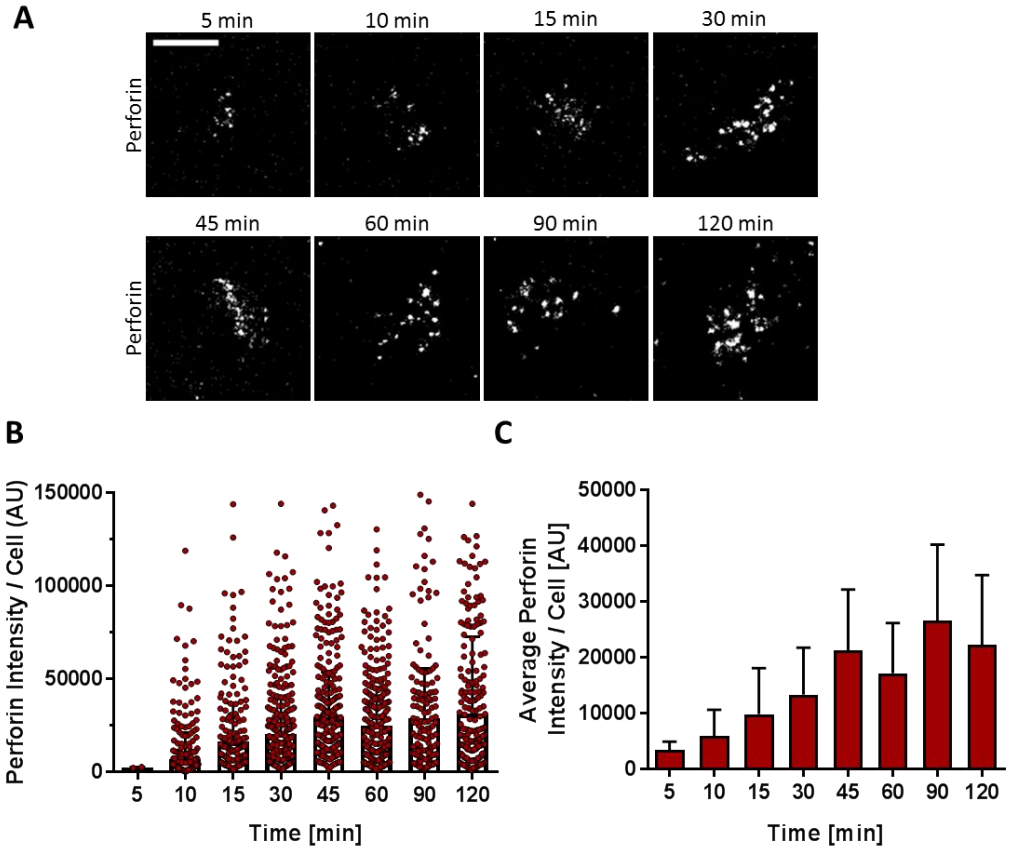

Figure 3.4: Time course of perforin secretion on rituximab. (A) Primary NK cells were incubated on rituximab-coated surfaces (with ICAM1) for 5 - 120 min. Cells were then removed and captured perforin was stained and imaged by confocal microscope. Representative images of captured perforin secreted from one cell. The scale bar is 10 µm. **(B)** Time course of integrated fluorescence intensity (IFI) values of captured perforin secreted per cell. Data from one representative donor are plotted (n ≥ 50, except for 5 min, where n = 2; median ± IQR). **(C)** Median IFI values from three different donors (n = 3, mean ± SEM).

5 min on MICA resulted in a comparable absolute amount of perforin secreted per cell as 120 min. Like on rituximab, there were more cells degranulating over time (Figure 3.5.). The number of degranulating cells on MICA reached a plateau at 45 min.

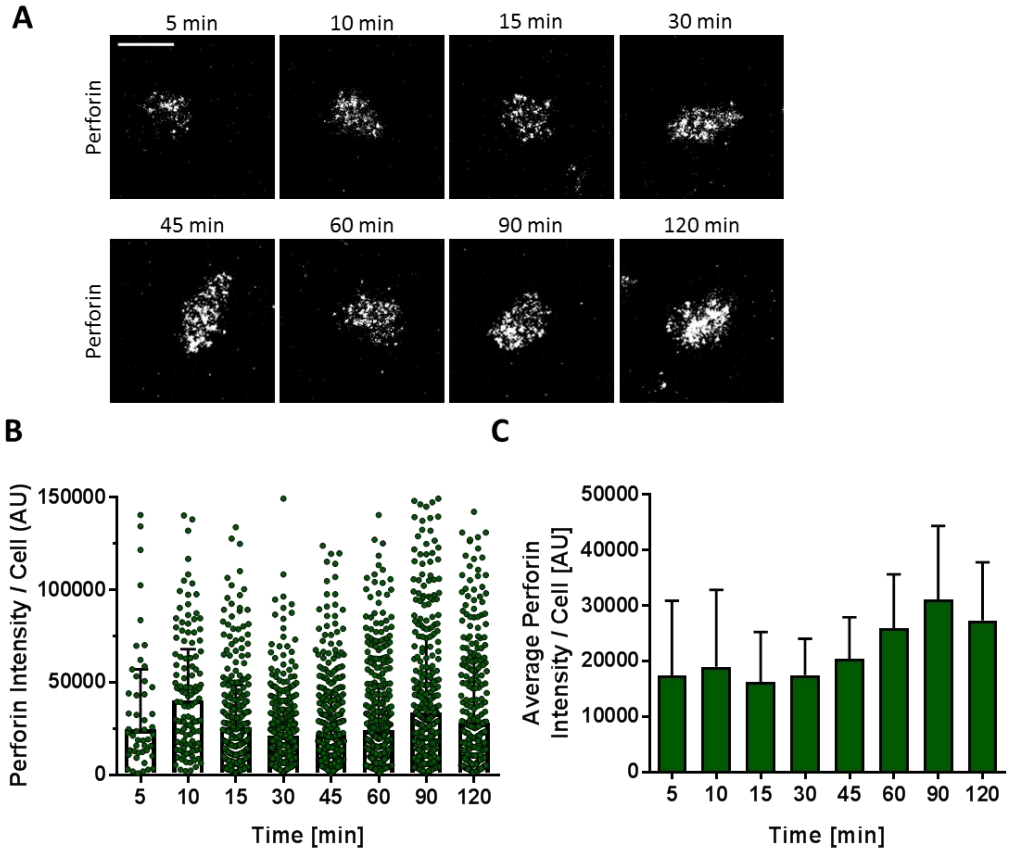

Figure 3.5: Time course of perforin secretion on MICA. (A) Primary NK cells were incubated on MICA-coated surfaces (with ICAM1) for 5 - 120 min. Cells were then removed and captured perforin was stained and imaged by confocal microscope. Representative images of captured perforin secreted from one cell. The scale bar is 10 µm. **(B)** Time course of integrated fluorescence intensity (IFI) values of captured perforin secreted per cell. Data from one representative donor are plotted (n ≥ 50, median ± IQR). **(C)** Median IFI values from three different donors (n = 3, mean ± SEM).

These data indicate that the decision to secrete perforin might be more binary on MICA than on rituximab. When the threshold for degranulation is reached on MICA, cells respond with rapid release of large amount of perforin. Thus, longer incubation time does not lead to greater secretion per cell. On the other hand, degranulation on rituximab is slower and is increasing over time.

3.3.3. Higher ligand concentration does not increase perforin secretion

In first section of this chapter (Figure 3.1) we defined concentrations of rituximab and MICA leading to optimal secretion of IFN-γ. However, the threshold for degranulation might be different from the one for cytokine secretion. Fauriat et al. demonstrated that one NK cell ligand expressed on Drosophila cells suffices for efficient degranulation response, while three different activating ligands have to be present for IFN-γ secretion (Fauriat et al., 2008). Thus, we wanted to test whether the concentrations found to elicit maximal cytokine response also induce optimal perforin secretion.

For this, activating ligands were titrated. Rituximab was used at 1 µg/ml and 20 µg/ml were used in addition to 10 µg/ml defined in Figure 3.1. For MICA, 1 µg/ml and 5 µg/ml were used in addition to 2.5 µg/ml. All surfaces were also coated with 2.5 µg/ml ICAM1. On 10 µg/ml rituximab, mean perforin secretion was 2-fold greater comparing to 1 µg/ml (7700 ± 6600 AU and 16100 ±15600 AU respectively). Interestingly, perforin intensity was slightly lower on higher concentration (20 µg/ml) of rituximab. There was no notable change in the number of perforin secreting cells.

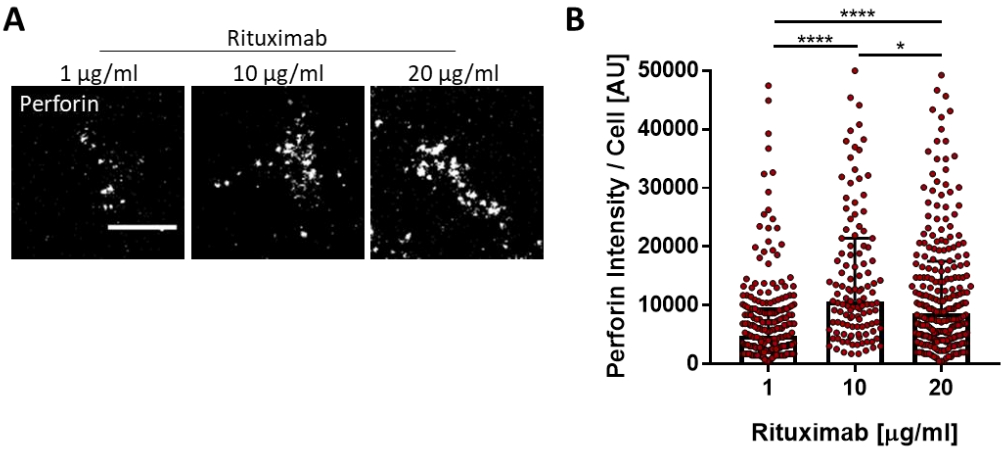

Figure 3.6: Rituximab concentration affects the extent of perforin secretion. (A) NK cells were incubated for 1h on slides coated with rituximab with ICAM1 at indicated concentrations. Captured perforin was stained with anti-perforin AF488 mAb after cells have been removed. Panels show representative images of captured perforin. The scale bar is 10 µm. **(B)** Integrated fluorescence intensity (IFI) values of captured perforin per cell from a representative donor. Each dot represents a mean value per cell (median ± IQR). *p<0.05, ****p<0.0001 calculated by Kruskal-Wallis test.

Similarly, there was a 2.8-fold increase of perforin fluorescence intensity on 2.5 µg/ml MICA comparing to 1 µg/ml (37500 ± 38100 AU to 13500 ± 16100 AU respectively). Increasing concentration of coated MICA (5 µg/ml) also resulted in reduced perforin intensity (20400 ± 20900 AU) comparing to 2.5 µg/ml. The number of perforin secreting cells was not apparently affected.

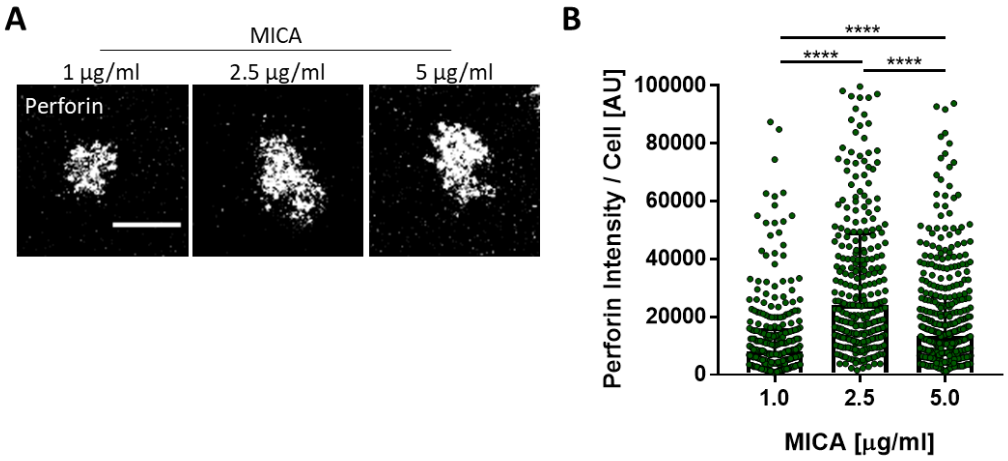

Figure 3.7: MICA concentration affects the extent of perforin secretion. (A) NK cells were incubated for 1h on slides coated with MICA and ICAM1 at indicated concentrations. Captured perforin was stained with AF488-labeled anti-perforin mAb after cells have been removed. Panels show representative images of captured perforin. The scale bar is 10 µm. **(B)** Integrated fluorescence intensity (IFI) values of captured perforin per cell from a representative donor. Each dot represents a mean value per cell (median ± IQR). ****p<0.0001 calculated by Kruskal-Wallis test.

These data indicate that the concentration of coated activating ligands that is triggering maximum IFN-γ response (Figure 3.1) is the same as the concentration reaching peaking perforin secretion for both ligands.

3.3.4. Rituximab and MICA trigger similar proportion of NK cells to degranulate

Besides the strength of responses of a single cell, it is also important to understand the population responses. As shown above, the responses from individual cells can vary significantly. Thus, we wanted to assess rituximab and MICA potential to trigger global degranulation.

To estimate the proportion of cells that degranulated upon stimulation on coated slides the following assay was performed. The same number of cells was incubated on two identical activating surfaces in parallel. Cells were then removed from one surface, and captured perforin was imaged, while on the other cells were fixed and stained for F-actin using phalloidin labelled with AF488. To calculate the percentage of degranulating cells, the number of perforin secreting cells (counted as the number of captured perforin patches, presumably secreted from one cell) was divided by the total number of fixed cells on the parallel surface. According to this, 13 ± 5 % cells degranulated on ICAM1 control surface, 50 ± 18 % degranulated on rituximab and 42 ± 12 % on MICA (Figure 3.8). The variability between donors was greater when cells were stimulated on rituximab (between 33 % and 76 % degranulating cells), while between 22 % and 52 % cells degranulated on MICA.

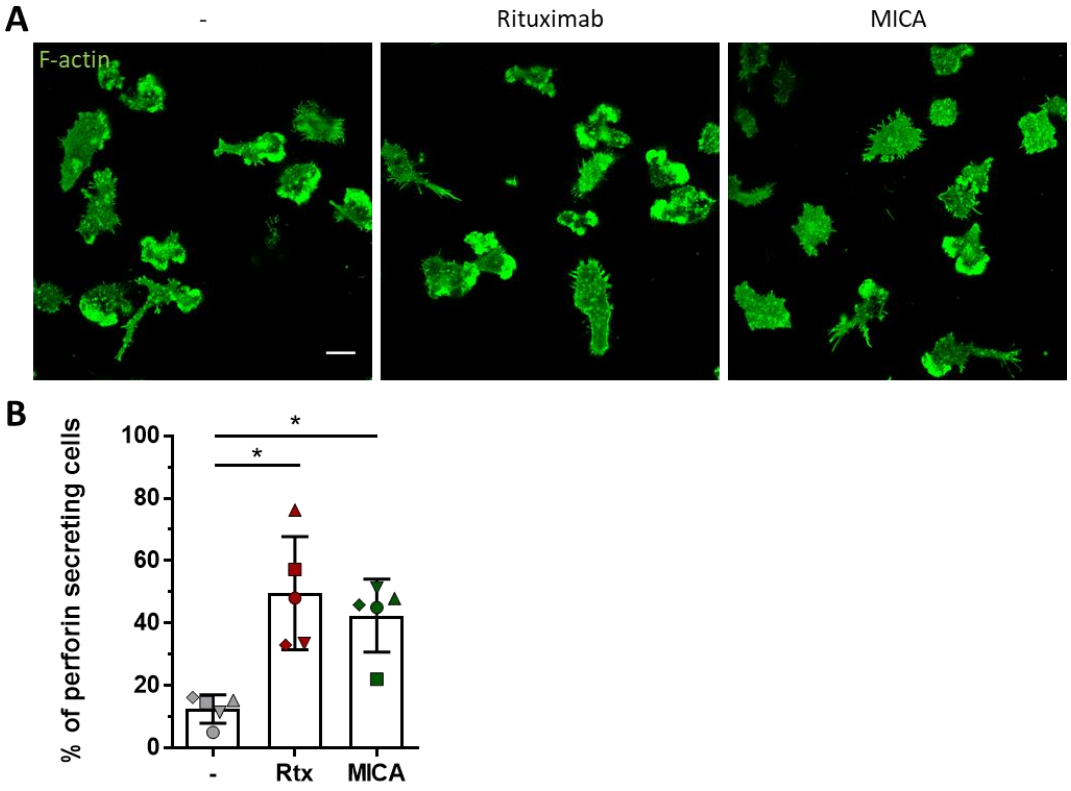

Figure 3.8: Proportion of perforin secreting cells. To estimate the percentage of perforin secreting cells, two sets of coated surfaces (rituximab or MICA, both with ICAM1, or ICAM1 alone (-)) were used in parallel. Same number of cells was incubated in each well. One well was used for the perforin capture assay, while cells were fixed and stained with phalloidin in the parallel well **(A)** Representative images of cells, incubated on activating surfaces for 1h, fixed and stained with phalloidin AF488. The scale bar is 10 µm. **(B)** The proportion of perforin secreting cells was calculated by dividing the number of perforin secreting cells by the total number of cells in the field of view (n = 5, mean ± SD). Rtx: rituximab. *p<0.05, calculated by one-way ANOVA.

To test whether the results obtained from the perforin secretion assay provide a reliable estimation of NK cell responses, we compared them to degranulation responses assessed by an established method, detecting CD107a levels by flow cytometry. CD107a (Lysosomal-associated membrane protein 1, LAMP1) is a protein found on the surface of lytic granules (Kannan et al., 1996) and can be detected on the cell surface upon cell degranulation (when granules fuse with the cell membrane) (Betts et al., 2003).

For CD107a detection, cells were incubated on activating or control surfaces for 4 hours. Protein transport inhibitors brefeldin A and monensin were added in order to ensure that total CD107a was detected, as they inhibited its secretion and prevented internalisation (Betts et al., 2003). Following stimulation, cells were removed and

stained for surface CD107a, indirectly indicating the levels of degranulation. From acquired flow cytometry plots, live, single and $CD56^+$ cells were gated (Figure 3.9A). On ICAM1 19 ± 7 % of NK cells degranulated, on rituximab 37 ± 20 % and 62 ± 8 % on MICA (Figure 3.9 B, C). Again, the variability of responses between donors was the most significant on the stimulation through rituximab, while the responses through MICA were more consistent.

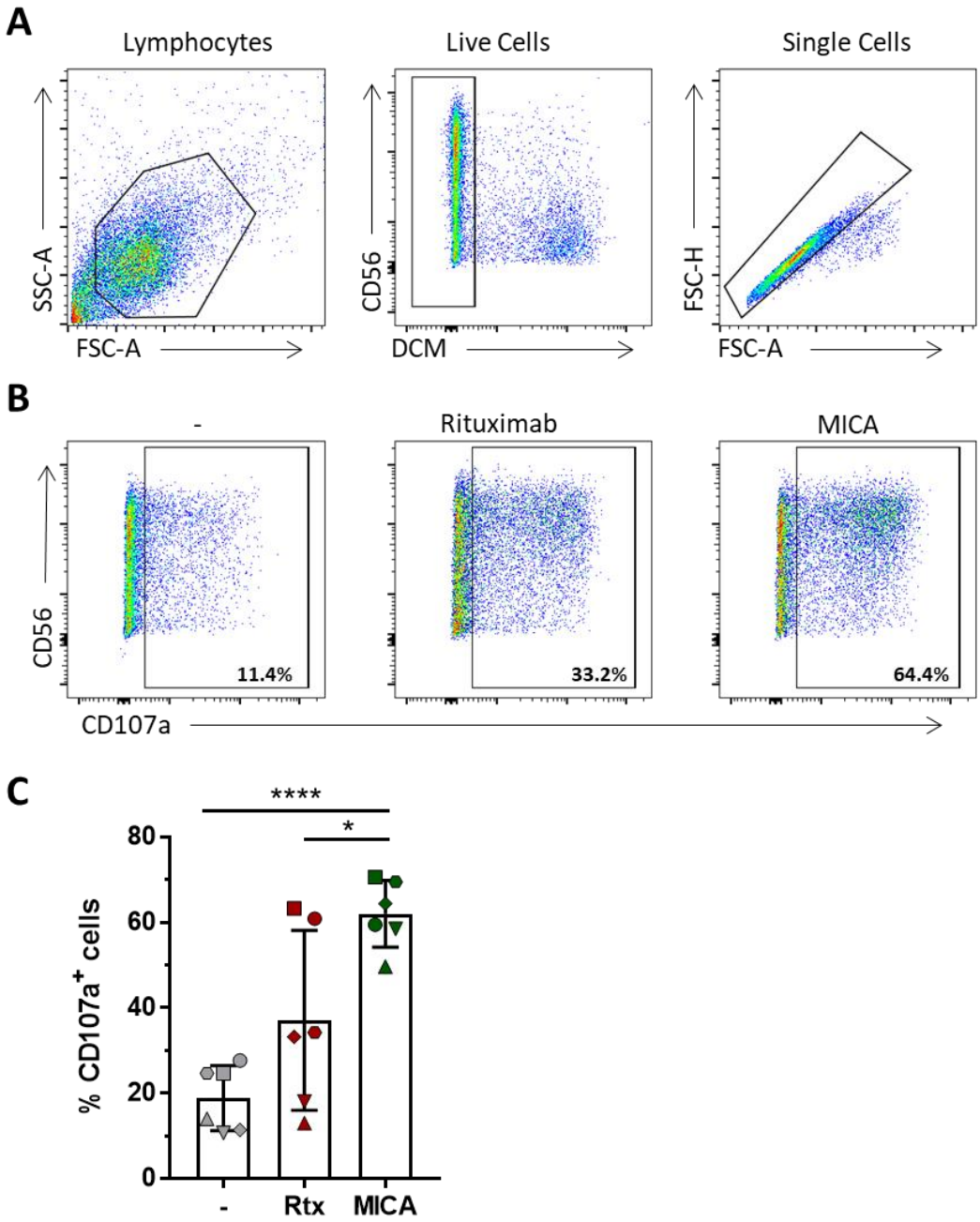

Figure 3.9: Surface levels of CD107a upon NK cell stimulation. Flow cytometric analysis of NK cell degranulation based on marker CD107a. NK cells were stimulated on glass slides coated with ICAM1 alone (-) or with rituximab or MICA, both with ICAM1 for 4h. **(A)** Representative gating strategy for the selection of CD56+ live NK cells and exclusion of doublets. **(B)** Dot plots representation of CD107a levels on CD56+ cells. CD107a was stained with anti-CD107a AF647 mAb, and CD56 with anti-CD56 BV421 mAb. Numbers indicate the percentage of cells contained in the corresponding gates. (C) Percentage of CD107a+ cells. Symbols represent different donors. Data pooled from six independent experiments (n = 6, mean ± SD). Rtx: rituximab, DCM: Dead cell marker. *p<0.05, **p<0.01, ***p<0.001, ****p<0.0001 calculated by Friedman test.

3.3.5. The sequence of receptor ligation determines the amount of secreted perforin

Like T cells, NK cells have also been reported to kill several targets sequentially. In a diseased tissue, NK cells encounter wide range of target cells expressing different activating ligands. Treatments with therapeutic antibodies that opsonise tumour cells additionally contribute to such diversity, by exposing their Fc portion to NK cell receptors. NK cells are thus required to respond to multiple stimuli and perform serial killing to various targets. However, it is not currently known how the sequential ligation of NK cell activating receptors affects their perforin secretion. To address this, cells were stimulated serially; first, cells were incubated on the rituximab coated surface for 1 hour. Then, cells were removed, washed and placed on fresh rituximab-coated surface for another hour. After this, cells were removed and washed again and split into two groups; one was incubated on rituximab for the third time, while the other was introduced to MICA-coated surface (Figure 3.10A). At all steps, secreted perforin was captured and after cells were removed, stained for imaging by confocal microscopy.

Repeated stimulation on rituximab resulted in decreasing perforin secretion per cell. In some donors, there was a slight increase between first and second stimulation in median fluorescence intensity of captured perforin, but by the third stimulation, perforin secretion was always severely impaired. Besides the intensity of secreted perforin per cell, there were also less cells responding to stimulation (as seen by fewer patches of captured perforin on slides and shown by individual data points in Figure 3.10C). Strikingly, upon the following stimulation on MICA, secretion of perforin was completely recovered (Figure 3.10 B-D). There were many cells that responded with strong perforin secretion. In some donors, cells secreted significantly more perforin upon this - third stimulation on MICA than upon the first stimulation on rituximab.

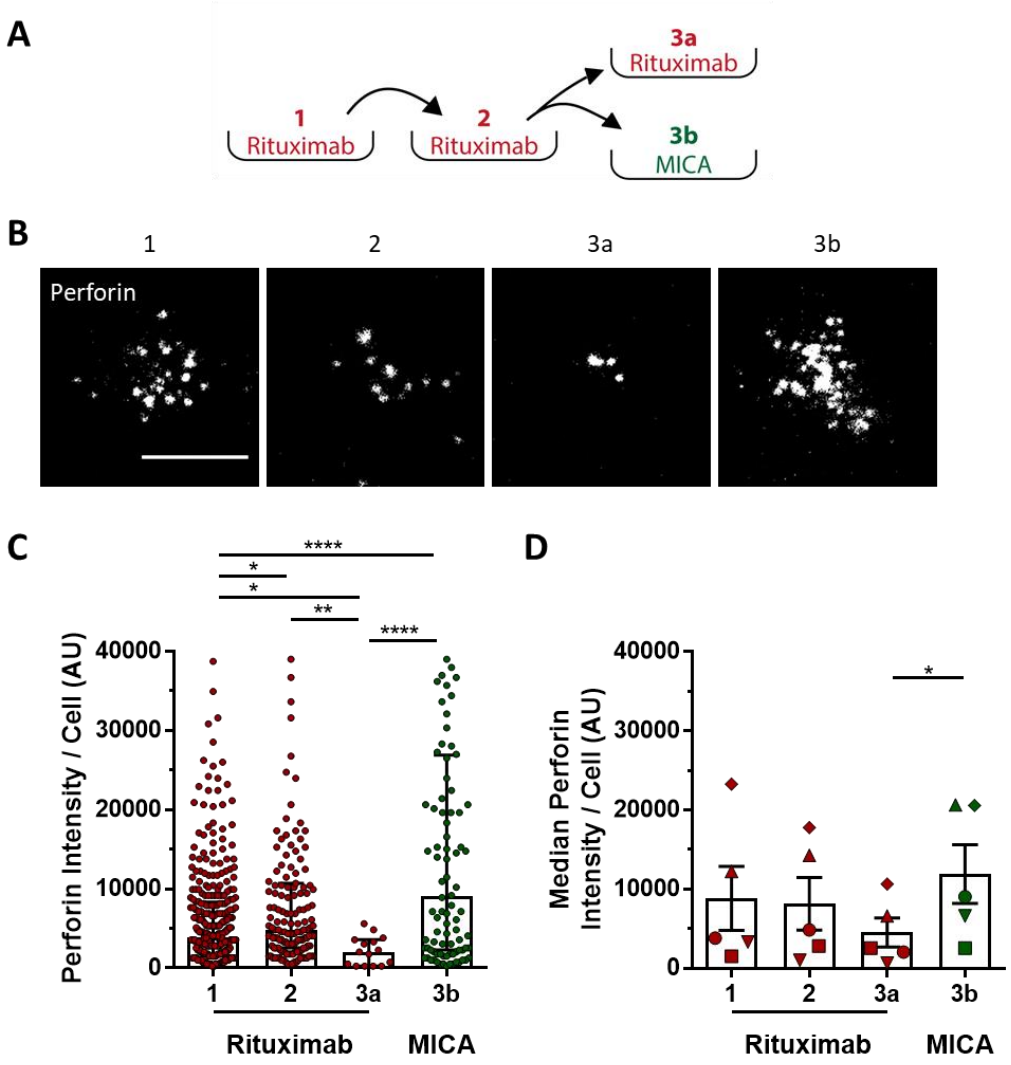

Figure 3.10: Perforin secretion per cell upon sequential stimulation. (A) Schematic representation of experimental set-up. Primary human NK cells were stimulated repeatedly for 1h on rituximab with recombinant human ICAM1. At the last step, cells were split in two and incubated on either rituximab or recombinant human MICA, both with ICAM1. **(B)** Representative images of captured perforin secreted from one cell upon sequential stimulation acquired by confocal microscopy. Perforin was stained with anti-perforin AF488 antibody after the cells were removed from the surfaces. The scale bar is 10 µm. **(C)** Integrated fluorescence intensity (IFI) values of captured perforin per cell from a representative donor. Each dot represents a value per cell (median ± IQR). **(D)** Median IFI values from different donors (n = 5, mean ± SEM, different donors are represented by different symbols). *p<0.05, **p<0.01, ***p<0.001, ****p<0.0001 calculated by Kruskal-Wallis test for C, and Friedman test for D.

When cells were first stimulated through NKG2D (Figure 3.11A), secretion of perforin decreased even more drastically upon each sequential step. By the third step, there were almost no cells responding with perforin secretion. Interestingly, stimulation on rituximab following MICA did not recover secretion of perforin (Figure 3.11 B, C).

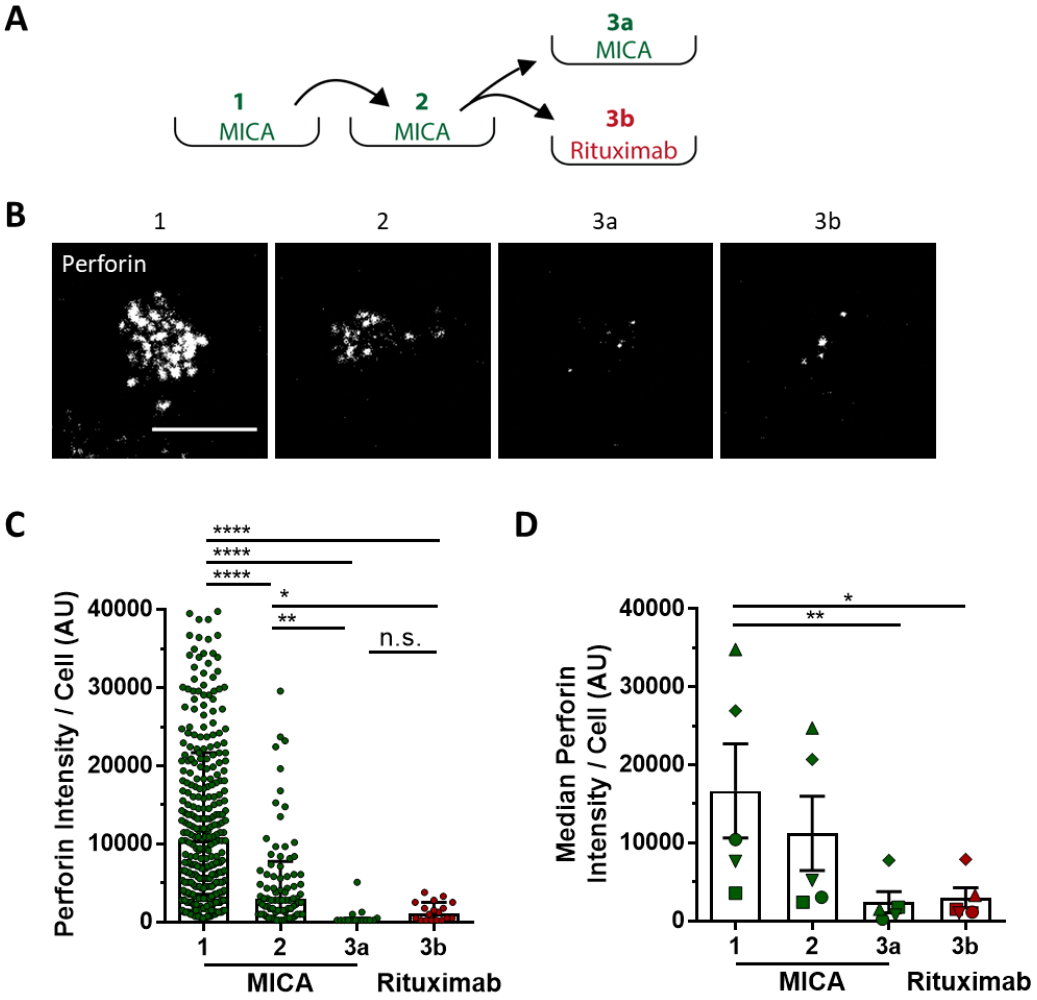

Figure 3.11: Perforin secretion per cell upon sequential stimulation. (A) Schematic representation of experimental set-up. Primary human NK cells were stimulated repeatedly for 1h on recombinant human MICA with ICAM1. After two rounds of activation on MICA, cells were split in two and then placed on either MICA or rituximab-coated surface, both with ICAM1 for the final hour of stimulation. **(B)** Representative images of perforin secreted from one cell upon sequential stimulation acquired by confocal microscopy. Perforin was stained with AF488-labeled anti-perforin antibody after the cells were removed from the surfaces. The scale bar is 10 µm. **(C)** Integrated fluorescence intensity (IFI) values of captured perforin per cell from a representative donor. Each dot represents a value per cell (median ± IQR). **(D)** Median IFI values from different donors (n = 5, mean ± SEM, different donors are represented by different symbols). *p<0.05, **p<0.01, ***p<0.001, ****p<0.0001 calculated by Kruskal-Wallis test for C, and Friedman test for D.

It has been previously reported that cells undergo exhaustion when activation persists for a long time (Schafer et al., 2015). However, our data suggests that it is not the exhaustion of cells, nor the depletion of perforin stocks that dictates the outcome of such sequential perforin secretion. Importantly, the order in which different activating ligands on NK cells are triggered dictates the strength of sequential responses.

3.3.6. NK cell stimulation affects receptor expression levels

One way in which NK cell sensitivity can be modified is by an alteration in the level of expression of its activating receptors. Thus, we assessed the changes in the expression levels of CD16 and NKG2D upon sequential stimulations.

First, surface levels of activating receptors, CD16 and NKG2D on unstimulated NK cells were assessed. Alongside activating receptors, cells were stained for CD56 and CD69. CD56 is a marker of NK cells, and CD69 is a commonly used marker of NK cell activation. The specificity of staining of each marker was evaluated by comparison with cells stained with an isotype-matched control mAb (Figure 3.12).

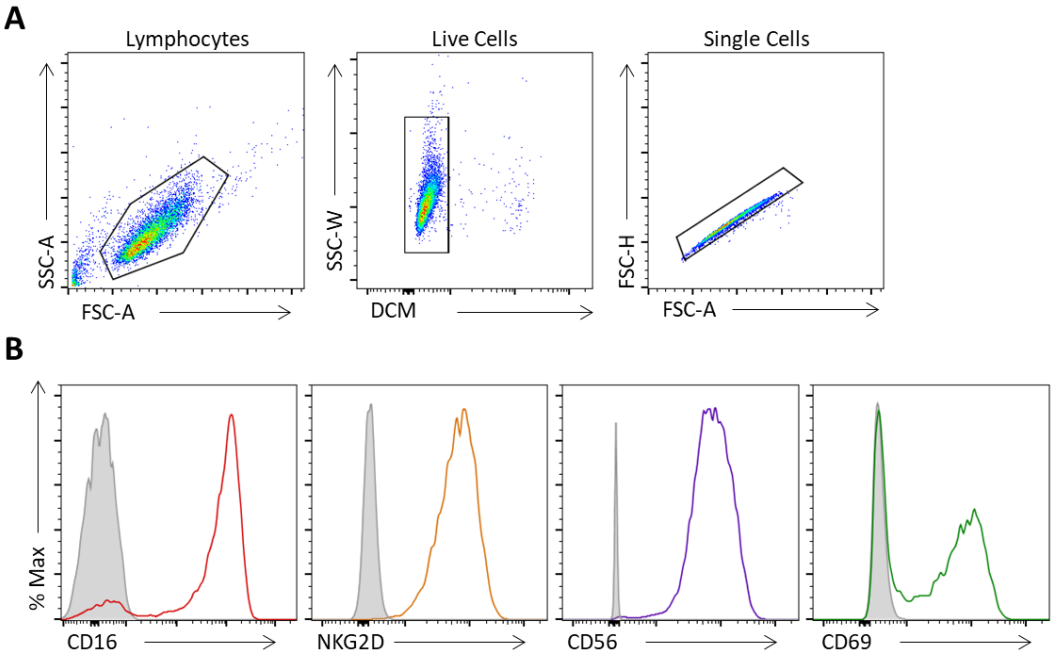

Figure 3.12: Surface expression of NK cell markers. Unstimulated NK cells were stained with anti-CD16 AF647, anti-NKG2D PE, anti-CD56 BV421, anti-CD69 AF488 alongside the staining for dead cells in Zombie Aqua. **(A)** Representative gating strategy for the selection of live NK cells and exclusion of doublets. **(B)** Representative histograms of NK cell surface proteins, CD16 (in red), NKG2D (in orange), CD56 (in violet) and CD69 (in green). Isotype control staining is plotted in grey. DCM: Dead cell marker.

The majority of human primary NK cells expressed CD16. All cells were highly positive for NKG2D and CD56. NK cells are known to be present as $CD56^{bright}$ and $CD56^{dim}$ (Cooper et al., 2001b, Cooper et al., 2001a). Culturing of cells in IL-2 supplemented media has been shown to reduce the proportion of the $CD56^{dim}$ population (Huenecke et al., 2010). This is the reason why cells used in this study are mainly $CD56^{bright}$. CD69 is an activation marker and thus, it is expected to upregulate upon stimulating signals. Here, cells were unstimulated and the expression of CD69 was low, as expected.

To assess the expression levels of activating receptors upon NK cell activation, cells from activating surfaces were collected and stained. Expression of activating receptors CD16 and NKG2D were compared to unstimulated cells. To assess the impact of non-enzymatic dissociation solution, unstimulated cells were incubated with the solution for the same time as activated cells. Moreover, the effect of incubating cells on surfaces, coated with non-activating protein, Noggin-Fc, or ICAM1 only was assessed (Figure 3.13). Overlay of histograms confirmed that none of the steps changed CD16, NKG2D, CD56 or CD69 expression levels. Thus, the experimental set-up was rigid enough to assess changes specific to NK cell activation.

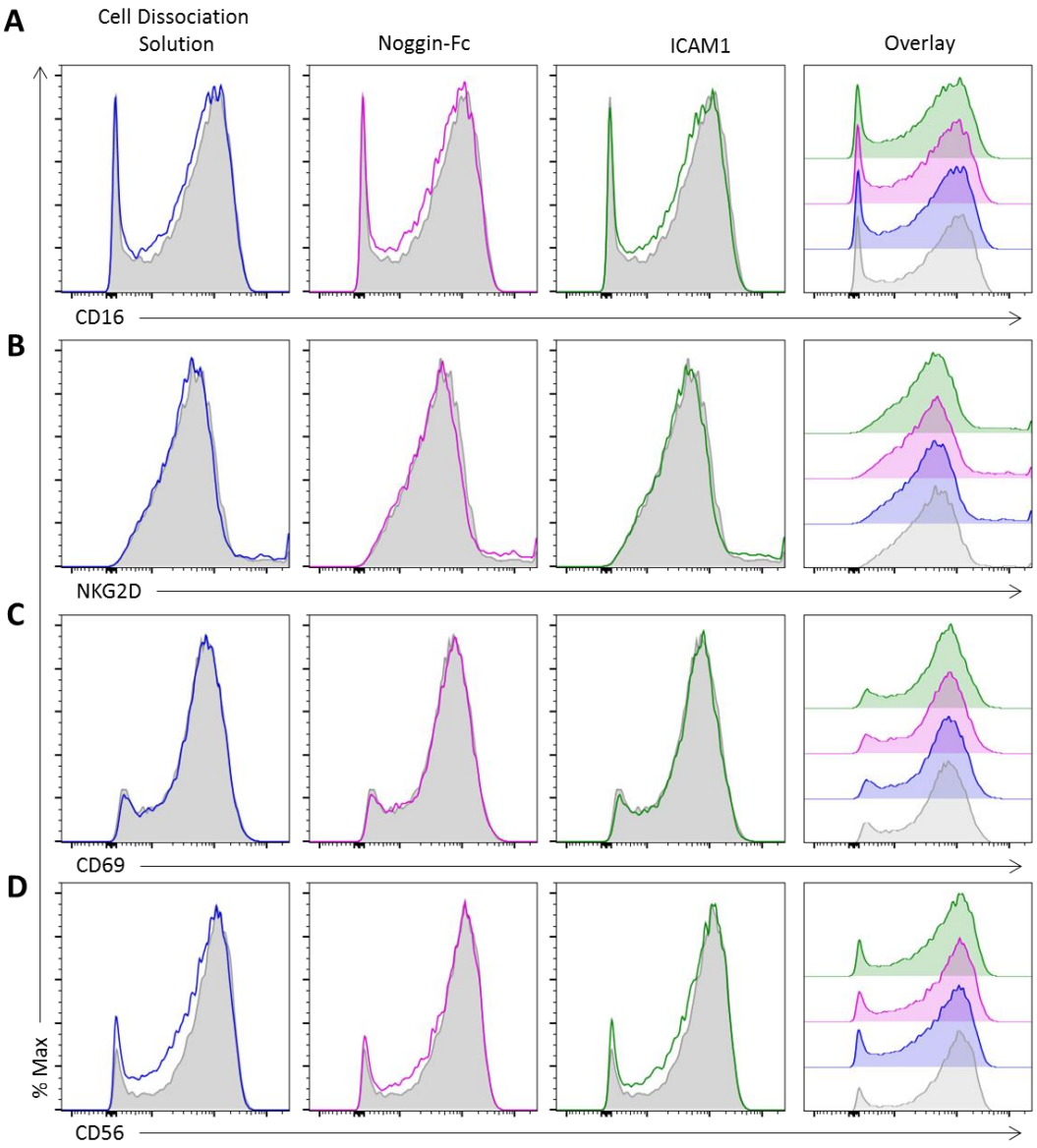

Figure 3.13: Surface expression of NK cell markers upon non-activating procedure. Effect of experimental procedure on NK cell markers was assessed by flow cytometry. Impact of cell dissociation solution was assessed by incubating NK cells with the solution for 15 min (blue line). The effect of incubation of cells on non-activating surfaces was assessed by incubating cells for 1h on Noggin-Fc (purple line) or ICAM1 (green line) coated surface. Treated cells were stained with anti-CD16 AF647, anti-NKG2D PE, anti-CD56 BV421, anti-CD69 AF488. Representative histograms for CD16 **(A)**, NKG2D **(B)**, CD69 **(C)** and CD56 **(D)**. Isotype control staining are plotted in grey.

To assess the activating receptor levels in sequentially stimulated cells, cells removed from the activating surfaces from the perforin capture experiment (Figure 3.11 and 3.12) were used. Compared to unstimulated cells, stimulation with rituximab resulted in a decrease of CD16. Each sequential stimulation led to less $CD16^{+}$ cells and their gMFI was reduced. Following stimulation with MICA enhanced CD16 reduction further (Figure 3.14A, B). Activation through NKG2D resulted in even greater decline of CD16 levels and the subsequent stimulation through CD16 did not rescue it (Figure 3.14C, D).

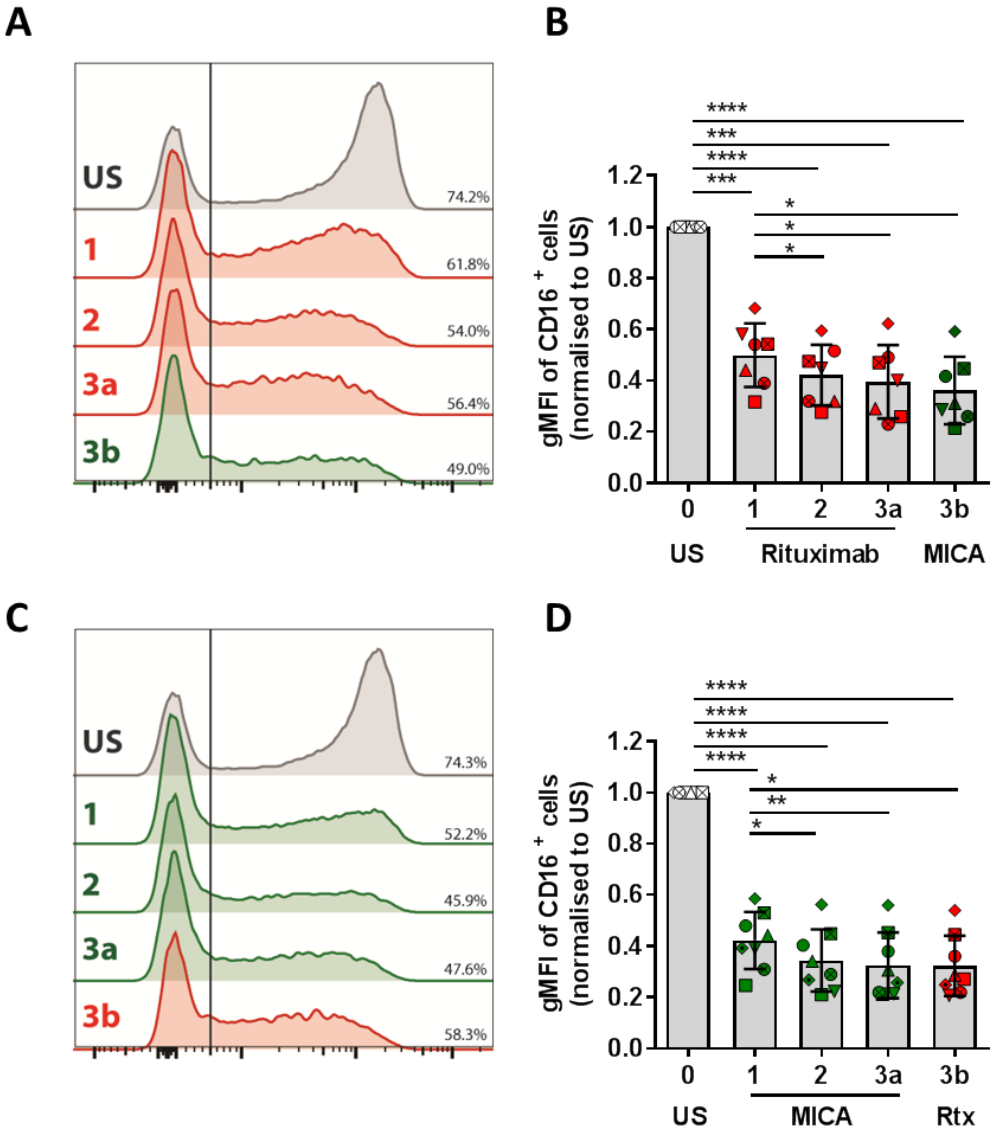

Figure 3.14: CD16 expression upon sequential stimulation. Primary NK cells were sequentially stimulated as described in Figure 3.10. **(A)** NK cells were stimulated repeatedly for 1h on rituximab with ICAM1 (red). At the last step, cells were split in two and incubated on either rituximab (red) or MICA (green), both with ICAM1. In **(C)** the order of stimulation was reversed. Cells were stimulated on MICA with ICAM1 (green) and at last step, cells were split in two groups and incubated on MICA (green) or rituximab (red), both with ICAM1. **(A, C)** Histograms from a representative donor display changes in CD16 expression upon each sequential stimulation, relative to unstimulated cells. Vertical line represents the gate for $CD16^+$ population. Numbers are $\%CD16^+$ population of a representative donor. **(B, D)** gMFI of $CD16^+$ populations, normalised to unstimulated control. Data are combined from seven (n=7) (A, B) or eight (n=8) (C, D) independent experiments and plotted as mean ± SD. US: unstimulated. *p<0.05, **p<0.01, ***p<0.001, ****p<0.0001 calculated by Friedman test.

Activation by MICA reduced NKG2D levels significantly (Figure 3.15C, D). Interestingly, in some donors the subsequent stimulation by rituximab recovered NKG2D expression (Figure 3.15D). Moreover, the sequential stimulation by rituximab increased NKG2D expression (Figure 3.15A, B).

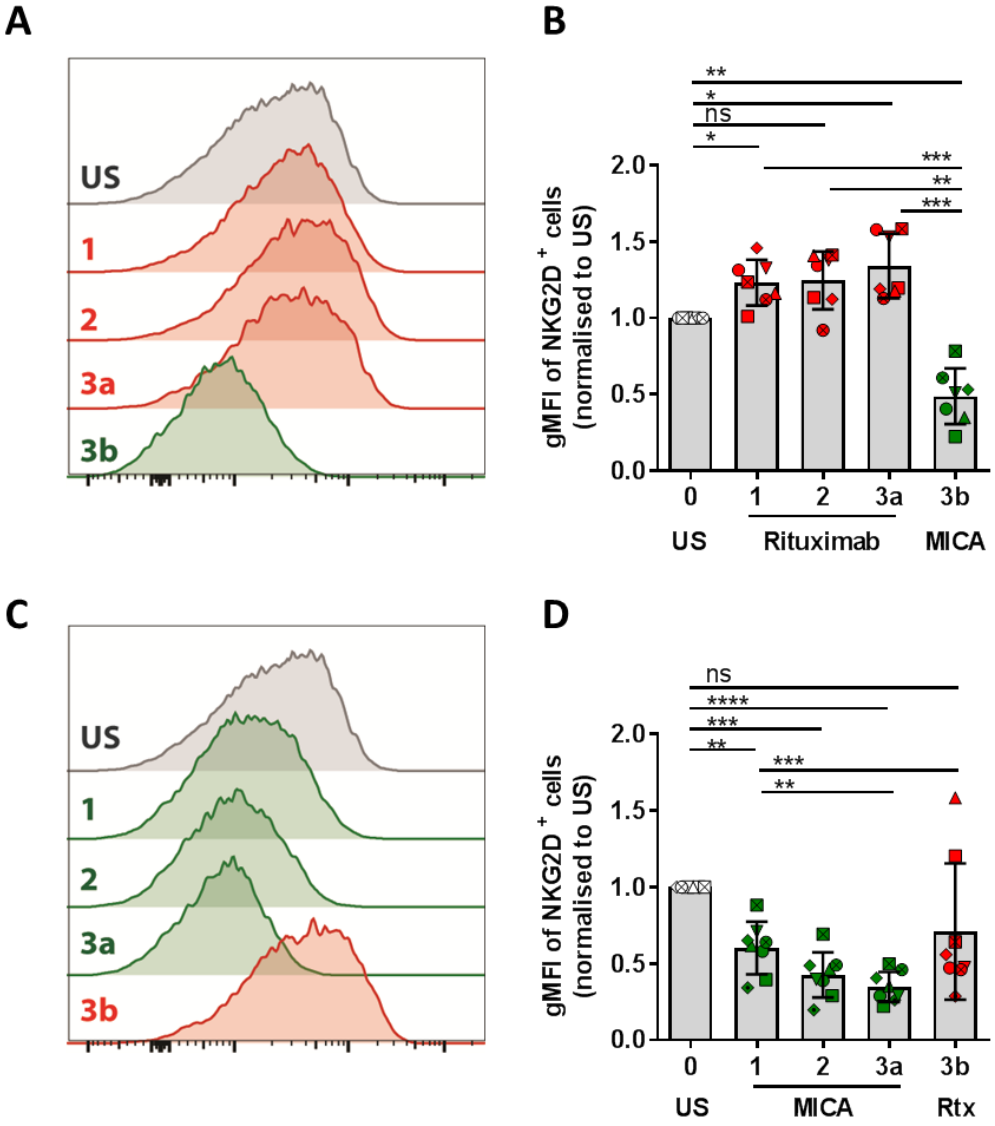

Figure 3.15: NKG2D expression upon sequential stimulation. Primary NK cells were sequentially stimulated as described in Figure 3.10. **(A)** NK cells were stimulated repeatedly for 1h on rituximab with ICAM1 (red). At the last step, cells were split in two and incubated on either rituximab (red) or MICA (green), both with ICAM1. In **(C)** the order of stimulation was reversed. Cells were stimulated on MICA with ICAM1 (green) and at last step, cells were split in two groups and incubated on MICA (green) or rituximab (red), both with ICAM1. **(A, C)** Histograms from a representative donor display changes in CD16 expression upon each sequential stimulation, relative to unstimulated cells. Vertical line represents the gate for $CD16^+$ population. Numbers are $\%CD16^+$ population of a representative donor. **(B, D)** gMFI of $CD16^+$ populations, normalised to unstimulated control. Data are combined from seven (n=7) (A, B) or eight (n=8) (C, D) independent experiments and plotted as mean ± SD. US: unstimulated. *p<0.05, **p<0.01, ***p<0.001, ****p<0.0001 calculated by Friedman test.

In summary, ligation of NK cell ligands affects NK cell receptors differently. CD16 is downregulated upon both types of stimulation, rituximab and MICA, as detected by the proportion of $CD16^+$ cells and their gMFI. On the other hand, NKG2D is reduced only upon binding to its cognate ligand and importantly, the sequential stimulation through CD16 can boost its re-expression.

3.3.7. CD16 is shed from cell surface upon NK cell activation

CD16 undergoes proteolytic cleavage by ADAM17 upon NK cell activation (Romee, Blood, 2013). Loss of CD16 has been shown to be proportional to the strength of activation, and is independent from the type of signal (Romee 2013 Blood, JI paper). To test, whether CD16 is shed in our system, ELISA for soluble CD16 was performed. Because normal media contains high levels of soluble CD16, freshly isolated NK cells were resuspended in serum depleted media, without IL-2. Such conditions are not ideal for NK cells and therefore it is likely that cells responded less strongly to stimulation. However, overnight incubation on rituximab or anti-CD16 coated surfaces resulted in increased levels of soluble CD16 in the supernatant (770 ± 380 pg/ml and 830 ± 150 pg/ml, respectively) compared to unstimulated cells (400 ± 20 pg/ml). There was also some non-specific background release of soluble CD16, because supernatant from unstimulated cells contained significantly more soluble CD16 than the media alone (Figure 3.16). These results confirmed that the activation of cells leads to CD16 shedding.

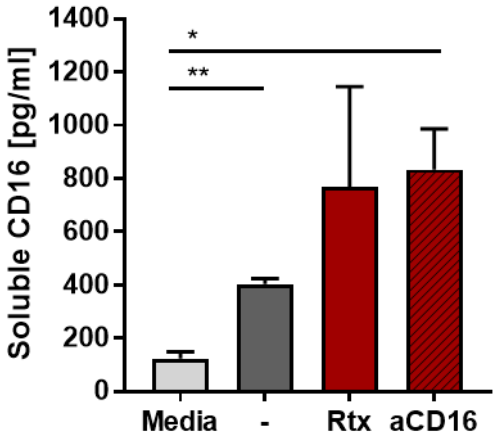

Figure 3.16: Soluble CD16 upon NK cell stimulation. Fresh NK cells were resuspended in serum reduced media and incubated on rituximab or anti-CD16 coated surfaces for 18h. Non-coated surface was used as a control. Soluble CD16 was detected from the supernatant by sandwich ELISA. Rtx: rituximab. Data is pooled from four independent experiments, mean ± SD. *p<0.05, **p<0.01, calculated by Friedman test.

3.3.8. Pre-activation of NK cells on slides reduces their cytotoxicity towards target cells

We next set out to assess whether the decreased perforin secretion upon sequential stimulation translates into reduced killing of target cells expressing different ligands. For this, the Daudi cell line, opsonized with rituximab or transfected to express MICA on the surface was used. Daudi is a well characterized B lymphoblast cell line, commonly used to study NK cell cytotoxicity. Opsonisation with rituximab was sufficient by incubating cells with the molecule for 30 min in normal culture media. Increasing the incubation to 4h, or incubation in PBS, did not increase the opsonisation (Figure 3.17A). Daudi cells express low levels of MICA. However, in transfected cells, the expression of MICA was significantly higher (Figure 3.17B).

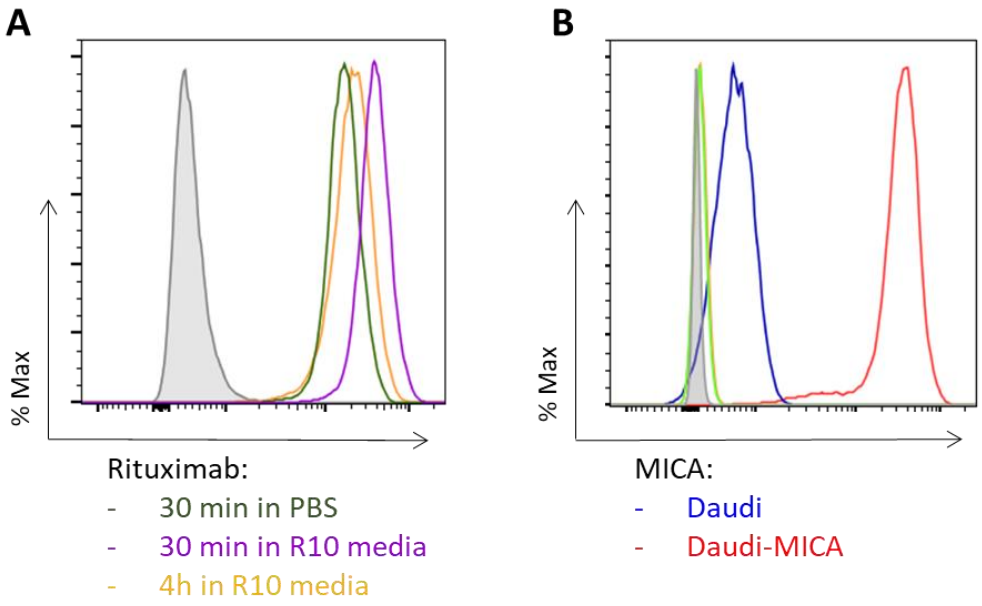

Figure 3.17: Rituximab and MICA on Daudi cells. (A) NK cells were opsonized with rituximab. For optimization of opsonisation, cells were washed and incubated with rituximab in PBS (green) or full R10 media (purple) for 30 min or in full R10 media for 4 hours (yellow). Rituximab was stained with anti-Fc-FITC antibody. Rituximab was compared to isotype control (grey). **(B)** Daudi cells (blue) and Daudi-MICA (red) were stained for surface MICA with anti-MICA-APC antibody. Expression levels are compared to isotype control staining (grey).

To address the effect of different pre-stimulations of NK cells on their cytotoxicity, NK cells were again activated on coated surfaces. After two rounds of 1h stimulation on either ICAM1 alone, rituximab or MICA or coated surfaces, NK cells were washed and incubated with Daudi, Daudi-rituximab or Daudi-MICA for another 1.5h (Figure 3.19A). The cytotoxicity of NK cells was measured by assessing target cell Caspase

3/7 activity, indicating apoptosis. To distinguish target cells from NK cells, Daudi cells were stained with anti-CD19 PE and NK cells with anti-CD56 BV421 antibody (Figure 3.18). CD19 is a B cell marker not expressed by NK cells, while CD56 is specific for NK cells.

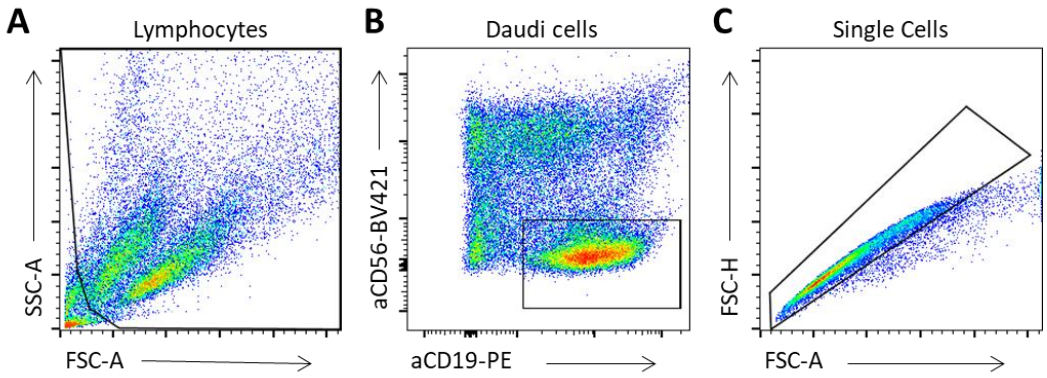

Figure 3.18: Gating strategy for Daudi population in co-culture with NK cells. Representative gating strategy for analysis of NK cells cytotoxicity towards Daudi, Daudi-rituximab and Daudi-MICA cells. **(A)** First cell debris was gated out using forward and side scatter signal area (FSC-A and SSC-A). **(B)** B cells were selected as $CD19^{+}CD56^{-}$ population. **(C)** Forward side scatter area and height (FSC-A and FSC-H) signals were used to exclude doublets.

Pre-incubation on ICAM1 or rituximab-coated surfaces did not affect the killing of Daudi-rituximab or Daudi-MICA target cells. Unstimulated NK cells killed 81 ± 11% Daudi-rituximab, pre-stimulation with ICAM1 or rituximab insignificantly reduced it (76 ± 7 % and 76 ± 7 %, respectively). Pre-stimulation on MICA-coated surfaces reduced killing by 21 %.

Similarly, pre-stimulation with ICAM1 or rituximab did not strongly affect the killing of Daudi-MICA. Pre-stimulation on ICAM1 reduced killing to 63 ± 8 % and on rituximab to 64 ± 8 % from 71 ± 17 % of untreated cells. When cells were pre-incubated on MICA, the killing of Daudi-MICA cells decreased by 32% (Figure 3.19 B, C).

These results indicate that the first contact with MICA impairs the consecutive NK cell – target cell interactions. On the other hand, initial contacts with non-stimulating ICAM1, or with rituximab-coated surfaces has less impact on the cytolytic response to successive target cells.

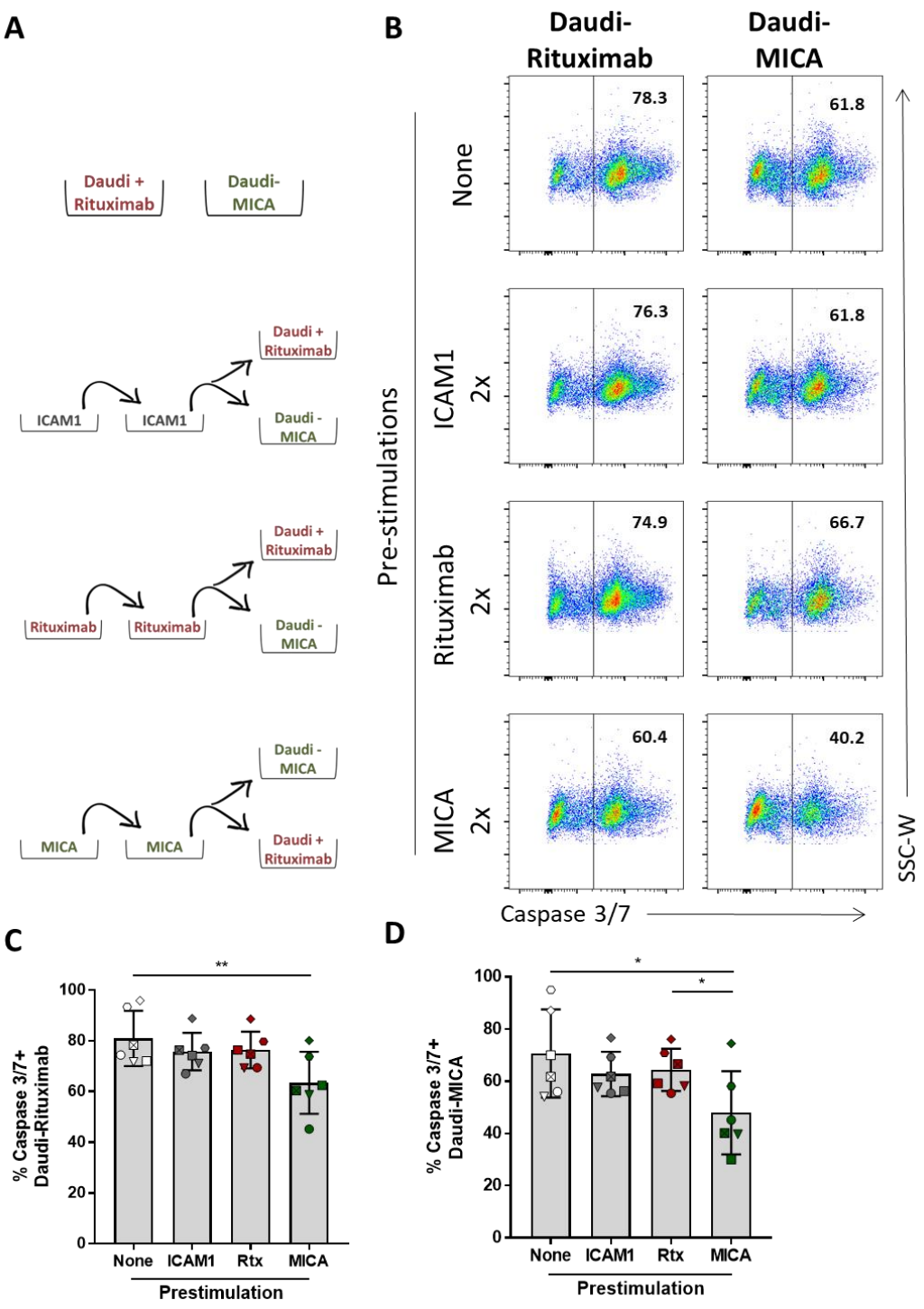

Figure 3.19: Target cell death upon incubation with pre-stimulated NK cells. (A) Schematic representation of experimental set-up. Primary NK cells were stimulated repeatedly for 1h at either, ICAM1 alone (-), or ICAM1 together with rituximab or MICA. After second stimulation, they were split in half and incubated with Daudi target cell line (opsonized with rituximab or overexpressing MICA) for additional 2h at E:T=1:1. **(B)** Daudi cell death was measured by staining Caspase 3/7 activity, and acquired by flow cytometry. Shown are representative plots from five independent experiments. **(C)** Percentage of Caspase 3/7 positive Daudi cells from (B). Data are pooled from five independent experiments (n=5) and plotted as mean ± SD. Symbols represent different donors. *p<0.05, **p<0.01, calculated by Friedman test.

3.3.9. The order of target cell engagement determines the efficiency of serial killing

Stimulation of NK cells on activating surfaces is a simplified system. Target cells express an array of potential NK cell ligands that coated surfaces do not account for. To address this, we first wanted to assess how the incubation with target cells, expressing different NK cell ligands (rituximab or MICA) affects their activating receptors. NK cells were incubated for 1h with Daudi alone, Daudi-rituximab or Daudi-MICA, all labelled with cell proliferation dye (Cell Trace Violet) (Figure 3.20).

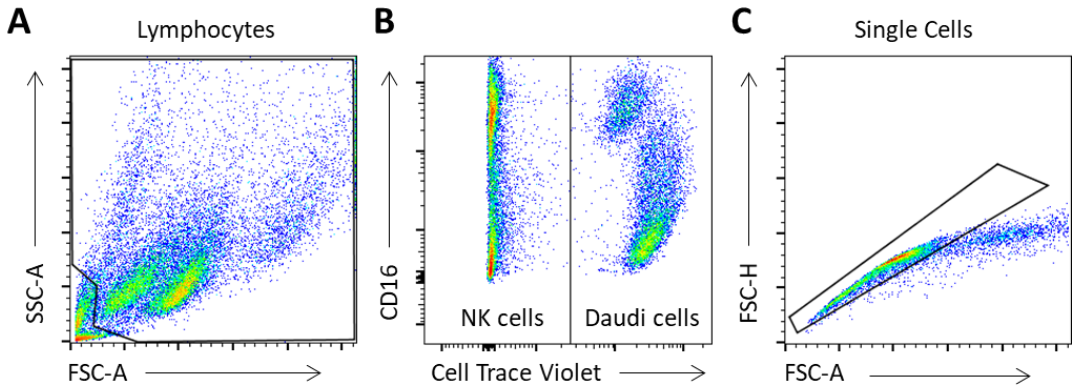

Figure 3.20: Gating strategy for Daudi-violet population. Representative gating strategy for analysis of NK cells cytotoxicity towards Daudi, Daudi-rituximab and Daudi-MICA cells. **(A)** First cell debris was gated out using forward and side scatter signal area (FSC-A and SSC-A). **(B)** B cells were gated as Cell Trace Violet $^{+}$ population. **(C)** Forward side scatter area and height (FSC-A and FSC-H) signals were used to exclude doublets.

Incubation with either target resulted in reduced levels of CD16 compared to non-stimulated cells, seen as a decrease in CD16^{+} cells and their gMFI value. Interestingly, the most significant reduction of CD16 was observed after the incubation with Daudi-rituximab (gMFI reduced to 73 ± 17 % of unstimulated cells) (Figure 3.21A, C). This is perhaps, because the opsonisation of targets with rituximab is more efficient than coating of the PLL-coated surfaces. On the surfaces, the orientation of the molecules is random, meaning that many molecules could have the CD16-ligating portion of rituximab in a position where the receptor could not reach it. This could lead to lower activation with the same number of molecules. On the other hand, orientation of the molecules on opsonized targets is defined by its Fab-portion, ligating CD20 on B cell surface.

Consistent with the results obtained from coated activating surfaces, NKG2D levels were only affected when this receptor was engaged, by Daudi-MICA (to 44 ± 12 % of

NKG2D on unstimulated cells) and less significantly by Daudi alone (expressing low levels of MICA, to 73 ± 11 % of unstimulated levels). Daudi-rituximab did not have any effects on NKG2D expression (Figure 3.21 B, D).

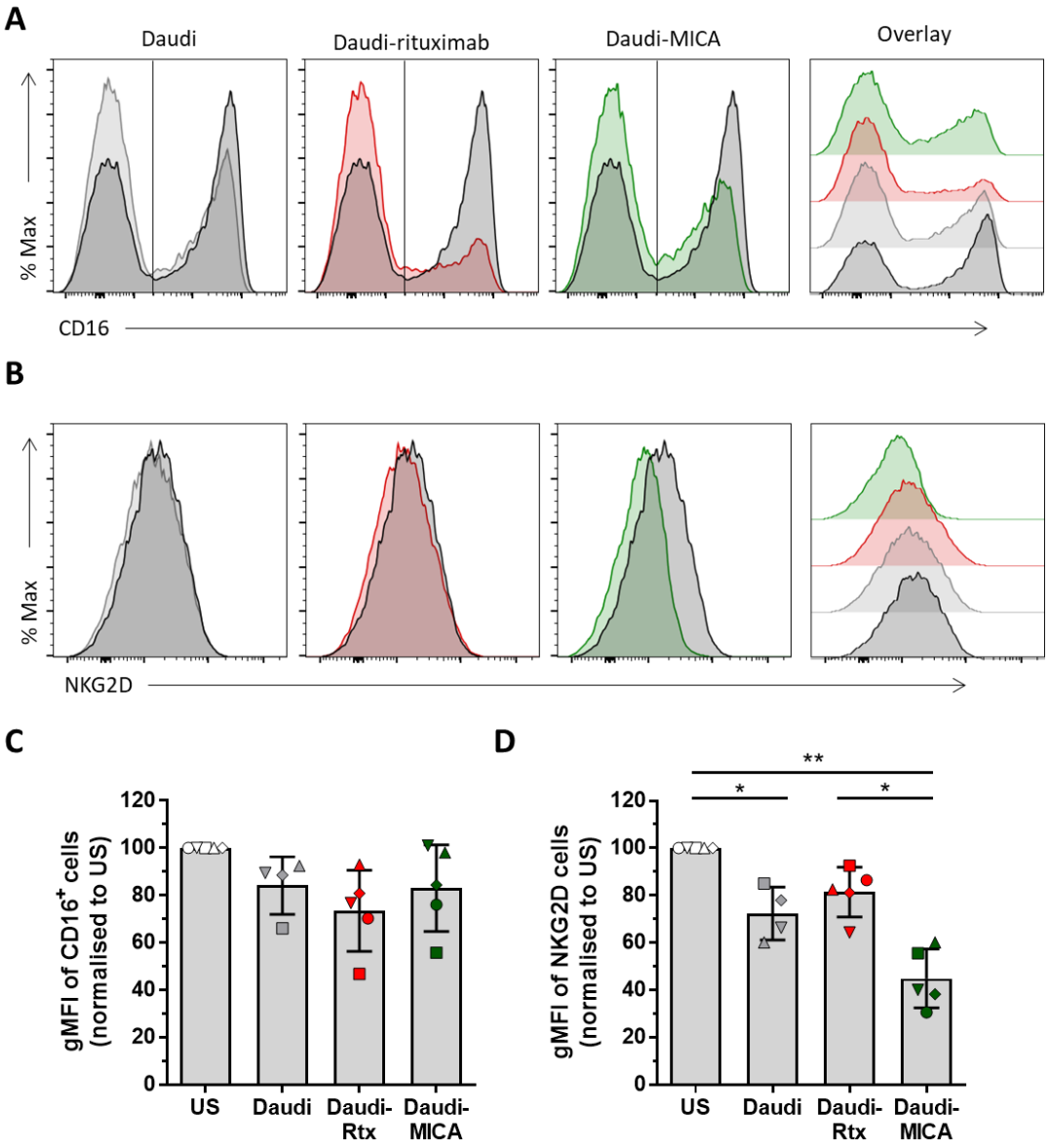

Figure 3.21: CD16 and NKG2D on NK cells upon incubation Daudi cells. NK cells were incubated with Daudi (grey), Daudi-rituximab (red) or Daudi-MICA (green), labelled with Cell Trace Violet. The expression levels of CD16 and NKG2D were assessed by flow cytometry and compared to expression levels on non-activated NK cells (black). **(A)** Representative histograms of CD16 upon incubation with targets. Vertical line indicates $CD16^+$ gate. **(B)** Representative histograms of NKG2D expression upon incubation with targets. **(C)** gMFI of $CD16^+$ NK cells. **(D)** gMFI of NKG2D. Data are pooled from five independent experiments (n=5) and plotted as mean ± SD. Symbols represent different donors. US: unstimulated cells. *p<0.05, **p<0.01 calculated by Friedman test.

To address whether the serial contacts with different target cells also impair their subsequent cytotoxic responses, the following assay was performed: NK cells were pre-activated with Daudi, Daudi-rituximab or Daudi-MICA. After 1.5 hour, additional targets, labelled with a fluorescent dye (Cell Trace Violet) were added for another 1.5 hour, in the presence of Caspase 3/7 dye, as indicated in scheme (Figure 3.22A). Unstimulated NK cells killed 74 ± 16 % of Daudi-rituximab and 49 ±% of Daudi-MICA. When NK cells were pre-incubated with either target, subsequent killing of Daudi-rituximab was reduced. The most significant reduction was observed after pre-incubation with Daudi-MICA, where the cytotoxicity was reduced by 31 %. Pre-incubation with Daudi alone led to 21 % less killing and pre-incubation with Daudi-rituximab resulted in 27 % less killing (Figure 3.22 B, C). Killing of Daudi-MICA was decreased when NK cells were pre-activated with Daudi alone (by 21 %) or Daudi-MICA (by 58 %). The pre-activation with Daudi-rituximab non-significantly increased the killing of Daudi-MICA by 8 % (Figure 3.22 B, D).

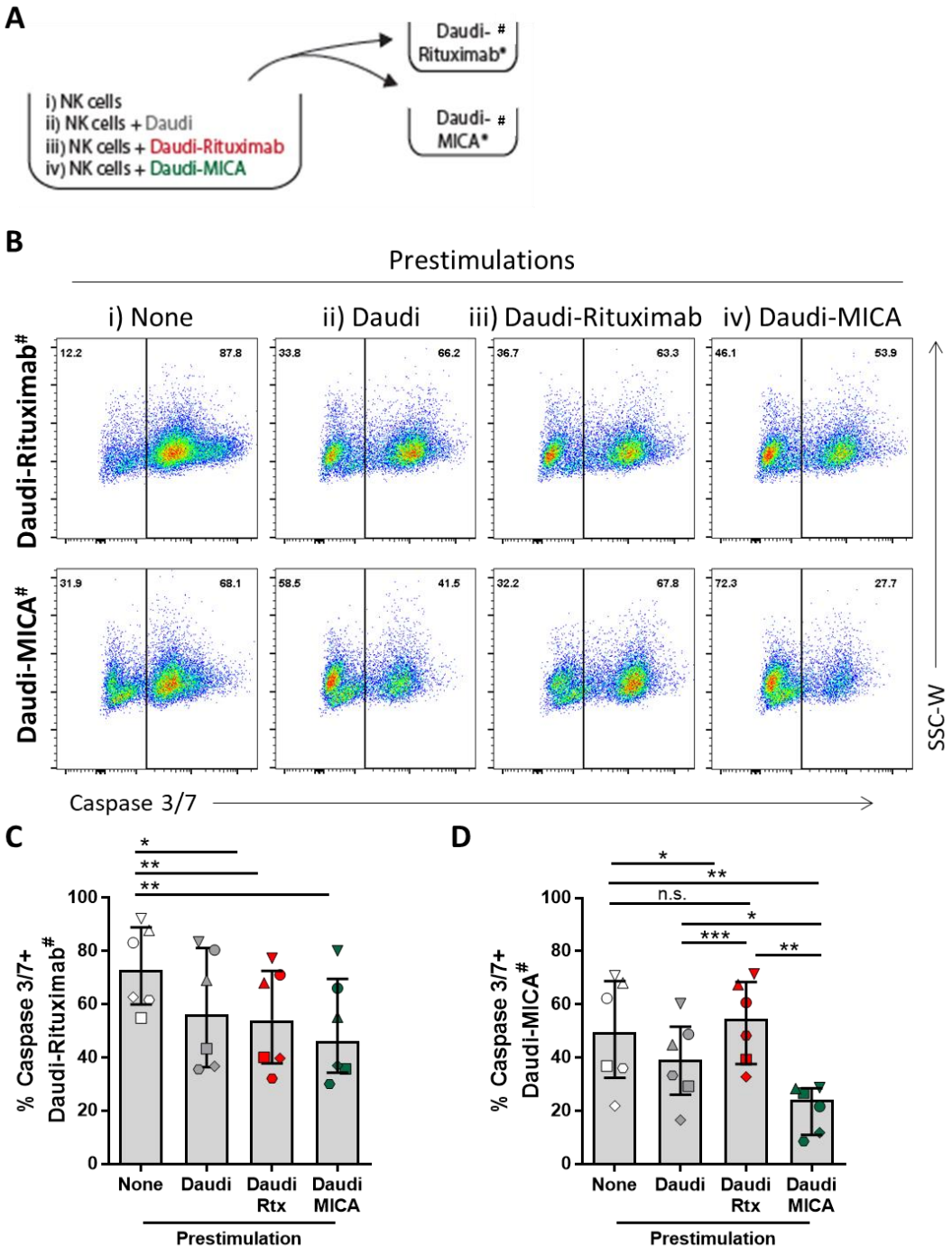

Figure 3.22: Target cell death upon incubation with pre-stimulated NK cells. (A) Schematic representation of experimental set-up. Primary NK cells were pre-stimulated with Daudi, Daudi-rituximab or Daudi-MICA for 1.5h at E:T=1:1. Unstimulated cells were used as a control. The, Daudi-rituximab or Daudi-MICA, labelled with Cell Trace Violet (#) were added and mixture was incubated for additional 1.5h. **(B)** Daudi cell death was measured by staining Caspase 3/7 activity (using Cell Event Dye), and acquired by flow cytometry. Shown are representative plots gated on labelled target cells (gated as in Figure 3.19) from six independent experiments. **(C, D)** Percentage of Caspase 3/7 positive Daudi-rituximab (C) and Daudi-MICA (D) cells from. Data are pooled from six independent experiments (n=6) and plotted as mean ± SD. Symbols represent different donors. *p<0.05, **p<0.01, ***p<0.001, ****p<0.0001 calculated by Friedman test.

To extend our observation on sequential cytotoxicity towards different targets, we performed live imaging. NK cells were incubated with both, Daudi-rituximab and Daudi-MICA within specially designed microchips, allowing tracking of individual NK cell-target cell interactions over several hours. Each well in such microchip had dimensions of 350 x 350 μm^2. Cells were labelled with different dyes; NK cells with Cell Trace Violet, Daudi-rituximab with Calcein Red-Orange and Daudi-MICA with Calcein Green. Target cell death was visualised by the loss of Calcein fluorescence and by obtaining the red dye from ToPro-3, a DNA dye, impermeable for live cells (Figure 3.23A, B). Cells were incubated at E:T:T=1:1.5:1.5. Imaging was performed at 37°C for 8 hours with an image acquired every 3 min. Images were then manually analysed.

Overall, the killing of Daudi-rituximab was longer than killing of Daudi-MICA, with the average killing time of 100 ± 103 min, while the killing of Daudi-MICA took 72 ± 86 min (Figure 3.23C). The first kill was performed faster than the sequential kills; when Daudi-rituximab was the first target killed, the mean killing time was 93 ± 107 min, while for Daudi-MICA it was 60 ± 81 min. The successive killing of Daudi-rituximab took 122 ± 82 min, and for Daudi-MICA it took 95 ± 93 min (Figure 3.23D).

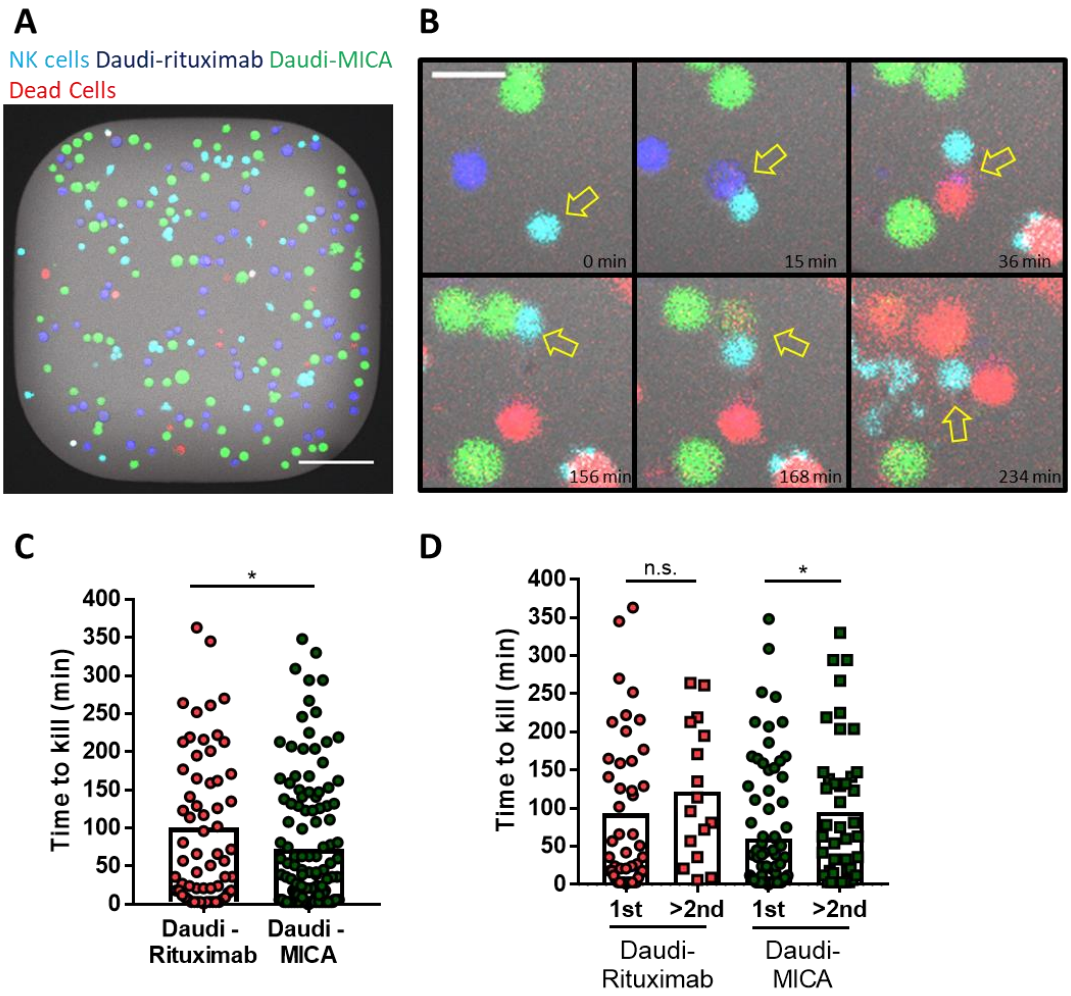

Figure 3.23: Time-lapse imaging of NK cells Daudi-rituximab and Daudi-MICA interactions in microchips. NK cells were incubated with Daudi-rituximab and Daudi-MICA at E:T:T=1:1.5:1.5 in microchips. **(A)** Representative image of one microwell in the microchip of dimensions 350 x 350 µm^2. NK cells were labelled with Cell Trace Violet, Daudi-rituximab with Calcein Red-Orange, Daudi-MICA with Calcein Green and cell death with ToPro-3. The scale bar is 100 µm. **(B)** Panels represent zoomed-in region from a microwell. Time-lapse imaging data showing an overlay of a fluorescence and bright-field image. In bottom right corner time (in minutes) is indicated. The scale bar is 20 µm. Arrows point to the same NK cell interacting with targets. An NK cell (cyan) made a contact with Daudi-rituximab (blue) at 15 min and killed it at 36 min. Following this, the cell detached and encountered Daudi-MICA at 156 min and killed it 12 min later. By 234 min both target cells were dead (red), and NK cells remained alive. **(C)** Time that NK cells needed to kill Daudi-rituximab and Daudi-MICA targets. (D) Time for target cell lysis stratifying 1st from the succeeding kills. Data are pooled from three experiments (n ≥ 40 cells per experiment) and plotted as mean ± SD**.** *p<0.05, calculated by Kruskal-Wallis test.

When the NK cell met Daudi-Rituximab first, 50 ± 10 % of all such contacts led to target cell lysis. Lysis of successive Daudi-rituximab was reduced to 39 ± 12 %. When Daudi-MICA was the first encountered target, the following killing of Daudi-Rituximab was successful only 14 ± 6 % of occasions (Figure 3.24A). On the other hand, 88 ± 2 % of first interactions with Daudi-MICA resulted in target cell lysis. This was barely affected when the NK cell killed Daudi-rituximab first, but was reduced to 64 ± 4 % when the preceding contact was with Daudi-MICA (Figure 3.24B).

When the NK cell encountered two Daudi-rituximab cells sequentially, 20 ± 17 % of interactions led to lysis of both targets. 24 ± 15 % interactions resulted in death of first target only and 24 ± 25 % resulted in death of the second target. 31 ± 12 % of interactions with multiple Daudi-Rituximab resulted in no kill (Figure 3.24C). When NK cell encountered multiple Daudi-MICA targets, both targets were killed in 68 ± 1 % of all interactions. 8 ± 9 % of interaction resulted in the survival of both targets and 21 ± 3 % in the lysis of the first target only. The failure to kill the first encountered Daudi-MICA was not recovered upon the sequential interaction with the same cell type (Figure 3.24E).

When the NK cell made a contact with Daudi-MICA following the interaction with Daudi-Rituximab, it either killed both targets (47 ± 14 %) or only the second one (38 ± 3 %). The first interaction with Daudi-Rituximab did not affect subsequent interactions with Daudi-MICA (Figure 3.24D). In contrast, when NK cell first encountered Daudi-MICA and consecutively Daudi-rituximab, the killing of the second target was impaired. In 74 ± 13 % of all interactions, only the first target was killed, while in only 12 ± 13 % of interactions both targets were killed (Figure 3.24F). Thus, NK cells that ligate CD16 first, have non-affected responses towards the second target, while NK cells that engage NKG2D first have decreased cytotoxicity towards rituximab-opsonized target cells.

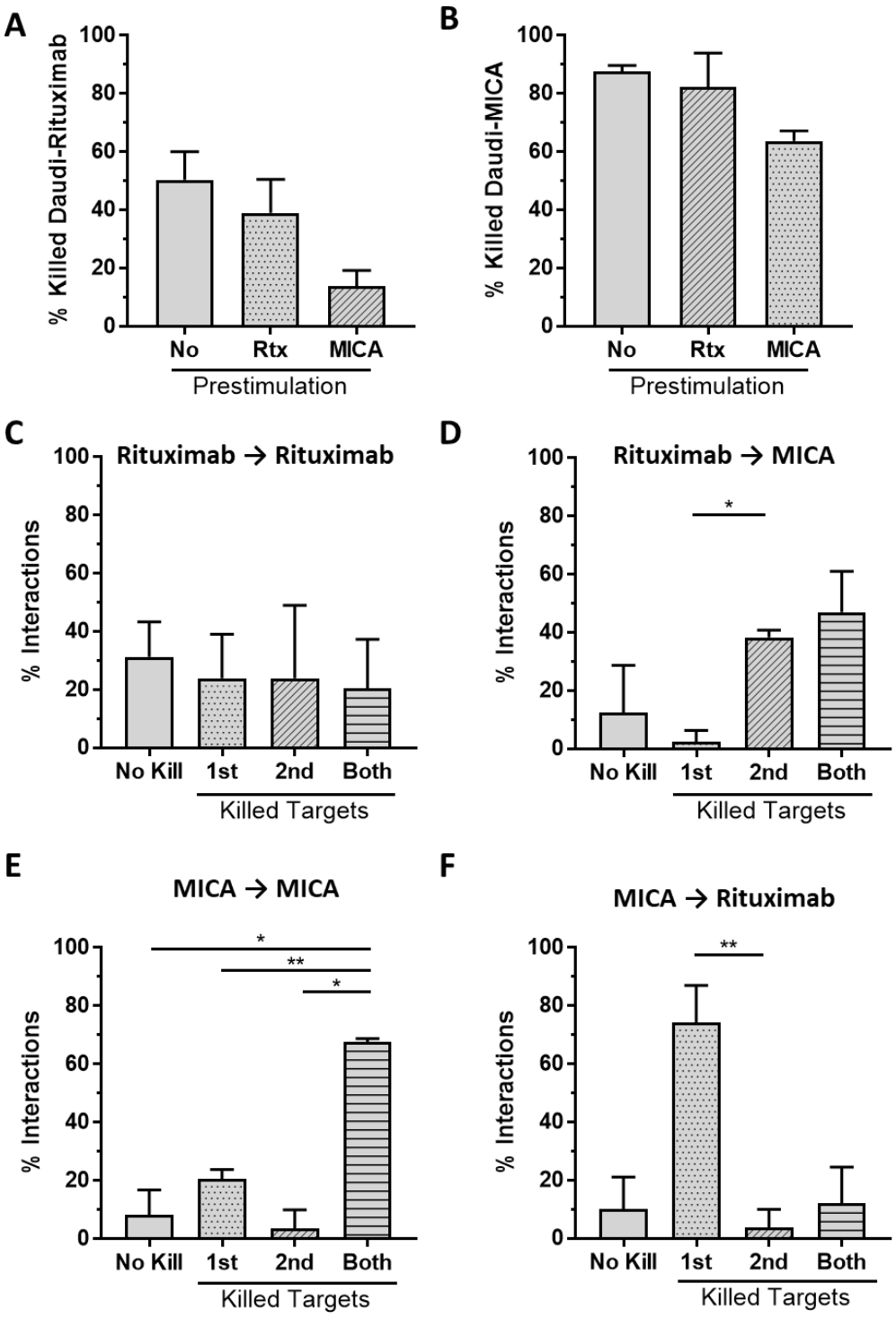

Figure 3.24: Efficiency of NK cell cytotoxicity in serial killing. Interactions of individual NK cells with their targets were acquired by time-lapse imaging in microwells. Killing efficiency was manually analysed. **(A)** Graphs summarize the percentage of target cell lysis when Daudi-rituximab was the first target, or when it was encountered following the contact with another Daudi-rituximab or Daudi-MICA. **(B)** The percentage of Daudi-MICA lysis when Daudi-MICA was the first target, or when it was met subsequent to Daudi-rituximab or Daudi-MICA. **(C)** The percentage of killed targets when two Daudi-rituximab targets were contacted sequentially. **(D)** Efficiency of target cell lysis, when NK cell encountered Daudi-rituximab first and Daudi-MICA was the second target. **(E)** The percentage of killed targets when two Daudi-

MICA were encountered sequentially. **(F)** Target cell lysis when the interaction with Daudi-rituximab followed Daudi-MICA contact. Data are pooled from three experiments (n ≥ 40 cells per experiment) and plotted as mean ± SD**.** *p<0.05, **p<0.01, ***p<0.001, ****p<0.0001 calculated by Friedman test.

3.3.10. CD16 loss is long-lived

The results above indicate that activation of NK cells through CD16 or NKG2D decrease surface levels of CD16. The functional consequence of this is the impaired ADCC. Next, we wanted to investigate, whether the CD16 expression can recover. For this, NK cells were stimulated on activating surfaces, coated with rituximab or MICA, both with ICAM1 for 1h. Then, cells were removed, washed and placed in full media. The expression levels of CD16 were assessed 4h, 12h and 24h after stimulation and compared to unstimulated cells. As shown above, the activation through both receptors led to loss of CD16 expression to 49 ± 1% or 36 ± 6 %, when triggered by ligation of CD16 or NKG2D, respectively). In 24h, its expression recovered to 74 ± 39 % of its original expression upon rituximab stimulation and 6 ± 38 % upon MICA stimulation. The expression of CD16 on unstimulated cells was not affected over the 24h time course (Figure 3.25).

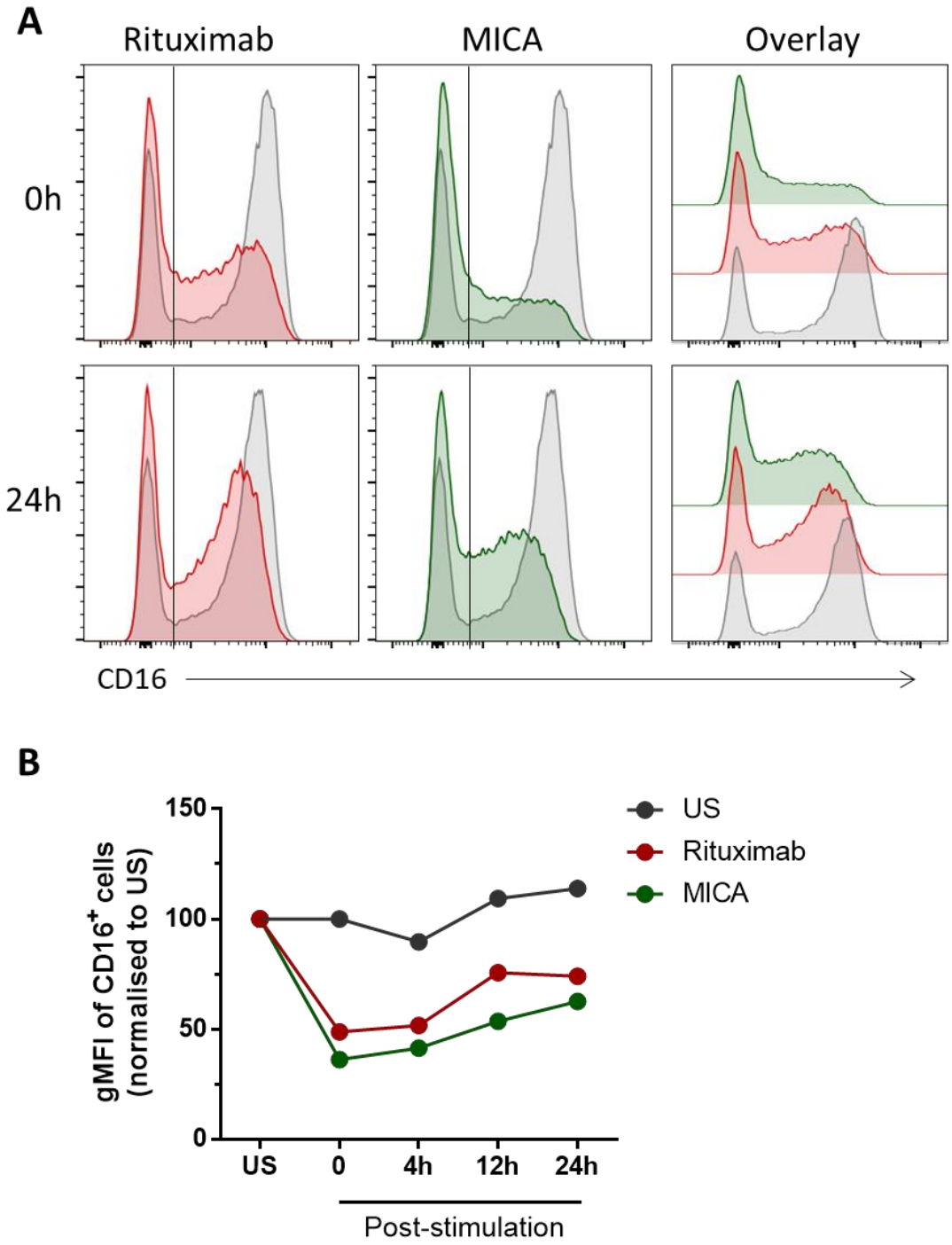

Figure 3.25: CD16 expression over 24h after stimulation. NK cells were stimulated on surfaces coated with rituximab (red) or MICA (green), both with ICAM1 for 1h. Then, they were removed, washed and incubated in clone media. The expression levels of CD16 were assessed by FACS at 0, 4, 12, and 24h post stimulation and compared to CD16 on non-activated NK cells (grey). **(A)** Representative histograms of CD16 0h and 24h post-stimulation. Vertical line indicates $CD16^+$ gate. **(B)** gMFI of CD16+ NK cells. Data are pooled from two independent experiments (n = 2) and plotted as mean. US: unstimulated cells.

3.3.11. IL-10 improves CD16 recovery

To assess whether treatment of activated NK cells with different cytokines improves their CD16 recovery, IL-18 and IL-10 were tested. IL-18 is well-known to induce NK cell activation, while IL-10 has been demonstrated to inhibit a variety of immune cell functions. The impact IL-10 has on NK cells is less understood. Mocellin et al. reported that IL-10 increased mRNA levels of cytotoxicity related genes and NK cell cytotoxicity towards Daudi cells without affecting migration or proliferation (Mocellin et al., 2004).

Preliminary data indicate, that the addition of IL-10 contributed to faster and greater recovery of CD16 receptor. 4h after the stimulation with rituximab, IL-10 increased CD16 levels to 71 ± 26 % of its original expression (compared to 51 ± 6 % of untreated cells). 24h post-stimulation, gMFI of $CD16^+$ cells reached 98 ± 60 % of unstimulated cells, while untreated cells only recovered to 74 ± 40 %. On the other hand, IL-18 additionally increased downregulation of CD16 (24h post-stimulation, CD16 was at 61 ± 34 % of its starting value) (Figure 3.26).

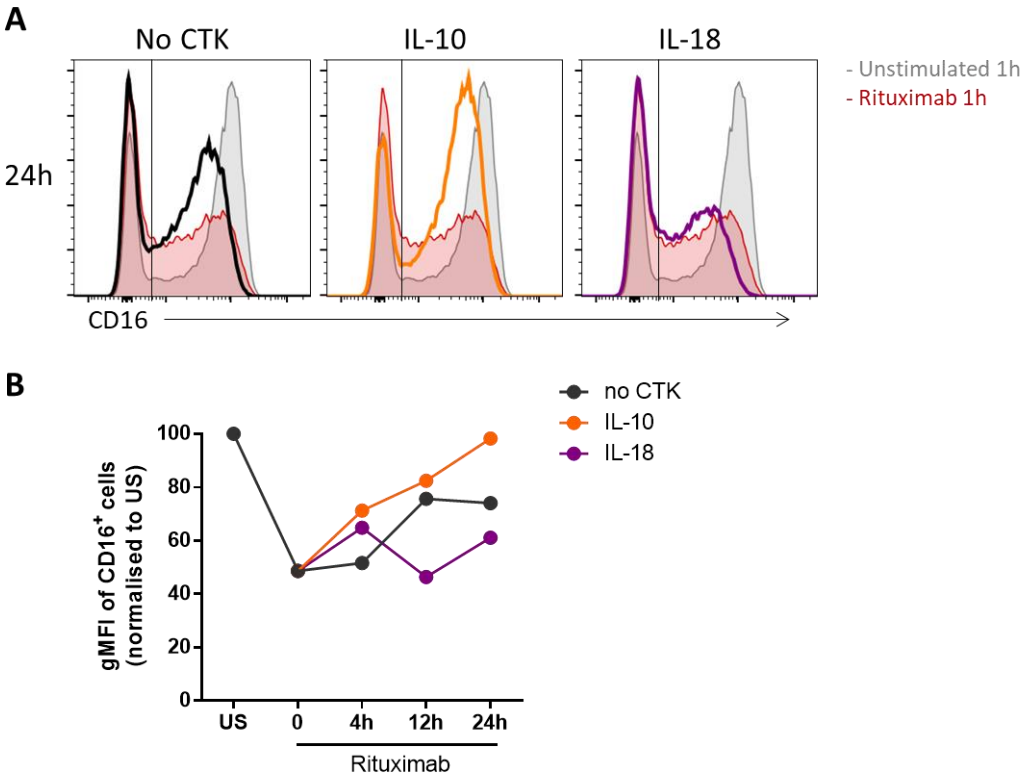

Figure 3.26: CD16 recovery post rituximab-stimulation upon IL-10 or IL-18 treatment. NK cells were stimulated on rituximab with ICAM1 (red) coated surfaces for 1h. Then, they were removed, washed and incubated in full media, supplemented with IL-10 (orange) or IL-18 (violet), as indicated. The expression levels of CD16 were assessed by flow cytometry at 0, 4, 12, and 24h post stimulation and compared to CD16 on unstimulated NK cells (grey). **(A)** Representative histograms of CD16 24h post-stimulation. Vertical line indicates $CD16^+$ gate. **(B)** gMFI of $CD16^+$ NK cells. Data are pooled from two independent experiments (n=2) and plotted as mean. CTK: cytokines, US: unstimulated cells.

Similar results were obtained from NK cells activated on a MICA-coated surface. Straight after stimulation, only 36 ± 6% of CD16 was left on cell surface. Upon treatment with IL-10, CD16 recovered to 81 ± 48 % of its starting expression, comparing to 63 ± 38 % of non-treated cells. IL-18 had again negative impact on CD16 expression, and kept its levels at 48 ± 26 % 24h post stimulation (Figure 3.27).

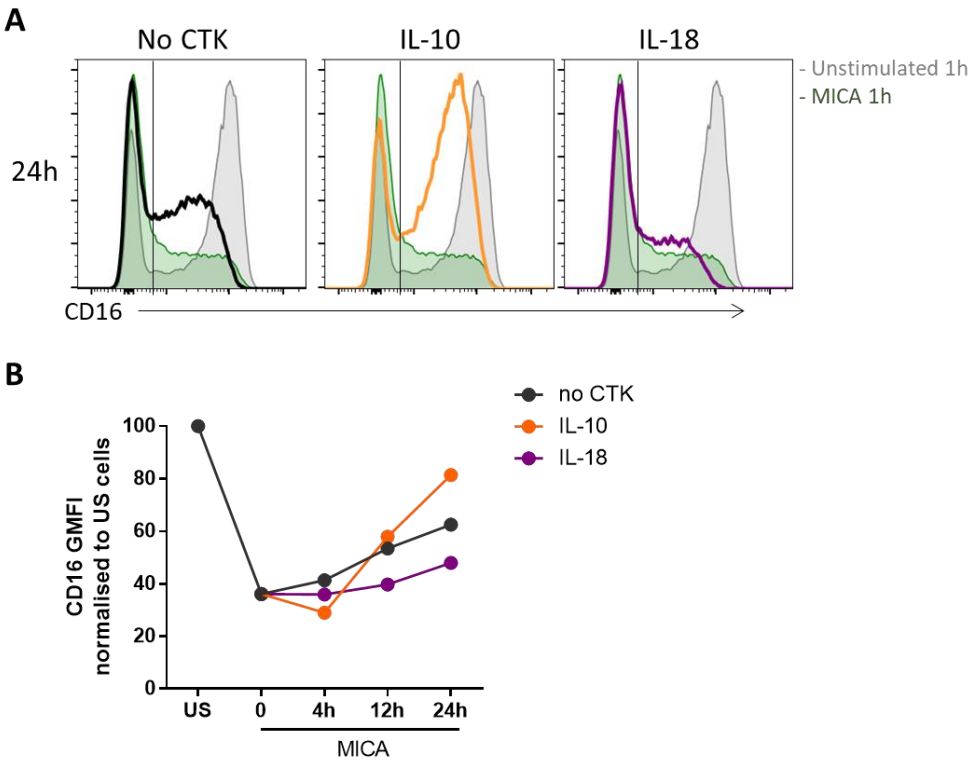

Figure 3.27: CD16 recovery post MICA-stimulation upon IL-10 or IL-18 treatment. NK cells were stimulated on surface coated with MICA with ICAM1 (green) for 1h. Then, cells were removed, washed and incubated in clone media, supplemented with IL-10 or IL-18, as indicated. The expression levels of CD16 were assessed by FACS at 0, 4, 12, and 24h post stimulation and compared to CD16 on non-activated NK cells (grey). **(A)** Representative histograms of CD16 24h post-stimulation. Vertical line indicates CD16+ gate. **(B)** gMFI of $CD16^{+}$ NK cells. Data are pooled from two independent experiments (n=2) and plotted as mean. CTK: cytokines, US: unstimulated cells.

Cytokines did not have an impact on CD16 expression on its own. When unstimulated cells were treated with IL-10 or IL-18, expression of CD16 remained unchanged (Figure 3.28).

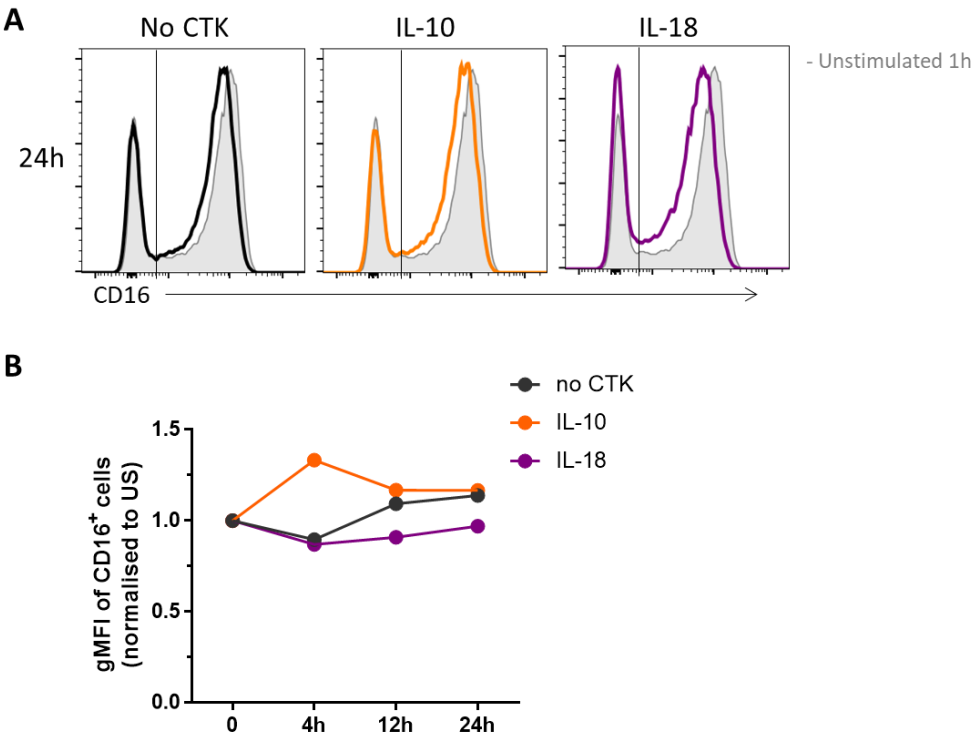

Figure 3.28: CD16 levels upon IL-10 or IL-18 treatment. Unstimulated NK cells were treated with IL-10 or IL-18, as indicated. The expression levels of CD16 were assessed by FACS at 0, 4, 12, and 24h and compared to CD16 on non-stimulated cells before the treatment (grey). **(A)** Representative histograms of CD16 24h post-stimulation. Vertical line indicates CD16+ gate. **(B)** gMFI of CD16+ NK cells. Data are pooled from two independent experiments (n=2) and plotted as mean. CTK: cytokines, US: unstimulated cells.

These preliminary results indicate that IL-10 treatment helps with CD16 recovery after NK cells stimulation. However, further experiments need to be done in order to assess the role of this cytokine thoroughly. Moreover, it remains to be determined whether such recovered CD16 is fully functional.

3.4. Discussion

3.4.1. Summary of results

The principal aim of this study was to examine cytotoxic responses and phenotypic changes of NK cells upon sequential stimulation through two different activating receptors.

For evaluating NK cell cytotoxicity, three main methods were used. Perforin, secreted from individual cells was measured upon controlled stimulation via specific ligand. A flow cytometric-based killing assay was used to study population cytotoxicity towards the Daudi target cell line, and microchips provided a platform for investigating single cell interactions with one or multiple targets over several hours. Changes in expression levels of surface receptors upon stimulation were evaluated by flow cytometry.

The main findings presented in this chapter established that:

i. Stimulation of NK cells by MICA leads to greater perforin secretion than by rituximab. Upon incubation on MICA-coated surfaces perforin is secreted in dense round clusters, while on rituximab perforin distribution is more elongated. Secretion on rituximab from an individual cell accumulates over time, while cells on MICA seem to respond quickly with saturating response.
ii. Serial stimulation through one receptor results in reduced perforin secretion. This is true for both CD16 and NKG2D. When both receptors are ligated sequentially, the order in which different activating ligands are encountered affects the strength of responses. Reduced perforin secretion upon repeated stimulation through CD16 can be recovered by consecutive stimulation through NKG2D. But, the stimulation through CD16 does not recover the reduced degranulation following the NKG2D ligation.
iii. Activation through both rituximab and MICA leads to loss of CD16 from NK cell surface, due to receptor shedding. In contrast, NKG2D levels are only affected when cells are in contact with MICA.
iv. Reduced perforin secretion upon sequential stimulation can be translated into reduced cytotoxicity towards Daudi target cell line. NK cells that were pre-stimulated through either CD16 or NKG2D are less efficient at killing

of Daudi-rituximab. On the other hand, killing of Daudi-MICA is mainly affected when NKG2D was previously ligated.

v. Recovery of CD16 expression can take a long time. Cell that have been activated by rituximab or MICA recover only a small proportion of surface CD16 within 24h. The preliminary results suggest that the treatment with IL-10 post-activation boosts CD16 surface expression.

3.4.2. Significance of the results

In this study, we used a technique, developed in our laboratory that allowed us to assess the secretion of perforin from individual cells upon the engagement of different NK cell receptors. Perforin is an essential protein for the execution of target cell lysis as, by using knockout mice, it has been established that cells lacking perforin completely abolished granule-dependent cell death while a knockout of granzyme genes produced less severe phenotypes (Müllbacher et al., 1999, Pardo et al., 2002, Simon et al., 1997). Until this work, it has never been addressed how much perforin specifically is secreted from individual NK cell upon activation and whether different stimulations trigger perforin secretion differently. Here, the secreted perforin from human primary NK cells, stimulated on coated surfaces, was captured on glass, stained and imaged by confocal microscope. The method allowed us to qualitatively and quantitatively compare perforin secretion on different conditions and at different time points.

Perforin capture assay revealed that cells stimulated on MICA-coated surfaces secreted more perforin per cell than cells stimulated on surfaces coated with rituximab. Both activating ligands triggered perforin secretion more efficiently than non-stimulating ICAM1. On MICA, perforin was secreted into round dense patches, while on rituximab it was scattered in elongated shapes. On all conditions, there was a great heterogeneity in the range of individual NK cell responses, with some cells secreting up to 100-times more perforin than others. There was also a significant donor-to-donor variability, but the trend of responses was always comparable.

NK cell degranulation is more commonly assessed by flow cytometry-based degranulation assay, assessing CD107a levels. CD107a glycoprotein primarily resides on the membrane of lytic granules and is fused with the cell membrane upon degranulation and can be therefore used as a marker of degranulation (Kannan et al., 1996). The results obtained by perforin capture assay were in line with assays of

CD107a expression, displaying the greatest degranulation on MICA, weaker on rituximab and very weak on ICAM1. The consistency between the two assays suggests that perforin capture is a reliable method for detecting NK cell degranulation levels.

Despite lower perforin secretion, rituximab consistently triggered higher IFN-γ secretion than MICA. This indicates that NK cells were indeed responsive to rituximab, and that their response especially favoured cytokine secretion rather than degranulation. Some studies report, that the $CD56^{bright}$ NK cell subset is responsible for cytokine secretion while $CD56^{dim}$ degranulate better upon the stimulation (De Maria et al., 2011, Orange, 2013, Vivier et al., 2008, Cooper et al., 2001b). A conflicting study demonstrated that $CD56^{dim}$ subset is responsible for both lytic granule and cytokine secretion (Fauriat et al., 2010). However, the $CD56^{bright}$ NK cell subset does not express CD16, and thus upon the stimulation with rituximab, $CD56^{dim}$ subset was likely to be responsible for both degranulation and cytokine production.

ICAM1 has been previously shown to positively impact NK cell responses. NK cell degranulation was increased on bilayers carrying anti-CD16 antibody, when ICAM1 was added (Steblyanko et al., 2015). The crosslinking of NKG2D with anti-NKG2D antibody alone has been reported to be insufficient in triggering NK cell activation and that additional signal is required (Bryceson et al., 2006). In our experiments, the addition of ICAM1 had no impact on the extent of degranulation on rituximab or MICA. This could be perhaps explained by different strategies used to ligate both receptors; in the previous studies antibodies were used (anti-CD16 or anti-NKG2D, respectively), while we used their ligands. Also, cells adhere less efficiently to lipid bilayers than they do to glass surfaces. This is perhaps why ICAM1 plays a significant role on lipid bilayers while it is not essential for activation on coverslips.

The assay for capturing perforin reported here also allowed us to assess how the duration of stimulation affects degranulation. When NK cells were stimulated on rituximab or MICA for 5 – 120 min, the longer incubation resulted in increased number of degranulating cells, as detected by the number of perforin clusters. Surprisingly, the intensity of perforin clusters, corresponding to the amount of perforin secreted per cell, upon 5 min stimulation on MICA did not differ significantly from 120 min long stimulation. This suggests that when the threshold for degranulation is reached, cells rapidly respond with maximum perforin release. Interestingly however, the amount of perforin secreted by cells stimulated with rituximab increased over time. While degranulation stimulated by MICA seems to be binary (either complete secretion or

no secretion), secretion on rituximab is continuous. This perhaps also explains why there is less perforin secreted on rituximab within a limited time frame. Thus, there might be two different mechanisms regulating the extent of degranulation through CD16 and NKG2D.

Using this assay, we also addressed the secretion of perforin upon NK cell sequential stimulations. Serial killing is an important feature of NK cells and according to some studies, most NK cell kills are done in a sequential manner (Vanherberghen et al., 2013, Choi and Mitchison, 2013). Considering the relatively small number of NK cells comparing to the number of potential targets, especially within solid tumours, the capability of each NK cell to kill more than one target seems essential. However, factors that determine the capacity of NK cells to perform sequential kills have not been well understood. Moreover, tumour cells display a heterogeneous array of NK cell ligands and how efficiently can NK cells kill multiple targets in such complex environment has never been addressed.

Here, we have shown that the order in which target cells expressing different ligands are met affects the strength of NK cell cytolytic responses. When NK cells were repeatedly activated by rituximab, perforin secretion decreased with each stimulation. Interestingly, perforin levels were restored to its initial levels upon subsequent activation by MICA. Repeated stimulation of NK cells via MICA also decreased degranulation capacity of NK cells but, strikingly, this effect could not be rescued by a subsequent stimulation with rituximab. We found that the mechanism underlying these differential outcomes involves shedding of CD16, which occurs upon NK cell activation through both, CD16 and NKG2D. Shedding of CD16 renders the cells insensitive to further activation via that receptor but they remain competent for further activation through NKG2D. These results indicate that rather than cell exhaustion or the depletion of perforin, decreased expression of activating receptors dictates the potency of NK cell to kill.

Upon MICA ligation, NKG2D was greatly downregulated. But, in some donors, the following stimulation through CD16 boosted the expression of NKG2D. NKG2D levels were also increased when cells were stimulated on rituximab-coated surfaces. NKG2D levels slightly decreased when NK cells incubated with Daudi-rituximab, but it is likely that NKG2D ligands expressed by Daudi cells contributed to this. A study in murine NK cells showed that ligation of NKG2D by its soluble ligand MULT1 leads to higher release of IFN-γ upon stimulation through NKp46 or NKRP1C (Deng et al., 2015). Thus, these results taken together perhaps indicate that when cells desensitize

some activating receptors they enhance their responses through others. This suggests that NK cells might be more efficient eliminating tumours expressing multiple activating ligands.

In most donors, cells secreted more perforin upon NKG2D ligation and sequential stimulations through both receptors led to decreased values. However, it is not known how much perforin is required to kill a target and thus the impact of such perforin decrease had to be assessed using target cells. Here we performed live cell imaging of NK cell interactions with Daudi target cell line, opsonized with rituximab, or transfected to express MICA on the surface. Long-term imaging of cell-cell interactions can be technically challenging because NK cells are very motile in search for their targets. To overcome this, we used microchips containing small confined wells, keeping cells within the field-of-view throughout acquisition. We found that the lysis of Daudi-rituximab was reduced when cells encountered Daudi-MICA first, but killing of Daudi-MICA was not affected by Daudi-rituximab as an initial contact. This is consistent with the impact of sequential stimulation on perforin secretion. In microwells, the time it took to kill a second Daudi-rituximab target cell was comparable to the killing of the first target, while for Daudi-MICA killing of the second target took longer. This correlates with greater decrease in perforin secretion upon sequential stimulation with MICA and their all-or-nothing responses on MICA.

Compared to assays of degranulation by flow-cytometry, the cytotoxicity towards Daudi-rituximab was reduced in microwells. Besides having cells seeded at different E:T ratio, the density of cells in microwells was much lower and thus the interactions between cells were less frequent compared to those used in the flow cytometry assay. It is possible that the nature of CD16-ligation allowed cells to make multiple short-term cytolytic contacts that all resulted in target cell lysis, when cells were incubated in bulk. The killing of Daudi-MICA however, was much more efficient in microwells. This is perhaps because NKG2D engagement requires a stable synapse. Once this is formed, target can be efficiently eliminated. However, only one target at a time can be killed and thus in limited time of flow cytometry-based assay, lower proportion of Daudi-MICA was killed. In wells, Daudi-rituximab killing also took longer than killing of Daudi-MICA, possibly due to lower perforin secretion.

So far, we have shown that the loss of CD16 due to NK cell activation contributes to decreased cytotoxic responses in sequential stimulations by this receptor. Therefore, we wanted to assess whether the expression of CD16 can recover. Consistent with other studies (Riley, 2016), NK cells maintained low CD16 levels 24 hours post

stimulation on both, rituximab or MICA. But surprisingly, expression of CD16 recovered within 24 hours upon treatment with IL-10 cytokine. IL-10 is known as an anti-inflammatory cytokine that has a central role in limiting the immune response to pathogens and thereby preventing damage to the host. Specifically, in Th1 cells it decreases the secretion of IL-2, IFN-γ and granulocyte macrophage colony-stimulating factor (GM-CSF) as well as their proliferative response (Mocellin et al., 2004). However, in B cells IL-10 contributes to B cell maturation, antibody production and prevents apoptosis of germinal centre B cells (Xu et al., 2004). The addition of PEG-ylated recombinant human IL-10 increased degranulation and TCR-dependent IFN-γ secretion of CD8+ T cells (Chan et al., 2015). Consistently, in NK cells IL-10 has been reported to increase the production of cytotoxicity-related molecules (Mocellin et al., 2004). Hence, it would be interesting to investigate whether the treatment with IL-10 could positively contributes to NK cells' ADCC overall and it could be thus used as an additive to antibody-based cancer therapies. This might be particularly relevant for NK cells that lost CD16 due to over-activation in tumour tissues.

Overall, in this chapter we have shown here that CD16 shedding, caused by NK cell activation renders cells less responsive to sequential ADCC. However, following ADCC the cytotoxicity through other receptors is maintained. In fact, activation through CD16 could even enhance the following responses through NKG2D. Therefore, for successful serial killing, the order in which targets expressing different ligands are encountered can determine the strength of NK cell responses. Moreover, we have shown that the perforin capture assay is a reliable method for detection of perforin secretion from individual cell. Finally, our preliminary data suggests, that treatment with IL-10 can recover CD16 on NK cells within 24h after. Thus, it would be important to address whether the antibody-based cancer therapies could benefit from the addition of IL-10.

Chapter 4:

Effects of CD16 shedding on ADCC synapse

4.1. Introduction

The interactions between NK cells and target cells can be described in three phases; free migration, conjugation with potential target cell lysis, and detachment. In the migration phase, NK cells are more elongated and they move freely until they find a potential target. In the conjugation phase, they form an intercellular contact with the target, and sometimes deliver a lethal hit by the release of cytolytic granules into the target. Finally, in the detachment phase, NK cells dissociate from the target. NK cells often stay attached for a while, even after they gain the migrating elongated shape back. When cells finally come apart, NK cells are ready to meet new potential targets (Vanherberghen et al., 2013).

Following conjugation with a diseased cell expressing ligands for activating receptors, downstream signals lead to the formation of an activating immunological synapse (IS) at the interface between the two cells. To facilitate successful degranulation, several events must occur; F-actin reorganization at the synapse (Lagrue et al., 2013, Lagrue et al., 2015, Mace et al., 2012, Ritter et al., 2015), clustering of the receptors (Bálint et al., in print, Abeyweera et al., 2011, Liu et al., 2012, Giurisato et al., 2007), polarization of MTOC and lytic granules, and final fusion of the granules with the membrane and their secretion into the sealed synaptic cleft (Cartwright et al., 2014, Liu et al., 2011, Orange, 2008). After the lytic hit is successfully delivered to the target, activating signals terminate and NK cells can detach.

While the activating immune synapse formation has been widely studied, the understanding on how the activating signalling ends and how NK cells dissociate from lysed targets is very limited. Jenkins et al. showed that failed target lysis caused by the inhibition of target caspases prolonged the contact time between the murine NK cell and its target, indicating that dying targets cells play significant role in dictating

the detachment rate. Failure to detach leads to increased secretion of cytokines and chemokines, leading to hyper-inflammatory state (Jenkins et al., 2015).

The engagement of inhibitory receptors on the other hand has been shown to reduce contact times. An early study demonstrated that when using transfected cells with defined receptor-ligand combinations the ligation of inhibitory KIR on human NK cells by MHC class I molecule on targets decreased cell-cell contact formation (Burshtyn et al., 2000). TIRF imaging of the NKL cell line transfected to express KIR2DL2 on supported lipid bilayers containing activating (ULBP3 and ICAM1) and inhibitory (HLA-Cw3) ligands showed that the interaction with inhibitory ligands stops cells from spreading on the surface. Instead, cells formed small, and in some cases highly dynamic contacts. Upon photo-chemical stimulation of KIR2DL2 during ongoing activating responses, inhibitory receptors formed microclusters in the plasma membrane, the peripheral actin cytoskeleton collapsed and the cells retracted from the surface within minutes (Abeyweera et al., 2011).

Moreover, live imaging of sorted primary NK cells showed that an educated subset of cells, only expressing NKG2A inhibitory receptor, but negative for KIR ($CD56^{dim}CD57^{-}KIR^{-}NKG2A^{+}$) display more dynamic migratory behaviour than cells lacking all inhibitory receptors (IR^{-}; $CD56^{dim}CD57^{-}KIR^{-}NKG2A^{-}$). $CD56^{dim}CD57^{-}KIR^{-}NKG2A^{+}$ cells also made more contacts with target cells and were more cytolytic. Conjugates formed between IR^{-} NK cells and HEK293T cells were generally more short-lived than with $NKG2A^{+}$. However, in the cytolytic interactions, there was no difference in the duration of contacts between IR^{-} and $NKG2A^{+}$ subsets (Forslund et al., 2015).

Many activating receptors like NKG2D, 2B4 or NKp46 undergo internalization and degradation upon their ligation and this could also help to terminate the conjugation (McCann et al., 2007, Sandusky et al., 2006, Molfetta et al., 2016). CD16 on the other hand undergoes proteolytic cleavage upon NK cell activation (Romee et al., 2013, Jing et al., 2015, Lajoie et al., 2014). Here we set out to investigate if and how shedding of CD16 impacts synapse formation and duration.

4.2. Aims and objectives

Upon activation, NK cells downregulate their activating receptors. The decrease in expression levels normally occurs upon the ligation of the cognate ligand. NKG2D, like many other receptors, undergoes endocytosis and enzymatic degradation (Ogasawara et al., 2003, Cerboni et al., 2009). CD16 on the other hand, undergoes proteolytic cleavage of its extracellular part upon general NK cell activation (Romee et al., 2013, Lajoie et al., 2014, Jing et al., 2015). While NKG2D is recycled in a cell, CD16 is lost. In the previous Chapter, I have shown that loss of CD16 decreases the potential for NK cells to kill target cells sequentially. Here, we set to investigate the impact CD16 shedding on the immune synapse formation and its stability.

To study synapse formation and its character, we used live cell imaging of primary NK cells interacting with surfaces, coated with activating ligands. To investigate NK cell interactions with target cells, we performed live imaging. To keep the cells within the field of view throughout the acquisition, cells were imaged in microwells. The specific role of CD16 shedding on NK cell synapse was addressed using TAPI-0 (ADAM17 inhibitor) and an NK92 cells line transfected with a WT (cleavable) and mutant (non-cleavable) version of CD16.

The Specific aims of this chapter were:

i. To compare the formation of the NK cell immune synapse on rituximab and MICA- coated surfaces;
ii. To investigate the motility of NK cells on rituximab and MICA- coated surfaces;
iii. To address the role of CD16 shedding in NK cell motility on rituximab-coated surfaces;
iv. To study how the shedding of CD16 affects the single-cell interactions between NK cells and rituximab-opsonized targets.

4.3. Results

4.3.1. NK cells do not form actin rings on rituximab-coated surface

When NK cells establish an activating synapse, their F-actin accumulates in a dense ring on the edge of the interface. This is considered as one of the hallmarks of NK cell activation (Culley et al., 2009, Orange, 2008, Lagrue et al., 2013, Lagrue et al., 2015). Thus, we first assessed the formation of such actin rings upon the ligation of CD16 or NKG2D.

NK cells were incubated on surfaces coated with rituximab, MICA or ICAM1. Cells were left to spread for 5 min and then fixed and stained with phalloidin. Consistent with previous work (Culley et al., 2009), confocal microscopy revealed that activation of cells by MICA, triggered accumulation of F-actin in dense rings at the periphery of the synapse in 58 ± 11 % of cells. On ICAM1, the assembly of F-actin ring was rare (observed in 13 ± 3 %). Surprisingly, activation through rituximab also did not trigger significant F-actin accumulation in rings, with only 25 ± 6 % of cells displaying such phenotype (Figure 1A, 1B). Similar to ICAM1, cells on rituximab formed more migratory-like shape with asymmetric actin accumulation in the leading edge of the cell (31 ± 12 % and 34 ± 6 % respectively) (Figure 1A, 1C). On MICA, only 9 ± 6 % cells displayed a migratory phenotype (after 5 min of incubation).

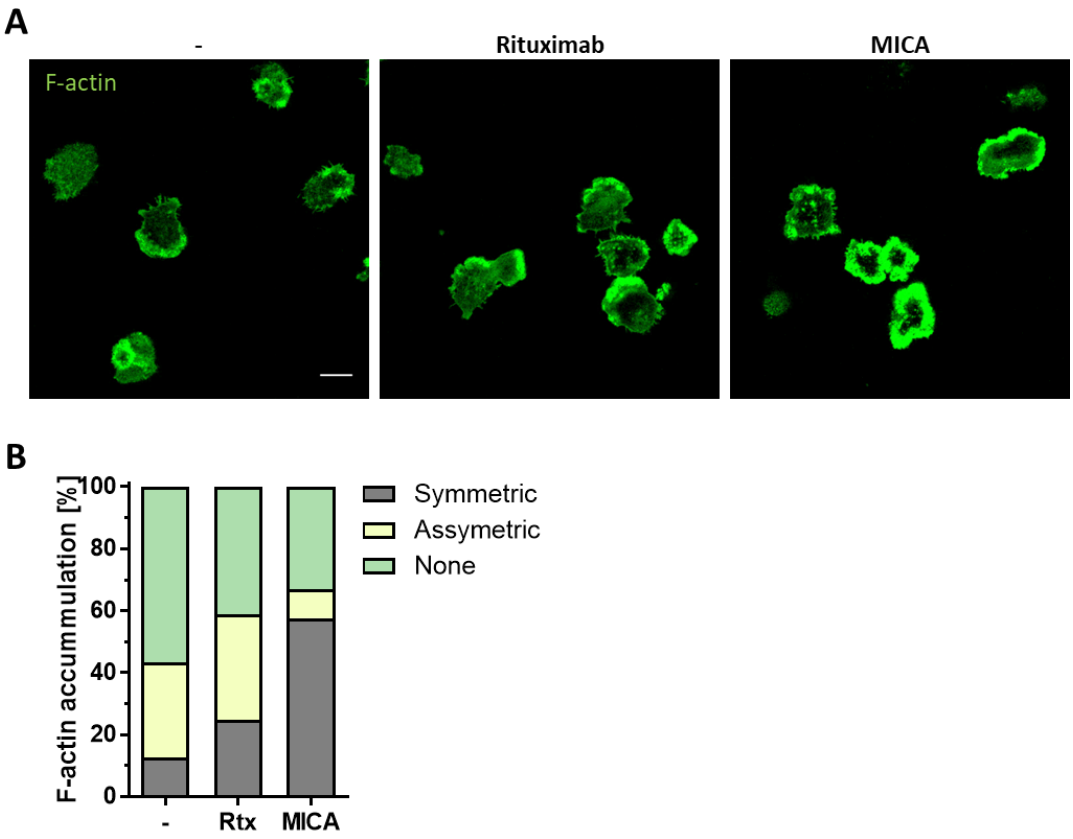

Figure 4.1: F-actin accumulation. Cells were incubated for 5 min on slides coated with rituximab or MICA, both with ICAM1 or ICAM1 alone. Then they were fixed and F-actin was stained with AF488 phalloidin. **(A)** Representative confocal images of F-actin. The scale bar is 10 µm. **(B)** Cells were stratified according to their F-actin distribution; in some cells F-actin accumulated in symmetrical rings (grey), in some it accumulated asymmetrically at the leading edge (yellow) and in some cells, it was evenly distributed across the interface (green).

To address whether the dynamics of formation of actin rings varies according to the way in which cells were activated, cells were assessed at different times. NK cells were let to spread on rituximab-coated surface for 5, 10 or 30 min and then cells were fixed and stained for F-actin. The most actin rings were detected upon 5 min stimulation (18 ± 7 %). By 10 min the percentage of actin rings decreased (6 ± 1 %) and stayed low by 30 min (4 ± 2 %). On the other hand, the percentage of cells with migratory shaped didn't change over time (30 ± 3, 36 ± 21, 33 ± 15 % respectively).

These data indicate that the shape of the immune synapse depends on the activating signal. While cells on MICA form dense F-actin rings 5 min upon landing on the surface, cells on rituximab rapidly form a migratory shape which they maintain throughout 30 min upon interacting with the surface.

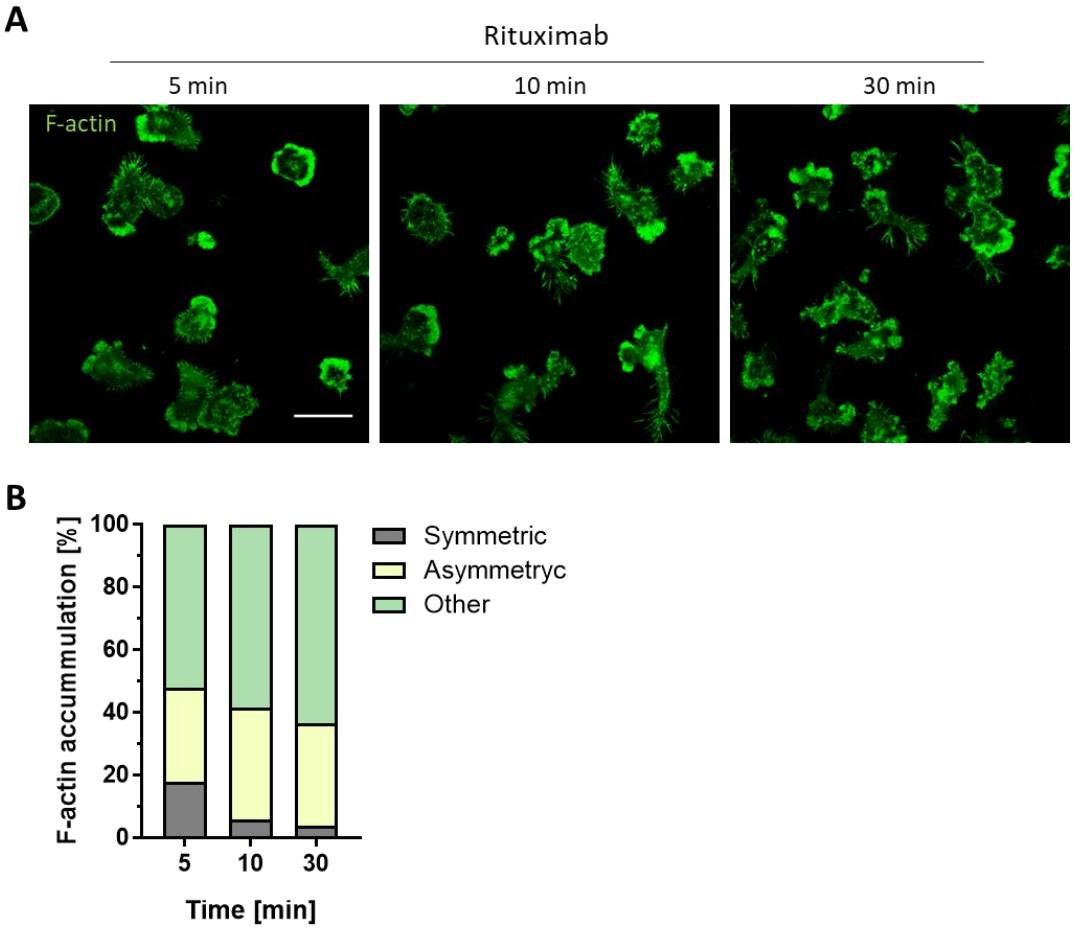

Figure 4.2: Time course of F-actin accumulation on rituximab. Cells were incubated on rituximab with iCAM1 for 5, 10 or 30 min. Then cells were fixed and F-actin was stained with AF488 phalloidin. **(A)** Representative confocal images of F-actin. The scale bar is 10 µm. **(B)** Cells were stratified according to their F-actin distribution; in some cells F-actin accumulated in symmetrical rings (in grey), in some it accumulated asymmetrically in the leading edge (in yellow) and in some cells, it was evenly distributed across the interface (in green).

4.3.2. Cells spread differently on rituximab-coated surface than on MICA-coated surface

To further address the formation of the immune synapse on coated surfaces, we performed time-lapse internal reflection microscopy (IRM). IRM is a label-free technique allowing the visualisation of dynamic contacts made by cells interacting with a coverslip (Bunnell et al., 2001, Ashdown et al., 2017). Technique is based on the observation that cells in tight contact with a glass coverslip disrupt the coherent reflection of light, which allows the visualisation of attachments as regions of low or zero intensity (Verschueren, 1985). Cells were imaged live, while landing on coated slides and establishing an activating synapse. Their interactions with the surfaces were recorded for up to 30 min, with an image acquired every second. Acquisition time for some cells was shorter, because they moved out of the field of view. The main changes occurred in the first few minutes, therefore only first 6 min of acquisition are represented in the figure below.

On rituximab, NK cells spread more than on MICA (Figure 4.3 A, B). On rituximab, the maximal area of the interface was reached around 1 min upon landing (232 ± 65 μm^2). At around 2 min after landing, the contact area started to decline 2. These cells often had long and very thin tails, which were excluded from the analysis, as the software failed to apply the correct threshold to them. This has likely contributed to the surface area decline over time. Surface area of cells on MICA reached a plateau at around 1 min (133 ± 71 μm^2). After this, their area slowly increased up to 5 min, when they reached their maximal spread (154 ± 100 μm^2).

Cells that landed on MICA-coated surface formed a round synapse and stayed symmetrical throughout the acquisition. Cells on rituximab first started rounding up, but then they quickly developed an asymmetrical migratory shape. After 1.8 min, their shape started to become less and less round (Figure 4.3 A, C).

Importantly, cells interacting with MICA were very static and didn't move much from the original point of landing, while cells on rituximab did (Figure 4.3 A). This indicates that the synapse formed through NKG2D is not only more symmetrical, but also much more stable than the CD16-synapse.

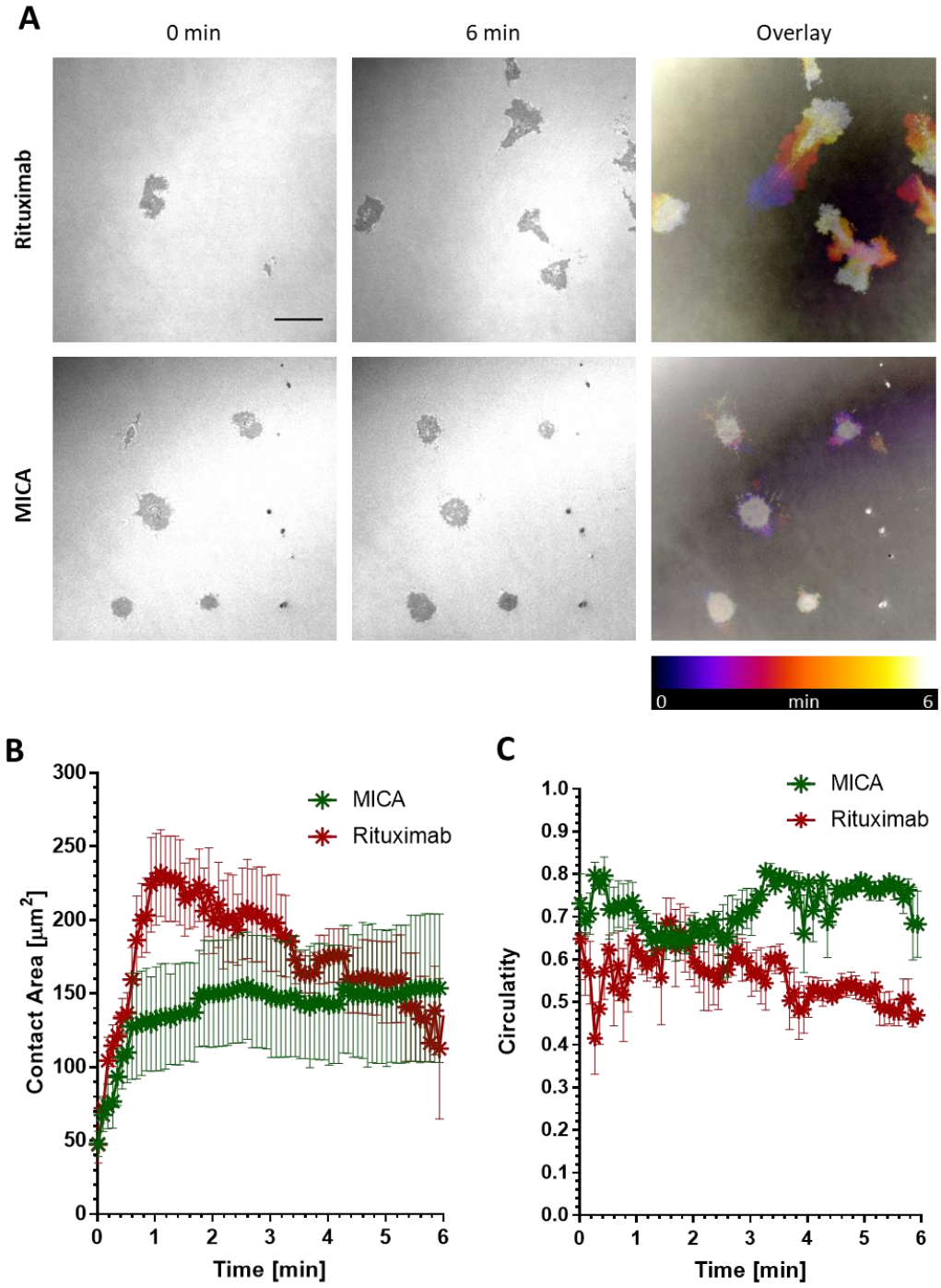

Figure 4.3: Live imaging of the immunological synapse formation on rituximab and MICA. Cells were imaged live while landing on slides and forming a synapse with activating surfaces (rituximab or MICA, both with ICAM1). Image was acquired every 1 sec for up to 30 min. For the purpose of clarity, only first 6 min are shown. **(A)** Representative IRM images of the cell interface at time 0 and 6 min. In last column, the overlay of all 360 frames is shown. As indicated in the legend below, blue indicates the position where cells landed first and white shows the position in the last frame. The scale bar is 20 µm. **(B)** Contact area was measured using ImageJ. **(C)** Circularity of cells was assessed using ImageJ. Values approaching value 1 indicate more circular shape, while 0 indicates elongated shape.

4.3.3. NK cells are more motile on rituximab-coated surface than on MICA-coated surface

Upon CD16 engagement with rituximab, the receptor is cleaved from cell surface by ADAM17. To study whether such shedding of the receptor contributes to NK cell motility on rituximab-coated surfaces, TAPI-0, a non-specific ADAM17 inhibitor was used. Besides ADAM17, TAPI-0 also inhibits collagenase and gelatinase.

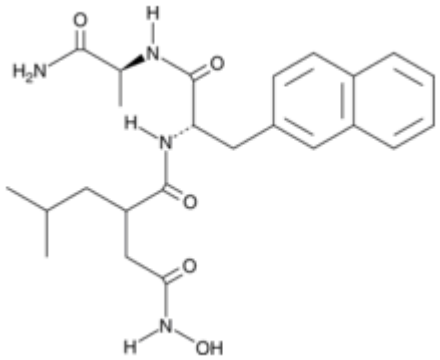

Figure 4.4 Molecular structure of TAPI-0. (www.ADOOQ.com, 2017)

The concentration of TAPI-0 required to stop the cleavage of CD16 was determined by titration (0.2, 0.5, 1.0, 1.5 µM). CD16 levels upon NK cell activation were assessed by flow cytometry. After 1h activation on rituximab or MICA coated surfaces, NK cells were removed and stained with anti-CD16 antibody. Both ligands induced downregulation of CD16 (rituximab and MICA reduced expression of CD16 to 67 ± 8 % or 43 ± 2 % of its level on unstimulated cells respectively). Already 0.2 µM of TAPI-0 abrogated this loss of CD16, maintaining its expression at 85 ± 16 % on rituximab and 73 ± 28 % on MICA. The plateau of inhibition of CD16 shedding was reached at 1.0 µM, where CD16 was on average reduced only to 93 ± 14 % on rituximab and 84 ± 25 % on MICA (Figure 4.5).

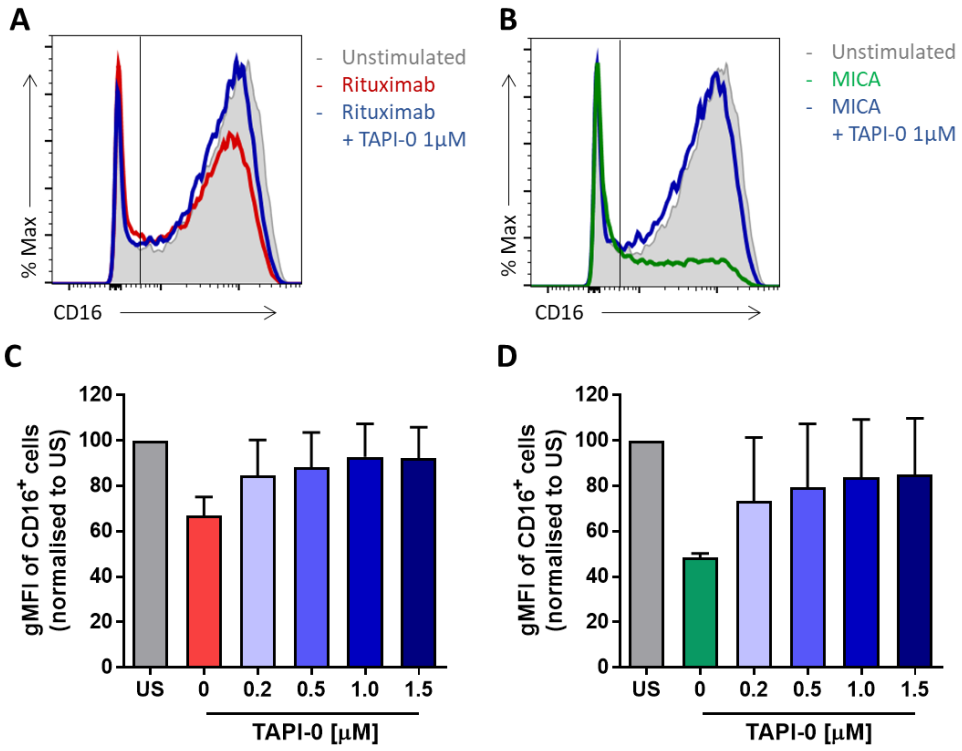

Figure 4.5: TAPI-0 titration. NK cells were incubated on rituximab or MICA coated surfaces in the presence of increasing concentrations of TAPI-0 (as indicated). Unstimulated cells were used as a control. After 1h, cells were removed, and CD16 was stained with anti-CD16 AF647 mAb. Levels of CD16 were assessed by flow cytometry. **(A)** Representative histograms. Unstimulated cells are plotted in shaded grey, cells activated on rituximab in red, cells activated on MICA in green and cells treated with TAPI-0 on either condition in blue. Vertical line represents the gate for $CD16^+$ cells. **(B, C)** gMFI of $CD16^+$ cells normalised to unstimulated cells upon activation on rituximab **(B)** or MICA **(C)**. Data is pooled from three independent experiments (n = 3) and presented as mean ± SD. US: unstimulated.

While 1.0 µM of TAPI-0 significantly inhibited shedding of CD16 (Figure 4.6A), it had no effect on NKG2D expression (Figure 4.6B) or NK cell viability (Figure 4.6C), as assessed by flow cytometry.

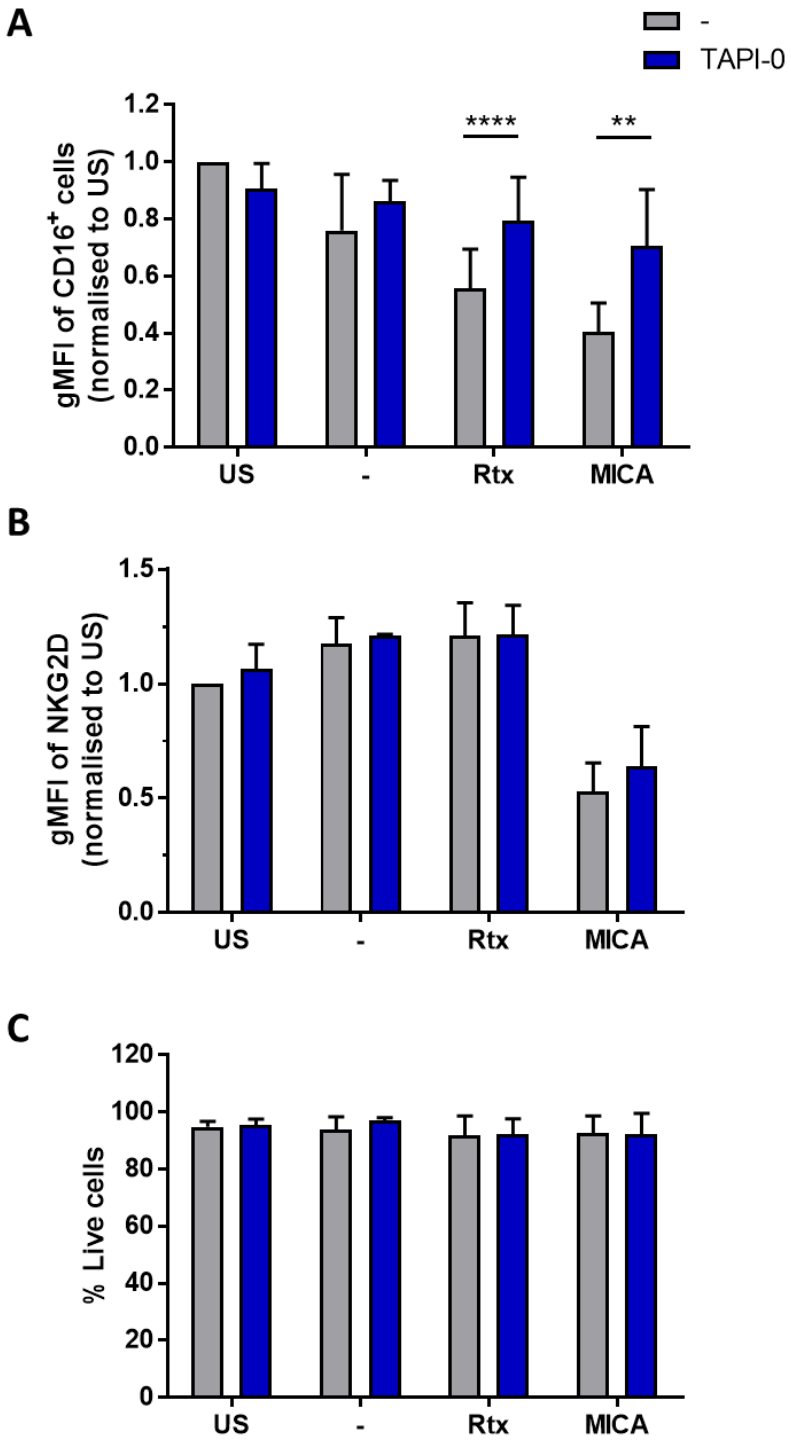

Figure 4.6: TAPI-0 does not affect NKG2D or cell viability. NK cells were incubated on surfaces coated with ICAM1 alone (-) or rituximab or MICA, both with ICAM1 in the presence of 1.0 µM TAPI-0 (as indicated). Unstimulated cells were used as a control. After 1h, cells were removed and stained for flow cytometry. **(A)** CD16 was labelled with anti-CD16 AF647 mAb. gMFI of $CD16^+$ cells was normalised to unstimulated cells. **p<0.01 and ***p<0.0001 were calculated by student t-test. **(B)** NKG2D was stained with anti-NKG2D PE mAb. gMFI of NKG2D was normalised to unstimulated cells. **(C)** Cell viability was assessed using dead cell marker. Cell debris was gated out prior the assessment. Data is pooled from seven independent experiments (n = 7), except for ICAM1, where only two donors were assessed (n = 2), and presented as mean ± SD. US: unstimulated, Rtx: rituximab

To investigate the motility of NK cells on different activating surfaces further, time-lapse imaging of NK cells on rituximab, MICA or ICAM1 coated surfaces was performed for 45 min, with an image acquired every 30 seconds. As not all cells adhere and interact with a surface, IRM images were acquired to ensure that only cells interacting with surfaces were counted, alongside bright-field images. Live cells were identified by calcein staining that leaks out of dead cells. For the analysis, IRM, bright-field and fluorescence image were merged together and each cell was tracked manually.

Quantitative analysis revealed that cells were significantly more motile on ICAM1 and rituximab-coated surface than cells on MICA, as seen from plotted tracks (Figure 4.7A). When comparing the motility of cells from one donor, with comparable degranulation on both, rituximab and MICA (data not shown), cells moved the most on ICAM1, with the average speed 0.081 ± 0.038 μm/s. On rituximab cells slowed down a bit, reaching 0.058 ± 0.033 μm/s and on MICA their movement was significantly reduced (0.030 ± 0.028 μm/s) (Figure 4.7B). The motility of cells from one donor on ICAM1 or rituximab varied a lot, but on MICA there were no fast-moving cells. The average speed of cells on ICAM1 from multiple donors was slightly, but not significantly faster than on rituximab (0.074 ± 0.029 μm/s and 0.065 ± 0.021 μm/s respectively). On MICA, cells were more static, with the average speed 0.023 ± 0.007 μm/s (Figure 4.7C). This indicates that the interactions with coated surfaces through NKG2D are more static and perhaps stronger than interactions established through CD16.

To establish the role of CD16 shedding on NK cell motility on rituximab-coated surfaces TAPI-0 was added to cells at the concentration that was shown to inhibit CD16 shedding with no effect on NKG2D or NK cell viability (Figure 4.6). The addition of TAPI-0 led to significant decrease in cell dynamics on rituximab, but did not affect cells on ICAM1 or MICA (Figure 4.7). The average speed of cells from one donor on rituximab decreased to 0.033 ± 0.022 μm/s. The average speed of cells from multiple donors was reduced by 44 % to 0.036 ± 0.017 μm/s. Cells on ICAM1 or MICA were not affected by the drug. These data suggest that ADAM17-induced cleavage of CD16 enhances the motility of NK cells on rituximab coated surface.

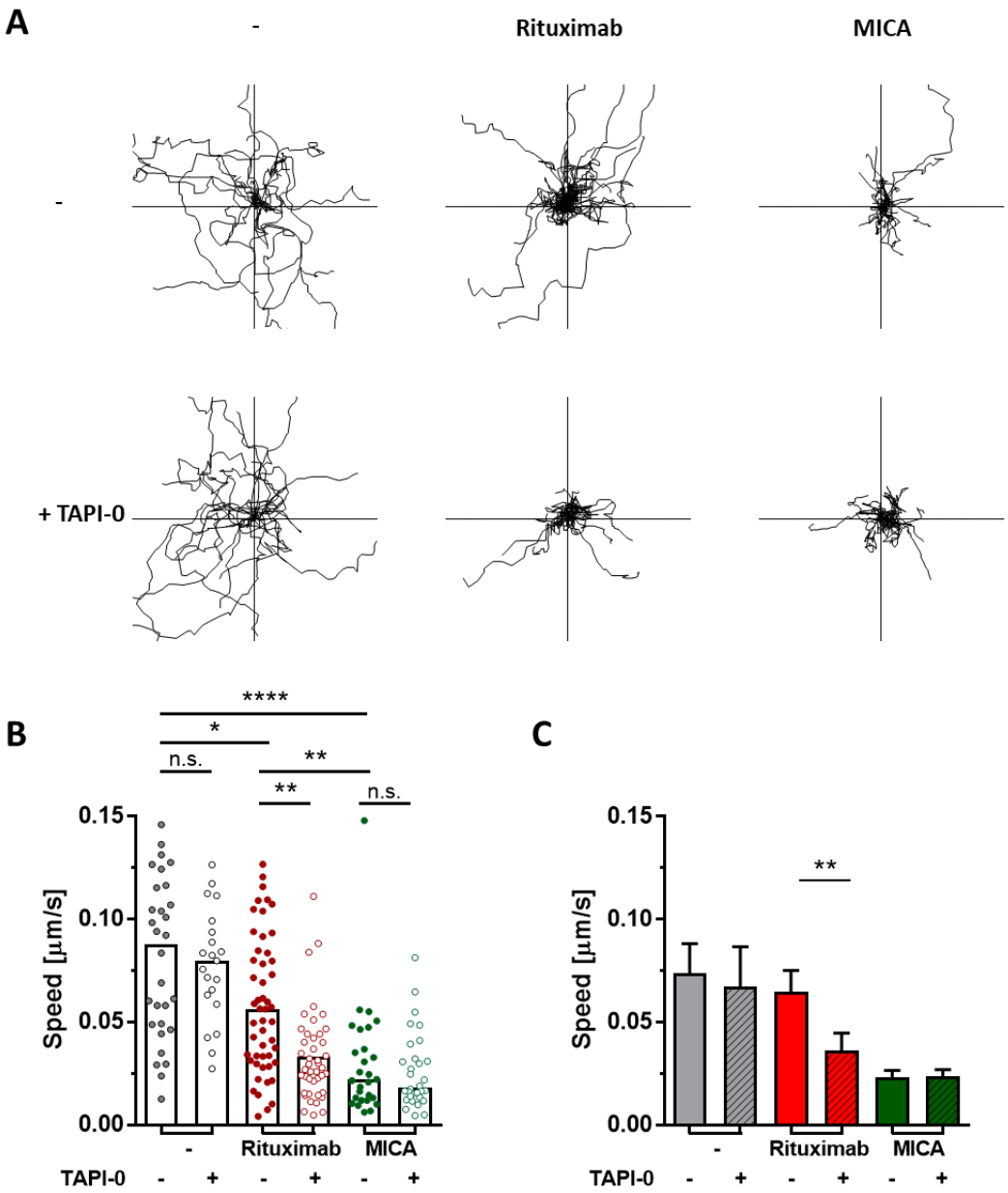

Figure 4.7: NK cell motility on coated surfaces. NK cells were labelled with calcein dye and incubated on surfaces coated with ICAM1 (-), rituximab or MICA, both with ICAM1, with or without 1.0 µM TAPI-0 (as indicated). Bright-field, IRM and fluorescence images were acquired for 45 min in 30 sec intervals. Cells were tracked manually using Cell Tracker, a Mat Lab based program (Piccinini et al., 2015). Cell movements were quantitatively assessed. **(A)** Tracks of 20 individual cells from one donor on ICAM1, rituximab or MICA. Axis lengths are +/- 300 µm. **(B)** Speed of NK cells from one donor. Each dot represents an average speed of an individual cell. Bars represent a mean value. *p<0.05, **p<0.01, ***p<0.001, ****p<0.0001 calculated by one-way ANOVA. **(C)** Mean NK cell speed from four different donors (n = 4) for ICAM1 and MICA, and five for rituximab. Plotted as mean ± SEM. **p<0.01 calculated by student t-test.

To address whether the concentration of activating ligands affect NK cell motility, NK cells were placed on two different concentrations of activating ligands, 1 µg/ml and 10 µg/ml of rituximab or 0.25 µg/ml and 2.50 µg/ml MICA. The concentration of rituximab did not significantly affect cell motility (Figure 4.8). Average NK cells speed on 1 µg/ml was 0.062 ± 0.016 µg/ml and on 10 µg/ml it was 0.064 ± 0.021 µg/ml. However, the degranulation was increased on the higher concentration of the ligand.

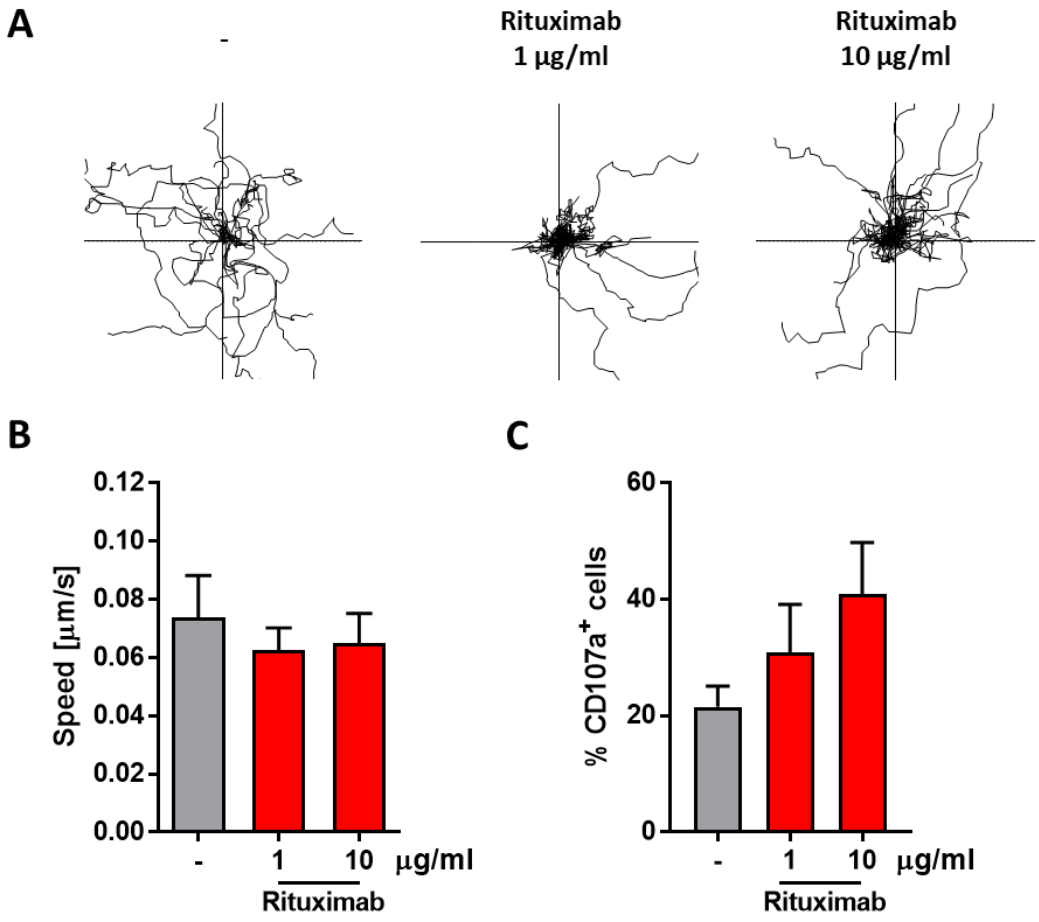

Figure 4.8: Effect of rituximab concentration on NK cell motility. NK cells were labelled with calcein and put on ICAM1 alone (-) or rituximab (1 or 10 µg/ml) with ICAM1. Bright-field, IRM and fluorescence images were acquired for 45 min in 30 sec intervals. All images were merged and cells were manually tracked using Cell Tracker, a Mat Lab based program (Piccinini et al., 2015). Cell movement was quantitatively assessed. **(A)** Tracks of 20 individual cells from one donor on ICAM1 or rituximab (1 or 10 µg/ml). Axis lengths are +/- 300 µm. Tracks for cells incubated on slides coated with ICAM1 and 10 µg/ml rituximab with ICAM1 (first and last panel in (A)) are replotted from Figure 4.7. **(B)** Mean NK cell speed from four different donors (n = 4) on ICAM1 and rituximab (1 or 10 µg/ml). Plotted as mean ± SEM. **(C)** Flow cytometry analysis of NK cell degranulation based on degranulation marker CD107a. NK cells were stimulated activating surfaces for 4h. Then, cells were removed and stained with anti-CD107a AF647 mAb and anti-CD56 BV421 mAb. Live, single, CD56+ cells were gated and % of CD107a+ was assessed. Data pooled from six independent experiments (n = 6, mean ± SD).

The impact of MICA concentration on NK cell motility was more pronounced. Increasing concentration of the ligand led to reduced NK cell movements on the surface. The average speed on 0.25 µg/ml MICA was 0.047 ± 0.020 µm/s but on 2.50 µg/ml cells slowed down by 51% (average speed was 0.023 ± 0.007 µm/s) (Figure 4.9). The concentration of MICA also significantly affected the degranulation response.

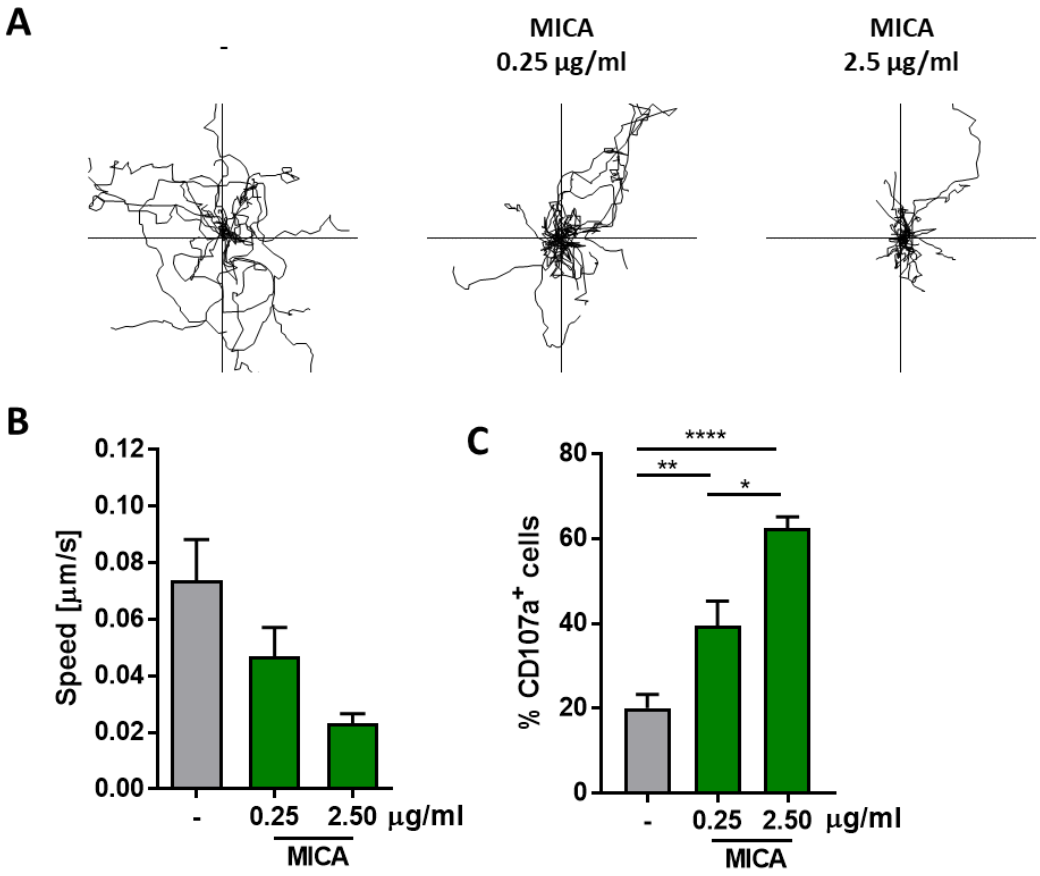

Figure 4.9: Effect of MICA concentration on NK cell motility. NK cells were labelled with calcein dye and put on ICAM1 (-) or MICA (0.25 or 2.50 µg/ml) with ICAM1. Bright-field, IRM and fluorescence images were acquired for 45 min in 30 sec intervals. All images were merged and cells were manually tracked using Cell Tracker, a Mat Lab based program (Piccinini et al., 2015). Cell movements were quantitatively assessed. **(A)** Tracks of 20 individual cells from one donor on ICAM1 or MICA (0.25 or 2.50 µg/ml). Axis lengths are +/- 300 µm. Tracks for ICAM1 and 2.50 µg/ml MICA with ICAM1 (first and last panel in (A)) are replotted from Figure 4.7. **(B)** Mean NK cell speed from four different donors (n = 4) on ICAM1 and MICA (0.25 or 2.50 µg/ml). Plotted as mean ± SEM. **(C)** Flow cytometry analysis of NK cell degranulation based on degranulation marker CD107a. NK cells were stimulated activating surfaces for 4h. Then, cells were removed and stained with anti-CD107a AF647 mAb and anti-CD56 BV421 mAb. Live, single, CD56+ cells were gated and % of CD107a+ was assessed. Data pooled from six independent experiments (n = 6, mean ± SD).

Lower concentrations of both ligands correlate with lower functional responses, such as lower degree of degranulation. This indicates that for full responses triggered by MICA, cells have to make a stable static synapse with the surface. Increased MICA concentration increases the likelihood of this. On the other hand, lower concentration of rituximab does not affect NK motility but it does result in lower functional responses. Thus, it seems that the stability of the synapse does not affect the CD16-induced responses to the same extent.

4.3.4. Inhibition of CD16 shedding does not affect NK cell cytotoxicity, but it does increase the production of IFN-γ on rituximab coated slides

Inhibition of ADAM17 with TAPI-0 results in reduced CD16 shedding from NK cell surface upon their activation. To address whether the maintained higher levels of CD16 lead to altered functional outcomes degranulation and IFN-γ secretion were measured.

Cells were stimulated on slides coated with ICAM1, rituximab or MICA, in the presence or absence of TAPI-0 and the extent of degranulating cells was measured by CD107a expression. CD107a is a marker, expressed on lytic granules and is presented on cell membrane upon lytic granule fusion (Kannan et al., 1996). To prevent its internalisation, protein transport inhibitors brefeldin A and monensin (Betts et al., 2003) were added to detect total level of degranulation throughout the whole duration of the assay. After 4h, cells were removed and stained for surface CD107a. From acquired flow cytometry plots, live, single and $CD56^+$ cells were gated. $CD107a^+$ gate was defined based on unstimulated cells. In addition, IFN-γ secretion was assessed by ELISA for NK cells incubated on coated surfaces for 18 hours.

The addition of TAPI-0 did not have any effect on the extent of degranulation. On ICAM1 20 ± 8 % of NK cells degranulated, on rituximab 36 ± 22 % and 63 ± 6 % on MICA. When TAPI-0 was added 17 ± 9 % degranulated on ICAM1, 32 ± 17 % on rituximab and 63 ± 10 % on MICA (Figure 4.10A). On the opposite, IFN-γ secretion triggered by rituximab was increased when CD16 shedding was inhibited (from 1580 ± 1130 pg/ml to 3480 ± 2720 pg/ml with TAPI-0). The drug did not affect cells on ICAM1 or MICA (130 ± 90 pg/ml to 170 ± 160 with TAPI-0 on ICAM1 and 620 ± 240 pg/ml to 720 ± 190 pg/ml with TAPI-0 on MICA).

TAPI-0 inhibited shedding of CD16 and this led to reduced motility on rituximab-coated surfaces. The drug did not affect the levels of degranulation, but it significantly increased levels of IFN-γ on rituximab. This indicates that the stable synapse is not required for CD16-induced cytotoxicity. However, the prolonged contact with the ligand triggered higher secretion of the cytokine.

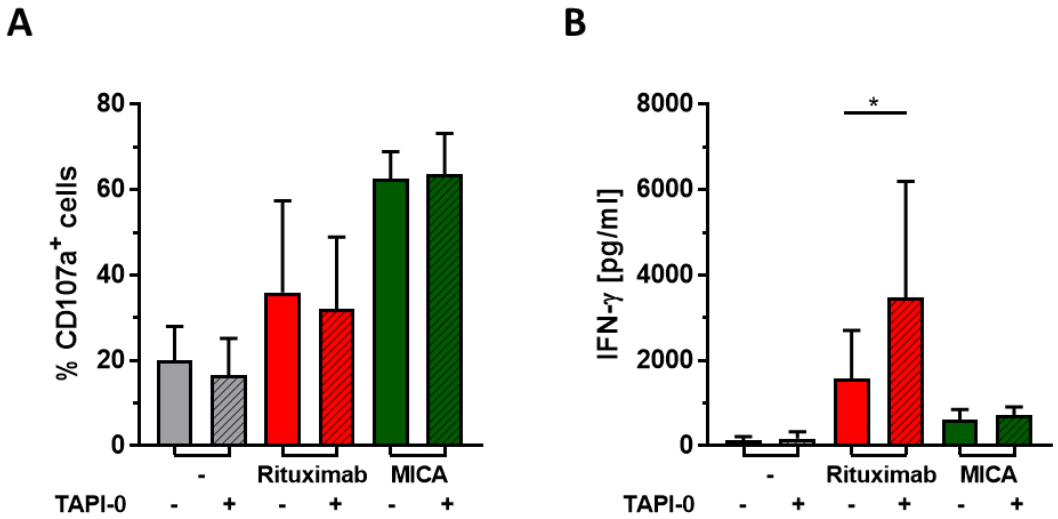

Figure 4.10: TAPI-0 affects IFN-γ secretion on rituximab, but has no effect on NK cell degranulation. (A) Flow cytometry analysis of NK cell degranulation based on degranulation marker CD107a. NK cells were stimulated on glass slides coated with ICAM1, rituximab or MICA. After 4h cells were removed and stained with anti-CD107a AF647 mAb and anti-CD56 BV421 mAb. Live, single, $CD56^+$ cells were gated and % of $CD107a^+$ was assessed. Data pooled from six independent experiments (n = 6, mean ± SD). **(B)** NK cells were incubated in 96-well plate coated with activating ligands, as indicated, for 18h. IFN-γ production was measured from the supernatants by ELISA (n = 5, mean ± SD). *p<0.05 calculated by student t-test.

4.3.5. Donors that do not shed CD16

CD16 shedding upon NK cell activation was a phenomenon observed in the majority of blood donors. However, we identified a few donors whose cells did not cleave CD16 upon their activation. When these cells were incubated for 1h on ICAM1, rituximab or MICA, the levels of CD16 did not change, as assessed by flow cytometry. Interestingly, upon stimulation, there were no $CD16^-$ NK cells, like in normal donors (Figure 4.11A). However, these cells did respond with downregulation of surface NKG2D upon activation on MICA (Figure 4.11B). Cells from such donor also expressed normal levels of ADAM17 (Figure 4.11C). It would be interesting to investigate what the reasons behind such behaviour are. Maybe some genetic mutation of either CD16 or ADAM17 prevents CD16 from cleavage. Or perhaps, different polymorphic variants of CD16 undergo cleavage with different potency. This remains to be addressed.

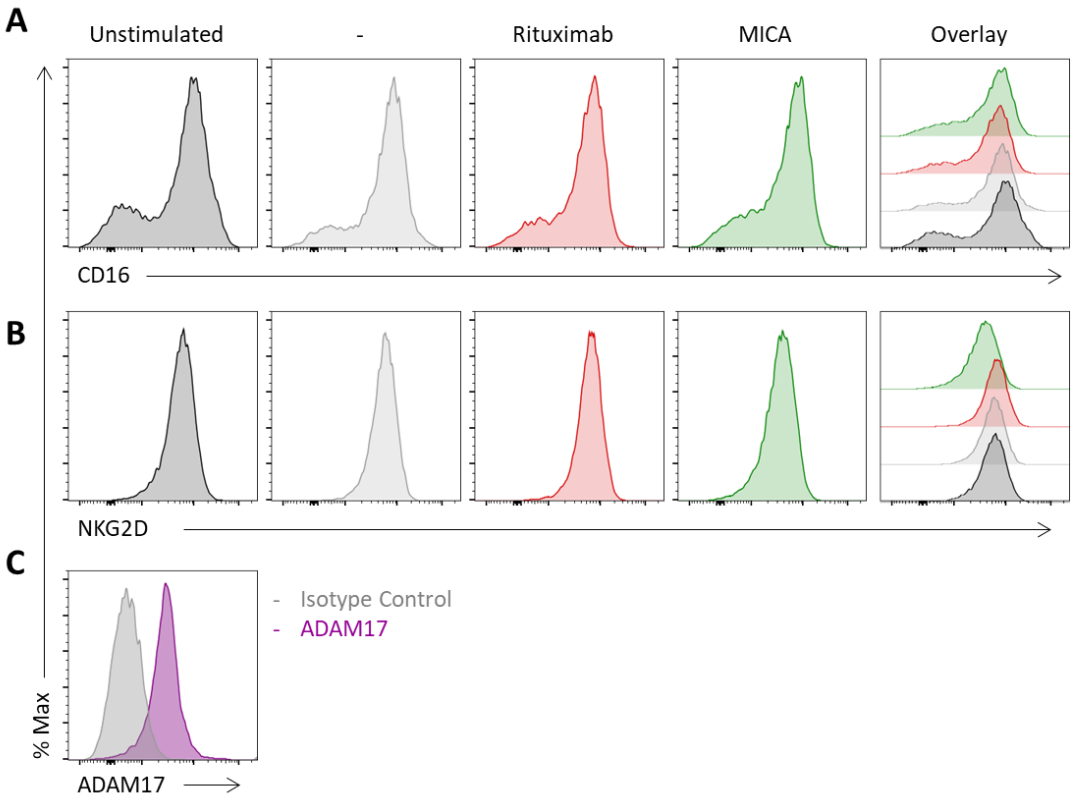

Figure 4.11: Cells that do not cleave CD16 upon NK cell activation. NK cells were stimulated on ICAM1 (grey), rituximab (red) or MICA (green) -coated surfaces. After 1h incubation, cells were removed and levels of surface CD16 and NKG2D were assessed by flow cytometry. **(A)** Histograms of CD16 expression on unstimulated cells or cells collected from activating surfaces and their overlay. **(B)** Histograms of NKG2D expression on unstimulated cells or cells, activated through coated surfaces. **(C)** Histogram of ADAM17 expression in unstimulated cells comparing to the isotype control staining.

We next set to assess whether the lack of CD16 cleavage affects the motility of these cells on coated surfaces. For this, cells were incubated on ICAM1 or rituximab for 45 min, and bright-field, fluorescence and IRM image was acquired every 30 sec. Cells were then manually tracked and their speed was calculated with Cell Tracker software. Cells from a donor that did not shed CD16 were less motile on both, ICAM1 and rituximab coated surfaces (Figure 4.12). Since these cells were significantly less motile also on ICAM1, it is possible that some other mechanism, non-related to CD16 shedding play role.

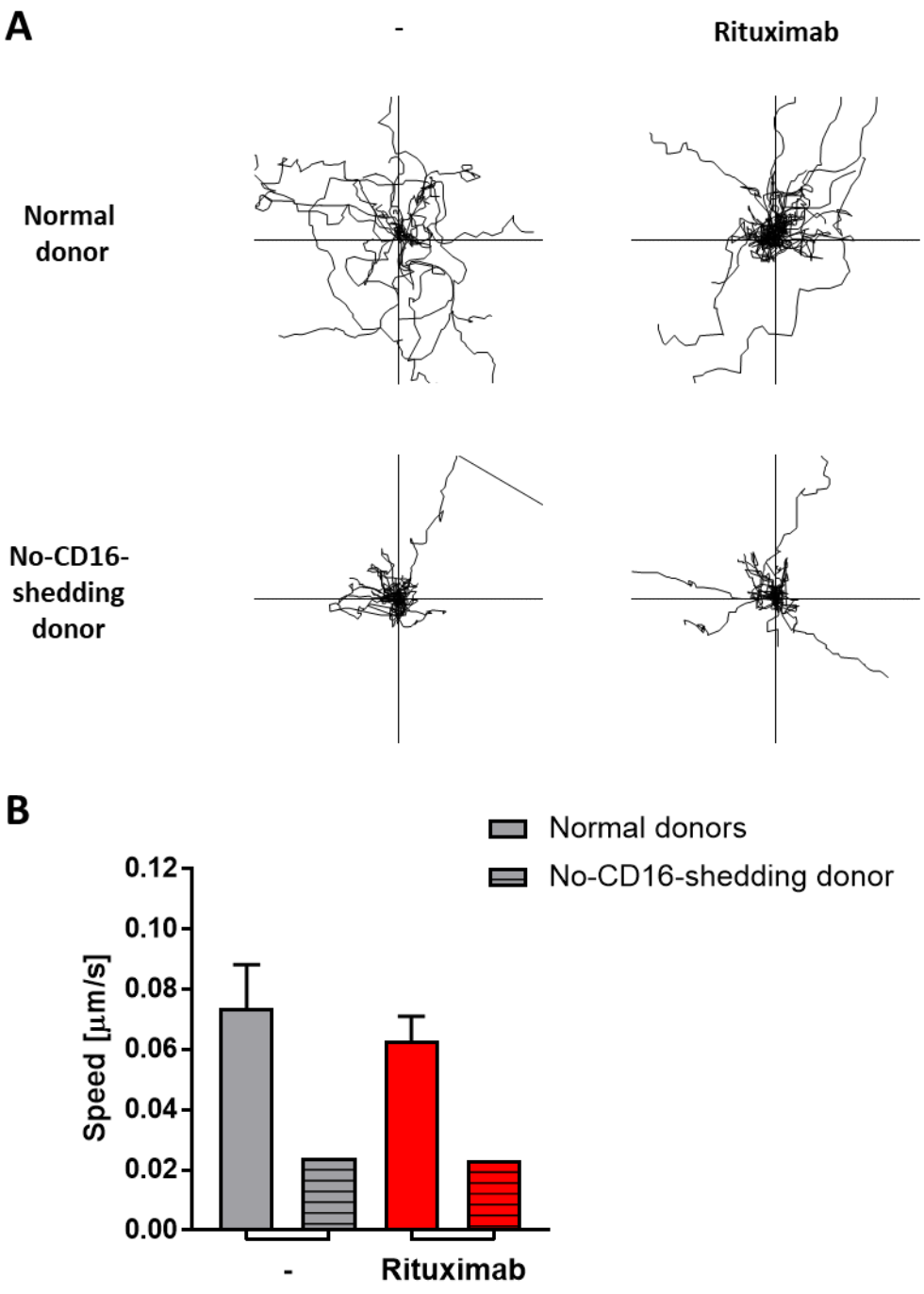

Figure 4.12: Motility of NK cells from donor that did not shed CD16. NK cells were labelled with calcein dye and put on ICAM1 or rituximab with ICAM1-coated surfaces. Bright filed, IRM and fluorescence images were acquired for 45 min in 30 sec intervals. All images were merged and cells were manually tracked using Cell Tracker, a Mat Lab based software (Piccinini et al., 2015). Cell movements were quantitatively assessed. **(A)** Tracks of 20 individual cells from a normal donor and donor that did not shed CD16 on ICAM1 or rituximab. Axis lengths are +/- 300 µm. Tracks from normal donor are replotted from Figure 4.7. **(B)** Mean NK cell speed from four different donors (n = 4) on ICAM1 and rituximab and mean speed of NK cells from a no-CD16-shedding donor. Plotted as mean ± SEM.

4.3.6. ADAM17-induced cleavage promotes NK cells detachment from opsonized targets

To investigate whether the cleavage of CD16 promotes the detachment from opsonized targets, we performed live imaging of NK cells with rituximab-coated Daudi cells. During imaging cells move around freely and can easily disappear from the field of view. This makes manual tracking of interactions between NK cells and their targets over time difficult and the analysis time consuming. To overcome this, we used multi-well micro-chips (Guldevall et al., 2010, Vanherberghen et al., 2013), designed to confine small number of cells (NK cells together with their targets) into separate imaging wells. These chips allowed time-lapse imaging of live cells for several hours which enabled the investigation of the interactions between cells, the cytotoxicity, and serial killing capacity. The distinction between NK cells and target cells was achieved using different fluorescent calcein dyes. Cell lysis was identified as the loss of the calcein staining and by the gain of the dead cell dye resulting in the change of fluorescence. To simulate the physiological environment for the cells, microwells were coated with fibronectin (Khorshidi et al., 2011). TAPI-0 was used to inhibit the shedding of CD16. An image was acquired every 3 min for 8 hours. Then, individual cell-cell interactions were manually quantified.

First, micro-chips containing multiple wells of dimensions 50 x 50 μm^2 were used. One field of view contained 81 such wells (Figure 4.13). NK cells were placed into wells with targets at ratio E:T = 1:3, with 2 – 5 cells per well on average.

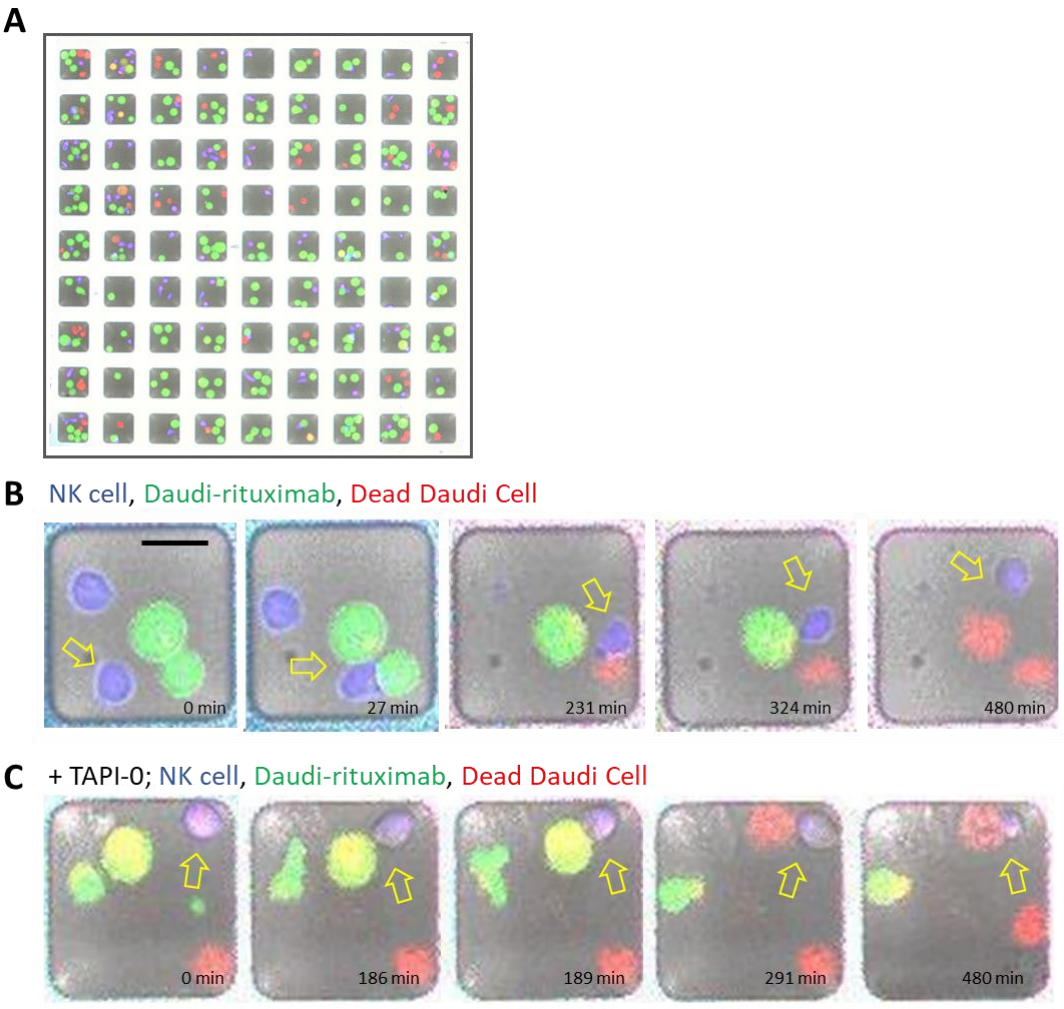

Figure 4.13: Time-lapse imaging in small microwells with NK cells and opsonized Daudi targets. Primary NK cells were incubated with Daudi cells that were opsonized with Rituximab in the presence or absence of TAPI-0. Cells were imaged every 3 min for 8h. **(A)** Representative image of one well in a chip, segregated in 81 smaller wells of dimensions 50 x 50 μm^2. Image shows an overlay of fluorescence and bright-filed images. **(B, C)** Representative time-lapse zoomed-in images of the individual wells, showing an overlay of a fluorescence and bright-field images. In bottom right corner time from the start of acquisition (in minutes) is indicated. The scale bar is 20 µm. **(B)** An NK cell (in blue) migrated to form a conjugate with the target cell (in green) (27 min). After the delivery of a cytolytic hit (231 min), which is seen in decreased green fluorescence intensity and the appearance of a red fluorescence, NK cell slowly detached from the killed target and moved onto a fresh target (324 min). By the 480 min it killed also the second target and resumed free migration. **(C)** ADAM17 inhibitor TAPI-0 was added to cells. Here NK cell established a contact with the target after 186 min. The killing of a target (132 min) did not result in the detachment from the target cell (480 min).

In this set-up, NK cells killed on average 59 ± 21 % of targets they encountered over 8h (Figure 4.14). The addition of TAPI-0 did not affect this outcome (54 ± 3 %). After establishing a contact with a target, the NK cell needed on average 56 ± 91 min to kill. There was a pronounced variability in how long individual NK cells took to kill a target. Some targets were killed in less than three minutes, while others were killed in several hours. When TAPI-0 was added, the killing took significantly longer (128 ± 119 min).

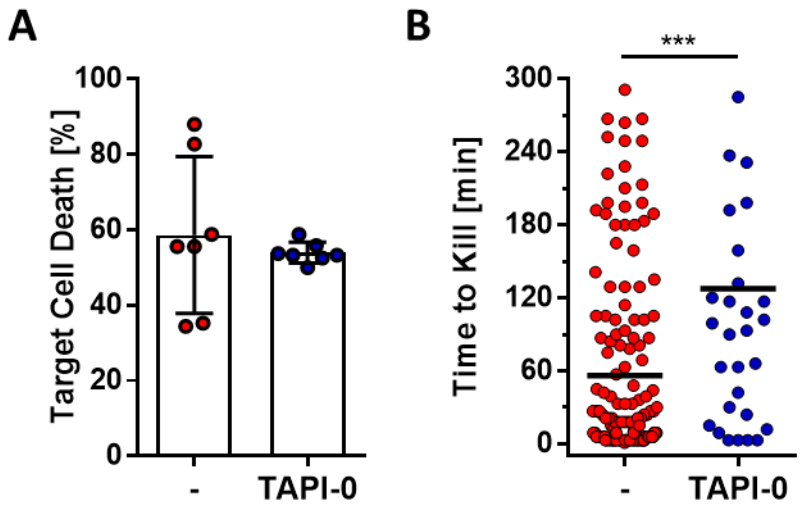

Figure 4.14: Killing of opsonized Daudi-rituximab cells in small microwells. Primary NK cells were incubated with Daudi cells that were opsonized with rituximab in the presence or absence of TAPI-0. **(A)** Percentage of all NK cell-target cell interactions that resulted in target cell lysis. Each dot represents the percentage of cells from one field-of view. **(B)** Time an NK cell needed to kill a target. Each dot represents an individual cytolytic NK cell – target cell interaction. Data are pooled from three independent experiments (n>150) and plotted as mean ±SD. ***p<0.001 calculated by student t-test.

After killing a target, 59 ± 30 % NK cell detached (Figure 4.15). NK cells stayed in contact with the target for 220 ± 170 min. When TAPI-0 was added, the detachment was significantly impaired, with only 21 ± 16 % NK cells coming apart. Also, the contact time was extended 1.9-times, to 418 ± 106 min. However, this is an underestimation, because after 8h of acquisition, many cells were still in contact. For the purpose of comparison, these cells were counted as if they detached in the last frame acquired. In the graph, these cells are plotted in yellow, to distinguish them from the truly detached cells. For cell-cell conjugates that did not lead to target cell lysis, 70 ± 20 % of NK cells detached. This rate too was decreased upon the addition of TAPI-0 (to 35 ± 18 %).

During the acquisition 23 ± 11 % NK cells died. For this, only NK cells that made a contact with the target were counted. The addition of TAPI-0 did not affect this (27 ± 7 %).

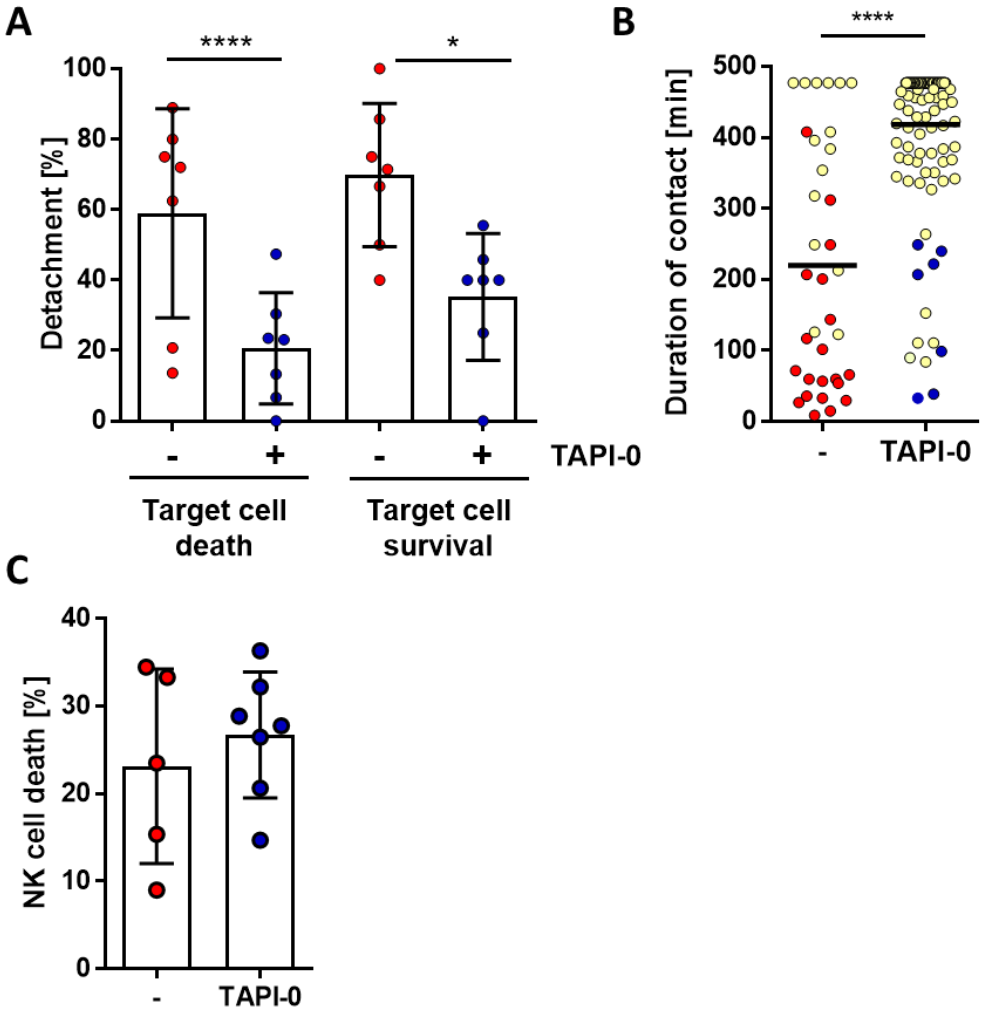

Figure 4.15: The detachment from opsonised Daudi cells is impaired upon the inhibition of CD16 shedding, as imaged in small microwells. Primary NK cells were incubated with Daudi cells that were opsonized with Rituximab in the presence or absence of TAPI-0. **(A)** Graph indicates the percentage of NK cells that detached from the target cell upon target cell lysis or survival. Each dot represents the percentage of cells from one field-of view. *p<0.05, ****p<0.0001 calculated by one-way ANOVA. **(B)** Time of all NK cell-target cell contacts. The contact duration of cells still in conjugates at the end of the acquisition (480 min) was calculated as if cells detached in the last frame and plotted in yellow. Each dot represents an individual contact. ****p<0.0001 calculated by student t-test. **(C)** Percentage of NK cells that underwent apoptosis after the contact with the target. Cells that did not encounter a target were excluded from calculation. Each dot represents the percentage of cells from one field-of view. Data are pooled from three independent experiments (n>150) and plotted as mean ±SD.

However, in these small confined wells the number of target cells per NK cell as well as their free movement was very limited. To avoid forced contact formation we used larger wells allowing more interactions to occur. The dimensions of larger microwells were 450 x 450 μm^2 (Figure 4.16). Cells were again plated in E:T = 3:1 ratio, and their interactions were acquired for 8h at 3 min interval.

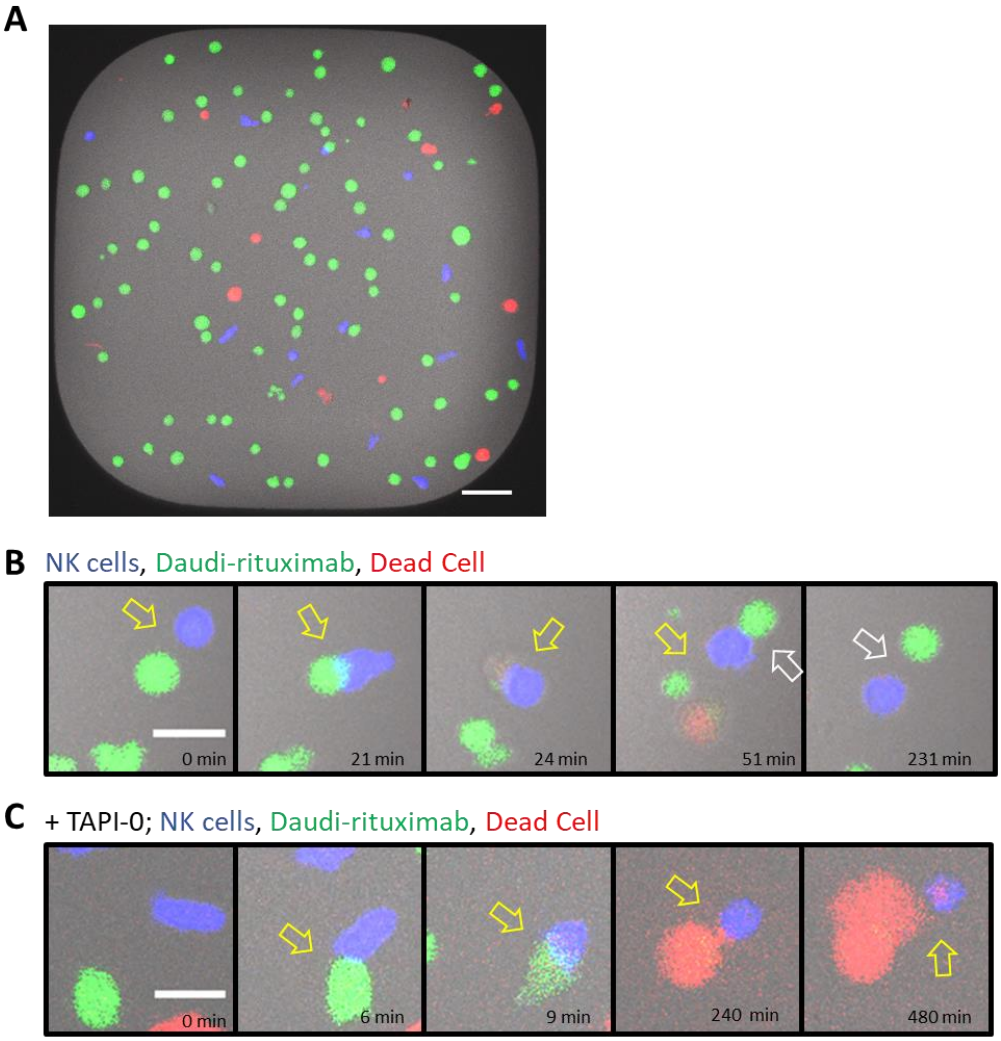

Figure 4.16: Time-lapse imaging in large microwells with NK cells and Daudi-rituximab. Primary NK cells were incubated with Daudi cells, opsonized with rituximab. To inhibit ADAM17, TAPI-0 was added. Cells were imaged every 3 min for 8h. **(A)** Representative image of one well in a chip. The dimensions of the well were 450 x 450 μm^2. The scale bar is 50 µm. Image shows an overlay of fluorescence and bright-filed images. **(B, C)** Representative time-lapse zoomed-in images, showing an overlay of a fluorescence and bright-field images. In the bottom right corner, time from the start of acquisition (in minutes) is indicated. **(B)** An NK cell (in blue) formed a contact with Daudi-rituximab (in green) (21 min, yellow arrow). After cytolytic action (24 min), seen as decreased green fluorescence and the appearance of red fluorescence, NK cell detached from the killed target and moved onto a fresh target (51 min, white arrow). The second target was not killed, and by 231 min NK detached from it. **(C)** TAPI-0 was added to cells. NK cell established a contact with the target after 6 min. After the lysis of the target (9 min), NK cell did not detach (480 min).

In larger wells 48 ± 17 % of interactions led to cytolytic target cell death (Figure 4.17A). The addition of TAPI-0 did not affect this (50 ± 5 %). Killing of targets took 89 ± 91 min on average, and 107 ± 113 min with the drug (Figure 4.17B). Again, cell-to-cell variability was significant. 30 ± 10 % of NK cells did not kill any target that they encountered (35 ± 11 % when TAPI-0 was added). 58 ± 11 % killed one target cell, while in the presence of TAPI-0, 10 % less NK cells killed only one target (48 ± 14 %). 11 ± 9 % NK cells killed two target cells (13 ± 5 % with TAPI-0) and 1 ± 2 % killed more than three targets (4 ± 4 %with TAPI-0) (Figure 4.17C). There were very few cells that were capable of killing more than two cells, probably because of the loss of CD16. The inhibition of shedding did result in slight, but consistent increase of serial killing capacity.

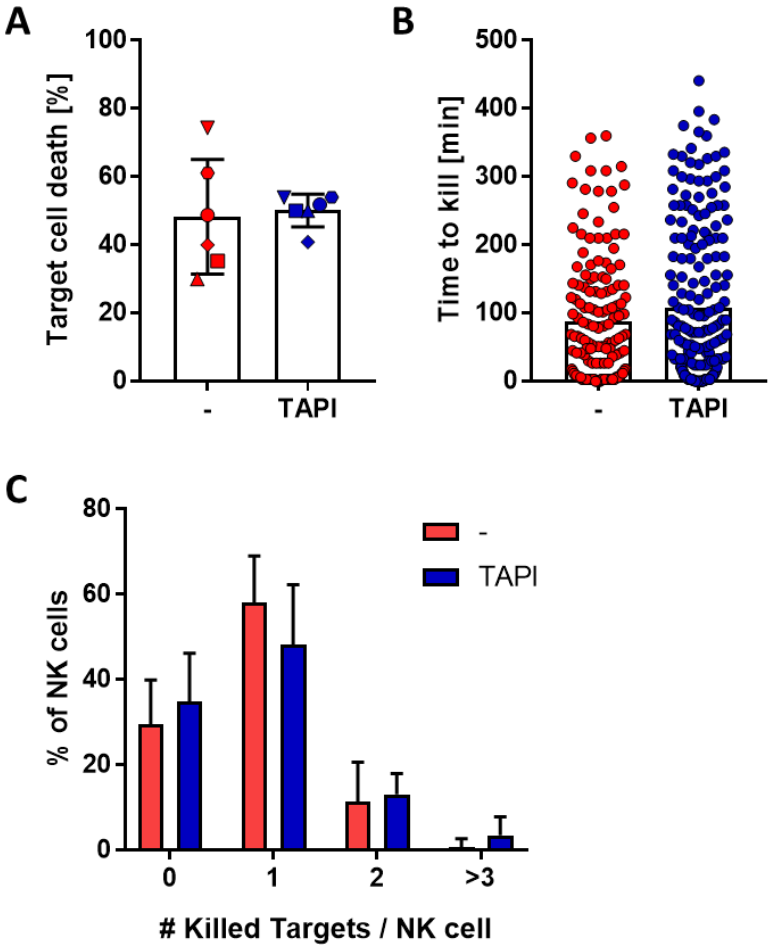

Figure 4.17: Inhibition of CD16 shedding does not affect target cell lysis. NK cells and Daudi-rituximab were placed to microchips at E:T = 3:1 in the presence or absence of TAPI-0. **(A)** Percentage of all NK cell-target cell interactions that resulted in target cell lysis. Each dot represents the percentage of lysed targets from one donor. **(B)** Time required to kill an individual target. Each dot represents an individual cytolytic NK cell – target cell interaction. **(C)** Number of target cells killed by individual NK cell. Data are pooled from six independent experiments and plotted as mean ± SD.

Like in smaller wells, the detachment from targets was significantly impaired (Figure 4.18A). Without TAPI-0, 60 ± 14 % NK cells detached from lysed targets, and 73 ± 19 % from targets that were not killed in the conjugate. When the drug was added, only 20 ± 9 % of NK cells were able to detach from killed Daudi-rituximab, and 40 ± 24 % detached from targets surviving the contact. When the cell-cell interaction resulted in target cell lysis, cell stayed in contact for 226 ± 155 min. The inhibitor of CD16 shedding prolonged this time to 325 ± 147 min. This result is entirely accurate, as many cells maintained the contact by the end of the acquisition. Contact time for these cells was again calculated as if they detached in the very last frame. For the representation, these cells are coloured in yellow (Figure 4.18B). We observed that the detachment was generally enhanced when NK cell encountered a new potential target (data not shown).

Interestingly, the inhibition of ADAM17 did not affect how many target cells were in contact with an individual NK cell (Figure 2K). Within the 8h acquisition 56 ± 13 % of NK cells formed contact with one target, 29 ± 6 % with two and 15 ± 13 % with three or more targets. The addition of TAPI-0 did not change this ratio (55 ± 8, 27 ± 9 and 17 ± 8 % respectively) (Figure 4.18C).

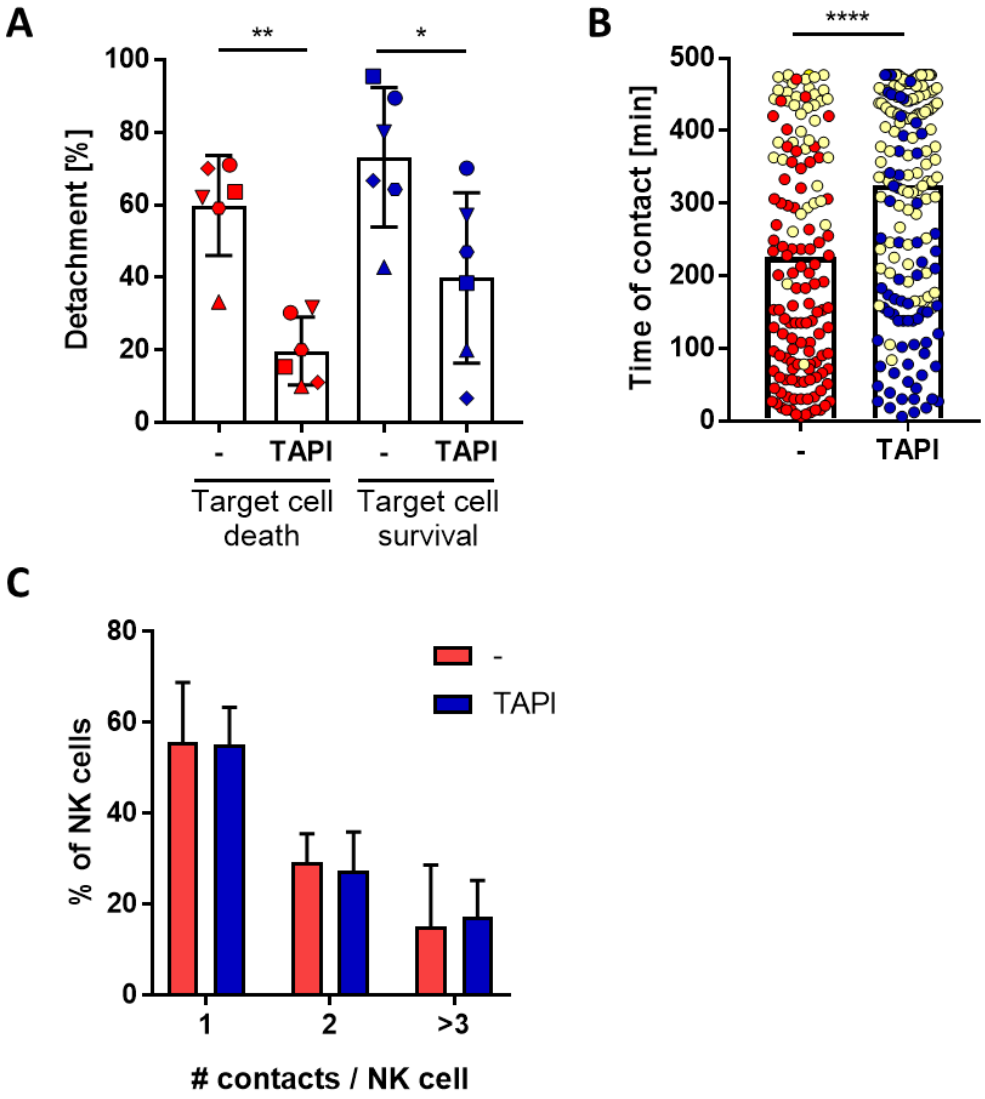

Figure 4.18: NK cell detachment from Daudi-rituximab was impaired when CD16 shedding was inhibited, as imaged in large microwells. NK cells were put into large microwells together with rituximab-opsonized Daudi cells. ADAM17 was inhibited with TAPI-0. **(A)** NK cell – Daudi cell interactions that resulted in the detachment from the conjugate. Each dot represents the percentage of interactions, resulting in a detachment from one donor. Different symbols represent different donors. *p<0.05, **p<0.01 calculated by one-way ANOVA. **(B)** Time that cells stayed in conjugates upon cytolytic contacts. The contact duration of cells in conjugates at the end of the acquisition (480 min) was calculated as if cells detached in the last frame and plotted in yellow. Each dot represents an individual contact, bars represent mean value. ****p<0.0001 calculated by student t-test. **(C)** Number of target cells encountered by individual NK cell. Data are pooled from six independent experiments and plotted as mean ± SD.

Flow cytometry-based data showed that TAPI-0 does not affect NK cell viability (Figure 4.6C). But, live imaging revealed that the addition of TAPI-0 leads to 38 % increase of NK cell death in microwells (Figure 4.19A). While 23 ± 10 % of NK cells died without TAPI-0, the drug increased this to 38 ± 6 %. Only NK cells that encountered a target were considered. However, there was not much death in NK cells, not forming a contact. In both conditions, the majority of all NK cell deaths happened when NK cells failed to detach from their target (72 ± 27 % and 87 ± 11% upon the inhibition of ADAM17) (Figure 4.19B). Thus, the detachment seems to be an important factor in the survival of NK cells upon their cytolytic activities. These data suggest that shedding of surface receptors might be not only an important mechanism for the detachment from targets, but might also be crucial for their survival and consequently their serial killing capacity.

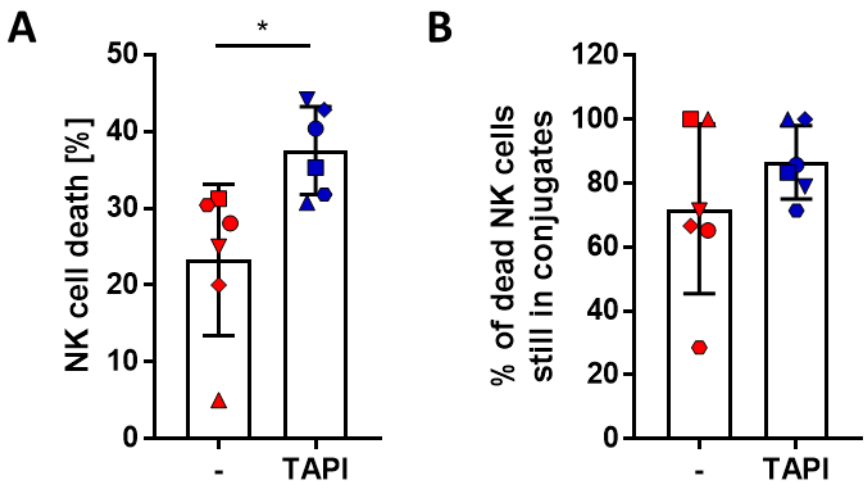

Figure 4.19: NK cell death upon the conjugate formation. NK cells were incubated with Daudi-rituximab in large microwells with or without TAPI-0. Time-lapse imaging was performed for 8h. **(A)** NK cells that died after contacting the target. Cells that did not encounter a target were excluded from calculation. **(B)** From all NK cells that underwent apoptosis, the percentage of those that failed to detach was calculated. Each point represents the percentage of cells from one donor, symbols indicate different donors. Data are pooled from six independent experiments and plotted as mean ± SD.

4.3.7. Analysis of CD16^{+} NK92 cell line

So far, this chapter shows that ADAM17 activity promotes the detachment of NK cells from rituximab-opsonized target cells and the motility of NK cells on rituximab coated surface. However, TAPI-0 is a non-specific inhibitor of ADAM17, and ADAM17 cleaves multiple molecules on NK cell surface. To address whether detachment of Nk cells from target cells is specifically facilitated by shedding of CD16, a cell line NK92 was transfected to express either wild-type CD16 or a non-cleavable variation of CD16.

NK92 cells do not express CD16 on their surface (Figure 4.20A). However, they do express CD3ζ, required for CD16-induced signalling (Figure 4.20B) and ADAM17 (Figure 4.20C).

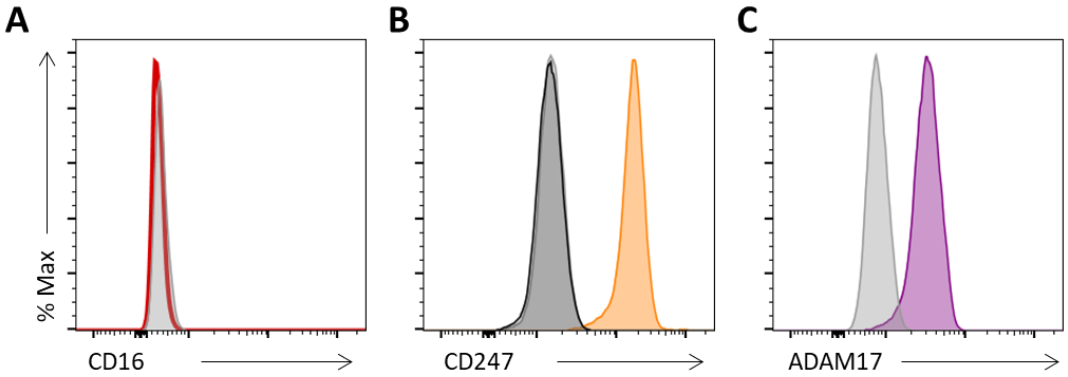

Figure 4.20: NK92 cell line. NK92 cells were assessed for expression of CD16, CD3ζ (CD247) and ADAM17. **(A)** Representative histograms of CD16 expression. NK92 cells were stained for surface CD16 using anti-CD16 AF647 mAb (in red). Matched mouse isotype was used as a control (in grey). **(B)** Representative histograms of CD3ζ expression. Intracellular CD3ζ was stained using anti-CD247 mAb and AF488-labelled secondary mAb (in orange). Isotype matched control with the secondary antibody (in grey) and only secondary antibody staining (in black) were used as a control. **(C)** Representative histograms of ADAM17. ADAM17 was stained intracellularly, using directly labelled anti-ADAM17 AF647 mAb.

Using mass spectrometry, the nucleotide sequence where ADAM17 cleaves CD16 has been identified (Jing et al., 2015, Lajoie et al., 2014). Jing et al. designed a mutant of CD16 that is not susceptible for such cleavage (Jing et al., 2015). The cleavage of CD16 was prevented if the serine at position 175 was replaced with proline (S197P) (Figure 4.21A, B). We have used a mutagenesis kit to introduce this mutation into the wild type CD16 sequence. CD16-WT and CD16-S197P were inserted into retroviral vector and transduced into NK92 cells (Figure 4.21C). Expression levels were matched at first. The expression of CD16-WT varied on daily basis, and decreased in

culture, probably due to spontaneous shedding. CD16-S197P expression was not changed over time.

When NK92 cells were exposed to Daudi-rituximab, CD16-WT was cleaved to the similar extent as upon the activation by PMA/ionomycin. However, the extent of cleavage depended on the starting expression level. The higher expression of CD16-WT was, the more it was cleaved upon NK cell activation. CD16-S197P levels remained intact (Figure 4.21D, E).

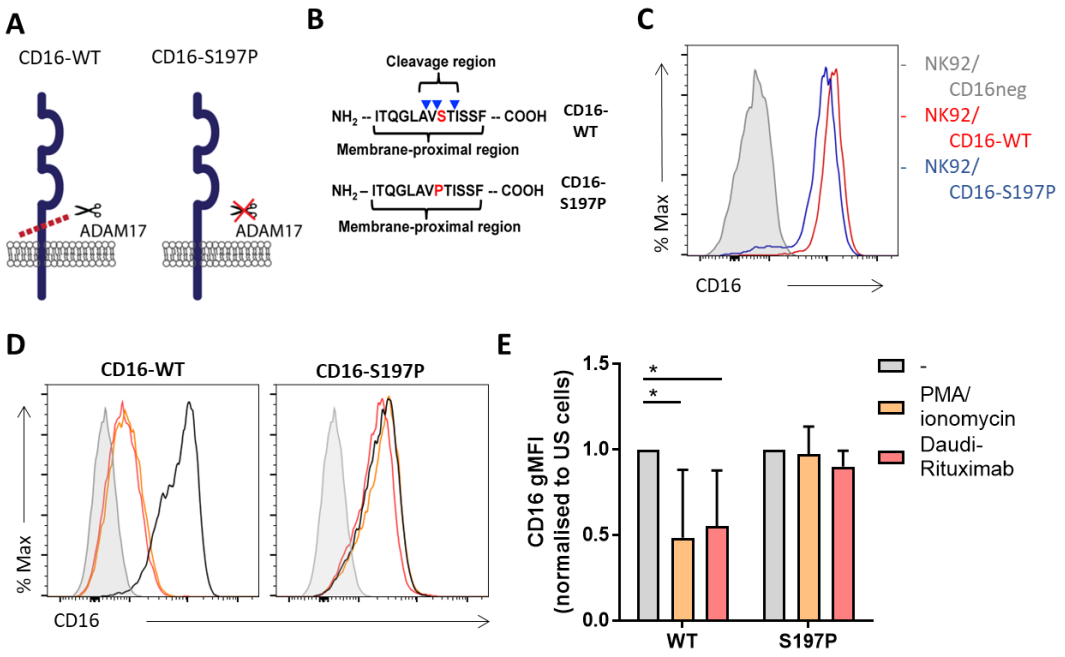

Figure 4.21: NK92 transduced with CD16-WT and CD16-S197P. **(A)** Schematic representation of CD16-WT and CD16-S197P. Extracellular portion of CD16-WT is cleaved by ADAM17. Upon the mutation, ADAM17 can no longer cleave CD16. **(B)** Amino acid sequence of the cleavage region. CD16-S197P was created by single-point mutation from the CD16-WT. Panel is adapted from (Jing et al., 2015). **(C)** NK92 cell line was transduced to express CD16-WT and CD16-S197P using retroviral vector. Shown are representative histograms of CD16 expression in NK92 cells upon the transfection. CD16 was stained using anti-CD16 AF647 mAb. In red, the expression of CD16-WT and in blue, the expression of CD16-S197P is shown. NK92 parental cells were used as a negative control (in grey). **(D, E)** NK92 cells were co-incubated with Daudi-rituximab for 2h or stimulated with PMA/ionomycin for 30 min. Upon activation, levels of CD16 were assessed. (D) Representative histograms of CD16 expression in NK92/CD16$^+$ cells (black) and in parental cell line (grey, shaded) before and after the activation with Daudi-rituximab (red) or PMA/ionomycin (orange). (E) CD16 expression levels were normalised to unstimulated CD16$^+$ cells. Data were pooled from three independent experiments and plotted as mean ± SD. *p<0.05 calculated by two-way ANOVA.

To assess the functionality of transfected NK92 cells, we quantified their degranulation upon stimulation on rituximab-coated slides or by PMA/ionomycin (Figure 4.22). For this, NK92 cells were incubated on ICAM1 or rituximab coated surfaces for 4h in the presence of brefeldin and monensin (Betts et al., 2003). Cells were incubated with PMA/ionomycin for 30 min. Surface CD107a was used as a marker of degranulation and its levels were assessed by flow cytometry. NK92/CD16-WT and NK92/CD16-S197P both degranulated to the same extent. Upon stimulation by rituximab, around 30 % of cells were CD107a^{+} and 30 min with PMA/ionomycin led to 88 % for CD16-WT and 75 % for CD16-S197P degranulating cells. Thus, the cytotoxic potential of both CD16 variants was comparable.

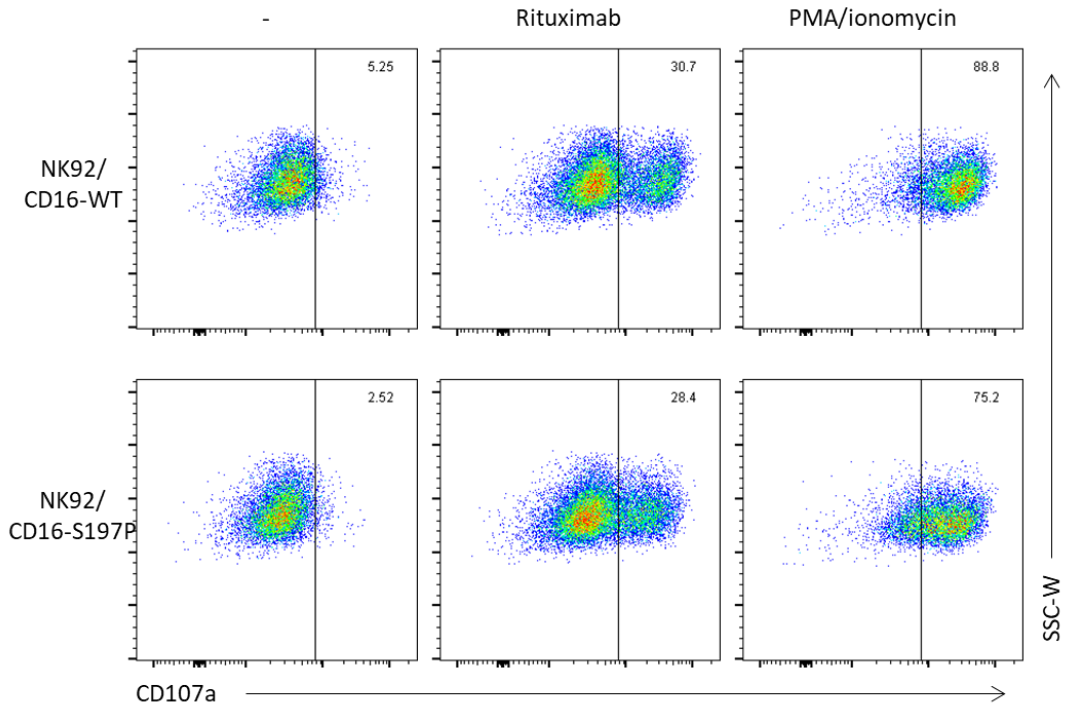

Figure 4.22: Degranulation of NK92/CD16-WT and NK92/CD16-S197P. Representative dot plots from the degranulation assay. NK92/CD16-WT and NK92/CD16-S197P were activated on either ICAM1 or rituximab for 4h, or with PMA/ionomycin for 30 min. Surface CD107a was stained with anti-CD107a AF647 mAb and assessed by flow cytometry. Live and single cells were gated and plotted.

4.3.8. Detachment of NK92/CD16-S197P from opsonized targets is impaired

To study single cell interactions, transfected cells were incubated with rituximab-opsonized Daudi targets in large microwells and time-lase images was acquired (Figure 4.23A, B). The killing efficiency was slightly but not significantly reduced when the cleavage of CD16 was prevented. NK92/CD16-WT killed 45 ± 20 % of the encountered targets, and NK92/CD16-S197P killed 31 ±13 % (Figure 4.23C). The killing time of the mutant was significantly longer than of the WT. NK92/CD16-WT killed on average in 67 ± 82 min, while NK92/CD16-S197P killed their targets in 172 ± 134 min (Figure 4.23D). 42 ± 29 % NK92/CD16-WT cells did not kill any target they encountered, while 60 ± 8 % NK92/CD16-S197P failed to kill. 49 ± 22 % NK92/CD16-WT killed only one target and 10 ± 9 % killed two, while 32 ± 7 % NK92/CD16-S197P killed one Daudi and 8 ± 1 % killed two.

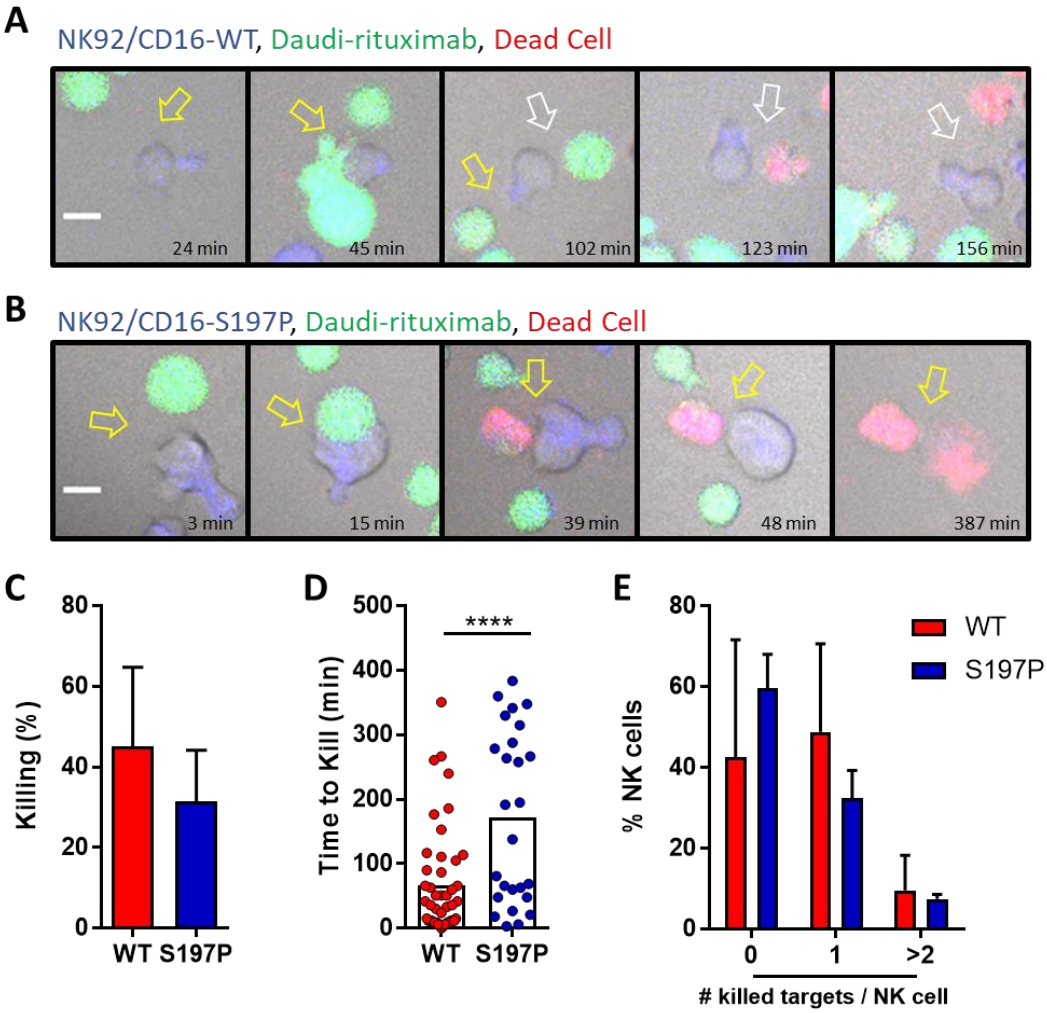

Figure 4.23: Time-lapse imaging of NK92/CD16+ cells with Daudi-rituximab in large microwells. NK92/CD16-WT or NK92/CD16-S197P were incubated with Daudi-rituximab cells. Wells were imaged every 3 min for 8h. **(A, B)** Representative time-lapse zoomed-in images, showing an overlay of a fluorescence and bright-field images. In the bottom right corner time from the start of acquisition (in minutes) is indicated. **(B)** An NK92/CD16-WT cell (in blue) formed a contact with Daudi-rituximab (in green) (45 min, yellow arrow). 57 min later, it detached from the target without killing it and established contact with a new target (white arrow). Second target was killed at 123 min and at 156 min NK92 cell detached and resumed free migration. **(B)** NK92/CD16-S197P formed a contact with its target (15 min). After the lysis of the target, cells stayed in contact. At 387 min NK92 cell died still attached to the target. **(C)** Percentage of all NK cell-target cell interactions that resulted in target cell lysis. **(D)** Time required to kill an individual target. Each dot represents an individual cytolytic NK cell – target cell interaction. **(E)** Number of Daudi cells killed by an individual NK92 cell. Data are pooled from three independent experiments and plotted as mean ± SD. ****p<0.0001 calculated by student t-test.

Regardless of whether the target cell survived the contact or it was killed, the detachment of the mutant was significantly impaired, with only 10 ± 14 % NK92 detaching from killed targets, comparing to 70 ± 7 % in the wild type and 16 ± 1 % of them detaching from the targets that survived the contact, comparing to 81 ± 9 % of the WT (Figure 4.24A). The number of target cells that were encountered by each individual NK92 cell was not affected by the mutation of CD16 (Figure 4.24B).

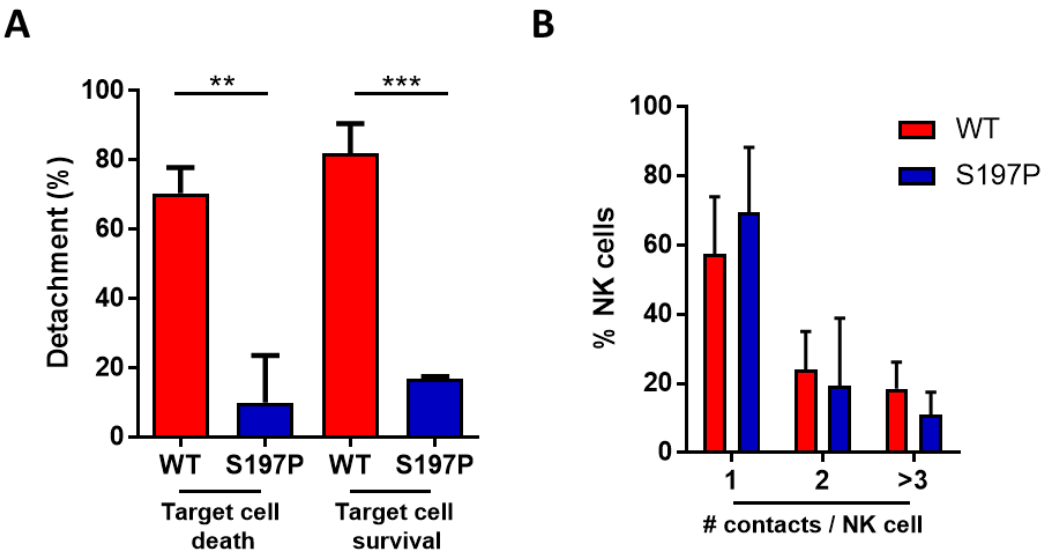

Figure 4.24: Interactions between NK92/CD16+ cells and opsonized Daudi cells in large microwells. NK cells were put into large microwells together with Daudi-rituximab. **(A)** Percentage of NK cell – Daudi cell conjugates that detached by the end of the acquisition. **p<0.01, ***p<0.001 calculated by one-way ANOVA. **(B)** Number of target cells encountered by individual NK cell. Data are pooled from three independent experiments and plotted as mean ± SD.

The increased time required for the killing by the mutant (Figure 4.23) was perhaps the result of the prolonged contact time. While cells with CD16-WT detached and left targets unharmed, the mutant was not capable of detaching and some of these extended contacts led to target cell killing after longer period. These results together indicate that CD16 shedding by ADAM17 promotes the detachment from opsonized target cells.

4.3.9. NK92/CD16-S197P form more F-actin rings on rituximab-coated surface

Next, we set to assess how the mutation in CD16 affects synapse formation on rituximab-coated glass surfaces. NK92 cells were incubated on slides coated with ICAM1 or rituximab for 5 min. Then cells were fixed and their F-actin was stained with phalloidin. Preliminary data shows that few cells formed actin rings on ICAM1 (3 % NK92/CD16^{neg}, 6 % NK92/CD16-WT and 7 % NK92/CD16-S197P). NK92/CD16^{neg} cells and NK92/CD16-WT also did not form many actin rings on rituximab (2 and 11 % respectively). But, 60% NK92/CD16-S197P formed dense actin rings.

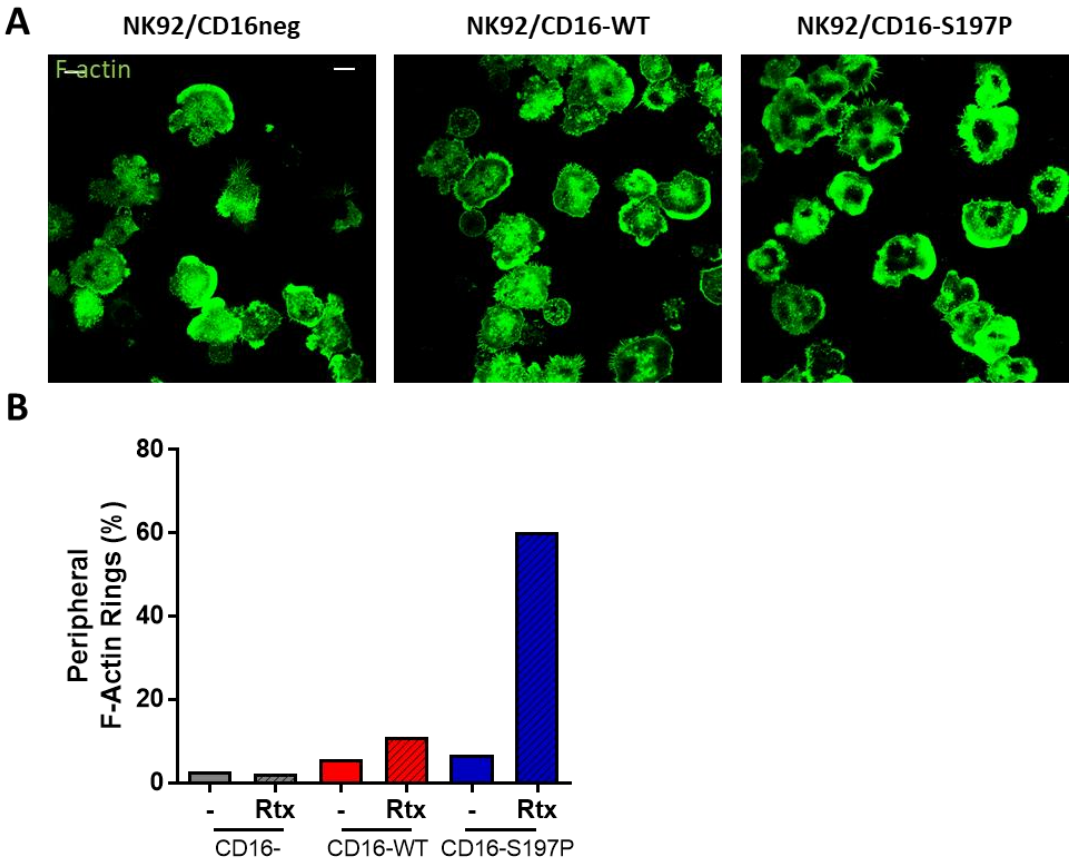

Figure 4.25: Peripheral F-actin rings on rituximab coated surface. NK92 cells were incubated on ICAM1 or rituximab-coated surfaces for 5 min. Then, cells were fixed and stained with AF488 phalloidin. **(A)** Representative images of NK92/CD16^{neg}, NK92/CD16-WT and NK92/CD16-S197P on rituximab. **(B)** Percentage of NK92 cells forming peripheral F-actin rings. Data are from one experiments.

Above we reported that both, NK92/CD16-WT and NK92/CD16-S197P degranulate to the same extent when activated on rituximab-coated surfaces. Here however we show that NK92/CD16-S197P forms significantly more F-actin rings. This indicates that F-actin rings are not prerequisite for degranulation on rituximab. When CD16 is ligated, cells do activate regardless of its shedding. However, only when the shedding of CD16 is inhibited, stable synapse with dense actin rings can be formed.

4.4. Discussion and further directions

4.4.1. Summary of results

In this chapter, we aimed to address whether the shedding of CD16 receptor affects ADCC synapse formation, contact stability and NK cell function. For this, we used live cell imaging of primary NK cells interacting with activating surfaces or with opsonized target cells. IRM time-lapse images of individual NK cells landing on rituximab or MICA coated surfaces allowed us to study early stages of synapse formation and its dynamics. NK cell motility on activating surfaces was visualised by live microscopy and assessed by tracking the movements of individual cells. Imaging in microchips allowed us to investigate individual NK cell-target cell interactions over 8h. The role of CD16 cleavage in NK cell motility and detachment from targets was addressed using ADAM17 inhibitor TAPI-0 and NK92 cell line, transfected to express wild type or a non-cleavable variant of CD16.

The main findings presented in this chapter established that:

i. CD16-synapse is more dynamic than the NKG2D-synapse.
   - Upon synapse formation on rituximab-coated surfaces NK cells do not accumulate F-actin into dense rings, like they do on MICA. Instead, F-actin is distributed asymmetrically at the leading edge, indicating a migratory phenotype.
   - NK cells on MICA form a round, static synapse while cells on rituximab rapidly develop a migratory shape and start crawling around the surface.

ii. Shedding of CD16 is important for NK cell detachment.
   - CD16 shedding enables NK cell motility on rituximab-coated surfaces. When the shedding is inhibited, cells become more static on rituximab, but their dynamics are not affected on other surfaces.
   - Inhibition of CD16 shedding by TAPI-0 significantly reduces NK cell detachment from lysed opsonized targets as well as from opsonized targets that survived the contact.
   - The detachment from opsonized targets is severely impaired when NK92 are transfected with a non-cleavable mutant of CD16, comparing to the WT.

4.4.2. Significance of results

It is well established, that cytotoxic cells need to establish a stable immune synapse in order to execute target cell lysis. By the initial definition, immune synapse requires the adhesion, polarization and stability (Dustin, 2008). Using IRM microscopy allowing the investigation of cell contact with the surface, we demonstrated that cells formed stable symmetric cytolytic synapse quickly upon landing on MICA. On rituximab, cells did adhere, but surprisingly they quickly developed a migratory shape and started crawling. CD16 (on rituximab) and NKG2D (on MICA) -synapses also displayed different F-actin distribution; on MICA F-actin accumulated into dense symmetrical rings while stimulation by rituximab led to F-actin relocation into the leading edge of the cell. While cells on MICA stayed attached to the surface through NKG2D, CD16 shedding allowed NK cells to move on rituximab. When shedding of CD16 was inhibited, cell motility on rituximab was reduced, but remained unaffected on other surfaces. Comparing to ICAM1, cells were less dynamic on rituximab, consistent with the hypothesis that some inhibition of movement is required for the execution of a cytolytic response. However, the inability of cells to form static symmetrical synapse on rituximab did not prevent their degranulation or cytokine secretion. Taken together, the CD16-synapse fits two out of three criteria for immune synapse definition; cells on rituximab adhere and polarize, but are not stable. Such phenomena of motile contacts leading to signalling have been previously described between T cells and antigen presenting cells (APCs) and named kinapse (Dustin, 2008, Valitutti et al., 1995). Hence, we propose that cells on CD16 form a cytolytic kinapse rather than a static synapse because of their kinetic properties.

Studying individual interactions between NK cells and their targets can be technically challenging, as cells can move over time and disappear from field of view. To overcome this, we performed imaging in microchips confining a few individual cells into separated compartments (Guldevall et al., 2010, Vanherberghen et al., 2013). This allowed us to image and precisely evaluate individual cell-cell contacts over long periods of time. Using this we discovered that NK cell detachment process from opsonized targets is driven by the shedding of the CD16 receptor. The inhibition of CD16 cleavage, either by TAPI-0 (ADAM17 inhibitor) or by mutating the cleavage region of CD16, resulted in prolonged contact times, even after the target cell lysis. When CD16 shedding was prevented, many NK cells failed to dissociate even several hours after target cell lysis. The failed detachment did not affect the number of encountered targets; however, we postulate that in complex environment keeping a

dead target on the surface would reduce NK cell motility and consequently lead to less efficient serial killing.

Interestingly, the use of TAPI-0 inhibitor did not increase NK cell degranulation on rituximab or affect their cytotoxicity against opsonized targets. But, IFN-γ secretion was augmented. This suggests that the regulation of the secretion of lytic granules is different to the secretion of cytokines. NK cells with impaired CD16 shedding could continue secreting cytokines while they stay in conjugate, even after the target is killed. This could contribute to hyper-activation of the immune system and to over-exhaustion or activation-induced cell death (AICD) of NK cells. Consistent with this, prolonged contact with a target cell caused by impaired target cell lysis results in cytokine hypersecretion potentially leading to recruitment and activation of myeloid cells and systemic inflammation (Jenkins et al., 2015).

NK cells that remained in conjugates were more likely to undergo apoptosis. Such NK cell death, occurring when CD16 shedding was inhibited was specific to failed detachment, as NK cell death was not changed in unattached cells. Thus, perhaps NK cells that remained attached died because of the activation induced cell death, which can occur after prolonged exposure to activating signals (Maher et al., 2002).

Here we only addressed NK cell detachment from opsonized targets. However, besides CD16, ADAM17 cleaves multiple NK cell ligands, such as MICA, ULBP-2, ICAM1, MULT-1 (Deng et al., 2015) on target cells. In neutrophils, it has been shown that the apoptosis of cells triggers ADAM17 activation via caspase-8 (Walcheck et al., 2006, Wang et al., 2013). Therefore, it is interesting to speculate that cleavage of proteins might be the main mechanism for the detachment of effector cells from lysed targets. As we show here, in a case of ADCC, the detachment is dictated by the NK cell, while in other forms of interactions, the detachment might be dictated by the target cell. Jenkins et al. showed that the inhibition of caspases impairs the detachment from targets (Jenkins et al., 2015). This supports the idea that the main mechanism for the detachment is ADAM17 cleavage of NK cell ligands.

One important question that remains open is why is CD16 cleaved when the receptor is not ligated. One possibility is that soluble CD16 acts as a signal to other immune cells. However, the concentrations of soluble CD16 in human serum are constantly high and dying neutrophils have been previously proposed to be the main source of it (Wang et al., 2013). NK cell contribution to soluble CD16 pool is small and it is not clear if the CD16 shedding upon NK cell activation leads to the recruitment of other immune cells. As we demonstrated in the previous chapter (Chapter 3), shedding of

CD16 impairs NK cell ADCC capacity. Thus, perhaps shedding occurs in order to prevent the hyper-activation of the immune system. Upon infection, stress-induced ligands can be relatively quickly expressed on infected cell surfaces (Venkataraman et al., 2007, Groh et al., 1998, Stern-Ginossar et al., 2008), while the production of specific antibodies during a first infection takes weeks (Song et al., 1998). Thus, when target cells already express specific activating ligands, ADCC action is less required. Therefore, the removal of CD16 serves as a mechanism to enable precise response. But, upon the secondary infection the pool of specific antibodies is already pre-formed, and thus ADCC can provide a quick and specific elimination of the disease.

In this study, we observed that levels of CD16 shedding from different donors varied significantly. Interestingly, some donors displayed no shedding of the receptor upon NK cell activation through CD16 or NKG2D. Thus, it would be interesting to investigate what are the factors affecting CD16 shedding and what are the functional consequences of this. Could having constantly high levels of CD16 be beneficial for therapies with therapeutic antibodies, or would it lead to less efficient tumour elimination due to failed detachment from lysed cells (and non-specific hyper-responses by elevated IFN-γ secretion)? There were several attempts to inhibit ADAM17 therapeutically, but none of them proved to be successful so far (Saftig and Reiss, 2011, Murumkar et al., 2010), indicating that perhaps some levels of CD16 shedding are essential for NK cell function. However, it should be noted that ADAM17 activity is not limited to NK cells and therefore its inhibition could have several side effects. Alternatively, therapies could rather focus on finding a way to boost CD16 re-expression upon its cleavage to ensure correct NK cell responses.

Overall, we have shown here that CD16 shedding promotes the detachment from opsonized targets. By this, it limits the IFN-γ hypersecretion and NK cell death. This indicates that the shedding of this NK cell activating receptor does not only control immune response, but also promotes NK cell specific serial killing by keeping NK cells alive and motile.

Chapter 5:

Nano-scale organisation of CD16 at the NK cell surface

5.1. Introduction

NK cells recognise and kill diseased cells through specialised contacts, immunological synapses (Davis et al., 1999, Orange, 2008). Fluorescence imaging demonstrated that upon the contact many proteins at the NK-target cell interface rearrange into highly organised structure. The progress in knowledge about the distribution of surface proteins at the immune synapse has been enabled by recent advances in super-resolution microscopy which allows imaging of individual protein molecules with great precision (Betzig et al., 2006, Hell and Wichmann, 1994, Hess et al., 2006, Rust et al., 2006). In many immune cells, including NK cells, the nature and distribution of protein clusters can change upon the ligation of activating or inhibitory ligands (Liu et al., 2012, Oddos et al., 2008, Pageon et al., 2013, Almeida and Davis, 2006, Bálint et al., in print). For example, the engagement of the NK cell activating receptor NKG2D triggers reorganisation of the inhibitory receptor KIR2DL1 into smaller and denser nanoclusters (Pageon et al., 2013). Moreover, the ligation of different activating ligands by the same receptor can lead to formation of nanoclusters with different properties.

When NKG2D ligates ULBP2, NKG2D nanoclusters become larger than in resting state while the ligation of MICA triggers rearrangement into smaller clusters. The ligation of ULBP2, but not MICA, also induces nanoscale reorganization of the IL-15 receptor that leads to spatial association between NKG2D and IL-15 receptor (Bálint et al., in print). Such reorganisation might have an importance in NK cell functional output. Cells stimulated by ULBP2 degranulate less efficiently than cells stimulated by MICA, but the co-ligation of IL-15 receptor by trans-presentation of IL-15 could boost the amount of degranulation of ULBP2-activated cells to that of MICA-activated cells. Thus, the proximity of the nanoclusters of NKG2D and IL-15 receptor likely facilitates the integration of the activating signal.

There are indications that suggest that clusters and their characteristics contribute to receptor signalling. Nanocluster of the activating receptor KIR2DS1 and its adaptor molecule DAP12 are juxtaposed in the resting cell state but coalesce upon receptor ligation. Moreover, the phosphorylation of the kinase ZAP-70 or phosphatase SHP-1 is favoured in larger KIR nanoclusters (Oszmiana et al., 2016). In T cells, clusters of TCR have also been described to mix with clusters of LAT and ZAP-70 upon activation (Sherman et al., 2011, Lillemeier et al., 2010). However, these are only correlations and the real importance of clusters still remains to be proven.

CD16 is one of the best studied NK cell receptors. However, CD16 clusters have been only reported on a microscale (Liu et al., 2012). The incubation of human primary NK cells on lipid bilayers carrying IgG1 Fc as a ligand for CD16 led to accumulation of the Fc into a central micro-cluster. When an inhibitory ligand HLA-E was added to the bilayer, the formation of the Fc micro-cluster was inhibited, but its central accumulation was not disturbed. The distribution of CD16 on NK cell surface has not yet been studied using super-resolution techniques and thus its nanoscale organisation is yet to be described.

The importance of nanoscale organisation of CD16 on NK cell surface for the receptor-ligand interactions was perhaps best illustrated in a study where primary human NK cells were incubated on gold nanospheres coated with ligands for CD16. The distribution of ligands was controlled in nanoscale. Increasing the inter-ligand distance above 104 nm led to decreased NK cell responses (Delcassian et al., 2013). Moreover, a recent work has shown that immobilising CD16 ligands on graphene particles with a median size of 150 nm induced greater NK cell degranulation and IFN-γ production than soluble ligands (Loftus et al., submited). These results indicate that cells perhaps respond best when ligands are presented in bundles matching the sizes of immune cell receptor clusters.

5.2. Aims and objectives

The overall aim of this chapter was to investigate nanoscale organisation of CD16 receptor on NK cells in their resting and activated state. Super-resolution images of the fixed cells were acquired by GSD microscopy, a technique providing single-molecule localisation precision. Localisations of detected CD16 molecules were analysed using quantitative point pattern analysis. However, as GSD microscopy, like other super-resolution techniques, is prone to artefacts, a thoughtful optimisation of data processing needed to be carried out.

Cells in the resting state were imaged on PLL or ICAM1 coated coverslips. To study the rearrangement of the receptor upon its ligation, cells were imaged on surfaces coated with rituximab. As described in previous chapters of this thesis, CD16 receptor is shed from cell surface upon NK cell activation. It is unknown if shedding leads to loss of nanoclusters and whether the cluster size or their density change when the receptor is cleaved. To address this, two different antibodies were used for labelling the receptor; anti-CD16 mAb staining the extracellular portion of CD16 and anti-CD16 mAb recognizing its intracellular portion. The inhibitor of CD16 shedding, TAPI-0, was used to investigate differences in nanoscale organisation upon rituximab ligation in the absence of shedding.

Specific aims of this chapter were:

i. To optimise GSD microscopy acquisition and data processing for single-molecule detection and localisation;
ii. To establish quantitative analytical methods for assessing patterns of receptor distribution at the cell surface;
iii. To quantitatively describe nanoscale organisation of CD16 on NK cells in resting state and upon the ligation with rituximab;
iv. To investigate potential changes in CD16 nanoscale organisation upon the inhibition of CD16 shedding.

5.3. Results

5.3.1. Optimisation of CD16 staining for super-resolution microscopy

Sample preparation can have a significant impact on the quality of acquired microscopy images. For super-resolution techniques, labelling of individual molecules with bright fluorophores is particularly important (Bittel et al., 2015). Therefore, it is crucial to optimise sample staining to ensure that the receptors of interest are brightly labelled and could be detected by single molecule localisation microscopy in high resolution.

To study constitutive organisation of CD16 receptor on NK cells in a resting state, cells were imaged on slides, coated with PLL, to facilitate their adhesion and spreading. After 5 min incubation on PLL-coated surfaces cells were fixed in formaldehyde and stained for 1h. There are several different antibody clones commercially available for detecting CD16. They vary in the specificity and affinity for the receptor recognition and this could be further affected by the fixation of the sample. To ensure high-quality staining of the sample for CD16 imaging, we tested two different clones, 3G8 and B73.1, both recognizing the extracellular portion of CD16 receptor. Both antibodies were directly conjugated to AF647 dye.

To visualise the efficiency of staining of the receptor, total internal reflection fluorescence (TIRF) microscopy was used. TIRF is a widely used imaging technique for envisioning membrane proteins, because of its property to illuminate and excite only fluorophores within a near distance from the interface. Fluorophores in the rest of the cell are barely excited and consequently, background fluorescence is reduced due to the improved signal-to-noise ratio.

In acquired TIRF images, the difference in the quality of staining between the two antibodies were clearly visible and thus no further analysis was required (Figure 5.1). Increasing the concentration of the antibody did not improve the quality of the staining (data not shown).

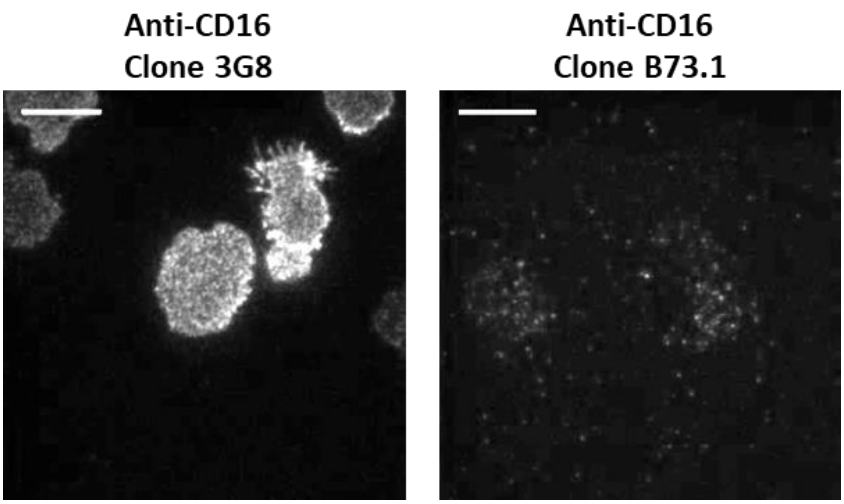

Figure 5.1: CD16 staining with two different clones of anti-CD16 AF647 mAbs. Primary NK cells were incubated on PLL-coated slides for 5 min, fixed and stained with 10 µg/ml anti-CD16 AF647 mAbs (clones 3G8 or B73.1, as indicated). Images were acquired by TIRF microscopy. The scale bar is 10 µm.

CD16 recognizes the Fc portion of IgG antibodies, including the Fc of the labelling antibodies, and thus it is crucial to test for the non-specific staining of the antibody isotype. The specificity of the 3G8 clone for CD16 was tested by using the same concentrations of mouse isotype control IgG1 AF647 mAb to stain primary NK cells (Figure 5.2). Again, the staining of the 3G8 clone was bright and stained cells specifically with very low background fluorescence. In contrary, when samples were stained with the isotype matched control fluorescence signal was barely detectable. Thus, these data indicate that staining with 10 µg/ml antiCD16 3G8 AF647 mAb could be used for the labelling and detection of CD16 molecules on fixed cells by microscopy.

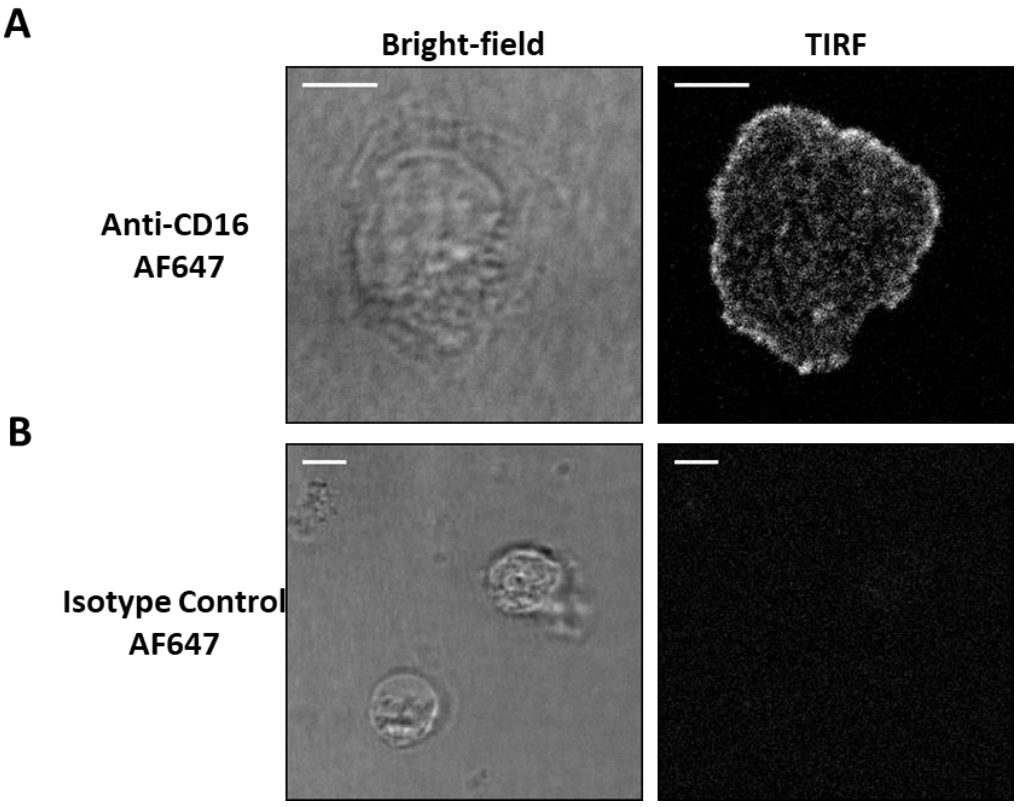

Figure 5.2: Specificity of anti-CD16 (clone 3G8) AF647 mAb staining. NK cells were incubated on PLL-coated surface for 5 min, fixed and stained with 10 µg/ml of anti-CD16 mAb (clone 3G8) **(A)** or the same concentration of isotype matched control **(B)**. Both antibodies were directly conjugated to AF647. The scale bar is 5 µm.

NK cells can be divided in two different populations, based on their CD16 expression; $CD16^+$ and $CD16^-$ (De Maria et al., 2011, Orange, 2013, Cooper et al., 2001b). Moreover, as described in previous chapters, the expression of the receptor on $CD16^+$ primary NK cells varies between cells (Figure 5.3A). To visualise the differences in CD16 expression by TIRF microscopy, NK cells were stained for surface CD16 together with F-actin. F-actin was used to visualise the cells, even in the absence of CD16. As shown in two representative images in Figure 5.3B, some cells expressed high levels of CD16 and some had very few CD16 molecules on the surface. For super-resolution images of high quality, bright samples are required and therefore only $CD16^{bright}$ cells were considered in this study.

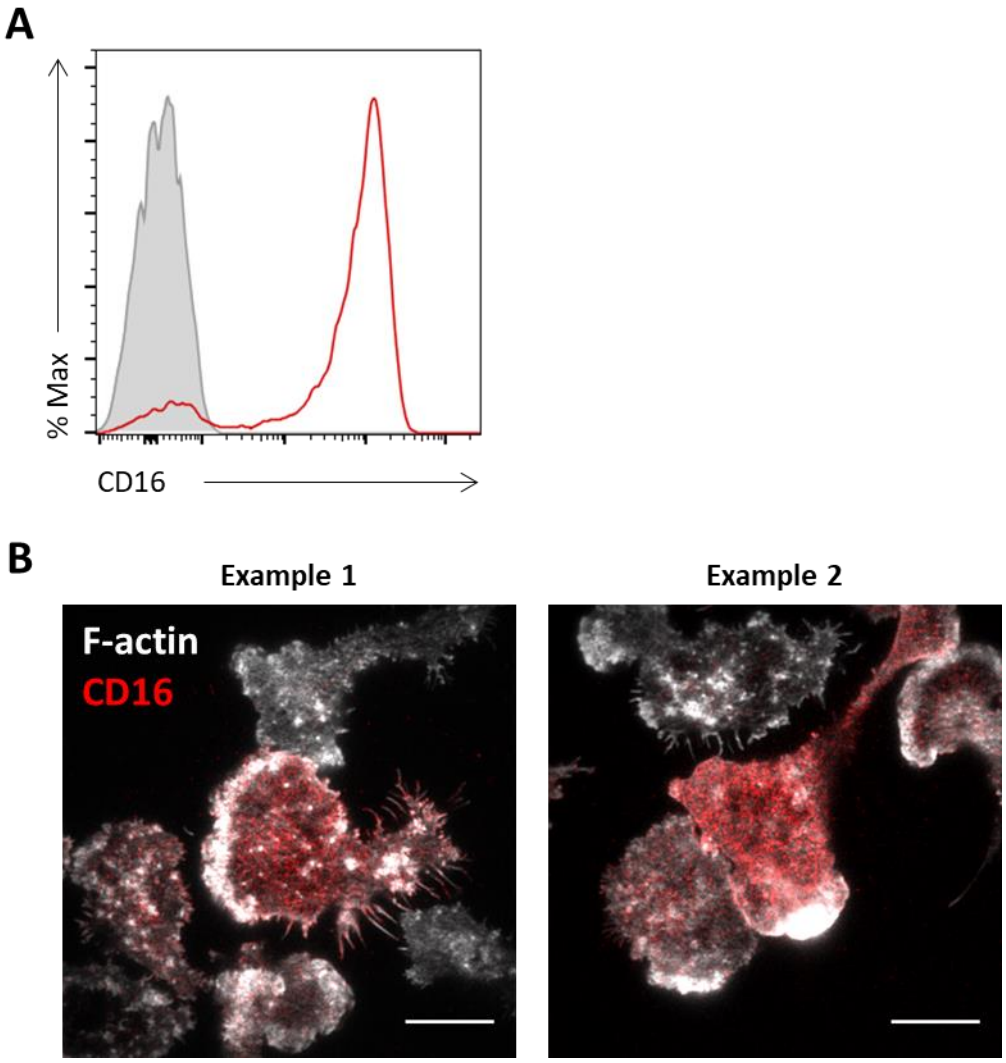

Figure 5.3: Expression of CD16 on primary NK cells. (A) Unstimulated NK cells were stained with anti-CD16 AF647 mAb (red) and acquired by flow cytometry. Live and single NK cells were gated prior receptor expression was assessed. Isotype control staining is plotted in grey. **(B)** An overlay of representative TIRF images of F-actin (white) and CD16 staining (red) of fixed primary NK cells, incubated for 5 min on PLL. The scale bar is 10 µm.

5.3.2. GSD data processing

To investigate nanoscale organisation of individual CD16 molecules we used GSD microscopy. GSD is based on stochastic excitation of photo-switchable dyes that enables us to image small subsets of non-overlapping fluorophores at a time. By this, the position of individual molecules can be localised with a nanoscale precision. To detect the molecules at the coverslip-cell interface, GSD imaging was performed using TIRF illumination. It should be noted that in this chapter, mention of GSD always refers to super-resolution imaging, combining GSD with TIRF. On the other hand, TIRF is used when images were acquired using TIRF only.

Rather than a snapshot image, the camera on the GSD microscope records the localisations of individual detections which can be later reconstructed into a super-resolution image (Betzig et al., 2006, Hess et al., 2006, Rust et al., 2006). But for the accurate and precise localisation of single-molecules, choosing appropriate parameters for image acquisition as well as for data processing is essential. Here, the post-processing of acquired CD16 super-resolution images was carried out using ThunderSTORM ImageJ plug-in (Ovesný et al., 2014). Specifically, four ThuderSTORM-based operations were performed, in the order they are listed in: (i) molecule detection and localisation, (ii) data filtering, (iii) lateral drift correction and (iv) merging of multiple detections (Figure 5.4). This section specifically addresses the optimisation of these tasks.

First, individual photo-switching events were detected by identifying the brightest pixels in each image and the PSF intensity profile of each fluorophore was mathematically fitted into two-dimensional Gaussian curves. The sub-pixel (x,y) coordinates of the underlying molecule were estimated within tens of nanometres, based on the peak of the fitted Gaussian curve (Thompson et al., 2002). Then, non-specific localisations associated with background noise were filtered out. Background was defined by lower signal intensity (based on photon intensity), poor localisation precision (based on sigma, a standard deviation of the Gaussian distribution used to fit the localisation of this molecule) and high localisation uncertainty. For CD16 data analysis, fluorophores emitting less than 500 photos with sigma value below 15 nm and above 250 nm and localisation uncertainty of more than 50 nm were considered as background noise and were thus removed (Figure 5.5).

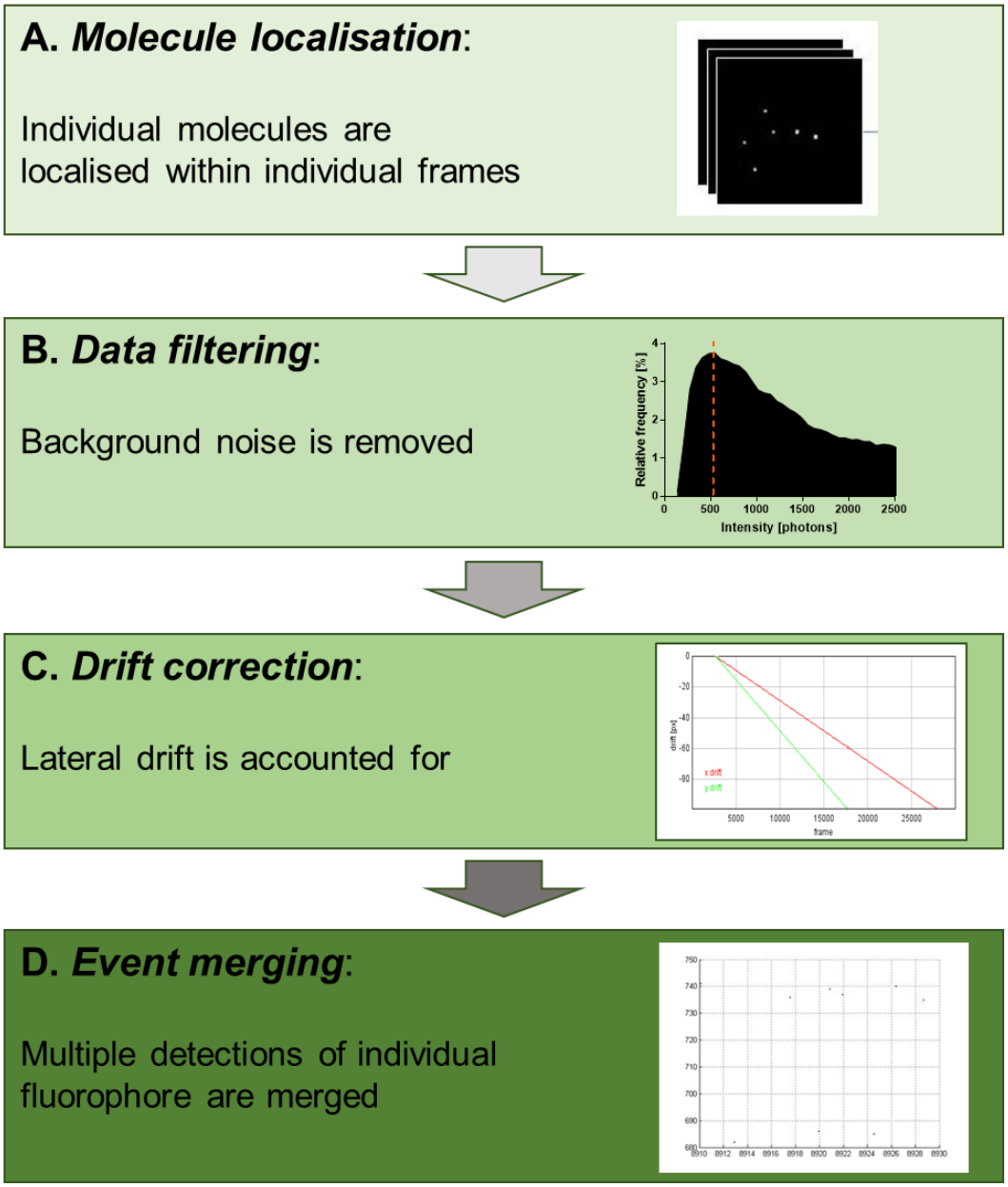

Figure 5.4: GSD data post-processing flowchart. Schematic diagram of the four main steps involved in GSD data post-processing. **(A)** Localisation of individual photo-switching events in each frame is done by Gaussian fitting. The (x-y) coordinates are calculated for the underlying fluorophores. **(B)** The intensity and localisation precision of detected molecules are used to filter out the background noise. **(C)** The (x-y) coordinates of molecules are corrected for lateral drift using image cross-correlation. **(D)** Multiple detections of the same photo-switching event are merged into one molecule.

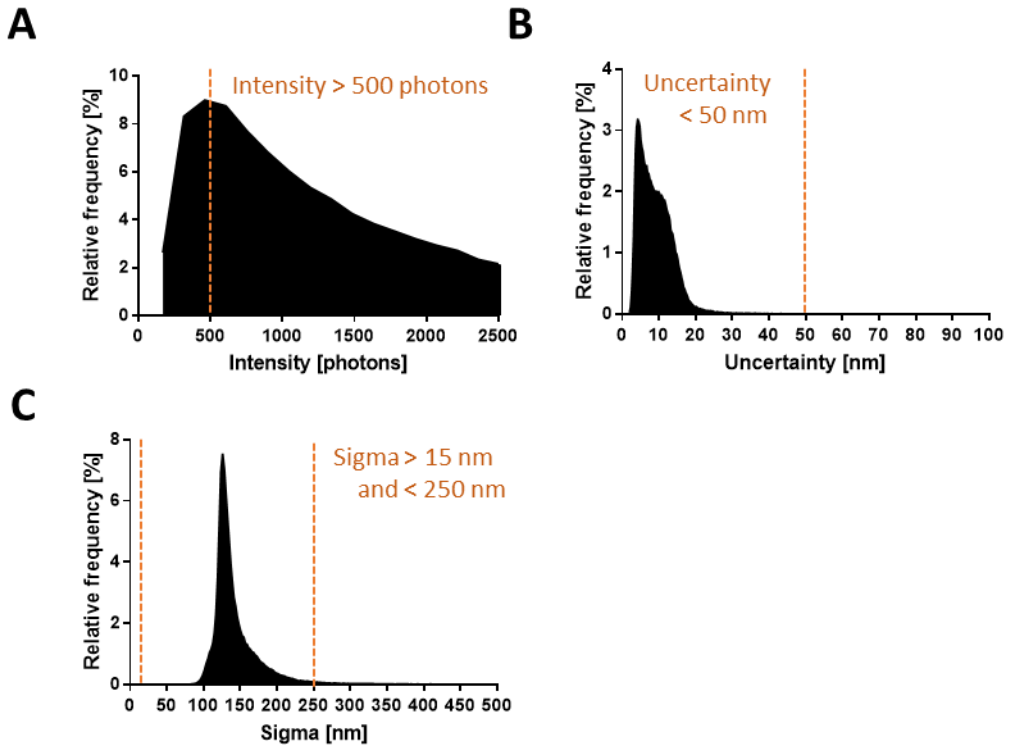

Figure 5.5: Parameters used for CD16 GSD data filtering. Background noise from GSD images was removed based on three main parameters: photon intensity, localisation uncertainty, and the standard deviation of the Gaussian fit (sigma). CD16 analysis was restricted to events that were detected with an intensity superior to 500 photons **(A)**, an uncertainty of less than 50 nm **(B)** and a sigma value above 15 nm and below 250 nm **(C)**.

The acquisition of individual image by GSD microscope takes several minutes and thus, it is impossible to avoid minimal sample drift in x and y dimensions. This lateral drift can be mathematically corrected by ThunderSTORM using cross-correlation (Mlodzianoski et al., 2011). The principal of the method is the assumption that similar structures will appear in all reconstructed images. Based on this, the lateral shift between the intensity maximum peaks of blinking events in subsequent frames is calculated (Figure 5.6). For the reconstruction of the final image, the resulting drift plot is accounted for.

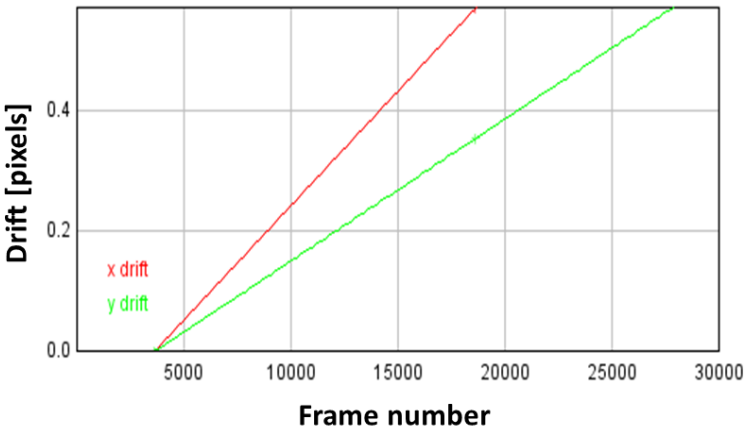

Figure 5.6: Drift correction by image cross-correlation. Drift correction was calculated using cross-correlation method by the ThunderSTORM. For this, the image sequence was divided into different segments and the images obtained from each segment were correlated to the previous one to monitor drift in the x-axis (red) and y-axis (green). The resulting cross-correlation plot was then used to adjust the x-y coordinates of detected events for lateral drift.

In GSD microscopy, multiple rounds of photo-activation of individual dye molecule contribute to a brighter signal but also result in repeated detections of the same molecule. If not corrected, this could lead to false interpretation of the data, as a single CD16 molecule could be recorded multiple times and seen as a cluster of molecules. However, such re-blinking is a property of the dye and can be accounted for. Here, we merged the detected events detected within a short distance and a defined number of consecutive frames into one. The position of a molecule was then calculated as the mean value of the original data. To determine the parameters required for appropriate merging of repeated detections, we performed GSD imaging of a very diluted (< 0.5 ng/ml) anti-CD16 AF647 mAb adsorbed onto glass surfaces. This strategy allowed us to distinguish individual antibodies. The localisations of individual blinking events were then visualised in MatLab (MathWorks) (Figure 5.7A, B). The radius and number of consecutive frames required for merging were defined empirically by analysing the same representative dataset with different merging parameters. After applying the chosen parameters, the re-blinking events (reappearing within 30 nm of each other and 20 consecutive frames) were considered as one molecule (5.7C, D).

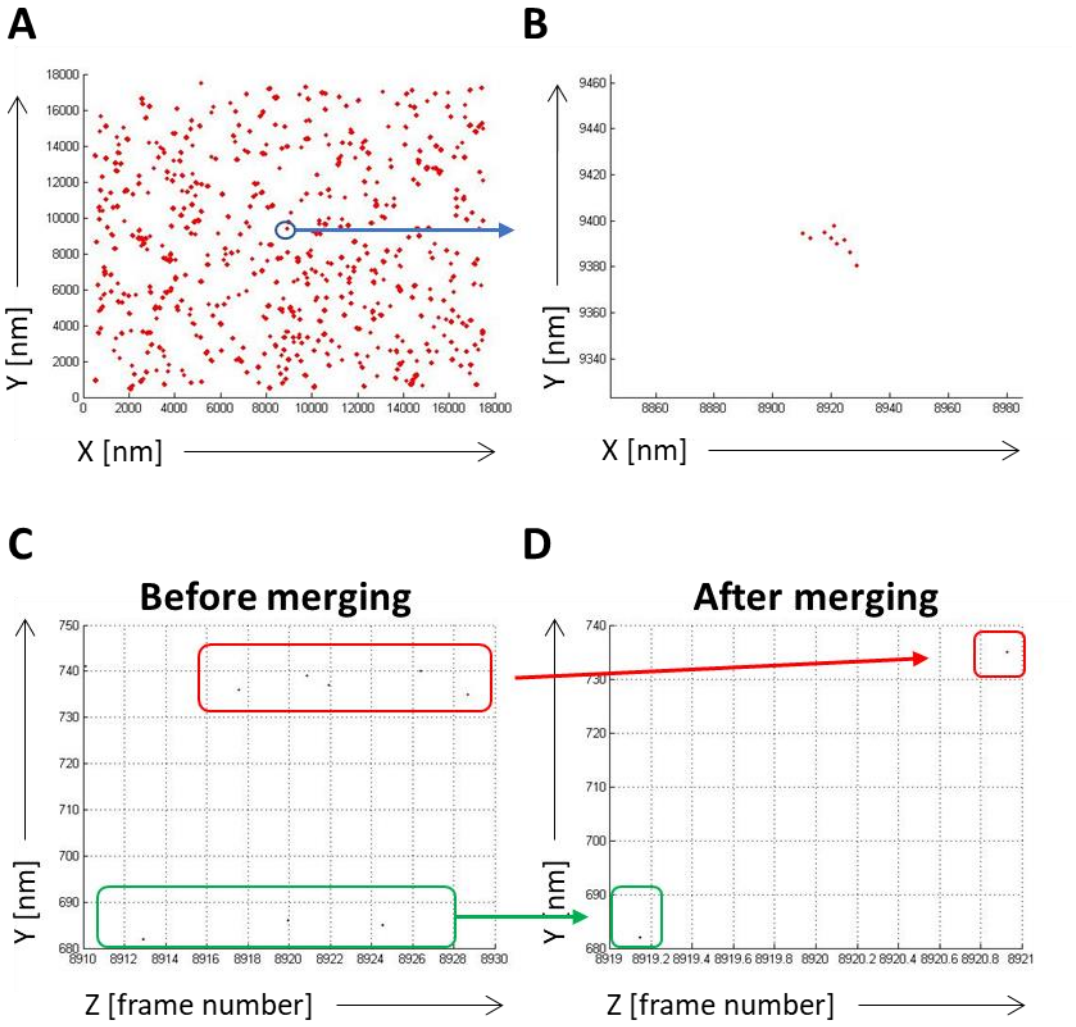

Figure 5.7: Elimination of re-appearing events by merging. CD16 AF647 mAb was adsorbed onto glass coverslips in a very low concentration and imaged by GSD microscopy. Obtained data were then processed using the ThunderSTORM plug-in with or without merging of multiple detections of the same molecule. **(A)** Detected events were filtered by their intensity and localisation precision and plotted on X and Y coordinates. **(B)** The selected cluster of detected events was zoomed-in and a Y-coordinate of each detected event was plotted against the frame number in which they appeared (Z-axis) to assess the re-blinking of single molecules **(C)**. Representative Y-Z plot of photo-switching events detected over time **(C)** before merging and **(D)** after merging was of events occurring within 30 nm and 20 off-frames was applied.

Once all above defined parameters were applied to obtained GSD data, super-resolution images of CD16 were constructed. The nanoscale precision of individual molecules provided a significant improvement in image quality when compared to diffraction-limited TIRF images (Figure 5.8). Smaller clusters that could not be distinguished by TIRF microscopy are clearly resolved in GSD image. Also, the background noise is significantly reduced in GSD images. Analysis of the

fluorescence intensity profiles along the indicated lines, shows that there was a clear reduction in the full width at half maximum (FWHM) of the peaks in intensity obtained by GSD microscopy, compared to TIRF images (Figure 5.8B, D). FWHM of these peaks suggest that the resolution of approximately 40 nm could be achieved in GSD images. Thus, using GSD microscopy with the above defined post-processing parameters we could image CD16 receptor on NK cells with a single molecule precision. The obtained images could be used for further quantification of the spatial organisation of the receptor in different conditions, e.g. upon NK cell activation.

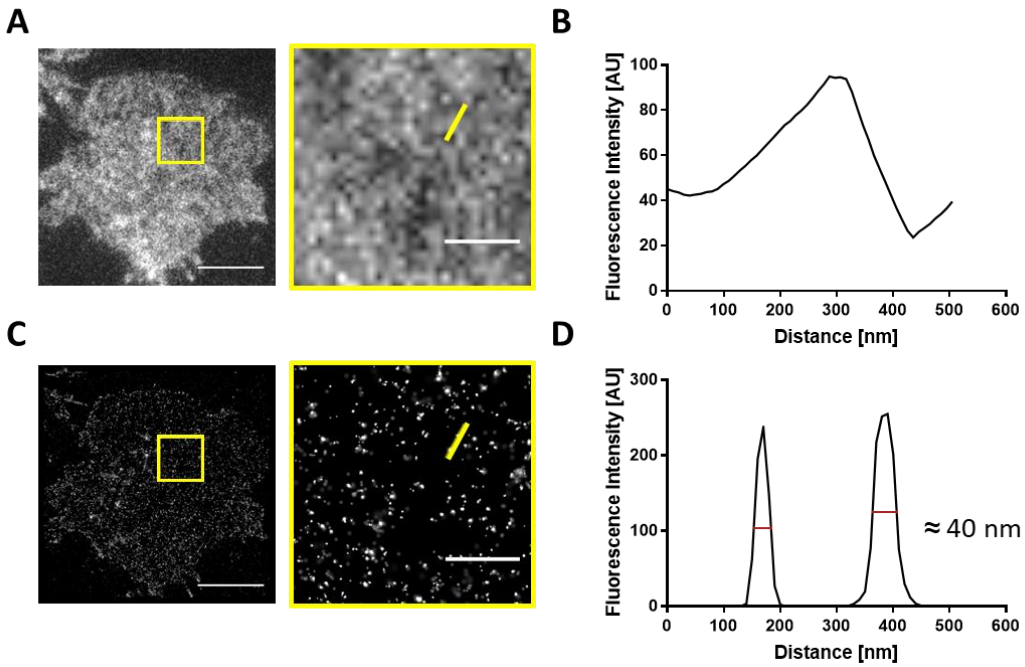

Figure 5.8: Resolution improvement from TIRF to GSD microscopy. Primary NK cells were incubated for 5 min on PLL-coated slides, fixed and stained with anti-CD16 AF647 mAb. **(A)** Representative TIRF image of CD16 (left) and zoomed-in region (right) outlined in yellow. The scale bars are 5 µm and 1 µm. **(C)** Representative GSD image of CD16 (left) and zoomed-in region (right) outlined in yellow. The scale bars are 5 µm and 1 µm. **(B, D)** Fluorescence intensity along the indicated yellow lines (in A, C) was used to compare the resolution obtained by TIRF and GSD microscopy. GSD imaging resolution was estimated at ≈40 nm, based on the full width at half maximum of peaks in fluorescence intensity. AU: arbitrary units.

5.3.3. Quantification of the surface protein distribution by spatial point pattern analysis

The (x-y) coordinates of single-molecule localisations, obtained from processed GSD data, were used for quantitative analysis of protein distribution on the cell surface (Figure 5.9). For this, between 1 and 7 non-overlapping 3 µm × 3 µm regions were defined within each cell (depending on the size of the cell) (Figure 5.9B). Membrane folding on the cell edge could contribute to untypical protein patterns and thus these areas were excluded from localisation analysis.

To describe the spatial organisation of CD16 molecules, point pattern analysis was performed on the data from selected regions (Figure 5.9C). For this, two different methods were used; to describe global patterns of molecule distribution relative to randomised simulations Ripley's K function was used (5.9E). To quantify the extent of clustering and to obtain information about individual clusters (e.g. size or density) Getis and Franklin's local point pattern analysis was carried out (Figure 5.9D).

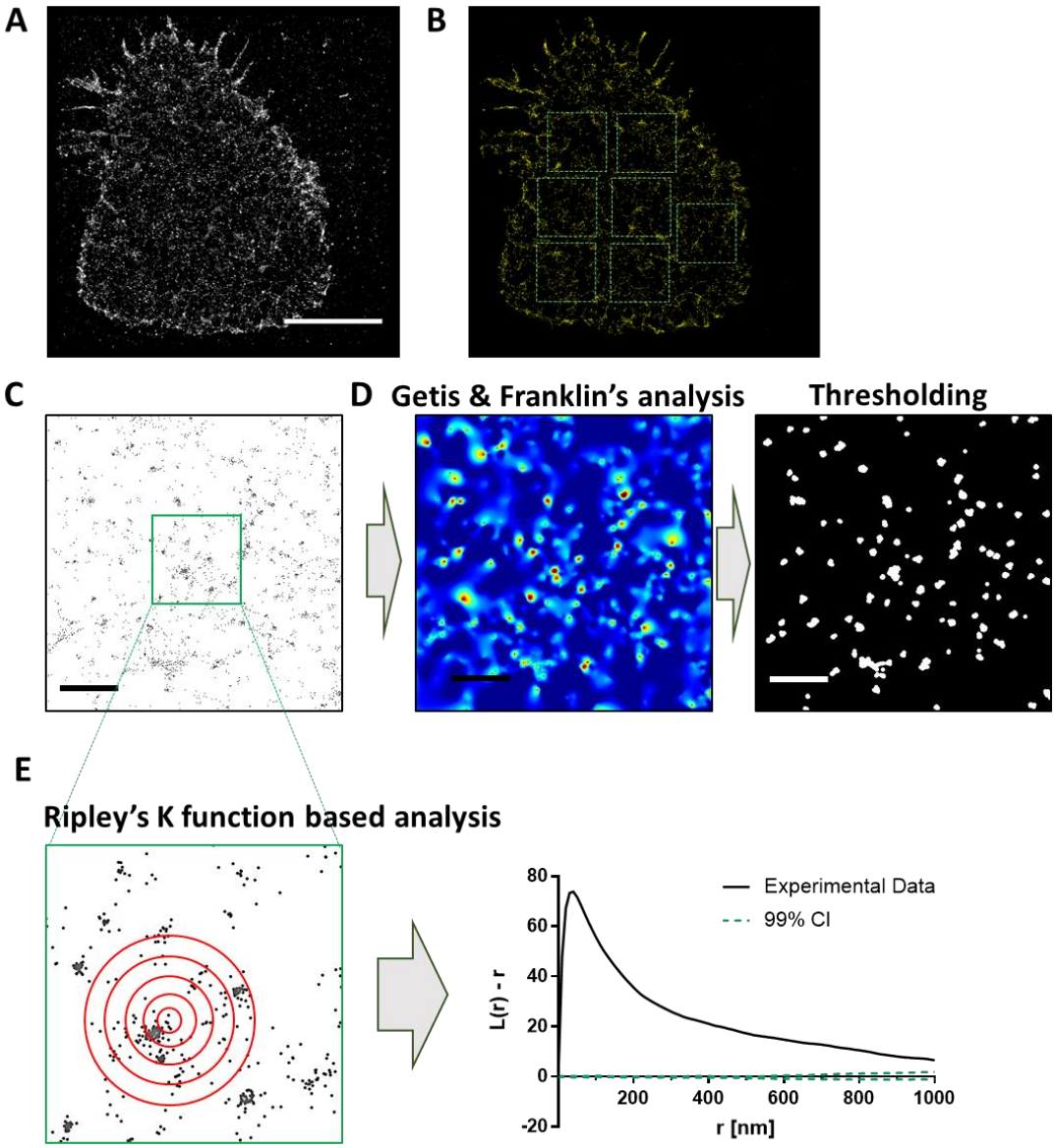

Figure 5.9: Post-detection GSD data analysis workflow. (A) Representative GSD image of a primary NK cell stained with anti-CD16 AF647 mAb and imaged by super-resolution GSD microscopy. The scale bar is 5 µm. **(B)** For the analysis of CD16 organisation, multiple 3 x 3 μm^2 regions were selected within each cell, as highlighted in green. **(C)** X and Y coordinates of detected events in each region from (B) were plotted and used for quantitative analysis. The scale bar is 500 nm. **(D)** Pseudo-colour heat-maps and binary maps were created based on Getis and Franklin's analysis method. Data obtained by this method was used to quantify relative density of CD16 molecules and to characterise CD16 clusters. **(E)** Ripley's K function-based analysis of experimental data was compared against the 99% confidence intervals of a simulated randomised distribution of the same density (dotted green lines). This analysis method provided information about the nanoscale organisation of CD16 (e.g. clustered or homogeneous).

To quantify receptor clustering, binary maps were created by overlaying a disc element of 25 nm radius around all point localisations with L(30) above a threshold value, L(30) ≥ 70. The appropriate threshold value was chosen by creating randomised data containing the same number of molecules as the representative selected regions from CD16 images. L(30) was then calculated for molecules within the randomised regions and the distribution of L(30) values was compared between randomised regions and corresponding regions from the experimental data (Figure 5.10A). Based on this, the value for the threshold was chosen to be L(30) ≥ 70 nm, above which molecules were identified as localised within a cluster and included in the binary maps. For the CD16 dataset, decreasing the threshold from 70 nm to 60 nm did not have a significant impact on the size and number of detected clusters (Figure 5.10B – D). However, a few random assemblies of molecules that we did not consider as a true cluster, were excluded by the higher threshold value, while true clusters were not affected (Figure 5.10B).

From the binary maps, the descriptors of clusters were extracted using ImageJ. Binary maps combined with the localisations of detected events allowed us to characterise CD16 clusters – cluster size, number of clusters, as well as density of molecules within clusters and the percentage of detected molecules within clusters.

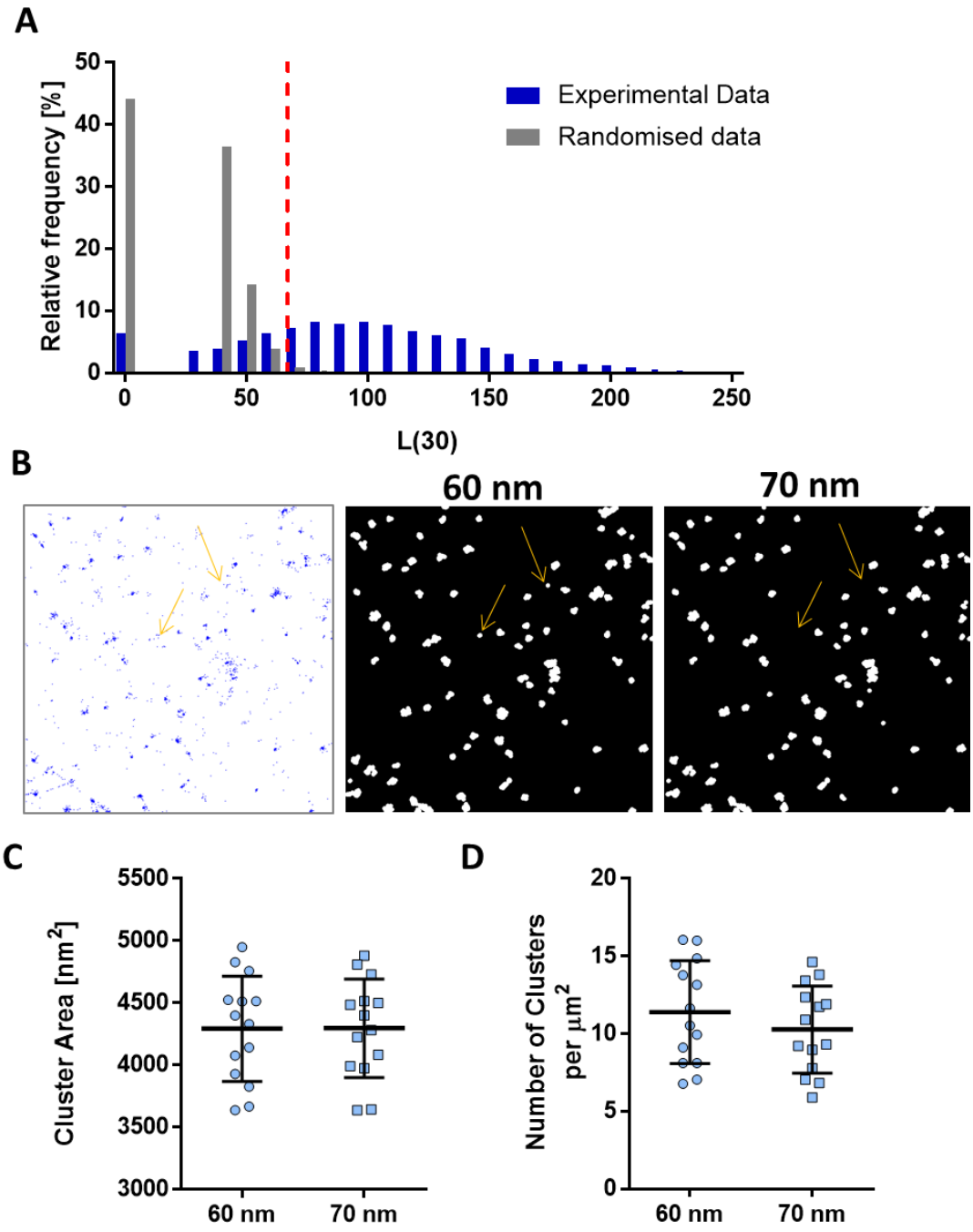

Figure 5.10: Selection of a binary threshold for CD16 cluster analysis. Primary NK cells were stained with anti-CD16 AF647 mAb and imaged on PLL-coated slides by GSD microscopy. **(A)** Getis and Franklin analysis was used to calculate L(r) values using a search radius r = 30 nm, in both experimental data and simulated randomised data of the same density. The relative frequency of L(30) values obtained for experimental CD16 data and randomised data are shown overlaid. Dotted red line represents a value, selected as a threshold for cluster analysis of the GSD data. **(B)** Representative selected 3 x 3 μm^2 region from a GSD image (left). Middle and right panels show binary maps using different threshold value. **(C, D)** Quantitative analysis of the data using two different threshold values (60 or 70 nm). Cluster area (C) and number of clusters per μm^2 (D) were compared. Each data point represents an average value per cell. Mean ± SD, n = 14 cells from two different donors.

5.3.4. Nanoscale organization of CD16 on rituximab-coated slide

Optimized conditions and analysis parameters were used to investigate CD16 nanoscale spatial organization on the NK cell surface in their resting state and upon activation by rituximab. For this, fresh primary NK cells were incubated on PLL or rituximab-coated surfaces for 5 min, fixed and stained with anti-CD16 mAb directly conjugated to AF647 dye. Super-resolution images were acquired by GSD microscopy. To characterize the spatial distribution of CD16, x and y coordinates of individual CD16 localisations were assessed by spatial point pattern analysis.

Visual inspection of diffraction limited TIRF images of CD16 on slides coated with PLL or rituximab did not reveal dramatic differences between the two (Figure 5.11A). As described above, GSD microscopy provided a significant improvement in image resolution. However, even the improved detection of CD16 molecules did not display any obvious differences between the organisations of CD16 on resting or activated NK cells. As calculated by Ripley's K function analysis the area of CD16 clusters was comparable on both surfaces. On PLL L(r) – r function reached maximum peak at 74 nm, and at 80 nm on rituximab (Figure 5.11B).

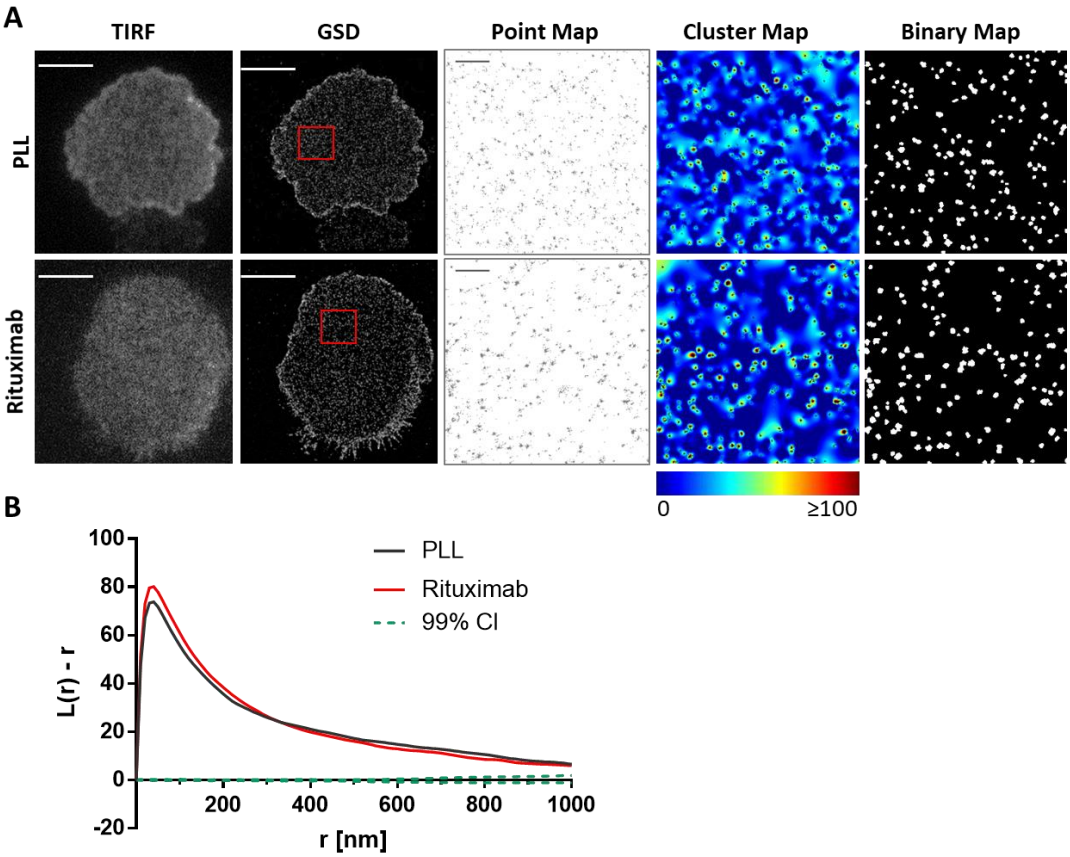

Figure 5.11: Analysis of CD16 clustering on resting and activating surfaces. Fresh primary NK cells were incubated on PLL or rituximab coated surfaces. Cells were then fixed and stained with anti-CD16 AF647 mAb (clone 3G8). TIRF and GSD images were acquired. GSD data was used for further analysis of CD16 nanoscale organisation. **(A)** Representative images of TIRF and GSD images of CD16 on PLL (upper row) and rituximab (lower row) coated surface (the scale bar is 5 μm). Zoomed in 3 x 3 μm^2 regions (red boxes in GSD image, the scale bar is 500 nm) were used to create two-dimensional pseudo-colour heat-maps of clustering. Binary maps were created by overlaying a disc element around all point localisations with L(30) ≥ 70. **(B)** Ripley's K function of CD16 events in the selected regions shown in (A) (red boxes). L(r) – r represents the degree of clustering at different spatial scales relative to simulated random distributions, indicated by the 99% confidence intervals (CI). r is the radial scale.

To ensure that the CD16 clusters are not an artefact of data processing, CD16 data was compared to data of the same density, in which the position of each localisation was randomised. When Getis and Franklin's cluster analysis was performed and the defined threshold was applied, randomised data yield no clusters, as expected (Figure 5.12). The difference between experimental data and randomised data was very clear so no further quantification was performed on randomised data. This also suggested that CD16 is indeed organised in nanoclusters.

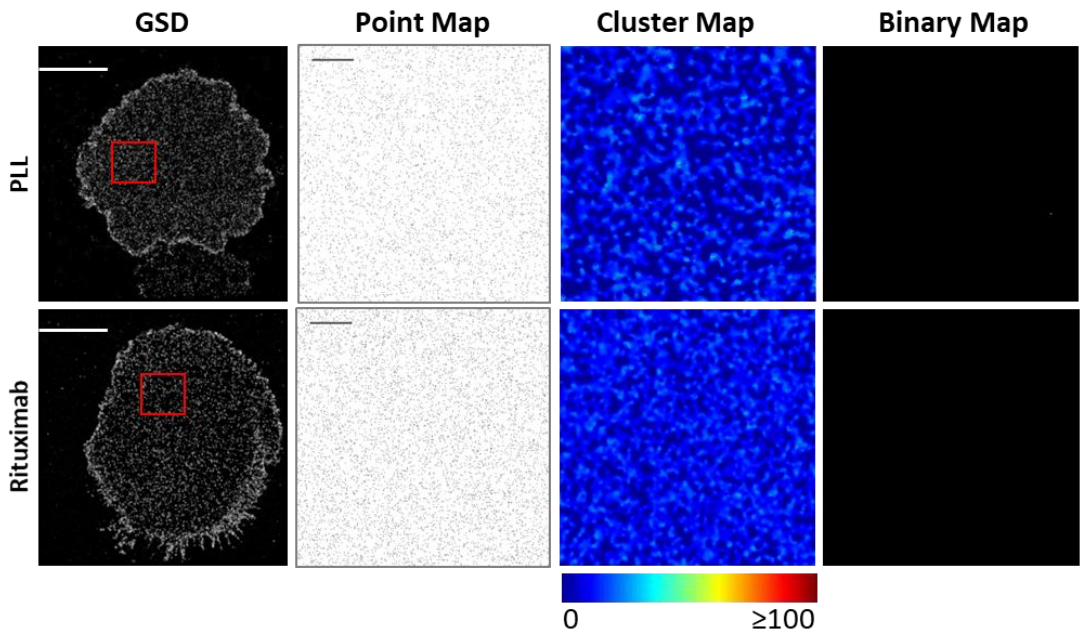

Figure 5.12: Representative maps of randomised CD16 data. Data from the selected 3 x 3 μm^2 regions (highlighted in red) of representative GSD images of CD16 on primary NK cells were used to create randomised data with the same molecule density. Simulated data was used to create the corresponding colour-coded density heat maps and binary cluster maps. The scale bars are 5 μm and 500 nm respectively.

To quantify CD16 clusters, Getis and Franklin's cluster analysis of GSD data was performed. Analysis of cluster maps revealed that the size of CD16 clusters slightly but significantly increased when cells were stimulated on rituximab (Figure 5.13A). Their mean area on PLL was 4300 ± 500 nm^2 and on rituximab it was 4600 ± 700 nm^2. The corresponding mean diameter of these clusters was 37 nm on PLL and 38 nm on rituximab. The density of CD16 clusters was comparable on both surfaces (10 ± 3 clusters/μm^2 on PLL and 11 ± 4 clusters/μm^2 on rituximab) (Figure 5.13B). The shape of clusters did not change upon the receptor ligation. On both conditions, clusters were relatively circular (Figure 5.13C). When focusing on individual molecules, there were on average 230 ± 150 CD16 events/ μm^2 detected on PLL and 290 ± 240 CD16 events/ μm^2 on rituximab, but the difference was not statistically significant (Figure 5.13D). From all events, around 75 % were found within clusters (75 ± 8 % on PLL and 76 ± 7 % on rituximab) (Figure 5.13F). On PLL there were 170 ± 108 events/ μm^2 and 210 ± 150 events/ μm^2 on rituximab found within CD16 clusters. Again, these differences were not statistically significant.

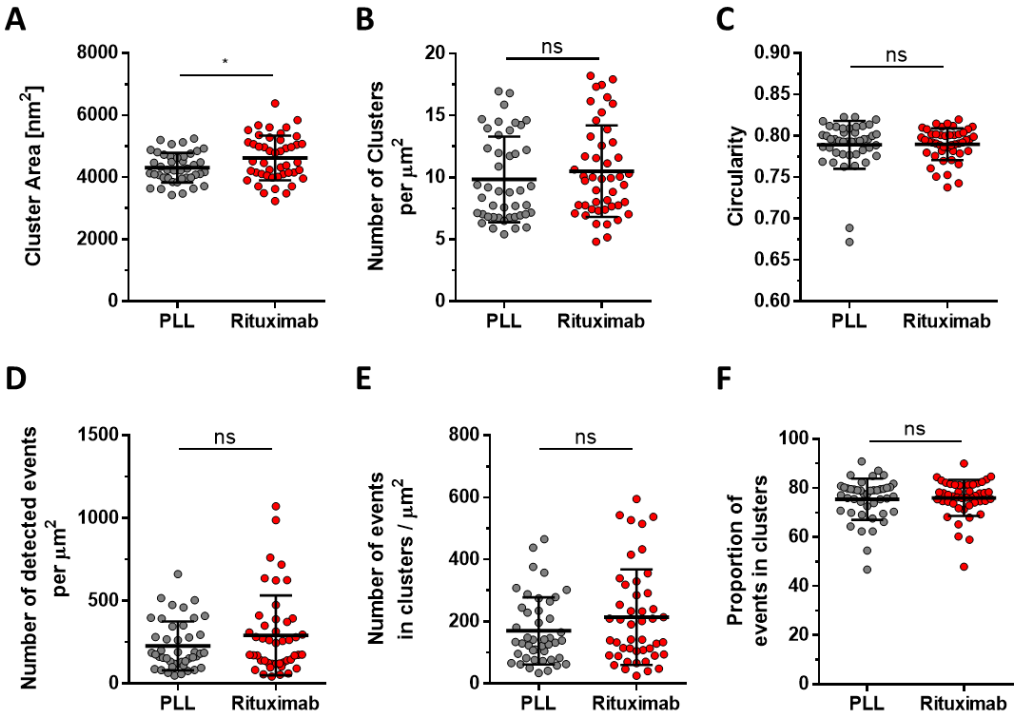

Figure 5.13: Quantitative analysis of CD16 clustering. Primary NK cells were incubated on PLL or rituximab coated surfaces. After 5 min, cells were fixed and stained with anti-CD16 AF647 mAb. Distribution of CD16 on acquired GSD images was characterised by Getis and Franklin's cluster analysis. Graphs show average cluster area **(A)**, number of clusters per µm2 **(B)**, average cluster circularity **(C)**, overall density of detected CD16 molecules **(D)**, density of CD16 molecules within clusters **(E)** and the proportion of detected molecules within clusters **(F)**. Mean ± SD, ns non-significant, * $p < 0.05$ calculated by two-tailed unpaired student t-test.

Taken together, super-resolution imaging of CD16 indicates that the receptor is clustered in small circular clusters at the NK cell surface. The ligation of the receptor by rituximab slightly increases cluster area, but other cluster properties are not affected. However, since NK cell activation also triggers shedding of CD16, it is possible that potential reorganisation of CD16 molecules cannot be detected using 3G8 clone, as its epitope is cleaved. There might be also more receptors recruiting to the synapse upon the ligation, and that could explain the slight increase in cluster area. However, it is impossible to evaluate the impact of shedding and recruitment independently. The staining of the intracellular CD16 might be more appropriate to address the surface distribution of CD16 upon its ligation, as it might be less affected by the cleavage.

5.3.5. Super-resolution imaging of intracellular CD16

In the previous chapters of this thesis, I have shown that CD16 receptor undergoes proteolytic cleavage upon NK cell activation. This could also interfere with the characterisation of receptor surface distribution. To improve the detection of CD16 molecules upon NK cell activation the CD16 labelling antibody was changed. Instead of mAb clone 3G8 which recognizes the extracellular (EC) portion of the receptor we used clone SP175 recognising the intracellular (IC) part of it. This allowed us to detect the localisation of the receptor even after the extracellular part has been cleaved. However, it should be noted that it is not known how long the tails of the cleaved receptors stay in the membrane and whether the cleavage affects the organisation.

First, anti-CD16 SP175 clone mAb was conjugated with AF647 dye and tested by confocal microscopy. For this, fresh primary NK cells were incubated on ICAM1 alone or ICAM1 with rituximab-coated surfaces for 5 min, fixed and stained. Clone SP175 provided a very bright staining (brighter than 3G8 clone used above) with very low background noise (Figure 5.14). Thus, the antibody could be used for super-resolution imaging.

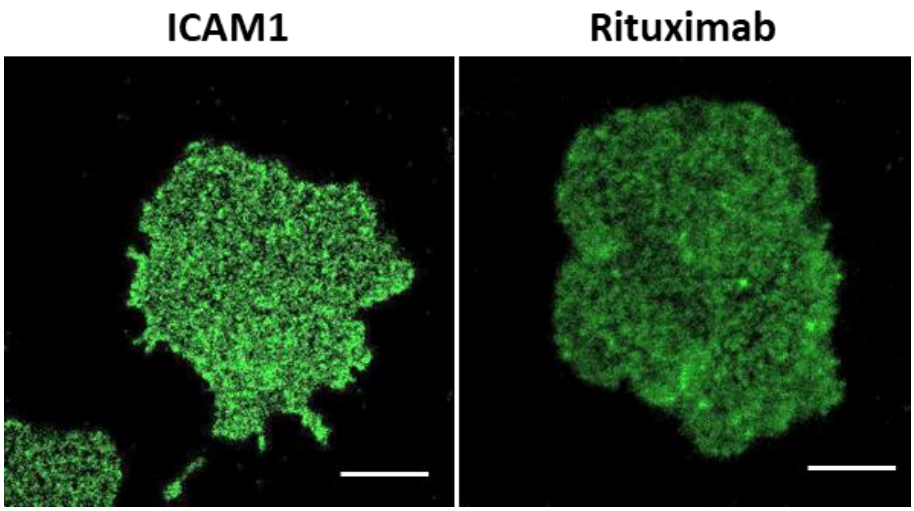

Figure 5.14: Confocal images of CD16, stained with SP175 clone. Primary NK cells were incubated on ICAM1 only or rituximab and ICAM1 coated slides for 5 min, fixed and stained with anti-CD16 (clone SP175) AF647 mAb.

Next, we set to compare clustering patterns of CD16 stained with 3G8 clone (EC CD16) and SP175 clone (IC CD16). Cells were let to spread on PLL for 5 min, fixed and stained. When stained with SP175 clone, cells were in general brighter and there were fewer cells too dim to image by GSD as compared to 3G8 staining. However, no obvious differences were observed in the acquired images of CD16 (Figure 5.15). CD16 clusters were quantified by Getis and Franklin's spatial pattern analysis.

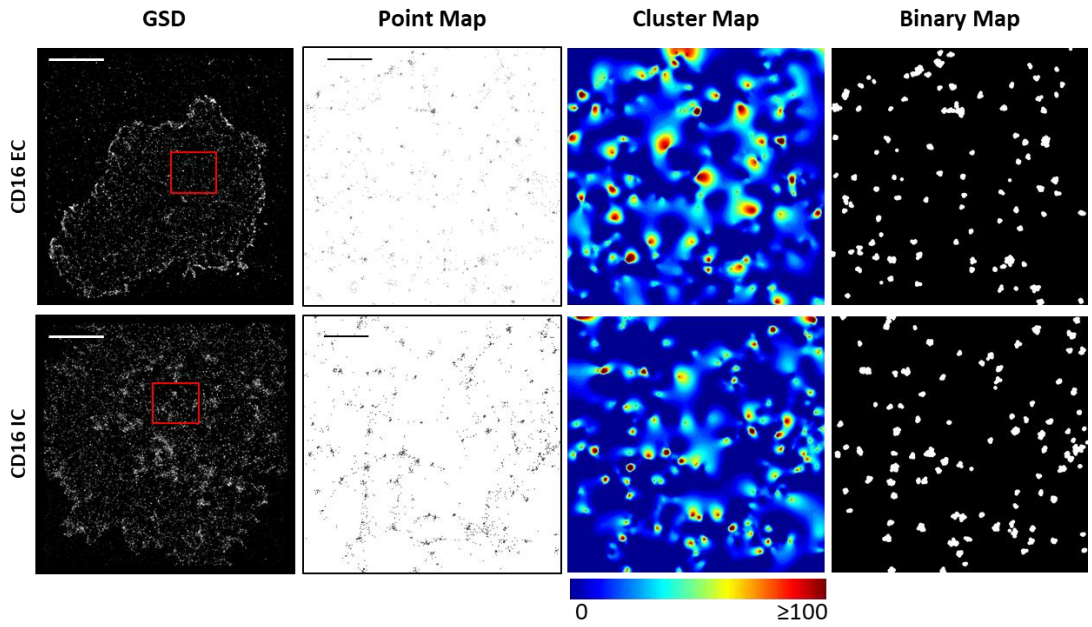

Figure 5.15: Comparison of CD16 clusters stained with 3G8 and SP175 anti-CD16 clones. Fresh primary NK cells were incubated on PLL-coated surfaces. Cells were then fixed and stained with anti-CD16 - clone 3G8 (EC, top row) and anti-CD16 – clone SP175 (IC, bottom row), both directly conjugated with AF647. GSD images were acquired and Getis and Franklin's cluster analysis was performed. Panels show representative GSD images (the scale bar is 5 µm), enlarged 3 x 3 µm^2 regions (red boxes in GSD image, the scale bar is 500 nm), two-dimensional pseudo-colour heat-maps of clustering and corresponding binary maps. Binary maps were created overlaying a disc element around all point localisations with L(30) ≥ 70.

On PLL, the average area of CD16 nanoclusters increased when the intracellular portion of CD16 was labelled (4200 ± 400 nm^2 for CD16 EC and 4600 ± 600 nm^2 for CD16 IC) (Figure 5.16A). The number of clusters per µm^2 did not increase much when the IC portion was stained (9 ± 3 clusters/µm^2 for EC and 10 ± 1 clusters/µm^2 for IC) (Figure 5.16B). With IC anti-CD16, there were 1.9-fold more events per µm^2 detected overall (180 ± 110 CD16 events/ µm^2 for the EC and 340 ± 220 CD16 events/ µm^2 for the IC) (Figure 5.16C) and more events detected within clusters (120 ± 70 events/ µm^2 for the EC and 190 ± 60 events/ µm^2 for the IC) (Figure 5.16D). However, the proportion of molecules in clusters did not change when the IC CD16 is stained (76 ± 5 % for the EC and 75 ± 5 % for the IC). Taken together, IC staining provided brighter samples with more CD16 molecules detected which also resulted in slightly larger CD16 clusters. This is likely the result of constitutive cleavage of CD16, which prevents better detection of extracellular CD16, but allows the imaging of the remaining intracellular part. However, the ratio between molecules inside clusters and outside clusters remained the same. Thus, using SP175 clone for super-resolution

imaging of CD16 could contribute to better description of CD16 clusters upon NK cell activation.

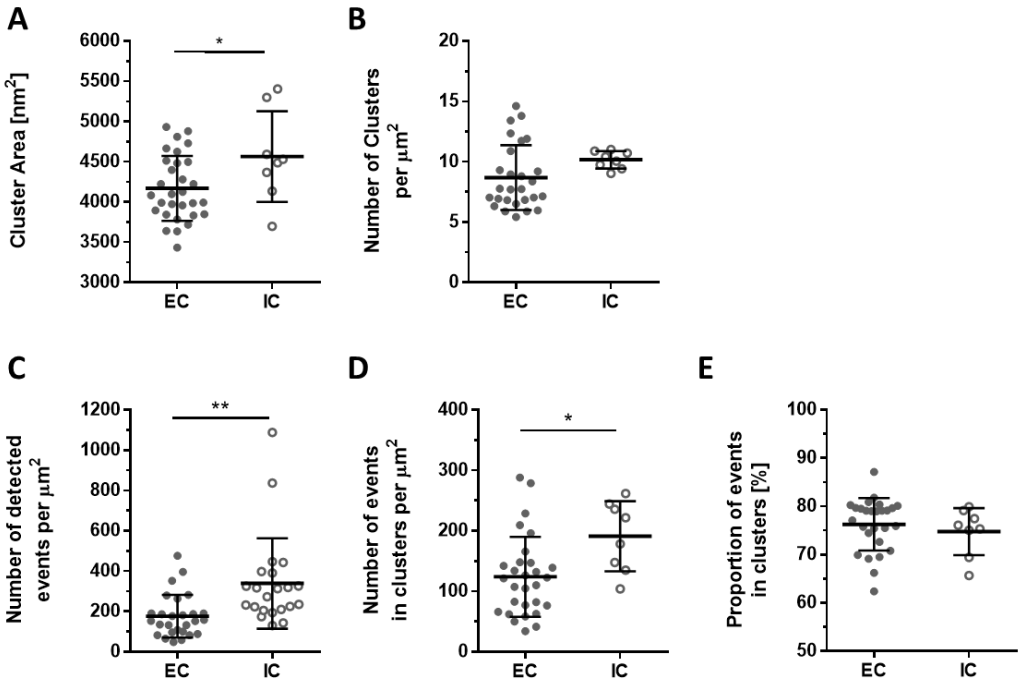

Figure 5.16: Clustering of the intracellular and extracellular portion of the surface CD16. Primary NK cells were incubated on PLL for 5 min. Then, cells were fixed and stained with two different clones of anti-CD16 (3G8 and SP175) conjugated to AF647. CD16 clustering was analysed by Getis and Franklin's cluster analysis from GSD images. Graphs show average cluster area **(A)**, number of clusters per µm^2 **(B)**, overall density of detected CD16 molecules **(C)**, density of CD16 molecules within clusters **(D)** and the proportion of detected molecules within clusters **(E)**. Data is pooled from three independent experiments and plotted as mean ± SD. *p<0.05 and **p<0.01 calculated by two-tailed unpaired student t-test.

5.3.6. CD16 nanoscale distribution upon the inhibition of CD16 shedding

To assess CD16 nanoscale reorganisation on the surface of NK cells upon the activation despite the shedding of the receptor, two steps were taken. First, to stain the sample we used an antibody recognising the intracellular portion of CD16 (clone SP175). Second, shedding of CD16 was inhibited with TAPI-0, the inhibitor of ADAM17 (as defined in Chapter 4).

As in previous experiments, NK cells were incubated for 5 min on ICAM1 alone or ICAM1 with rituximab-coated surfaces, fixed and stained with anti-CD16 conjugated to AF647. Super-resolution images were acquired using GSD microscopy and CD16 clusters were analysed using Getis and Franklin's spatial point analysis (Figure 5.17).

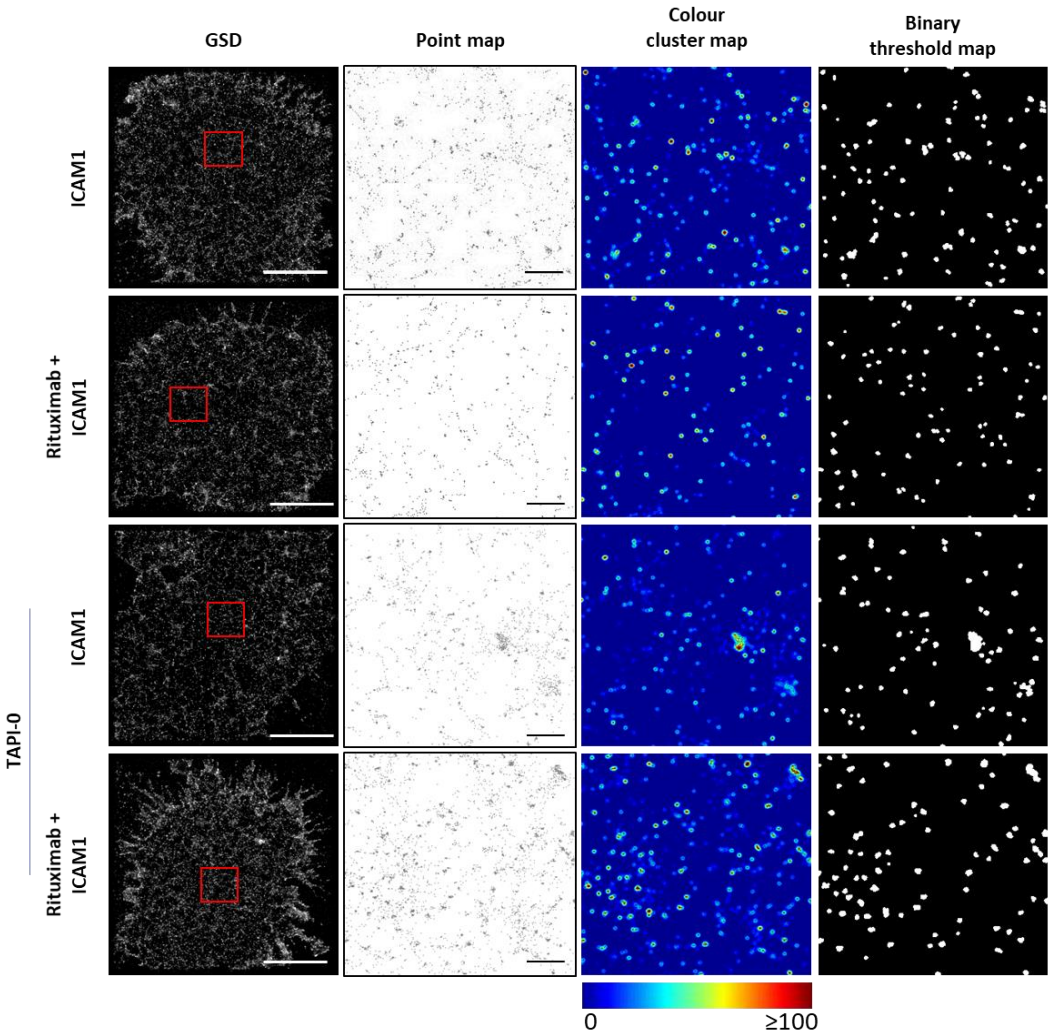

Figure 5.17: Clustering of CD16 on resting and rituximab-activated NK cells. Fresh primary NK cells were incubated for 5 min on ICAM1 alone or rituximab and ICAM1-coated surfaces with or without TAPI-0. Cells were then fixed and stained with anti-CD16 (clone SP175) conjugated with AF647. GSD images were acquired and Getis and Franklin's cluster analysis was performed. Panels show representative GSD images (the scale bar is 5 μm), enlarged 3 x 3 μm^2 regions (red boxes in GSD image, the scale bar is 500 nm), two-dimensional pseudo-colour heat-maps of clustering and corresponding binary maps. Binary maps were created overlaying a disc element around all point localisations with L(30) ≥ 70.

The mean cluster area on ICAM1 was 4100 ± 320 nm^2 and on rituximab it was 4200 ± 340 nm^2 (Figure 5.18A). The inhibition of CD16 shedding did not affect their size (4140 ± 280 nm^2 on ICAM1 and 4230 ± 320 nm^2 on rituximab). Upon activation of NK cells with rituximab, the number of clusters/μm^2 decreased (from 10 ± 2 on ICAM1 to 8 ± 2 on rituximab) (Figure 5.18B) and this reduction in density was prevented upon the addition of TAPI-0 (10 ± 2 and 10 ± 1 clusters/μm^2). Consistent with the cluster number, the number of all detected events was also reduced upon the activation with rituximab (Figure 5.18C, D). The number of all detected events decreased from 340 ± 240 to 200 ± 100 events / μm^2 and the number of events inside clusters from 180 ± 60 to 120 ± 50 events / μm^2. Upon the inhibition of CD16 shedding, the number of detected events, was not affected by rituximab. In the presence of TAPI-0, the total number of detected events was 300 ± 140 on ICAM1 and 320 ± 140 events/μm^2 on rituximab. Of total events, 190 ± 60 on ICAM1 and 190 ± 60 events/μm^2 on rituximab were found within clusters. However, on rituximab, there were significantly more CD16 events inside clusters, when shedding of CD16 was prevented. Neither, the ligation of CD16 nor the inhibition of CD16 shedding had any impact on the distribution of CD16 molecules within or outside clusters (Figure 5.18E). 62 ± 16 % molecules were found within clusters on ICAM1 and 64 ± 11 % on rituximab. In the presence of TAPI-0 65 ± 10 % lied within clusters on ICAM1 and 63 ± 12 % on rituximab. On ICAM1, there were on average 18 ± 4 detected events inside each cluster and 16 ± 4 upon the receptor ligation. Upon the inhibition of CD16 shedding, 19 ± 4 molecules were on average found per cluster on ICAM1 and 20 ± 5 on rituximab. Again, when TAPI-0 was added, the number of events per cluster increased upon CD16 ligation.

Thus, the use of ADAM17 inhibitor contributes to a better detection of CD16 molecules upon CD16 ligation. But these data indicate that the surface organisation of CD16 is not affected by the ligation of rituximab, other than through shedding a fraction of the protein. It seems that the shedding of CD16 happens equally inside and outside CD16 nanoclusters. Or, perhaps the proteins are dynamically moving in and out of clusters in order to keep the clusters unaffected from shedding.

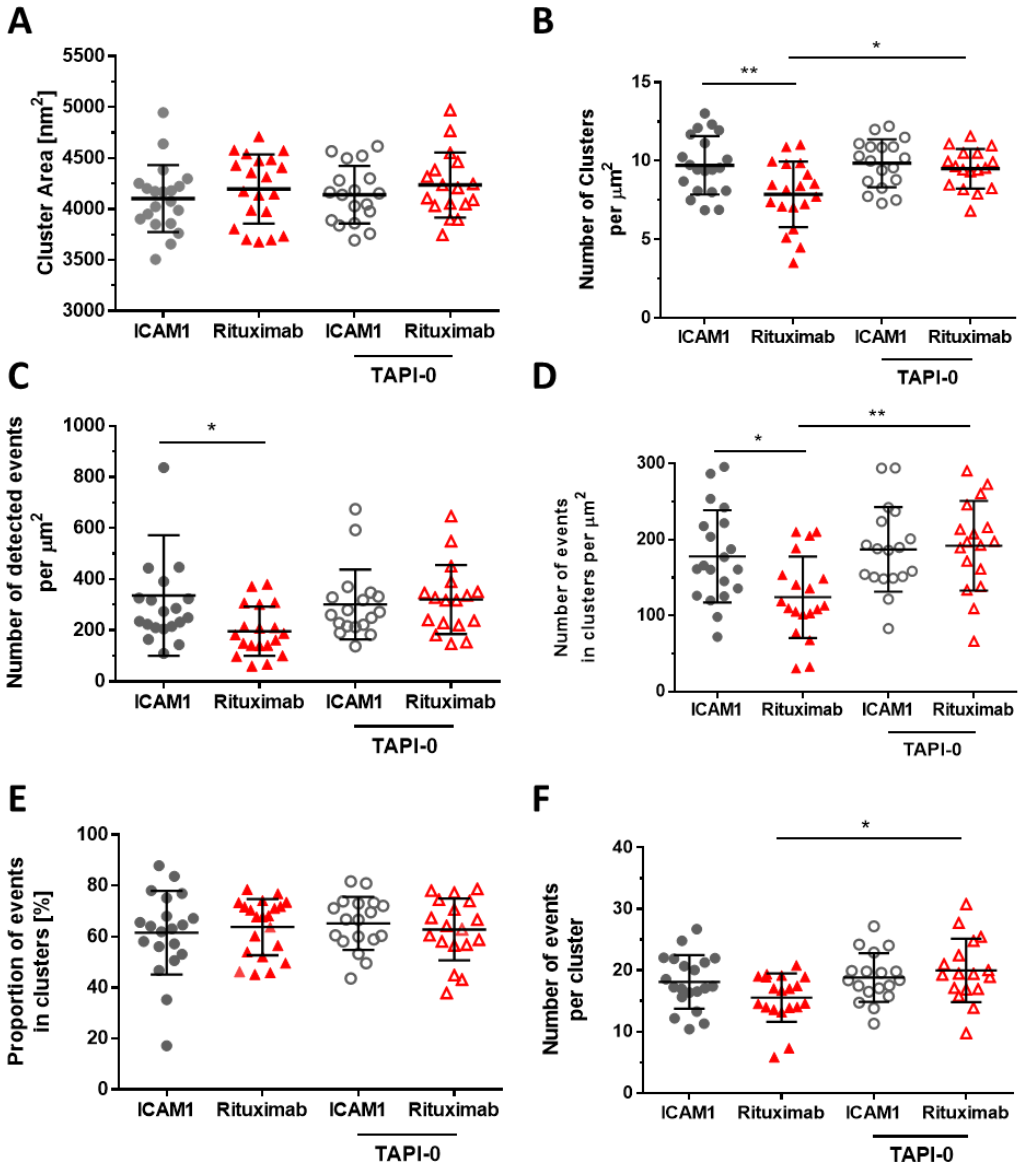

Figure 5.18: Analysis of CD16 clusters upon the receptor ligation. Primary NK cells were incubated on PLL or rituximab coated surfaces for 5 min, fixed and stained with anti-CD16 AF647 mAb, clone SP175. Distribution of CD16 on acquired GSD images was characterised by Getis and Franklin's cluster analysis. Graphs show average cluster area **(A)**, number of clusters per µm^2 **(B)**, overall density of detected CD16 molecules **(C)**, density of CD16 molecules within clusters **(D)**, the proportion of detected molecules within clusters **(E)** and the number of individual events within each cluster **(F)**. Data is pooled from three independent experiments and plotted as mean ± SD. *p<0.05 and **p<0.01 calculated by one-way ANOVA.

5.4. Discussion and further directions

5.4.1. Summary of results

The aim of this chapter was to study CD16 nanoscale organisation on NK cells in their resting state and to quantify any potential changes upon CD16 ligation by rituximab. This was achieved using GSD super-resolution microscopy. In order to ensure accuracy and precision of localisations of individual CD16 molecules, several parameters for GSD data post-processing and cluster analysis needed to be optimised. The spatial distribution of surface CD16 proteins was then assessed by point pattern analysis methods. The main findings derived from this chapter are as follows:

i. With optimised super-resolution GSD microscopy, the resolution of 40 nm can be achieved and thus the technique can be used to study nanoscale organisation of CD16;
ii. Around 75 % of all CD16 molecules on NK cell surface are organised in small dense clusters, in both, resting state and upon NK cell activation;
iii. CD16 ligation by rituximab leads to reduction of CD16 molecules at the NK cell-coverslip interface, but the inhibition of CD16 shedding by TAPI-0 prevents it;
iv. In the presence of TAPI-0, incubation on rituximab did not affect CD16 surface distribution.

5.4.2. Relation to earlier studies

Many immune cell receptors have been reported to be organised in a defined structure in the plasma membrane. Early studies showed that receptors form supramolecular microclusters and the advances in microscopy revealed that clusters are organised also on nanoscale level. There are extensive studies on changes in the distribution of TCR or BCR upon their engagement including the reorganisation of their signalling molecules. Nanoscale organisation of NK cell receptors has been mainly demonstrated by our group (Bálint et al., in print, Oszmiana et al., 2016, Pageon et al., 2013).

However, there are no reports on the nano-organisation of CD16 receptor in NK cells. But, CD16 has been previously demonstrated to form microclusters upon its ligation.

In a study, using planar lipid bilayers displaying IgG1 Fc as a ligand for CD16, Fc accumulated at the centre of the synapse. Live imaging further confirmed that Fc forms peripheral microclusters which move towards the centre over time. The addition of inhibitory HLA-E to the bilayer led to the reduction of Fc cluster numbers, but their size or central accumulation were not affected (Liu, Immunity, 2012). Another study using planar lipid bilayers carrying anti-CD16 antibody addressed the effects of β_2-integrin signalling on the size and dynamics of receptor microclusters (Steblyanko et al., 2015). When NK92/CD16$^+$ cells landed on bilayers containing ICAM1, area of CD16 microcluster was almost twice as large as the area of microclusters on bilayers without ICAM1. The addition of ICAM1 to bilayers also increased the mobility of CD16 microclusters in concentration-dependent manner. However, greater displacement of CD16 clusters in the presence of ICAM1 could be attributed to the larger spreading area of the cell. The changes observed on bilayers carrying ICAM1 coincided with greater degranulation which indicates that larger CD16 clusters correspond to greater response.

The current study has demonstrated the existence of CD16 nanoclusters. By labelling CD16 with two different antibodies, recognising epitopes on either intracellular or extracellular CD16 we observed that the majority of CD16 molecules on NK cells is assembled in nanoclusters. But interestingly, the size and distribution of clusters were not affected by receptor ligation to rituximab. This was perhaps because the ligands in our study were immobilised on glass surfaces. Thus, cells could not have pushed them into specific areas.

The mean area of CD16 clusters was 4200 nm^2 as assessed by the anti-EC CD16 mAb or 4600 nm^2 by the anti-IC CD16 mAb. The corresponding diameters were 73 nm or 77 nm, respectively. Small differences in the size between the two might result from inter-donor variability. Spontaneous shedding of CD16 might also contribute to slightly smaller clusters recognised by the antibody, ligating the extracellular (shed) part. In comparison to other NK cell receptors, CD16 nanoclusters were smaller. In human primary NK cells, the median area of clusters of an activating receptor KIR2DS1 was 16600 nm^2 with the corresponding diameter of 145 nm. The clusters of an inhibitory receptor KIR2DL1 measured in the same study were 6700 nm^2, with a corresponding diameter of 92 nm (Oszmiana et al., 2016). Mean NKG2D cluster area was 15600 nm^2 and their corresponding diameter 140 nm (Bálint et al., in print). KIR2DS1 and KIR2DL1 were both expressed at much higher level than CD16, as shown by the total density of detected molecules (around 1000 events/µm^2 for both vs. 170 or 390 events/µm^2 for EC or IC CD16 respectively). On the other hand, around

75 % of CD16 molecules were found within cluster structures, while less than 20 % of KIR2DL1 was clustered. These results combined suggest that the distribution of molecules on NK cell surface is very specific to each receptor.

One thing one should keep in mind when studying nanoscale distribution of surface proteins is that like any other super-resolution technique, GSD also has its caveats. There are several parameters that can contribute to the final interpretation of the data. Every step, from sample preparation (e.g. fixation method, labelling strategy) to image acquisition (e.g. number of frames acquired, laser power) and data processing (e.g. parameters for data filtering, threshold values) can have a significant impact on final information on clustering. Thus, it is essential to optimise the experiment with great precision and apply the same method to all conditions.

However, our understanding of super-resolution data is constantly improving. This leads to alternative approaches to data processing which can sometimes affect the obtained results. For instance, average diameter of KIR2DL1 clusters at the surface of human primary NK cells was first reported to be 146 nm (Pageon et al., 2013). In a more recent study, the diameter of the same molecule was estimated to be much smaller (92 nm) (Oszmiana et al., 2016). The difference could be explained by a slight difference in the data analysis. In the first study, the pseudo-colour heat-maps were created by interpolating values of L(50) on a grid and binary maps were created by thresholding these interpolated pseudo-colour heat-maps. Such way of cluster mapping occasionally resulted in merging two or more clusters localized near each other although they appeared as separate structures in the corresponding super-resolution images. In the second study Oszmiana et al. overcame this problem by reducing the search radius for Getis and Franklin's cluster analysis to a value, empirically defined for a specific dataset. Moreover, the binary maps were not generated by thresholding of the colour maps, but by drawing a disc object with a diameter equal to the threshold uncertainty value (50 nm) around each molecule for which $L(30) \geq 65$. The $L(30) \geq 65$ threshold was chosen by comparing the distribution of L(30) values in experimental and randomized regions. The changes improved the localisation precision of individual molecules and resulted in smaller sizes of KIR2DL1 clusters. The later strategy was also used to assess CD16 clusters.

Baumgart et al. recently proposed a method that is insensitive to artefacts generated by over-counting of blinking fluorophores and thus merging of the re-appearing events is not necessary (Baumgart et al., 2016). The method relies on deliberate variation of labelling density combined with cluster analysis and can efficiently discriminate

clustered from randomly distributed molecules. To provide another layer of evidence that CD16 is indeed organised in clusters, this approach could be used.

Importantly however, the characterisation of molecule distribution will always depend on the analytical method and selected parameters and should be considered as indicative rather than definitive. Thus, the absolute values of protein clusters cannot be compared between different studies, but best serves as an indication. However, the technique can be used reliably for a relative comparison between different conditions (e.g. resting NK cell vs. activated NK cell) when acquired and processed in the same way.

NK cell receptors have been shown to change their nanoscale organisation upon the ligation of their cognate ligands. KIR2DS1 clusters became larger upon ligation of anti-KIR2DL/S1 mAb (Oszmiana et al., 2016). The reorganisation of NKG2D clusters depends on the ligand; the engagement through MICA leads to smaller NKG2D clusters while the ligation by ULBP2 results in larger clusters (Bálint et al., in print). Moreover, redistribution of one NK cell receptor can be triggered by the engagement of another one. Upon the ligation of NKG2D, KIR2DL1 clusters became smaller and denser than in resting state (Pageon et al., 2013). In this chapter, we assessed the changes in CD16 distribution upon its ligation by rituximab. When using staining antibody that recognizes the EC CD16, cluster area was slightly larger upon receptor engagement. However, that was not seen when IC CD16 was stained. In fact, the labelling of CD16 revealed that rituximab leads to the reduction of CD16 molecules at the interface. Observation that this reduction was prevented when CD16 shedding inhibitor (TAPI-0) was used indicates that there are less molecules on the surface because CD16 is cleaved upon rituximab ligation. Thus, shedding of the receptor interferes with the detection of CD16 molecules on the surface. TAPI-0 does inhibit the shedding, however when present the shedding is not completely prevented. Thus, even with the drug, the detection of CD16 molecules is likely not entirely accurate.

However, the inhibition of shedding did not lead to any changes in CD16 cluster distribution on rituximab. This is perhaps due to the unique property of the receptor to be cleaved upon activation. It is possible that other receptors need to reorganise in order to provide suitable signalling platform, while CD16 uses different mechanisms. In previous chapter of this work I have shown that cells make stable synapse through NKG2D but motile kinapse on rituximab. These differences might explain different requirements for cluster rearrangements. While cells on MICA are static, their clusters need to reorganise in order to come in contact with the signalling

molecules. In line with this, Oszmiana et al reported that larger KIR2DS1 clusters are more often associated with its adaptor molecule DAP12 (Oszmiana et al., 2016). On the other hand, the motile nature of NK cells on rituximab might enforce contacts between CD16 and its signalling molecules by moving the entire cell body and thus the redistribution of CD16 clusters is not needed.

5.4.3. Future directions

There are several questions about CD16 nanoscale distribution that remain open. First, it would be important to address to relation between CD16 receptor and its signalling adaptor molecules. The ligation of CD16 can lead to signal transduction through homodimers of FcεRIγ or CD3ζ or with heterodimers of FcεRIγ and CD3ζ (Lanier, 2008). It is not known whether the associations between CD16 and its adaptors are completely random or do different signals lead to different associations. Another unknown is whether the assembly with different signalling molecules translates into differential functional outcome. However, there is some data supporting this idea. A subset of NK cells missing FcεRIγ chain has been shown to respond with greater IFN-γ production upon CD16 ligation comparing to conventional NK cells, while its degranulation was not affected (Lee et al., 2015). Therefore, the engagement of different adaptors might indeed define the nature of NK cell responses. Using super-resolution microscopy, it would be interesting to address if different types of CD16 clusters preferentially associate with a specific adaptor. By understanding the cluster requirements for triggering certain type of immune response, they could be therapeutically regulated.

On the other hand, imaging of signalling molecules in relation to CD16 could address the above-mentioned question whether the reorganisation of CD16 clusters is not necessary because the signalling molecules are pushed to CD16 as a result of NK cell movement (and thus, the size or shape of CD16 clusters is irrelevant).

The potential importance of CD16 nanoscale organisation was indicated in a study, where CD16 ligands were coated on gold nanospheres with controlled spacing. When the distance between ligands exceeded 104 nm, NK cell responses were decreased (Delcassian et al., 2013). Moreover, the ligation of CD16 by soluble ligands does not trigger NK cell activation. But, NK cell responses can be efficiently triggered by slightly larger immune complexes, consisting of multiple antibodies (Nimmerjahn and Ravetch, 2008) . Also, when soluble ligands were immobilised to 150 nm large graphene particles, IFN-γ production and NK cell degranulation were significantly

enhanced comparing to soluble ligands (Loftus et al., submited). These results together suggest that the ligation of individual CD16 molecule or the ligation of CD16 molecules that are too far apart does not lead to efficient activation. Thus, perhaps multiple CD16 receptors within the same cluster need to be crosslinked in order to provide strong activating signal.

Finally, it would be important to establish the relation between the CD16 receptor and ADAM17, the enzyme responsible for its cleavage. ADAM17 has been previously demonstrated to be sequestered in lipid rafts (Tellier et al., 2006). The shedding of TNF and TNFR was limited to these cholesterol-rich membrane microdomains. Outside lipid rafts ADAM17 substrates were not reachable to the enzyme and thus protected from the shedding. When cholesterol was depleted from cell membrane by cyclodextrins, its shedding capacity was increased, likely because of the increased access to its substrates. Based on this, it is intuitive to speculate that stopping CD16 from entering lipid rafts could prevent CD16 shedding and therefore modulate CD16-induced NK cell responses.

Super-resolution microscopy enables visualisation of changes on the nanoscale level that might crucially impact NK cell responses. However, studying CD16 nanoscale distribution is particularly challenging, as it is difficult to segregate changes occurring because of receptor ligation and changes that result from shedding. In this study data, obtained by two labelling strategies suggests that CD16 is indeed organised in nanoclusters whose size is independent from receptor ligation. The observation that their area remains the same even upon the reduced density resulting from the receptor cleavage indicates that perhaps CD16 cluster size is indeed important for CD16 function.

Chapter 6:

Final conclusions

CD16 is one of the most studied NK cell receptors. Because of its ability to trigger antibody-dependent cellular cytotoxicity (ADCC) with therapeutic antibodies, its intact function can be of immense importance for treatments of cancers or viral diseases. However, NK cell activation has been shown to lead to the cleavage of CD16 extracellular portion – the part that serves as an epitope for IgG antibodies. Importantly, this results in very low levels of CD16 on the surface of NK cells from patients with chronic diseases (cancer or chronic viral infections). Such CD16 downregulation has been correlated with poor responses to therapies with therapeutic antibodies.

Here we aimed to address three different outcomes CD16 shedding might have on NK cell function. First, we wanted to address how the shedding of the receptor affects NK cell serial killing capacity. Then, we set out to investigate the impact the cleavage of the receptor has on synapse formation and the stability of conjugates with opsonised targets. And finally, we aimed to describe CD16 nanoscale spatial organisation on NK cell surface and the changes that occur upon the ligation of the receptor and/or its shedding.

The main discoveries arising from this study are summarised below:

i. Shedding of CD16 reduces NK cell potential to execute ADCC. This occurs upon NK cell activation through CD16 or another activating NK cell receptor, NKG2D. But importantly, when the NK cell encounters an opsonised target first, their cytotoxicity towards targets expressing other ligands is not affected. Thus, effective re-stimulation of NK cells is dependent on the sequence of receptor ligation. (Chapter 3)

ii. CD16 shedding prevents the formation of a stable synapse and promotes the detachment from opsonised targets. Efficient detachment reduces the secretion of pro-inflammatory cytokine and prevents NK cell lysis due to

over-activation. This together could be beneficial for NK cell serial killing potential. (Chapter 4)

iii. CD16 molecules aggregate into small dense nanoclusters. The binding to the ligand or CD16 downregulation due to shedding do not affect the size of these clusters. However, cleavage of the receptors decreases the density of the clusters. Thus, perhaps a defined CD16 cluster size is required for appropriate CD16 function. (Chapter 5)

In summary, in this work we have demonstrated that CD16 shedding leads to decreased ADCC function, but at the same time it is crucial for the detachment from opsonised targets while preventing NK cell death. The maintained cytotoxicity through other receptors can lead to sequential lysis of other targets. Thus, CD16 shedding plays a significant role in efficient NK cell serial killing and its manipulation might have an important therapeutic potential, especially in combination with antibody-based treatments.

Bibliography

ABEYWEERA, T. P., MERINO, E. & HUSE, M. 2011. Inhibitory signaling blocks activating receptor clustering and induces cytoskeletal retraction in natural killer cells. *The Journal of cell biology,* 192**,** 675-690.

ADAM, C., KING, S., ALLGEIER, T., BRAUMÜLLER, H., LÜKING, C., MYSLIWIETZ, J., KRIEGESKORTE, A., BUSCH, D. H., RÖCKEN, M. & MOCIKAT, R. 2005. DC-NK cell cross talk as a novel CD4+ T-cell–independent pathway for antitumor CTL induction. *Blood,* 106**,** 338-344.

ALBA, A., PLANAS, R., CLEMENTE, X., CARRILLO, J., AMPUDIA, R., PUERTAS, M. C., PASTOR, X., TOLOSA, E., PUJOL-BORRELL, R. & VERDAGUER, J. 2008. Natural killer cells are required for accelerated type 1 diabetes driven by interferon-β. *Clinical & Experimental Immunology,* 151**,** 467-475.

ALBER, G., KENT, U. & METZGER, H. 1992. Functional comparison of Fc epsilon RI, Fc gamma RII, and Fc gamma RIII in mast cells. *The Journal of Immunology,* 149**,** 2428-2436.

ALBERTSSON, P. A., BASSE, P. H., HOKLAND, M., GOLDFARB, R. H., NAGELKERKE, J. F., NANNMARK, U. & KUPPEN, P. J. 2003. NK cells and the tumour microenvironment: implications for NK-cell function and anti-tumour activity. *Trends in immunology,* 24**,** 603-609.

ALMEIDA, C. R. & DAVIS, D. M. 2006. Segregation of HLA-C from ICAM-1 at NK cell immune synapses is controlled by its cell surface density. *The Journal of Immunology,* 177**,** 6904-6910.

ALTER, G., MARTIN, M. P., TEIGEN, N., CARR, W. H., SUSCOVICH, T. J., SCHNEIDEWIND, A., STREECK, H., WARING, M., MEIER, A. & BRANDER, C. 2007. Differential natural killer cell–mediated inhibition of HIV-1 replication based on distinct KIR/HLA subtypes. *Journal of Experimental Medicine,* 204**,** 3027-3036.

ANDERSON, D. H., SAWAYA, M. R., CASCIO, D., ERNST, W., MODLIN, R., KRENSKY, A. & EISENBERG, D. 2003. Granulysin crystal structure and a structure-derived lytic mechanism. *Journal of molecular biology,* 325**,** 355-365.

ANFOSSI, N., ANDRÉ, P., GUIA, S., FALK, C. S., ROETYNCK, S., STEWART, C. A., BRESO, V., FRASSATI, C., REVIRON, D. & MIDDLETON, D. 2006. Human NK cell education by inhibitory receptors for MHC class I. *Immunity,* 25**,** 331-342.

ARNON, T. I., ACHDOUT, H., LEVI, O., MARKEL, G., SALEH, N., KATZ, G., GAZIT, R., GONEN-GROSS, T., HANNA, J. & NAHARI, E. 2005. Inhibition of the NKp30 activating receptor by pp65 of human cytomegalovirus. *Nature immunology,* 6**,** 515.

ARNON, T. I., LEV, M., KATZ, G., CHERNOBROV, Y., PORGADOR, A. & MANDELBOIM, O. 2001. Recognition of viral hemagglutinins by NKp44 but not by NKp30. *European journal of immunology,* 31**,** 2680-2689.

ASHDOWN, G. W., BURN, G. L., WILLIAMSON, D. J., PANDŽIĆ, E., PETERS, R., HOLDEN, M., EWERS, H., SHAO, L., WISEMAN, P. W. & OWEN, D. M. 2017. Live-Cell Super-resolution Reveals F-Actin and Plasma Membrane Dynamics at the T Cell Synapse. *Biophysical Journal,* 112**,** 1703-1713.

AVRIL, T., FLOYD, H., LOPEZ, F., VIVIER, E. & CROCKER, P. R. 2004. The membrane-proximal immunoreceptor tyrosine-based inhibitory motif is critical for the inhibitory signaling mediated by Siglecs-7 and-9, CD33-related Siglecs expressed on human monocytes and NK cells. *The Journal of Immunology,* 173**,** 6841-6849.

BÁLINT, Š., LOPES, F. B. & DAVIS, D. M. in print. A nanoscale reorganization of IL-15 cytokine receptor is triggered by NKG2D in a ligand dependent manner.

BANKS, N. D., KINSEY, N., CLEMENTS, J. & HILDRETH, J. E. 2002. Sustained antibody-dependent cell-mediated cytotoxicity (ADCC) in SIV-infected macaques correlates with delayed progression to AIDS. *AIDS research and human retroviruses,* 18**,** 1197-1205.

BAO, G. & SURESH, S. 2003. Cell and molecular mechanics of biological materials. *Nat Mater,* 2**,** 715-725.

BÄR, E., WHITNEY, P. G., MOOR, K., E SOUSA, C. R. & LEIBUNDGUT-LANDMANN, S. 2014. IL-17 regulates systemic fungal immunity by controlling the functional competence of NK cells. *Immunity,* 40**,** 117-127.

BARBER, D. F., FAURE, M. & LONG, E. O. 2004. LFA-1 contributes an early signal for NK cell cytotoxicity. *The Journal of Immunology,* 173**,** 3653-3659.

BARTON, K., MUTHUSAMY, N., FISCHER, C., TING, C.-N., WALUNAS, T. L., LANIER, L. L. & LEIDEN, J. M. 1998. The Ets-1 transcription factor is required for the development of natural killer cells in mice. *Immunity,* 9**,** 555-563.

BAUER, S., GROH, V., WU, J., STEINLE, A., PHILLIPS, J. H., LANIER, L. L. & SPIES, T. 1999. Activation of NK cells and T cells by NKG2D, a receptor for stress-inducible MICA. *Science,* 285**,** 727-729.

BAUMGART, F., ARNOLD, A. M., LESKOVAR, K., STASZEK, K., FÖLSER, M., WEGHUBER, J., STOCKINGER, H. & SCHÜTZ, G. J. 2016. Varying label density allows artifact-free analysis of membrane-protein nanoclusters. *Nature methods,* 13**,** 661-664.

BERTONE, S., SCHIAVETTI, F., BELLOMO, R., VITALE, C., PONTE, M., MORETTA, L. & MINGARI, M. C. 1999. Transforming growth factor-β-induced expression of CD94/NKG2A inhibitory receptors in human T lymphocytes. *European journal of immunology,* 29**,** 23-29.

BETTS, M. R., BRENCHLEY, J. M., PRICE, D. A., DE ROSA, S. C., DOUEK, D. C., ROEDERER, M. & KOUP, R. A. 2003. Sensitive and viable identification of antigen-specific CD8+ T cells by a flow cytometric assay for degranulation. *Journal of immunological methods,* 281**,** 65-78.

BETZIG, E., PATTERSON, G. H., SOUGRAT, R., LINDWASSER, O. W., OLENYCH, S., BONIFACINO, J. S., DAVIDSON, M. W., LIPPINCOTT-SCHWARTZ, J. & HESS, H. F. 2006. Imaging intracellular fluorescent proteins at nanometer resolution. *Science,* 313**,** 1642-1645.

BHAT, R. & WATZL, C. 2007. Serial killing of tumor cells by human natural killer cells–enhancement by therapeutic antibodies. *PloS one,* 2**,** e326.

BIASSONI, R., FALCO, M., CAMBIAGGI, A., COSTA, P., VERDIANI, S., PENDE, D., CONTE, R., DI DONATO, C., PARHAM, P. & MORETTA, L. 1995. Amino acid substitutions can influence the natural killer (NK)-mediated recognition of HLA-C molecules. Role

of serine-77 and lysine-80 in the target cell protection from lysis mediated by" group 2" or" group 1" NK clones. *Journal of Experimental Medicine,* 182**,** 605-609.

BILLADEAU, D. D., UPSHAW, J. L., SCHOON, R. A., DICK, C. J. & LEIBSON, P. J. 2003. NKG2D-DAP10 triggers human NK cell–mediated killing via a Syk-independent regulatory pathway. *Nature immunology,* 4**,** 557-564.

BINSTADT, B. A., BRUMBAUGH, K. M., DICK, C. J., SCHARENBERG, A. M., WILLIAMS, B. L., COLONNA, M., LANIER, L. L., KINET, J.-P., ABRAHAM, R. T. & LEIBSON, P. J. 1996. Sequential involvement of Lck and SHP-1 with MHC-recognizing receptors on NK cells inhibits FcR-initiated tyrosine kinase activation. *Immunity,* 5**,** 629-638.

BITTEL, A. M., SALDIVAR, I., DOLMAN, N., NICKERSON, A. K., LIN, L.-J., NAN, X. & GIBBS, S. L. Effect of labeling density and time post labeling on quality of antibody-based super resolution microscopy images. SPIE BiOS, 2015. International Society for Optics and Photonics, 93310M-93310M-5.

BLÁZQUEZ-MORENO, A., PARK, S., IM, W., CALL, M. J., CALL, M. E. & REYBURN, H. T. 2017. Transmembrane features governing Fc receptor CD16A assembly with CD16A signaling adaptor molecules. *Proceedings of the National Academy of Sciences,* 114**,** E5645-E5654.

BLOUSHTAIN, N., QIMRON, U., BAR-ILAN, A., HERSHKOVITZ, O., GAZIT, R., FIMA, E., KORC, M., VLODAVSKY, I., BOVIN, N. V. & PORGADOR, A. 2004. Membrane-associated heparan sulfate proteoglycans are involved in the recognition of cellular targets by NKp30 and NKp46. *The Journal of Immunology,* 173**,** 2392-2401.

BLUM, K. S. & PABST, R. 2007. Lymphocyte numbers and subsets in the human blood: Do they mirror the situation in all organs? *Immunology letters,* 108**,** 45-51.

BOGGS, S. S., TREVISAN, M., PATRENE, K. & GEOGOPOULOS, K. 1998. Lack of natural killer cell precursors in fetal liver of Ikaros knockout mutant mice. *Natural immunity,* 16**,** 137-145.

BOLITHO, P., VOSKOBOINIK, I., TRAPANI, J. A. & SMYTH, M. J. 2007. Apoptosis induced by the lymphocyte effector molecule perforin. *Current opinion in immunology,* 19**,** 339-347.

BOTTINO, C., CASTRICONI, R., PENDE, D., RIVERA, P., NANNI, M., CARNEMOLLA, B., CANTONI, C., GRASSI, J., MARCENARO, S. & REYMOND, N. 2003. Identification of PVR (CD155) and Nectin-2 (CD112) as cell surface ligands for the human DNAM-1 (CD226) activating molecule. *Journal of Experimental Medicine,* 198**,** 557-567.

BRADY, J., HAYAKAWA, Y., SMYTH, M. J. & NUTT, S. L. 2004. IL-21 induces the functional maturation of murine NK cells. *The Journal of Immunology,* 172**,** 2048-2058.

BRANDT, C. S., BARATIN, M., EUGENE, C. Y., KENNEDY, J., GAO, Z., FOX, B., HALDEMAN, B., OSTRANDER, C. D., KAIFU, T. & CHABANNON, C. 2009. The B7 family member B7-H6 is a tumor cell ligand for the activating natural killer cell receptor NKp30 in humans. *Journal of Experimental Medicine,* 206**,** 1495-1503.

BRAUD, V. M., ALLAN, D. S., O'CALLAGHAN, C. A. & SODERSTROM, K. 1998a. HLA-E binds to natural killer cell receptors CD94/NKG2A, B and C. *Nature,* 391**,** 795.

BRAUD, V. M., ALLAN, D. S., O'CALLAGHAN, C. A., SÖDERSTRÖM, K., D'ANDREA, A., OGG, G. S., LAZETIC, S., YOUNG, N. T., BELL, J. I. & PHILLIPS, J. H. 1998b. HLA-E binds to natural killer cell receptors CD94/NKG2A, B and C. *Nature,* 391**,** 795-799.

BROWN, A. C., ODDOS, S., DOBBIE, I. M., ALAKOSKELA, J.-M., PARTON, R. M., EISSMANN, P., NEIL, M. A., DUNSBY, C., FRENCH, P. M. & DAVIS, I. 2011. Remodelling of cortical actin where lytic granules dock at natural killer cell immune synapses revealed by super-resolution microscopy. *PLoS biology,* 9**,** e1001152.

BROWN, M. H., BOLES, K., VAN DER MERWE, P. A., KUMAR, V., MATHEW, P. A. & BARCLAY, A. N. 1998. 2B4, the natural killer and T cell immunoglobulin superfamily surface protein, is a ligand for CD48. *Journal of Experimental Medicine,* 188**,** 2083-2090.

BRYCESON, Y. T., MARCH, M. E., BARBER, D. F., LJUNGGREN, H.-G. & LONG, E. O. 2005. Cytolytic granule polarization and degranulation controlled by different receptors in resting NK cells. *Journal of Experimental Medicine,* 202**,** 1001-1012.

BRYCESON, Y. T., MARCH, M. E., LJUNGGREN, H.-G. & LONG, E. O. 2006. Synergy among receptors on resting NK cells for the activation of natural cytotoxicity and cytokine secretion. *Blood,* 107**,** 159-166.

BUCKLEY, R. H., SCHIFF, R. I., SCHIFF, S. E., MARKERT, M. L., WILLIAMS, L. W., HARVILLE, T. O., ROBERTS, J. L. & PUCK, J. M. 1997. Human severe combined immunodeficiency: genetic, phenotypic, and functional diversity in one hundred eight infants. *The Journal of pediatrics,* 130**,** 378-387.

BUNNELL, S. C., HONG, D. I., KARDON, J. R., YAMAZAKI, T., MCGLADE, C. J., BARR, V. A. & SAMELSON, L. E. 2002. T cell receptor ligation induces the formation of dynamically regulated signaling assemblies. *The Journal of cell biology,* 158**,** 1263-1275.

BUNNELL, S. C., KAPOOR, V., TRIBLE, R. P., ZHANG, W. & SAMELSON, L. E. 2001. Dynamic actin polymerization drives T cell receptor–induced spreading: a role for the signal transduction adaptor LAT. *Immunity,* 14**,** 315-329.

BURSHTYN, D. N., SCHARENBERG, A. M., WAGTMANN, N., RAJAGOPALAN, S., BERRADA, K., YI, T., KINET, J.-P. & LONG, E. O. 1996. Recruitment of tyrosine phosphatase HCP by the killer cell inhibitory receptor. *Immunity,* 4**,** 77-85.

BURSHTYN, D. N., SHIN, J., STEBBINS, C. & LONG, E. O. 2000. Adhesion to target cells is disrupted by the killer cell inhibitory receptor. *Current biology,* 10**,** 777-780.

CALIGIURI, M. A. 2008. Human natural killer cells. *Blood,* 112**,** 461-469.

CAMPBELL, K. S. & HASEGAWA, J. 2013. Natural killer cell biology: an update and future directions. *Journal of Allergy and Clinical Immunology,* 132**,** 536-544.

CARISEY, A. F., MACE, E. M., SAEED, M. B., DAVIS, D. M. & ORANGE, J. S. under review. Nanoscale dynamism of F-actin enables secretory function in cytolytic cells.

CARTRON, G., DACHEUX, L., SALLES, G., SOLAL-CELIGNY, P., BARDOS, P., COLOMBAT, P. & WATIER, H. 2002. Therapeutic activity of humanized anti-CD20 monoclonal antibody and polymorphism in IgG Fc receptor FcγRIIIa gene. *Blood,* 99**,** 754-758.

CARTWRIGHT, A. N., GRIGGS, J. & DAVIS, D. M. 2014. The immune synapse clears and excludes molecules above a size threshold. *Nature communications,* 5.

CERBONI, C., ARDOLINO, M., SANTONI, A. & ZINGONI, A. 2009. Detuning CD8+ T lymphocytes by down-regulation of the activating receptor NKG2D: role of NKG2D ligands released by activated T cells. *Blood,* 113**,** 2955-2964.

CHAMPSAUR, M. & LANIER, L. L. 2010. Effect of NKG2D ligand expression on host immune responses. *Immunological reviews,* 235**,** 267-285.

CHAN, A. C. & CARTER, P. J. 2010. Therapeutic antibodies for autoimmunity and inflammation. *Nature reviews. Immunology,* 10**,** 301.

CHAN, H.-W., KURAGO, Z. B., STEWART, C. A., WILSON, M. J., MARTIN, M. P., MACE, B. E., CARRINGTON, M., TROWSDALE, J. & LUTZ, C. T. 2003. DNA methylation maintains allele-specific KIR gene expression in human natural killer cells. *The Journal of experimental medicine,* 197**,** 245-255.

CHAN, I. H., WU, V., BILARDELLO, M., MAR, E., OFT, M., VAN VLASSELAER, P. & MUMM, J. B. 2015. The Potentiation of IFN-γ and Induction of Cytotoxic Proteins by Pegylated IL-10 in Human CD8 T Cells. *Journal of Interferon & Cytokine Research,* 35**,** 948-955.

CHAN, W. K., SUTHERLAND, M. K., LI, Y., ZALEVSKY, J., SCHELL, S. & LEUNG, W. 2012. Antibody-dependent cell-mediated cytotoxicity overcomes NK cell resistance in MLL-rearranged leukemia expressing inhibitory KIR ligands but not activating ligands. *Clinical Cancer Research,* 18**,** 6296-6305.

CHEN, Y. Q. & SHI, H. Z. 2006. CD28/CTLA-4–CD80/CD86 and ICOS–B7RP-1 costimulatory pathway in bronchial asthma. *Allergy,* 61**,** 15-26.

CHESON, B. D. & LEONARD, J. P. 2008. Monoclonal antibody therapy for B-cell non-Hodgkin's lymphoma. *New England Journal of Medicine,* 359**,** 613-626.

CHEWNING, J. H., GUDME, C. N., HSU, K. C., SELVAKUMAR, A. & DUPONT, B. 2007. KIR2DS1-positive NK cells mediate alloresponse against the C2 HLA-KIR ligand group in vitro. *The Journal of Immunology,* 179**,** 854-868.

CHOI, P. J. & MITCHISON, T. J. 2013. Imaging burst kinetics and spatial coordination during serial killing by single natural killer cells. *Proceedings of the National Academy of Sciences,* 110**,** 6488-6493.

CICCONE, E., PENDE, D., VIALE, O., THAN, A., DI DONATO, C., ORENGO, A. M., BIASSONI, R., VERDIANI, S., AMOROSO, A. & MORETTA, A. 1992. Involvement of HLA class I alleles in natural killer (NK) cell-specific functions: expression of HLA-Cw3 confers selective protection from lysis by alloreactive NK clones displaying a defined specificity (specificity 2). *Journal of Experimental Medicine,* 176**,** 963-971.

CLYNES, R. A., TOWERS, T. L., PRESTA, L. G. & RAVETCH, J. V. 2000. Inhibitory Fc receptors modulate in vivo cytoxicity against tumor targets. *Nature medicine,* 6**,** 443.

COCA, S., PEREZ-PIQUERAS, J., MARTINEZ, D., COLMENAREJO, A., SAEZ, M. A., VALLEJO, C., MARTOS, J. A. & MORENO, M. 1997. The prognostic significance of intratumoral natural killer cells in patients with colorectal carcinoma. *Cancer,* 79**,** 2320-2328.

COLCHER, D., PAVLINKOVA, G., BERESFORD, G. & BOOTH, B. 1998. Pharmacokinetics and biodistribution of genetically-engineered antibodies. *The Quarterly Journal of Nuclear Medicine and Molecular Imaging,* 42**,** 225.

COLONNA, M., NAVARRO, F., BELLÓN, T., LLANO, M., GARCÍA, P., SAMARIDIS, J., ANGMAN, L., CELLA, M. & LÓPEZ-BOTET, M. 1997. A common inhibitory receptor for major histocompatibility complex class I molecules on human lymphoid and myelomonocytic cells. *Journal of Experimental Medicine,* 186**,** 1809-1818.

COLONNA, M. & SAMARIDIS, J. 1995. Cloning of immunoglobulin-superfamily members associated with HLA-C and HLA-B recognition by human natural killer cells. *Science,* 268**,** 405-408.

CONGY-JOLIVET, N., BOLZEC, A., TERNANT, D., OHRESSER, M., WATIER, H. & THIBAULT, G. 2008. FcγRIIIa expression is not increased on natural killer cells expressing the FcγRIIIa-158V allotype. *Cancer research,* 68**,** 976-980.

COOLEY, S., XIAO, F., PITT, M., GLEASON, M., MCCULLAR, V., BERGEMANN, T. L., MCQUEEN, K. L., GUETHLEIN, L. A., PARHAM, P. & MILLER, J. S. 2007. A subpopulation of human peripheral blood NK cells that lacks inhibitory receptors for self-MHC is developmentally immature. *Blood,* 110**,** 578-586.

COOPER, M. A., FEHNIGER, T. A. & CALIGIURI, M. A. 2001a. The biology of human natural killer-cell subsets. *Trends in immunology,* 22**,** 633-640.

COOPER, M. A., FEHNIGER, T. A., TURNER, S. C., CHEN, K. S., GHAHERI, B. A., GHAYUR, T., CARSON, W. E. & CALIGIURI, M. A. 2001b. Human natural killer cells: a unique innate immunoregulatory role for the CD56 bright subset. *Blood,* 97**,** 3146-3151.

COSMAN, D., FANGER, N., BORGES, L., KUBIN, M., CHIN, W., PETERSON, L. & HSU, M.-L. 1997. A novel immunoglobulin superfamily receptor for cellular and viral MHC class I molecules. *Immunity,* 7**,** 273-282.

COSTELLO, R. T., SIVORI, S., MARCENARO, E., LAFAGE-POCHITALOFF, M., MOZZICONACCI, M.-J., REVIRON, D., GASTAUT, J.-A., PENDE, D., OLIVE, D. & MORETTA, A. 2002. Defective expression and function of natural killer cell–triggering receptors in patients with acute myeloid leukemia. *Blood,* 99**,** 3661-3667.

COUDERT, J. D., SCARPELLINO, L., GROS, F., VIVIER, E. & HELD, W. 2008. Sustained NKG2D engagement induces cross-tolerance of multiple distinct NK cell activation pathways. *Blood,* 111**,** 3571-3578.

COUDERT, J. D., ZIMMER, J., TOMASELLO, E., CEBECAUER, M., COLONNA, M., VIVIER, E. & HELD, W. 2005. Altered NKG2D function in NK cells induced by chronic exposure to NKG2D ligand–expressing tumor cells. *Blood,* 106**,** 1711-1717.

CULLEY, F. J., JOHNSON, M., EVANS, J. H., KUMAR, S., CRILLY, R., CASASBUENAS, J., SCHNYDER, T., MEHRABI, M., DEONARAIN, M. P., USHAKOV, D. S., BRAUD, V., ROTH, G., BROCK, R., KÖHLER, K. & DAVIS, D. M. 2009. Natural Killer Cell Signal Integration Balances Synapse Symmetry and Migration. *PLoS Biol,* 7**,** e1000159.

DALBETH, N. & CALLAN, M. F. 2002. A subset of natural killer cells is greatly expanded within inflamed joints. *Arthritis & Rheumatology,* 46**,** 1763-1772.

DALL'OZZO, S., TARTAS, S., PAINTAUD, G., CARTRON, G., COLOMBAT, P., BARDOS, P., WATIER, H. & THIBAULT, G. 2004. Rituximab-dependent cytotoxicity by natural killer cells. *Cancer research,* 64**,** 4664-4669.

DAVIES, J., JIANG, L., PAN, L. Z., LABARRE, M. J., ANDERSON, D. & REFF, M. 2001. Expression of GnTIII in a recombinant anti-CD20 CHO production cell line: expression

of antibodies with altered glycoforms leads to an increase in ADCC through higher affinity for FCγRIII. *Biotechnology and bioengineering,* 74**,** 288-294.

DAVIS, D. M., CHIU, I., FASSETT, M., COHEN, G. B., MANDELBOIM, O. & STROMINGER, J. L. 1999. The human natural killer cell immune synapse. *Proceedings of the National Academy of Sciences,* 96**,** 15062-15067.

DAVIS, D. M. & DUSTIN, M. L. 2004. What is the importance of the immunological synapse? *Trends in immunology,* 25**,** 323-327.

DE MARIA, A., BOZZANO, F., CANTONI, C. & MORETTA, L. 2011. Revisiting human natural killer cell subset function revealed cytolytic CD56dimCD16+ NK cells as rapid producers of abundant IFN-γ on activation. *Proceedings of the National Academy of Sciences,* 108**,** 728-732.

DE VRIES, E., KOENE, H. R., VOSSEN, J. M., GRATAMA, J.-W., VON DEM BORNE, A., WAAIJER, J., HARALDSSON, A., DE HAAS, M. & VAN TOL, M. 1996. Identification of an unusual Fc gamma receptor IIIa (CD16) on natural killer cells in a patient with recurrent infections. *Blood,* 88**,** 3022-3027.

DELCASSIAN, D., DEPOIL, D., RUDNICKA, D., LIU, M., DAVIS, D. M., DUSTIN, M. L. & DUNLOP, I. E. 2013. Nanoscale Ligand Spacing Influences Receptor Triggering in T Cells and NK Cells. *Nano Letters,* 13**,** 5608-5614.

DENG, W., GOWEN, B. G., ZHANG, L., WANG, L., LAU, S., IANNELLO, A., XU, J., ROVIS, T. L., XIONG, N. & RAULET, D. H. 2015. A shed NKG2D ligand that promotes natural killer cell activation and tumor rejection. *Science,* 348**,** 136-139.

DERRE, L., CORVAISIER, M., PANDOLFINO, M.-C., DIEZ, E., JOTEREAU, F. & GERVOIS, N. 2002. Expression of CD94/NKG2-A on human T lymphocytes is induced by IL-12: implications for adoptive immunotherapy. *The Journal of Immunology,* 168**,** 4864-4870.

DI SANTO, J. P. 2006. Natural killer cell developmental pathways: a question of balance. *Annu. Rev. Immunol.,* 24**,** 257-286.

DÖHRING, C., SCHEIDEGGER, D., SAMARIDIS, J., CELLA, M. & COLONNA, M. 1996. A human killer inhibitory receptor specific for HLA-A1, 2. *The Journal of Immunology,* 156**,** 3098-3101.

DUGAST, A.-S., TONELLI, A., BERGER, C. T., ACKERMAN, M. E., SCIARANGHELLA, G., LIU, Q., SIPS, M., TOTH, I., PIECHOCKA-TROCHA, A. & GHEBREMICHAEL, M. 2011. Decreased Fc receptor expression on innate immune cells is associated with impaired antibody-mediated cellular phagocytic activity in chronically HIV-1 infected individuals. *Virology,* 415**,** 160-167.

DUNN, G. P., OLD, L. J. & SCHREIBER, R. D. 2004. The immunobiology of cancer immunosurveillance and immunoediting. *Immunity,* 21**,** 137-148.

DUSTIN, M. L. 2008. T-cell activation through immunological synapses and kinapses. *Immunological reviews,* 221**,** 77-89.

DUSTIN, M. L. 2012. Signaling at neuro/immune synapses. *The Journal of clinical investigation,* 122**,** 1149.

EISSMANN, P., BEAUCHAMP, L., WOOTERS, J., TILTON, J. C., LONG, E. O. & WATZL, C. 2005. Molecular basis for positive and negative signaling by the natural killer cell receptor 2B4 (CD244). *Blood,* 105**,** 4722-4729.

EISSMANN, P. & DAVIS, D. M. 2010. Inhibitory and regulatory immune synapses. *Immunological Synapse.* Springer.

ERKELLER-YÜKSEL, F., HULSTAART, F., HANNET, I., ISENBERG, D. & LYDYARD, P. 1993. Lymphocyte subsets in a large cohort of patients with systemic lupus erythematosus. *Lupus,* 2**,** 227-231.

ERKELLER-YUKSEL, F., LYDYARD, P. & ISENBERG, D. 1997. Lack of NK cells in lupus patients with renal involvement. *Lupus,* 6**,** 708-712.

ESENDAGLI, G., BRUDEREK, K., GOLDMANN, T., BUSCHE, A., BRANSCHEID, D., VOLLMER, E. & BRANDAU, S. 2008. Malignant and non-malignant lung tissue areas are differentially populated by natural killer cells and regulatory T cells in non-small cell lung cancer. *Lung cancer,* 59**,** 32-40.

FARAG, S. S. & CALIGIURI, M. A. 2006. Human natural killer cell development and biology. *Blood reviews,* 20**,** 123-137.

FAURE, M. & LONG, E. O. 2002. KIR2DL4 (CD158d), an NK cell-activating receptor with inhibitory potential. *The Journal of Immunology,* 168**,** 6208-6214.

FAURIAT, C., ANDERSSON, S., BJÖRKLUND, A. T., CARLSTEN, M., SCHAFFER, M., BJÖRKSTRÖM, N. K., BAUMANN, B. C., MICHAËLSSON, J., LJUNGGREN, H.-G. & MALMBERG, K.-J. 2008. Estimation of the size of the alloreactive NK cell repertoire: studies in individuals homozygous for the group A KIR haplotype. *The Journal of Immunology,* 181**,** 6010-6019.

FAURIAT, C., LONG, E. O., LJUNGGREN, H.-G. & BRYCESON, Y. T. 2010. Regulation of human NK-cell cytokine and chemokine production by target cell recognition. *Blood,* 115**,** 2167-2176.

FERNANDEZ, N. C., TREINER, E., VANCE, R. E., JAMIESON, A. M., LEMIEUX, S. & RAULET, D. H. 2005. A subset of natural killer cells achieves self-tolerance without expressing inhibitory receptors specific for self-MHC molecules. *Blood,* 105**,** 4416-4423.

FILIPE-SANTOS, O., BUSTAMANTE, J., CHAPGIER, A., VOGT, G., DE BEAUCOUDREY, L., FEINBERG, J., JOUANGUY, E., BOISSON-DUPUIS, S., FIESCHI, C. & PICARD, C. Inborn errors of IL-12/23-and IFN-γ-mediated immunity: molecular, cellular, and clinical features. Seminars in immunology, 2006. Elsevier, 347-361.

FOGLER, W. E., VOLKER, K., MCCORMICK, K. L., WATANABE, M., ORTALDO, J. R. & WILTROUT, R. H. 1996. NK cell infiltration into lung, liver, and subcutaneous B16 melanoma is mediated by VCAM-1/VLA-4 interaction. *The Journal of Immunology,* 156**,** 4707-4714.

FORSLUND, E., SOHLBERG, E., ENQVIST, M., OLOFSSON, P. E., MALMBERG, K.-J. & ÖNFELT, B. 2015. Microchip-Based Single-Cell Imaging Reveals That CD56dimCD57− KIR− NKG2A+ NK Cells Have More Dynamic Migration Associated with Increased Target Cell Conjugation and Probability of Killing Compared to CD56dimCD57− KIR− NKG2A− NK Cells. *The Journal of Immunology,* 195**,** 3374-3381.

FREUD, A. G., BECKNELL, B., ROYCHOWDHURY, S., MAO, H. C., FERKETICH, A. K., NUOVO, G. J., HUGHES, T. L., MARBURGER, T. B., SUNG, J. & BAIOCCHI, R. A. 2005. A human CD34 (+) subset resides in lymph nodes and differentiates into CD56 bright natural killer cells. *Immunity,* 22**,** 295-304.

FURUKAWA, H., YABE, T., AKAZA, T., TADOKORO, K., TOHMA, S., INOUE, T., TOKUNAGA, K., YAMAMOTO, K., GERAGHTY, D. & JUJI, T. 1999. Cell surface expression of HLA-E molecules on PBMC from a TAP1-deficient patient. *HLA,* 53**,** 292-295.

GALANDRINI, R., TASSI, I., MATTIA, G., LENTI, L., PICCOLI, M., FRATI, L. & SANTONI, A. 2002. SH2-containing inositol phosphatase (SHIP-1) transiently translocates to raft domains and modulates CD16-mediated cytotoxicity in human NK cells. *Blood,* 100**,** 4581-4589.

GAZIT, R., GRUDA, R., ELBOIM, M., ARNON, T. I., KATZ, G., ACHDOUT, H., HANNA, J., QIMRON, U., LANDAU, G. & GREENBAUM, E. 2006. Lethal influenza infection in the absence of the natural killer cell receptor gene Ncr1. *Nature immunology,* 7**,** 517.

GIURISATO, E., CELLA, M., TAKAI, T., KUROSAKI, T., FENG, Y., LONGMORE, G. D., COLONNA, M. & SHAW, A. S. 2007. Phosphatidylinositol 3-kinase activation is required to form the NKG2D immunological synapse. *Molecular and cellular biology,* 27**,** 8583-8599.

GLAS, R., FRANKSSON, L., UNE, C., ELORANTA, M.-L., ÖHLÉN, C., ÖRN, A. & KÄRRE, K. 2000. Recruitment and activation of natural killer (NK) cells in vivo determined by the target cell phenotype. *Journal of Experimental Medicine,* 191**,** 129-138.

GLEASON, M. K., VERNERIS, M. R., TODHUNTER, D. A., ZHANG, B., MCCULLAR, V., ZHOU, S. X., PANOSKALTSIS-MORTARI, A., WEINER, L. M., VALLERA, D. A. & MILLER, J. S. 2012. Bispecific and trispecific killer cell engagers directly activate human NK Cells through CD16 signaling and induce cytotoxicity and cytokine production. *Molecular cancer therapeutics,* 11**,** 2674-2684.

GONG, J.-H., MAKI, G. & KLINGEMANN, H. 1994. Characterization of a human cell line (NK-92) with phenotypical and functional characteristics of activated natural killer cells. *Leukemia,* 8**,** 652-658.

GONZÁLEZ, S., LÓPEZ-SOTO, A., SUAREZ-ALVAREZ, B., LÓPEZ-VÁZQUEZ, A. & LÓPEZ-LARREA, C. 2008. NKG2D ligands: key targets of the immune response. *Trends in immunology,* 29**,** 397-403.

GRAEF, T., MOESTA, A. K., NORMAN, P. J., ABI-RACHED, L., VAGO, L., AGUILAR, A. M. O., GLEIMER, M., HAMMOND, J. A., GUETHLEIN, L. A. & BUSHNELL, D. A. 2009. KIR2DS4 is a product of gene conversion with KIR3DL2 that introduced specificity for HLA-A* 11 while diminishing avidity for HLA-C. *Journal of Experimental Medicine,* 206**,** 2557-2572.

GRAKOUI, A., BROMLEY, S. K., SUMEN, C., DAVIS, M. M., SHAW, A. S., ALLEN, P. M. & DUSTIN, M. L. 1999. The immunological synapse: a molecular machine controlling T cell activation. *Science,* 285**,** 221-227.

GRIER, J. T., FORBES, L. R., MONACO-SHAWVER, L., OSHINSKY, J., ATKINSON, T. P., MOODY, C., PANDEY, R., CAMPBELL, K. S. & ORANGE, J. S. 2012. Human immunodeficiency-causing mutation defines CD16 in spontaneous NK cell cytotoxicity. *The Journal of clinical investigation,* 122**,** 3769.

GROH, V., STEINLE, A., BAUER, S. & SPIES, T. 1998. Recognition of stress-induced MHC molecules by intestinal epithelial γδ T cells. *Science,* 279**,** 1737-1740.

GROH, V., WU, J., YEE, C. & SPIES, T. 2002. Tumour-derived soluble MIC ligands impair expression of NKG2D and T-cell activation. *Nature,* 419**,** 734.

GROSS, C. C., BRZOSTOWSKI, J. A., LIU, D. & LONG, E. O. 2010. Tethering of intercellular adhesion molecule on target cells is required for LFA-1–dependent NK cell adhesion and granule polarization. *The Journal of Immunology,* 185**,** 2918-2926.

GULDEVALL, K., BRANDT, L., FORSLUND, E., OLOFSSON, K., FRISK, T. W., OLOFSSON, P. E., GUSTAFSSON, K., MANNEBERG, O., VANHERBERGHEN, B. & BRISMAR, H. 2016. Microchip screening Platform for single cell assessment of nK cell cytotoxicity. *Frontiers in immunology,* 7.

GULDEVALL, K., VANHERBERGHEN, B., FRISK, T., HURTIG, J., CHRISTAKOU, A. E., MANNEBERG, O., LINDSTRÖM, S., ANDERSSON-SVAHN, H., WIKLUND, M. & ÖNFELT, B. 2010. Imaging immune surveillance of individual natural killer cells confined in microwell arrays. *PloS one,* 5**,** e15453.

GUMPERZ, J. E., BARBER, L. D., VALIANTE, N. M., PERCIVAL, L., PHILLIPS, J. H., LANIER, L. L. & PARHAM, P. 1997. Conserved and variable residues within the Bw4 motif of HLA-B make separable contributions to recognition by the NKB1 killer cell-inhibitory receptor. *The Journal of Immunology,* 158**,** 5237-5241.

GUO, H., KUMAR, P., MORAN, T. M., GARCIA-SASTRE, A., ZHOU, Y. & MALARKANNAN, S. 2009. The functional impairment of natural killer cells during influenza virus infection. *Immunology and cell biology,* 87**,** 579.

GUR, C., PORGADOR, A., ELBOIM, M., GAZIT, R., MIZRAHI, S., STERN-GINOSSAR, N., ACHDOUT, H., GHADIALLY, H., DOR, Y. & NIR, T. 2010. The activating receptor NKp46 is essential for the development of type 1 diabetes. *Nature immunology,* 11**,** 121-128.

HALLE, S., KEYSER, K. A., STAHL, F. R., BUSCHE, A., MARQUARDT, A., ZHENG, X., GALLA, M., HEISSMEYER, V., HELLER, K. & BOELTER, J. 2016. In vivo killing capacity of cytotoxic T cells is limited and involves dynamic interactions and T cell cooperativity. *Immunity,* 44**,** 233-245.

HAMON, M., BIERNE, H. & COSSART, P. 2006. Listeria monocytogenes: a multifaceted model. *Nature reviews. Microbiology,* 4**,** 423.

HARTY, J. T. & BEVANT, M. J. 1995. Specific immunity to Listeria monocytogenes in the absence of IFNγ. *Immunity,* 3**,** 109-117.

HELL, S. W. & WICHMANN, J. 1994. Breaking the diffraction resolution limit by stimulated emission: stimulated-emission-depletion fluorescence microscopy. *Optics letters,* 19**,** 780-782.

HERBERMAN, R. B., NUNN, M. E., HOLDEN, H. T. & LAVRIN, D. H. 1975a. Natural cytotoxic reactivity of mouse lymphoid cells against syngeneic and allogeneic tumors. II. Characterization of effector cells. *International journal of cancer,* 16**,** 230-239.

HERBERMAN, R. B., NUNN, M. E. & LAVRIN, D. H. 1975b. Natural cytotoxic reactivity of mouse lymphoid cells against syngeneic and allogeneic tumors. I. Distribution of reactivity and specificity. *International journal of cancer,* 16**,** 216-229.

HERVIER, B., BEZIAT, V., HAROCHE, J., MATHIAN, A., LEBON, P., GHILLANI-DALBIN, P., MUSSET, L., DEBRÉ, P., AMOURA, Z. & VIEILLARD, V. 2011. Phenotype and function of natural killer cells in systemic lupus erythematosus: Excess interferon-γ production in patients with active disease. *Arthritis & Rheumatology,* 63**,** 1698-1706.

HESS, S. T., GIRIRAJAN, T. P. & MASON, M. D. 2006. Ultra-high resolution imaging by fluorescence photoactivation localization microscopy. *Biophysical Journal,* 91**,** 4258-4272.

HIBBS, M. L., TOLVANEN, M. & CARPEN, O. 1994. Membrane-proximal Ig-like domain of Fc gamma RIII (CD16) contains residues critical for ligand binding. *The Journal of Immunology,* 152**,** 4466-4474.

HÖGLUND, P. & BRODIN, P. 2010. Current perspectives of natural killer cell education by MHC class I molecules. *Nature reviews. Immunology,* 10**,** 724.

HSU, H.-T., MACE, E. M., CARISEY, A. F., VISWANATH, D. I., CHRISTAKOU, A. E., WIKLUND, M., ÖNFELT, B. & ORANGE, J. S. 2016. NK cells converge lytic granules to promote cytotoxicity and prevent bystander killing. *J Cell Biol,* 215**,** 875-889.

HSU, K. C., KEEVER-TAYLOR, C. A., WILTON, A., PINTO, C., HELLER, G., ARKUN, K., O'REILLY, R. J., HOROWITZ, M. M. & DUPONT, B. 2005. Improved outcome in HLA-identical sibling hematopoietic stem-cell transplantation for acute myelogenous leukemia predicted by KIR and HLA genotypes. *Blood,* 105**,** 4878-4884.

HUBERT, P., HEITZMANN, A., VIEL, S., NICOLAS, A., SASTRE-GARAU, X., OPPEZZO, P., PRITSCH, O., OSINAGA, E. & AMIGORENA, S. 2011. Antibody-dependent cell cytotoxicity synapses form in mice during tumor-specific antibody immunotherapy. *Cancer research,* 71**,** 5134-5143.

HUENECKE, S., ZIMMERMANN, S. Y., KLOESS, S., ESSER, R., BRINKMANN, A., TRAMSEN, L., KOENIG, M., ERBEN, S., SEIDL, C. & TONN, T. 2010. IL-2− driven Regulation of NK Cell Receptors With Regard to the Distribution of CD16+ and CD16− Subpopulations and In Vivo Influence After Haploidentical NK Cell Infusion. *Journal of immunotherapy,* 33**,** 200-210.

HUIZINGA, T., DE HAAS, M., KLEIJER, M., NUIJENS, J. H., ROOS, D. & VON DEM BORNE, A. 1990. Soluble Fc gamma receptor III in human plasma originates from release by neutrophils. *Journal of Clinical Investigation,* 86**,** 416.

HUSTON, J., GEORGE, A., ADAMS, G., STAFFORD, W., JAMAR, F., TAI, M., MCCARTNEY, J., OPPERMANN, H., HEELAN, B. & PETERS, A. 1996. Single-chain Fv radioimmunotargeting. *The quarterly journal of nuclear medicine: official publication of the Italian Association of Nuclear Medicine (AIMN)[and] the International Association of Radiopharmacology (IAR),* 40**,** 320-333.

HUYNH, M.-L. N., FADOK, V. A. & HENSON, P. M. 2002. Phosphatidylserine-dependent ingestion of apoptotic cells promotes TGF-β1 secretion and the resolution of inflammation. *The Journal of clinical investigation,* 109**,** 41.

IMAI, K., MATSUYAMA, S., MIYAKE, S., SUGA, K. & NAKACHI, K. 2000. Natural cytotoxic activity of peripheral-blood lymphocytes and cancer incidence: an 11-year follow-up study of a general population. *The Lancet,* 356**,** 1795-1799.

ISHIGAMI, S., NATSUGOE, S., TOKUDA, K., NAKAJO, A., CHE, X., IWASHIGE, H., ARIDOME, K., HOKITA, S. & AIKOU, T. 2000. Prognostic value of intratumoral natural killer cells in gastric carcinoma. *Cancer,* 88**,** 577-583.

ITO, M., MARUYAMA, T., SAITO, N., KOGANEI, S., YAMAMOTO, K. & MATSUMOTO, N. 2006. Killer cell lectin-like receptor G1 binds three members of the classical cadherin family to inhibit NK cell cytotoxicity. *The Journal of experimental medicine,* 203**,** 289-295.

IZEDDIN, I., EL BEHEIRY, M., ANDILLA, J., CIEPIELEWSKI, D., DARZACQ, X. & DAHAN, M. 2012. PSF shaping using adaptive optics for three-dimensional single-molecule super-resolution imaging and tracking. *Optics express,* 20**,** 4957-4967.

JAMES, A. M., HSU, H.-T., DONGRE, P., UZEL, G., MACE, E. M., BANERJEE, P. P. & ORANGE, J. S. 2013. Rapid activation receptor–or IL-2–induced lytic granule convergence in human natural killer cells requires Src, but not downstream signaling. *Blood,* 121**,** 2627-2637.

JAWAHAR, S., MOODY, C., CHAN, M., FINBERG, R., GEHA, R. & CHATILA, T. 1996. Natural killer (NK) cell deficiency associated with an epitope-deficient Fc receptor type IIIA (CD16-II). *Clinical & Experimental Immunology,* 103**,** 408-413.

JENKINS, M. R. & GRIFFITHS, G. M. 2010. The synapse and cytolytic machinery of cytotoxic T cells. *Current opinion in immunology,* 22**,** 308-313.

JENKINS, M. R., RUDD-SCHMIDT, J. A., LOPEZ, J. A., RAMSBOTTOM, K. M., MANNERING, S. I., ANDREWS, D. M., VOSKOBOINIK, I. & TRAPANI, J. A. 2015. Failed CTL/NK cell killing and cytokine hypersecretion are directly linked through prolonged synapse time. *Journal of Experimental Medicine***,** jem. 20140964.

JING, Y., NI, Z., WU, J., HIGGINS, L., MARKOWSKI, T. W., KAUFMAN, D. S. & WALCHECK, B. 2015. Identification of an ADAM17 cleavage region in human CD16 (FcγRIII) and the engineering of a non-cleavable version of the receptor in NK cells. *PloS one,* 10**,** e0121788.

JOHANSSON, M. H., HÖGLUND, E., NAKAMURA, M. C. & RYAN, J. C. 1998. α1/α2 domains of H-2Dd, but not H-2Ld, induce “missing self” reactivity in vivo–No effect of H-2Ld on protection against NK cells expressing the inhibitory receptor Ly49G2. *European journal of immunology,* 28**,** 4198-4206.

JONES, S. D. & MARASCO, W. A. 1998. Antibodies for targeted gene therapy: extracellular gene targeting and intracellular expression. *Advanced drug delivery reviews,* 31**,** 153-170.

KANNAN, K., STEWART, R. M., BOUNDS, W., CARLSSON, S. R., FUKUDA, M., BETZING, K. W. & HOLCOMBE, R. F. 1996. Lysosome-associated membrane proteins h-LAMP1 (CD107a) and h-LAMP2 (CD107b) are activation-dependent cell surface glycoproteins in human peripheral blood mononuclear cells which mediate cell adhesion to vascular endothelium. *Cellular immunology,* 171**,** 10-19.

KAPLAN, D. H., SHANKARAN, V., DIGHE, A. S., STOCKERT, E., AGUET, M., OLD, L. J. & SCHREIBER, R. D. 1998. Demonstration of an interferon γ-dependent tumor surveillance system in immunocompetent mice. *Proceedings of the National Academy of Sciences,* 95**,** 7556-7561.

KEEFE, D., SHI, L., FESKE, S., MASSOL, R., NAVARRO, F., KIRCHHAUSEN, T. & LIEBERMAN, J. 2005. Perforin triggers a plasma membrane-repair response that facilitates CTL induction of apoptosis. *Immunity,* 23**,** 249-262.

KHORSHIDI, M. A., VANHERBERGHEN, B., KOWALEWSKI, J. M., GARROD, K. R., LINDSTRÖM, S., ANDERSSON-SVAHN, H., BRISMAR, H., CAHALAN, M. D. &

ÖNFELT, B. 2011. Analysis of transient migration behavior of natural killer cells imaged in situ and in vitro. *Integrative Biology,* 3**,** 770-778.

KIESSLING, R., KLEIN, E. & WIGZELL, H. 1975. „Natural" killer cells in the mouse. I. Cytotoxic cells with specificity for mouse Moloney leukemia cells. Specificity and distribution according to genotype. *European journal of immunology,* 5**,** 112-117.

KLEIN, G. 1975. The Epstein-Barr virus and neoplasia. *New England Journal of Medicine,* 293**,** 1353-1357.

KOENE, H. R., KLEIJER, M., SWAAK, A. J., SULLIVAN, K. E., BIJL, M., PETRI, M. A., KALLENBERG, C. G., ROOS, D., VON DEM BORNE, A. E. & DE HAAS, M. 1998. T FcγRIIIA-158F allele is a risk factor for systemic lupus erythematosus. *Arthritis & Rheumatology,* 41**,** 1813-1818.

KÖHLER, K., XIONG, S., BRZOSTEK, J., MEHRABI, M., EISSMANN, P., HARRISON, A., CORDOBA, S.-P., ODDOS, S., MILOSERDOV, V. & GOULD, K. 2010. Matched sizes of activating and inhibitory receptor/ligand pairs are required for optimal signal integration by human natural killer cells. *PloS one,* 5**,** e15374.

KONJEVIĆ, G., MARTINOVIĆ, K. M., VULETIĆ, A., JOVIĆ, V., JURISIĆ, V., BABOVIĆ, N. & SPUŽIĆ, I. 2007. Low expression of CD161 and NKG2D activating NK receptor is associated with impaired NK cell cytotoxicity in metastatic melanoma patients. *Clinical & experimental metastasis,* 24**,** 1-11.

KUMAR, V. & MCNERNEY, M. E. 2005. A new self: MHC-class-I-independent natural-killer-cell self-tolerance. *Nature Reviews Immunology,* 5**,** 363-374.

KURSCHUS, F. C., FELLOWS, E., STEGMANN, E. & JENNE, D. E. 2008. Granzyme B delivery via perforin is restricted by size, but not by heparan sulfate-dependent endocytosis. *Proceedings of the National Academy of Sciences,* 105**,** 13799-13804.

LAGRUE, K., CARISEY, A., MORGAN, D. J., CHOPRA, R. & DAVIS, D. M. 2015. Lenalidomide augments actin remodeling and lowers NK-cell activation thresholds. *Blood,* 126**,** 50-60.

LAGRUE, K., CARISEY, A., OSZMIANA, A., KENNEDY, P. R., WILLIAMSON, D. J., CARTWRIGHT, A., BARTHEN, C. & DAVIS, D. M. 2013. The central role of the cytoskeleton in mechanisms and functions of the NK cell immune synapse. *Immunological reviews,* 256**,** 203-221.

LAJOIE, L., CONGY-JOLIVET, N., BOLZEC, A., GOUILLEUX-GRUART, V., SICARD, E., SUNG, H. C., PEIRETTI, F., MOREAU, T., VIÉ, H. & CLÉMENCEAU, B. 2014. ADAM17-mediated shedding of FcγRIIIA on human NK cells: identification of the cleavage site and relationship with activation. *The Journal of Immunology,* 192**,** 741-751.

LANIER, L., CHANG, C., AZUMA, M., RUITENBERG, J., HEMPERLY, J. & PHILLIPS, J. 1991. Molecular and functional analysis of human natural killer cell-associated neural cell adhesion molecule (N-CAM/CD56). *The Journal of Immunology,* 146**,** 4421-4426.

LANIER, L., LE, A. M., CIVIN, C., LOKEN, M. & PHILLIPS, J. 1986. The relationship of CD16 (Leu-11) and Leu-19 (NKH-1) antigen expression on human peripheral blood NK cells and cytotoxic T lymphocytes. *The Journal of Immunology,* 136**,** 4480-4486.

LANIER, L. L. 2008. Up on the tightrope: natural killer cell activation and inhibition. *Nature immunology,* 9**,** 495-502.

LANIER, L. L., CHANG, C. & PHILLIPS, J. H. 1994. Human NKR-P1A. A disulfide-linked homodimer of the C-type lectin superfamily expressed by a subset of NK and T lymphocytes. *The Journal of Immunology,* 153**,** 2417-2428.

LANIER, L. L., YU, G. & PHILLIPS, J. H. 1989. Co-association of CD3ζ with a receptor (CD16) for IgG Fc on human natural killer cells. *Nature,* 342**,** 803-805.

LARGHI, P., WILLIAMSON, D. J., CARPIER, J.-M., DOGNIAUX, S., CHEMIN, K., BOHINEUST, A., DANGLOT, L., GAUS, K., GALLI, T. & HIVROZ, C. 2013. VAMP7 controls T cell activation by regulating the recruitment and phosphorylation of vesicular Lat at TCR-activation sites. *Nature immunology,* 14**,** 723-731.

LAZAR, G. A., DANG, W., KARKI, S., VAFA, O., PENG, J. S., HYUN, L., CHAN, C., CHUNG, H. S., EIVAZI, A. & YODER, S. C. 2006. Engineered antibody Fc variants with enhanced effector function. *Proceedings of the National Academy of Sciences of the United States of America,* 103**,** 4005-4010.

LEE, J., ZHANG, T., HWANG, I., KIM, A., NITSCHKE, L., KIM, M., SCOTT, J. M., KAMIMURA, Y., LANIER, L. L. & KIM, S. 2015. Epigenetic modification and antibody-dependent expansion of memory-like NK cells in human cytomegalovirus-infected individuals. *Immunity,* 42**,** 431-442.

LEPPERS-VAN DE STRAAT, F., VAN DER POL, W., JANSEN, M., SUGITA, N., YOSHIE, H., KOBAYASHI, T. & VAN DE WINKEL, J. 2000. A novel PCR-based method for direct Fcγ receptor IIIa (CD16) allotyping. *Journal of immunological methods,* 242**,** 127-132.

LEUNG, K. & LEUNG, G. 1981. Induction of natural killer cells during murine influenza virus infection. *Immunobiology,* 160**,** 352-366.

LEVY, E. M., ROBERTI, M. P. & MORDOH, J. 2011. Natural killer cells in human cancer: from biological functions to clinical applications. *BioMed Research International,* 2011.

LIAO, N.-S., BIX, M., ZIJLSTRA, M., JAENISCH, R. & RAULET, D. 1991. MHC class I deficiency: susceptibility to natural killer (NK) cells and impaired NK activity. *Science,* 253**,** 199-202.

LILLEMEIER, B. F., MÖRTELMAIER, M. A., FORSTNER, M. B., HUPPA, J. B., GROVES, J. T. & DAVIS, M. M. 2010. TCR and Lat are expressed on separate protein islands on T cell membranes and concatenate during activation. *Nature immunology,* 11**,** 90-96.

LIU, D., MARTINA, J. A., WU, X. S., HAMMER III, J. A. & LONG, E. O. 2011. Two modes of lytic granule fusion during degranulation by natural killer cells. *Immunology and cell biology,* 89**,** 728.

LIU, D., PETERSON, M. E. & LONG, E. O. 2012. The adaptor protein Crk controls activation and inhibition of natural killer cells. *Immunity,* 36**,** 600-611.

LIU, Q., JIN, W.-N., LIU, Y., SHI, K., SUN, H., ZHANG, F., ZHANG, C., GONZALES, R. J., SHETH, K. N. & LA CAVA, A. 2017. Brain Ischemia Suppresses Immunity in the Periphery and Brain via Different Neurogenic Innervations. *Immunity,* 46**,** 474-487.

LIU, Q., SUN, Y., RIHN, S., NOLTING, A., TSOUKAS, P. N., JOST, S., COHEN, K., WALKER, B. & ALTER, G. 2009. Matrix metalloprotease inhibitors restore impaired NK cell-mediated antibody-dependent cellular cytotoxicity in human immunodeficiency virus type 1 infection. *Journal of virology,* 83**,** 8705-8712.

LOFTUS, C., SAEED, M., DAVIS, D. M. & DUNLOP, I. E. submited. Activation of human Natural Killer cells by graphene oxide-templated antibody nanoclusters.

LONG, E. O. 2008. Negative signaling by inhibitory receptors: the NK cell paradigm. *Immunological reviews,* 224**,** 70-84.

LONG, E. O., SIK KIM, H., LIU, D., PETERSON, M. E. & RAJAGOPALAN, S. 2013. Controlling natural killer cell responses: integration of signals for activation and inhibition. *Annual review of immunology,* 31**,** 227-258.

LÓPEZ-SOTO, A., FOLGUERAS, A., SETO, E. & GONZALEZ, S. 2009. HDAC3 represses the expression of NKG2D ligands ULBPs in epithelial tumour cells: potential implications for the immunosurveillance of cancer. *Oncogene,* 28**,** 2370-2382.

LÓPEZ-SOTO, A., HUERGO-ZAPICO, L., GALVÁN, J. A., RODRIGO, L., DE HERREROS, A. G., ASTUDILLO, A. & GONZALEZ, S. 2013a. Epithelial–Mesenchymal Transition Induces an Antitumor Immune Response Mediated by NKG2D Receptor. *The Journal of Immunology,* 190**,** 4408-4419.

LÓPEZ-SOTO, A., ZAPICO, L. H., ACEBES-HUERTA, A., RODRIGO, L. & GONZALEZ, S. 2013b. Regulation of NKG2D signaling during the epithelial-to-mesenchymal transition. *Oncoimmunology,* 2.

LOPEZ-VERGÈS, S., MILUSH, J. M., SCHWARTZ, B. S., PANDO, M. J., JARJOURA, J., YORK, V. A., HOUCHINS, J. P., MILLER, S., KANG, S.-M. & NORRIS, P. J. 2011. Expansion of a unique CD57+ NKG2Chi natural killer cell subset during acute human cytomegalovirus infection. *Proceedings of the National Academy of Sciences,* 108**,** 14725-14732.

LUETKE-EVERSLOH, M., CICEK, B. B., SIRACUSA, F., THOM, J. T., HAMANN, A., FRISCHBUTTER, S., BAUMGRASS, R., CHANG, H. D., THIEL, A. & DONG, J. 2014. NK cells gain higher IFN-γ competence during terminal differentiation. *European journal of immunology,* 44**,** 2074-2084.

LUNEMANN, S., MALONE, D. F., HENGST, J., PORT, K., GRABOWSKI, J., DETERDING, K., MARKOVA, A., BREMER, B., SCHLAPHOFF, V. & CORNBERG, M. 2013. Compromised function of natural killer cells in acute and chronic viral hepatitis. *The Journal of infectious diseases,* 209**,** 1362-1373.

MA, A., KOKA, R. & BURKETT, P. 2006. Diverse functions of IL-2, IL-15, and IL-7 in lymphoid homeostasis. *Annu. Rev. Immunol.,* 24**,** 657-679.

MACE, E. M., DONGRE, P., HSU, H.-T., SINHA, P., JAMES, A. M., MANN, S. S., FORBES, L. R., WATKIN, L. B. & ORANGE, J. S. 2014. Cell biological steps and checkpoints in accessing NK cell cytotoxicity. *Immunology and cell biology,* 92**,** 245.

MACE, E. M., WU, W. W., HO, T., MANN, S. S., HSU, H.-T. & ORANGE, J. S. 2012. NK cell lytic granules are highly motile at the immunological synapse and require F-actin for post-degranulation persistence. *The Journal of Immunology,* 189**,** 4870-4880.

MAHER, S., TOOMEY, D., CONDRON, C. & BOUCHIER-HAYES, D. 2002. Activation-induced cell death: the controversial role of Fas and Fas ligand in immune privilege and tumour counterattack. *Immunology and cell biology,* 80**,** 131.

MANDELBOIM, O., LIEBERMAN, N., LEV, M., PAUL, L., ARNON, T. I., BUSHKIN, Y., DAVIS, D. M., STROMINGER, J. L., YEWDELL, J. W. & PORGADOR, A. 2001. Recognition

of haemagglutinins on virus-infected cells by NKp46 activates lysis by human NK cells. *Nature,* 409**,** 1055-1060.

MARTIN, M. P., GAO, X., JEONG-HEE, L., NELSON, G. W., DETELS, R., GOEDERT, J. J., BUCHBINDER, S., HOOTS, K., VLAHOV, D. & TROWSDALE, J. 2002. Epistatic interaction between KIR3DS1 and HLA-B delays the progression to AIDS. *Nature genetics,* 31**,** 429.

MARTINVALET, D., ZHU, P. & LIEBERMAN, J. 2005. Granzyme A induces caspase-independent mitochondrial damage, a required first step for apoptosis. *Immunity,* 22**,** 355-370.

MARTZ, E. 1976. Multiple target cell killing by the cytolytic T lymphocyte and the mechanism of cytotoxicity. *Transplantation,* 21**,** 5-11.

MCCANN, F. E., EISSMANN, P., ÖNFELT, B., LEUNG, R. & DAVIS, D. M. 2007. The activating NKG2D ligand MHC class I-related chain A transfers from target cells to NK cells in a manner that allows functional consequences. *The Journal of Immunology,* 178**,** 3418-3426.

MENTLIK, A. N., SANBORN, K. B., HOLZBAUR, E. L. & ORANGE, J. S. 2010. Rapid lytic granule convergence to the MTOC in natural killer cells is dependent on dynein but not cytolytic commitment. *Molecular biology of the cell,* 21**,** 2241-2256.

MIN-OO, G., KAMIMURA, Y., HENDRICKS, D. W., NABEKURA, T. & LANIER, L. L. 2013. Natural killer cells: walking three paths down memory lane. *Trends in immunology*.

MINGARI, M. C., PONTE, M., BERTONE, S., SCHIAVETTI, F., VITALE, C., BELLOMO, R., MORETTA, A. & MORETTA, L. 1998. HLA class I-specific inhibitory receptors in human T lymphocytes: interleukin 15-induced expression of CD94/NKG2A in superantigen-or alloantigen-activated CD8+ T cells. *Proceedings of the National Academy of Sciences,* 95**,** 1172-1177.

MLODZIANOSKI, M. J., SCHREINER, J. M., CALLAHAN, S. P., SMOLKOVÁ, K., DLASKOVÁ, A., ŠANTOROVÁ, J., JEŽEK, P. & BEWERSDORF, J. 2011. Sample drift correction in 3D fluorescence photoactivation localization microscopy. *Optics express,* 19**,** 15009-15019.

MOCELLIN, S., PANELLI, M., WANG, E., ROSSI, C., PILATI, P., NITTI, D., LISE, M. & MARINCOLA, F. 2004. IL-10 stimulatory effects on human NK cells explored by gene profile analysis. *Genes and immunity,* 5**,** 621.

MOLFETTA, R., QUATRINI, L., ZITTI, B., CAPUANO, C., GALANDRINI, R., SANTONI, A. & PAOLINI, R. 2016. Regulation of NKG2D expression and signaling by endocytosis. *Trends in immunology,* 37**,** 790-802.

MONKS, C. R., FREIBERG, B. A., KUPFER, H., SCIAKY, N. & KUPFER, A. 1998. Three-dimensional segregation of supramolecular activation clusters in T cells. *Nature,* 395**,** 82-86.

MROZEK, E., ANDERSON, P. & CALIGIURI, M. 1996. Role of interleukin-15 in the development of human CD56+ natural killer cells from CD34+ hematopoietic progenitor cells. *Blood,* 87**,** 2632-2640.

MÜLLBACHER, A., HLA, R. T., MUSETEANU, C. & SIMON, M. M. 1999. Perforin is essential for control of ectromelia virus but not related poxviruses in mice. *Journal of virology,* 73**,** 1665-1667.

MURUMKAR, P. R., DASGUPTA, S., CHANDANI, S. R., GIRIDHAR, R. & YADAV, M. R. 2010. Novel TACE inhibitors in drug discovery: a review of patented compounds. *Expert opinion on therapeutic patents,* 20**,** 31-57.

MUSOLINO, A., NALDI, N., BORTESI, B., PEZZUOLO, D., CAPELLETTI, M., MISSALE, G., LACCABUE, D., ZERBINI, A., CAMISA, R. & BISAGNI, G. 2008. Immunoglobulin G fragment C receptor polymorphisms and clinical efficacy of trastuzumab-based therapy in patients with HER-2/neu–positive metastatic breast cancer. *Journal of Clinical Oncology,* 26**,** 1789-1796.

NARNI-MANCINELLI, E., GAUTHIER, L., BARATIN, M., GUIA, S., FENIS, A., DEGHMANE, A.-E., ROSSI, B., FOURQUET, P., ESCALIÈRE, B. & KERDILES, Y. M. 2017. Complement factor P is a ligand for the natural killer cell–activating receptor NKp46. *Science immunology,* 2.

NICOLL, G., AVRIL, T., LOCK, K., FURUKAWA, K., BOVIN, N. & CROCKER, P. R. 2003. Ganglioside GD3 expression on target cells can modulate NK cell cytotoxicity via siglec-7-dependent and-independent mechanisms. *European journal of immunology,* 33**,** 1642-1648.

NIETO, A., CÁLIZ, R., PASCUAL, M., MATARÁN, L., GARCÍA, S. & MARTÍN, J. 2000. Involvement of Fcγ receptor IIIA genotypes in susceptibility to rheumatoid arthritis. *Arthritis & Rheumatology,* 43**,** 735-739.

NIMMERJAHN, F. & RAVETCH, J. V. 2008. Fc [gamma] receptors as regulators of immune responses. *Nature reviews. Immunology,* 8**,** 34.

NORCROSS, M. A synaptic basis for T-lymphocyte activation. Annales de l'Institut Pasteur/Immunologie, 1984. Elsevier, 113-134.

O'SHEA, J. J., WEISSMAN, A. M., KENNEDY, I. & ORTALDO, J. R. 1991. Engagement of the natural killer cell IgG Fc receptor results in tyrosine phosphorylation of the zeta chain. *Proceedings of the National Academy of Sciences,* 88**,** 350-354.

ODDOS, S., DUNSBY, C., PURBHOO, M. A., CHAUVEAU, A., OWEN, D. M., NEIL, M. A., DAVIS, D. M. & FRENCH, P. M. 2008. High-speed high-resolution imaging of intercellular immune synapses using optical tweezers. *Biophysical journal,* 95**,** L66-L68.

OGASAWARA, K., HAMERMAN, J. A., HSIN, H., CHIKUMA, S., BOUR-JORDAN, H., CHEN, T., PERTEL, T., CARNAUD, C., BLUESTONE, J. A. & LANIER, L. L. 2003. Impairment of NK cell function by NKG2D modulation in NOD mice. *Immunity,* 18**,** 41-51.

OLDHAM, R. K. & HERBERMAN, R. B. 1973. Evaluation of cell-mediated cytotoxic reactivity against tumor associated antigens with 125I-iododeoxyuridine labeled target cells. *The Journal of Immunology,* 111**,** 1862-1871.

ORANGE, J. S. 2008. Formation and function of the lytic NK-cell immunological synapse. *Nature Reviews Immunology,* 8**,** 713-725.

ORANGE, J. S. 2013. Natural killer cell deficiency. *Journal of Allergy and Clinical Immunology,* 132**,** 515-525.

ORR, M. T., MURPHY, W. J. & LANIER, L. L. 2010. 'Unlicensed'natural killer cells dominate the response to cytomegalovirus infection. *Nature immunology,* 11**,** 321-327.

OSBORNE, J. M., CHACKO, G. W., BRANDT, J. T. & ANDERSON, C. L. 1994. Ethnic variation in frequency of an allelic polymorphism of human Fcγ RIIA determined with allele specific oligonucleotide probes. *Journal of immunological methods,* 173**,** 207-217.

OSZMIANA, A., WILLIAMSON, D. J., CORDOBA, S.-P., MORGAN, D. J., KENNEDY, P. R., STACEY, K. & DAVIS, D. M. 2016. The size of activating and inhibitory killer Ig-like receptor nanoclusters is controlled by the transmembrane sequence and affects signaling. *Cell reports,* 15**,** 1957-1972.

OVESNÝ, M., KŘÍŽEK, P., BORKOVEC, J., ŠVINDRYCH, Z. & HAGEN, G. M. 2014. ThunderSTORM: a comprehensive ImageJ plug-in for PALM and STORM data analysis and super-resolution imaging. *Bioinformatics***,** btu202.

PAGEON, S. V., CORDOBA, S.-P., OWEN, D. M., ROTHERY, S. M., OSZMIANA, A. & DAVIS, D. M. 2013. Superresolution Microscopy Reveals Nanometer-Scale Reorganization of Inhibitory Natural Killer Cell Receptors upon Activation of NKG2D. *Science signaling,* 6**,** ra62.

PAMER, E. G. 2004. Immune responses to Listeria monocytogenes. *Nature reviews. Immunology,* 4**,** 812.

PARDO, J., BALKOW, S., ANEL, A. & SIMON, M. M. 2002. Granzymes are essential for natural killer cell-mediated and perf-facilitated tumor control. *European journal of immunology,* 32**,** 2881-2886.

PARK, Y. W., KEE, S. J., CHO, Y. N., LEE, E. H., LEE, H. Y., KIM, E. M., SHIN, M. H., PARK, J. J., KIM, T. J. & LEE, S. S. 2009. Impaired differentiation and cytotoxicity of natural killer cells in systemic lupus erythematosus. *Arthritis & Rheumatology,* 60**,** 1753-1763.

PARRISH-NOVAK, J., DILLON, S. R., NELSON, A. & HAMMOND, A. 2000. Interleukin 21 and its receptor are involved in NK cell expansion and regulation of lymphocyte function. *Nature,* 408**,** 57.

PAUST, S. & VON ANDRIAN, U. H. 2011. Natural killer cell memory. *Nature immunology,* 12**,** 500-508.

PAZMANY, L. 2005. Do NK cells regulate human autoimmunity? *Cytokine,* 32**,** 76-80.

PEGRAM, H. J., ANDREWS, D. M., SMYTH, M. J., DARCY, P. K. & KERSHAW, M. H. 2010. Activating and inhibitory receptors of natural killer cells. *Immunology and cell biology,* 89**,** 216-224.

PENDE, D., BIASSONI, R., CANTONI, C., VERDIANI, S., FALCO, M., DI DONATO, C., ACCAME, L., BOTTINO, C., MORETTA, A. & MORETTA, L. 1996. The natural killer cell receptor specific for HLA-A allotypes: a novel member of the p58/p70 family of inhibitory receptors that is characterized by three immunoglobulin-like domains and is expressed as a 140-kD disulphide-linked dimer. *Journal of Experimental Medicine,* 184**,** 505-518.

PENDE, D., PAROLINI, S., PESSINO, A., SIVORI, S., AUGUGLIARO, R., MORELLI, L., MARCENARO, E., ACCAME, L., MALASPINA, A. & BIASSONI, R. 1999. Identification and molecular characterization of NKp30, a novel triggering receptor involved in natural cytotoxicity mediated by human natural killer cells. *The Journal of experimental medicine,* 190**,** 1505-1516.

PERRY, G. L. 2004. SpPack: spatial point pattern analysis in Excel using Visual Basic for Applications (VBA). *Environmental Modelling & Software,* 19**,** 559-569.

PERUZZI, G., FEMNOU, L., GIL-KRZEWSKA, A., BORREGO, F., WECK, J., KRZEWSKI, K. & COLIGAN, J. E. 2013. Membrane-type 6 matrix metalloproteinase regulates the activation-induced downmodulation of CD16 in human primary NK cells. *The Journal of Immunology,* 191**,** 1883-1894.

PESSINO, A., SIVORI, S., BOTTINO, C., MALASPINA, A., MORELLI, L., MORETTA, L., BIASSONI, R. & MORETTA, A. 1998. Molecular cloning of NKp46: a novel member of the immunoglobulin superfamily involved in triggering of natural cytotoxicity. *The Journal of experimental medicine,* 188**,** 953-960.

PICCININI, F., KISS, A. & HORVATH, P. 2015. CellTracker (not only) for dummies. *Bioinformatics,* 32**,** 955-957.

POGGE VON STRANDMANN, E., SIMHADRI, V. R., VON TRESCKOW, B., SASSE, S., REINERS, K. S., HANSEN, H. P., ROTHE, A., BÖLL, B., SIMHADRI, V. L. & BORCHMANN, P. 2007. Human leukocyte antigen-B-associated transcript 3 is released from tumor cells and engages the NKp30 receptor on natural killer cells. *Immunity,* 27**,** 965-974.

POIROT, L., BENOIST, C. & MATHIS, D. 2004. Natural killer cells distinguish innocuous and destructive forms of pancreatic islet autoimmunity. *Proceedings of the National Academy of Sciences of the United States of America,* 101**,** 8102-8107.

PROSS, H. & JONDAL, M. 1975. Cytotoxic lymphocytes from normal donors. A functional marker of human non-T lymphocytes. *Clinical and experimental immunology,* 21**,** 226.

QIU, W. Q., DE BRUIN, D., BROWNSTEIN, B. H., PEARSE, R. & RAVETCH, J. V. 1990. Organization of the Human and Mouse Low-Affinity Fc (gamma) R Genes: Duplication and Recombination. *Science,* 248**,** 732.

RADOJA, S., SAIO, M., SCHAER, D., KONERU, M., VUKMANOVIC, S. & FREY, A. B. 2001. CD8+ tumor-infiltrating T cells are deficient in perforin-mediated cytolytic activity due to defective microtubule-organizing center mobilization and lytic granule exocytosis. *The Journal of Immunology,* 167**,** 5042-5051.

RAVETCH, J. 2010. In vivo veritas: the surprising roles of Fc receptors in immunity. *Nature immunology,* 11**,** 183-185.

RAVETCH, J. V. & PERUSSIA, B. 1989. Alternative membrane forms of Fc gamma RIII (CD16) on human natural killer cells and neutrophils. Cell type-specific expression of two genes that differ in single nucleotide substitutions. *Journal of Experimental Medicine,* 170**,** 481-497.

RITTER, A. T., ANGUS, K. L. & GRIFFITHS, G. M. 2013. The role of the cytoskeleton at the immunological synapse. *Immunological reviews,* 256**,** 107-117.

RITTER, A. T., ASANO, Y., STINCHCOMBE, J. C., DIECKMANN, N., CHEN, B.-C., GAWDEN-BONE, C., VAN ENGELENBURG, S., LEGANT, W., GAO, L. & DAVIDSON, M. W. 2015. Actin depletion initiates events leading to granule secretion at the immunological synapse. *Immunity,* 42**,** 864-876.

ROBERTSON, M. J. 2002. Role of chemokines in the biology of natural killer cells. *Journal of leukocyte biology,* 71**,** 173-183.

ROMEE, R., FOLEY, B., LENVIK, T., WANG, Y., ZHANG, B., ANKARLO, D., LUO, X., COOLEY, S., VERNERIS, M. & WALCHECK, B. 2013. NK cell CD16 surface expression and function is regulated by a disintegrin and metalloprotease-17 (ADAM17). *Blood,* 121**,** 3599-3608.

ROSEN, D. B., BETTADAPURA, J., ALSHARIFI, M., MATHEW, P. A., WARREN, H. S. & LANIER, L. L. 2005. Cutting edge: lectin-like transcript-1 is a ligand for the inhibitory human NKR-P1A receptor. *The Journal of Immunology,* 175**,** 7796-7799.

RUDNICKA, D., OSZMIANA, A., FINCH, D. K., STRICKLAND, I., SCHOFIELD, D. J., LOWE, D. C., SLEEMAN, M. A. & DAVIS, D. M. 2013. Rituximab causes a polarization of B cells that augments its therapeutic function in NK-cell–mediated antibody-dependent cellular cytotoxicity. *Blood,* 121**,** 4694-4702.

RUGGERI, L., MANCUSI, A., CAPANNI, M., URBANI, E., CAROTTI, A., ALOISI, T., STERN, M., PENDE, D., PERRUCCIO, K. & BURCHIELLI, E. 2007. Donor natural killer cell allorecognition of missing self in haploidentical hematopoietic transplantation for acute myeloid leukemia: challenging its predictive value. *Blood,* 110**,** 433-440.

RUST, M. J., BATES, M. & ZHUANG, X. 2006. Sub-diffraction-limit imaging by stochastic optical reconstruction microscopy (STORM). *Nature methods,* 3**,** 793-796.

SAFTIG, P. & REISS, K. 2011. The “A Disintegrin And Metalloproteases” ADAM10 and ADAM17: novel drug targets with therapeutic potential? *European journal of cell biology,* 90**,** 527-535.

SAGE, D., KIRSHNER, H., PENGO, T., STUURMAN, N., MIN, J., MANLEY, S. & UNSER, M. 2015. Quantitative evaluation of software packages for single-molecule localization microscopy. *Nature methods,* 12**,** 717.

SALMON, J. E., NG, S., YOO, D. H., KIM, T. H., KIM, S. Y. & SONG, G. G. 1999. Altered distribution of Fcγ receptor IIIA alleles in a cohort of Korean patients with lupus nephritis. *Arthritis & Rheumatology,* 42**,** 818-823.

SANDUSKY, M. M., MESSMER, B. & WATZL, C. 2006. Regulation of 2B4 (CD244)-mediated NK cell activation by ligand-induced receptor modulation. *European journal of immunology,* 36**,** 3268-3276.

SCHAFER, J. L., MÜLLER-TRUTWIN, M. C. & REEVES, R. K. 2015. NK cell exhaustion: bad news for chronic disease? *Oncotarget,* 6**,** 21797.

SCHÖNBERG, K., SRIBAR, M., ENCZMANN, J., FISCHER, J. C. & UHRBERG, M. 2011. Analyses of HLA-C–specific KIR repertoires in donors with group A and B haplotypes suggest a ligand-instructed model of NK cell receptor acquisition. *Blood,* 117**,** 98-107.

SCHRODER, K., HERTZOG, P. J., RAVASI, T. & HUME, D. A. 2004. Interferon-γ: an overview of signals, mechanisms and functions. *Journal of leukocyte biology,* 75**,** 163-189.

SCOTT, A. M., WOLCHOK, J. D. & OLD, L. J. 2012. Antibody therapy of cancer. *Nature reviews. Cancer,* 12**,** 278.

SHANKARAN, V., IKEDA, H., BRUCE, A. T. & WHITE, J. M. 2001. IFN gamma and lymphocytes prevent primary tumour development and shape tumour immunogenicity. *Nature,* 410**,** 1107.

SHERMAN, E., BARR, V., MANLEY, S., PATTERSON, G., BALAGOPALAN, L., AKPAN, I., REGAN, C. K., MERRILL, R. K., SOMMERS, C. L. & LIPPINCOTT-SCHWARTZ, J.

2011. Functional nanoscale organization of signaling molecules downstream of the T cell antigen receptor. *Immunity,* 35**,** 705-720.

SHIELDS, R. L., NAMENUK, A. K., HONG, K., MENG, Y. G., RAE, J., BRIGGS, J., XIE, D., LAI, J., STADLEN, A. & LI, B. 2001. High resolution mapping of the binding site on human IgG1 for FcγRI, FcγRII, FcγRIII, and FcRn and design of IgG1 variants with improved binding to the FcγR. *Journal of Biological Chemistry,* 276**,** 6591-6604.

SHINKAWA, T., NAKAMURA, K., YAMANE, N., SHOJI-HOSAKA, E., KANDA, Y., SAKURADA, M., UCHIDA, K., ANAZAWA, H., SATOH, M. & YAMASAKI, M. 2003. The absence of fucose but not the presence of galactose or bisecting N-acetylglucosamine of human IgG1 complex-type oligosaccharides shows the critical role of enhancing antibody-dependent cellular cytotoxicity. *Journal of Biological Chemistry,* 278**,** 3466-3473.

SIMON, M. M., HAUSMANN, M., TRAN, T., EBNET, K., TSCHOPP, J., THAHLA, R. & MÜLLBACHER, A. 1997. In vitro–and ex vivo–derived cytolytic leukocytes from granzyme A× B double knockout mice are defective in granule-mediated apoptosis but not lysis of target cells. *Journal of Experimental Medicine,* 186**,** 1781-1786.

SIVORI, S., PENDE, D., BOTTINO, C., MARCENARO, E., PESSINO, A., BIASSONI, R., MORETTA, L. & MORETTA, A. 1999. NKp46 is the major triggering receptor involved in the natural cytotoxicity of fresh or cultured human NK cells. Correlation between surface density of NKp46 and natural cytotoxicity against autologous, allogeneic or xenogeneic target cells. *European journal of immunology,* 29**,** 1656-1666.

SMITH, C. S., JOSEPH, N., RIEGER, B. & LIDKE, K. A. 2010. Fast, single-molecule localization that achieves theoretically minimum uncertainty. *Nature methods,* 7**,** 373-375.

SMITH, K. G. & CLATWORTHY, M. R. 2010. FcγRIIB in autoimmunity and infection: evolutionary and therapeutic implications. *Nature Reviews Immunology,* 10**,** 328-343.

SMYTH, M. J., CROWE, N. Y. & GODFREY, D. I. 2001. NK cells and NKT cells collaborate in host protection from methylcholanthrene-induced fibrosarcoma. *International immunology,* 13**,** 459-463.

SMYTH, M. J., HAYAKAWA, Y., TAKEDA, K. & YAGITA, H. 2002. New aspects of natural-killer-cell surveillance and therapy of cancer. *Nature reviews. Cancer,* 2**,** 850.

SONDERMANN, P., HUBER, R., OOSTHUIZEN, V. & JACOB, U. 2000. The 3.2-A crystal structure of the human IgG1 Fc fragment-FcgammaRIII complex. *Nature,* 406**,** 267.

SONG, H., NIE, X., BASU, S. & CERNY, J. 1998. Antibody feedback and somatic mutation in B cells: regulation of mutation by immune complexes with IgG antibody. *Immunological reviews,* 162**,** 211-218.

STALLINGA, S. & RIEGER, B. 2010. Accuracy of the Gaussian point spread function model in 2D localization microscopy. *Optics express,* 18**,** 24461-24476.

STEBBINS, C. C., WATZL, C., BILLADEAU, D. D., LEIBSON, P. J., BURSHTYN, D. N. & LONG, E. O. 2003. Vav1 dephosphorylation by the tyrosine phosphatase SHP-1 as a mechanism for inhibition of cellular cytotoxicity. *Molecular and cellular biology,* 23**,** 6291-6299.

STEBLYANKO, M., ANIKEEVA, N., CAMPBELL, K. S., KEEN, J. H. & SYKULEV, Y. 2015. Integrins influence the size and dynamics of signaling microclusters in a Pyk2-dependent manner. *Journal of Biological Chemistry,* 290**,** 11833-11842.

STEIN-STREILEIN, J., BENNETT, M., MANN, D. & KUMAR, V. 1983. Natural killer cells in mouse lung: surface phenotype, target preference, and response to local influenza virus infection. *The Journal of Immunology,* 131**,** 2699-2704.

STEINLE, A., LI, P., MORRIS, D. L., GROH, V., LANIER, L. L., STRONG, R. K. & SPIES, T. 2001. Interactions of human NKG2D with its ligands MICA, MICB, and homologs of the mouse RAE-1 protein family. *Immunogenetics,* 53**,** 279-287.

STENGER, S., HANSON, D. A., TEITELBAUM, R., DEWAN, P., NIAZI, K. R., FROELICH, C. J., GANZ, T., THOMA-USZYNSKI, S., MELIÁN, A. N. & BOGDAN, C. 1998. An antimicrobial activity of cytolytic T cells mediated by granulysin. *Science,* 282**,** 121-125.

STEPP, S. E., DUFOURCQ-LAGELOUSE, R., LE DEIST, F., BHAWAN, S., CERTAIN, S., MATHEW, P. A., HENTER, J.-I., BENNETT, M., FISCHER, A. & DE SAINT BASILE, G. 1999. Perforin gene defects in familial hemophagocytic lymphohistiocytosis. *Science,* 286**,** 1957-1959.

STERN-GINOSSAR, N., GUR, C., BITON, M., HORWITZ, E., ELBOIM, M., STANIETSKY, N., MANDELBOIM, M. & MANDELBOIM, O. 2008. Human microRNAs regulate stress-induced immune responses mediated by the receptor NKG2D. *Nature immunology,* 9**,** 1065-1073.

STERN, M., RUGGERI, L., CAPANNI, M., MANCUSI, A. & VELARDI, A. 2008. Human leukocyte antigens A23, A24, and A32 but not A25 are ligands for KIR3DL1. *Blood,* 112**,** 708-710.

STEWART, C. A., LAUGIER-ANFOSSI, F., VÉLY, F., SAULQUIN, X., RIEDMULLER, J., TISSERANT, A., GAUTHIER, L., ROMAGNÉ, F., FERRACCI, G. & AROSA, F. A. 2005. Recognition of peptide–MHC class I complexes by activating killer immunoglobulin-like receptors. *Proceedings of the National Academy of Sciences of the United States of America,* 102**,** 13224-13229.

STINCHCOMBE, J. C., BOSSI, G., BOOTH, S. & GRIFFITHS, G. M. 2001. The immunological synapse of CTL contains a secretory domain and membrane bridges. *Immunity,* 15**,** 751-761.

STINCHCOMBE, J. C., MAJOROVITS, E., BOSSI, G., FULLER, S. & GRIFFITHS, G. M. 2006. Centrosome polarization delivers secretory granules to the immunological synapse. *Nature,* 443**,** 462.

STRASSER, A., JOST, P. J. & NAGATA, S. 2009. The many roles of FAS receptor signaling in the immune system. *Immunity,* 30**,** 180-192.

STREET, S. E., CRETNEY, E. & SMYTH, M. J. 2001. Perforin and interferon-γ activities independently control tumor initiation, growth, and metastasis. *Blood,* 97**,** 192-197.

SU, M., WALDEN, P. R., GOLAN, D. & EISEN, H. 1993. Cognate peptide-induced destruction of CD8+ cytotoxic T lymphocytes is due to fratricide. *The Journal of Immunology,* 151**,** 658-667.

SWANN, J. B. & SMYTH, M. J. 2007. Immune surveillance of tumors. *Journal of Clinical Investigation,* 117**,** 1137.

TAKAI, T. 2002. Roles of Fc receptors in autoimmunity. *Nature reviews. Immunology,* 2**,** 580.

TEILLAUD, J., BOUCHARD, C., ASTIER, A., TEILLAUD, C., TARTOUR, E., MICHON, J., GALINHA, A., MONCUIT, J., MAZIERES, N. & SPAGNOLI, R. 1994. Natural and recombinant soluble low-affinity FcγR: detection, purification, and functional activities. *Immunomethods,* 4**,** 48-64.

TELLIER, E., CANAULT, M., REBSOMEN, L., BONARDO, B., JUHAN-VAGUE, I., NALBONE, G. & PEIRETTI, F. 2006. The shedding activity of ADAM17 is sequestered in lipid rafts. *Experimental cell research,* 312**,** 3969-3980.

THIELENS, A., VIVIER, E. & ROMAGNÉ, F. 2012. NK cell MHC class I specific receptors (KIR): from biology to clinical intervention. *Current opinion in immunology,* 24**,** 239-245.

THOMPSON, R. E., LARSON, D. R. & WEBB, W. W. 2002. Precise nanometer localization analysis for individual fluorescent probes. *Biophysical Journal,* 82**,** 2775-2783.

TOMASELLO, E., BLERY, M., VELY, E. & VIVIER, E. Signaling pathways engaged by NK cell receptors: double concerto for activating receptors, inhibitory receptors and NK cells. Seminars in immunology, 2000. Elsevier, 139-147.

TRAPANI, J. A., JANS, D. A., JANS, P. J., SMYTH, M. J., BROWNE, K. A. & SUTTON, V. R. 1998. Efficient nuclear targeting of granzyme B and the nuclear consequences of apoptosis induced by granzyme B and perforin are caspase-dependent, but cell death is caspase-independent. *Journal of Biological Chemistry,* 273**,** 27934-27938.

TRINCHIERI, G. 1989. Biology of natural killer cells. *Advances in immunology,* 47**,** 187-376.

TRIPP, C. S., WOLF, S. F. & UNANUE, E. R. 1993. Interleukin 12 and tumor necrosis factor alpha are costimulators of interferon gamma production by natural killer cells in severe combined immunodeficiency mice with listeriosis, and interleukin 10 is a physiologic antagonist. *Proceedings of the National Academy of Sciences,* 90**,** 3725-3729.

TRUMP, B. F. & BEREZESKY, I. K. 1992. The role of cytosolic Ca2+ in cell injury, necrosis and apoptosis. *Current opinion in cell biology,* 4**,** 227-232.

UMANA, P., MOUDRY, R., AMSTUTZ, H. & BAILEY, J. E. 1999. Engineered glycoforms of an antineuroblastoma IgG1 with optimized antibody-dependent cellular cytotoxic activity. *Nature biotechnology,* 17.

VALITUTTI, S., DESSING, M., AKTORIES, K., GALLATI, H. & LANZAVECCHIA, A. 1995. Sustained signaling leading to T cell activation results from prolonged T cell receptor occupancy. Role of T cell actin cytoskeleton. *Journal of Experimental Medicine,* 181**,** 577-584.

VAN DER POL, W.-L. & VAN DE WINKEL, J. G. 1998. IgG receptor polymorphisms: risk factors for disease. *Immunogenetics,* 48**,** 222-232.

VANHERBERGHEN, B., OLOFSSON, P. E., FORSLUND, E., STERNBERG-SIMON, M., KHORSHIDI, M. A., PACOURET, S., GULDEVALL, K., ENQVIST, M., MALMBERG, K.-J. & MEHR, R. 2013. Classification of human natural killer cells based on migration behavior and cytotoxic response. *Blood,* 121**,** 1326-1334.

VENKATARAMAN, G. M., SUCIU, D., GROH, V., BOSS, J. M. & SPIES, T. 2007. Promoter region architecture and transcriptional regulation of the genes for the MHC class I-related chain A and B ligands of NKG2D. *The Journal of Immunology,* 178**,** 961-969.

VERSCHUEREN, H. 1985. Interference reflection microscopy in cell biology: methodology and applications. *Journal of Cell Science,* 75**,** 279-301.

VILLEGAS, F. R., COCA, S., VILLARRUBIA, V. G., JIMÉNEZ, R., CHILLÓN, M. A. J., JAREÑO, J., ZUIL, M. & CALLOL, L. 2002. Prognostic significance of tumor infiltrating natural killer cells subset CD57 in patients with squamous cell lung cancer. *Lung cancer,* 35**,** 23-28.

VIVIER, E., DA SILVA, A. J., ACKERLY, M., LEVINE, H., RUDD, C. E. & ANDERSON, P. 1993. Association of a 70-kDa tyrosine phosphoprotein with the CD16: ζ: γ complex expressed in human natural killer cells. *European journal of immunology,* 23**,** 1872-1876.

VIVIER, E., MORIN, P. M., O'BRIENM, C., SCHLOSSMAN, S. F. & ANDERSON, P. 1991. CD2 is functionally linked to the ζ-natural killer receptor complex. *European journal of immunology,* 21**,** 1077-1080.

VIVIER, E., NUNÈS, J. A. & VÉLY, F. 2004. Natural killer cell signaling pathways. *Science,* 306**,** 1517-1519.

VIVIER, E., TOMASELLO, E., BARATIN, M., WALZER, T. & UGOLINI, S. 2008. Functions of natural killer cells. *Nature immunology,* 9**,** 503-510.

VOSKOBOINIK, I. & TRAPANI, J. A. 2006. Addressing the mysteries of perforin function. *Immunology and cell biology,* 84**,** 66.

VYAS, Y. M., MANIAR, H. & DUPONT, B. 2002. Visualization of signaling pathways and cortical cytoskeleton in cytolytic and noncytolytic natural killer cell immune synapses. *Immunological reviews,* 189**,** 161-178.

VYAS, Y. M., MEHTA, K. M., MORGAN, M., MANIAR, H., BUTROS, L., JUNG, S., BURKHARDT, J. K. & DUPONT, B. 2001. Spatial organization of signal transduction molecules in the NK cell immune synapses during MHC class I-regulated noncytolytic and cytolytic interactions. *The Journal of Immunology,* 167**,** 4358-4367.

WALCH, M., DOTIWALA, F., MULIK, S., THIERY, J., KIRCHHAUSEN, T., CLAYBERGER, C., KRENSKY, A. M., MARTINVALET, D. & LIEBERMAN, J. 2014. Cytotoxic cells kill intracellular bacteria through granulysin-mediated delivery of granzymes. *Cell,* 157**,** 1309-1323.

WALCHECK, B., HERRERA, A. H., HILL, C. S., MATTILA, P. E., WHITNEY, A. R. & DELEO, F. R. 2006. ADAM17 activity during human neutrophil activation and apoptosis. *European journal of immunology,* 36**,** 968-976.

WALDMANN, T. A., DUBOIS, S. & TAGAYA, Y. 2001. Contrasting roles of IL-2 and IL-15 in the life and death of lymphocytes: implications for immunotherapy. *Immunity,* 14**,** 105-110.

WALZER, T., BLÉRY, M., CHAIX, J., FUSERI, N., CHASSON, L., ROBBINS, S. H., JAEGER, S., ANDRÉ, P., GAUTHIER, L. & DANIEL, L. 2007. Identification, activation, and selective in vivo ablation of mouse NK cells via NKp46. *Proceedings of the National Academy of Sciences,* 104**,** 3384-3389.

WANG, Y., WU, J., NEWTON, R., BAHAIE, N. S., LONG, C. & WALCHECK, B. 2013. ADAM17 cleaves CD16b (FcγRIIIb) in human neutrophils. *Biochimica et Biophysica Acta (BBA)-Molecular Cell Research,* 1833**,** 680-685.

WELTE, S., KUTTRUFF, S., WALDHAUER, I. & STEINLE, A. 2006. Mutual activation of natural killer cells and monocytes mediated by NKp80-AICL interaction. *Nature immunology,* 7**,** 1334-1342.

WENG, W.-K. & LEVY, R. 2003. Two immunoglobulin G fragment C receptor polymorphisms independently predict response to rituximab in patients with follicular lymphoma. *Journal of Clinical Oncology,* 21**,** 3940-3947.

WENSVEEN, F. M., JELENČIĆ, V., VALENTIĆ, S., ŠESTAN, M., WENSVEEN, T. T., THEURICH, S., GLASNER, A., MENDRILA, D., ŠTIMAC, D. & WUNDERLICH, F. T. 2015. NK cells link obesity-induced adipose stress to inflammation and insulin resistance. *Nature immunology,* 16**,** 376-385.

WIEMANN, K., MITTRÜCKER, H.-W., FEGER, U., WELTE, S. A., YOKOYAMA, W. M., SPIES, T., RAMMENSEE, H.-G. & STEINLE, A. 2005. Systemic NKG2D down-regulation impairs NK and CD8 T cell responses in vivo. *The Journal of Immunology,* 175**,** 720-729.

WILEY, S. R., SCHOOLEY, K., SMOLAK, P. J., DIN, W. S., HUANG, C.-P., NICHOLL, J. K., SUTHERLAND, G. R., SMITH, T. D., RAUCH, C. & SMITH, C. A. 1995. Identification and characterization of a new member of the TNF family that induces apoptosis. *Immunity,* 3**,** 673-682.

WILLIAMSON, D. J., OWEN, D. M., ROSSY, J., MAGENAU, A., WEHRMANN, M., GOODING, J. J. & GAUS, K. 2011. Pre-existing clusters of the adaptor Lat do not participate in early T cell signaling events. *Nature immunology,* 12**,** 655-662.

WU, J., EDBERG, J. C., REDECHA, P. B., BANSAL, V., GUYRE, P. M., COLEMAN, K., SALMON, J. E. & KIMBERLY, R. P. 1997. A novel polymorphism of FcgammaRIIIa (CD16) alters receptor function and predisposes to autoimmune disease. *Journal of Clinical Investigation,* 100**,** 1059.

WU, J. & LANIER, L. L. 2003. Natural killer cells and cancer. *Advances in cancer research,* 90**,** 127-156.

WWW.ADOOQ.COM. 2017. *TAPI-0* [Online]. Available: http://www.adooq.com/tapi-0.html [Accessed 26/9/2017.

XU, Q., KATAKURA, Y., YAMASHITA, M., FANG, S., TAMURA, T., MATSUMOTO, S.-E., AIBA, Y., TERUYA, K., OSADA, K. & NISHIKAWA, R. 2004. IL-10 augments antibody production in in vitro immunized lymphocytes by inducing a Th2-type response and B cell maturation. *Bioscience, biotechnology, and biochemistry,* 68**,** 2279-2284.

YU, J., HELLER, G., CHEWNING, J., KIM, S., YOKOYAMA, W. M. & HSU, K. C. 2007. Hierarchy of the human natural killer cell response is determined by class and quantity of inhibitory receptors for self-HLA-B and HLA-C ligands. *The Journal of Immunology,* 179**,** 5977-5989.

ZAMAI, L., AHMAD, M., BENNETT, I. M., AZZONI, L., ALNEMRI, E. S. & PERUSSIA, B. 1998. Natural killer (NK) cell–mediated cytotoxicity: differential use of TRAIL and Fas ligand by immature and mature primary human NK cells. *Journal of Experimental Medicine,* 188**,** 2375-2380.

ZHANG, T., SCOTT, J. M., HWANG, I. & KIM, S. 2013. Cutting Edge: Antibody-Dependent Memory-like NK Cells Distinguished by FcRγ Deficiency. *The Journal of Immunology,* 190**,** 1402-1406.

ZHANG, W., GORDON, M., SCHULTHEIS, A. M., YANG, D. Y., NAGASHIMA, F., AZUMA, M., CHANG, H.-M., BORUCKA, E., LURJE, G. & SHERROD, A. E. 2007a. FCGR2A and FCGR3A polymorphisms associated with clinical outcome of epidermal growth factor receptor–expressing metastatic colorectal cancer patients treated with single-agent cetuximab. *Journal of Clinical Oncology,* 25**,** 3712-3718.

ZHANG, Y., WALLACE, D. L., DE LARA, C. M., GHATTAS, H., ASQUITH, B., WORTH, A., GRIFFIN, G. E., TAYLOR, G. P., TOUGH, D. F. & BEVERLEY, P. C. 2007b. In vivo kinetics of human natural killer cells: the effects of ageing and acute and chronic viral infection. *Immunology,* 121**,** 258-265.

ZOMPI, S., HAMERMAN, J. A., OGASAWARA, K., SCHWEIGHOFFER, E., TYBULEWICZ, V. L., DI SANTO, J. P., LANIER, L. L. & COLUCCI, F. 2003. NKG2D triggers cytotoxicity in mouse NK cells lacking DAP12 or Syk family kinases. *Nature immunology,* 4**,** 565-572.